Experimental and numerical investigation of silicon carbide and refractory materials under extreme conditions

Zur Erlangung des akademischen Grades

Doktor der Ingenieurwissenschaften

Der Fakultät für Maschinenbau

Karlsruher Institut für Technologie (KIT)

genehmigte

Dissertation

von

M.Sc. Valentina Angelici Avincola

Tag der mündlichen Prüfung: Februar 4, 2016

Hauptreferent: Prof. Dr. Hans Jürgen Seifert

Korreferent: Prof. Dr.-Ing. Thomas Schulenberg

Thesis Summary

The chemical and mechanical aspects related to the use of refractory materials at high-temperatures and under oxidizing conditions were investigated. The behavior of silicon carbide and tantalum were studied with an emphasis on their performance as fuel cladding in nuclear power plants.

Currently, zirconium alloys are mainly employed as cladding materials for light water reactors (LWR). Although they have been optimized for decades, the need for a new fuel-cladding system, which would allow longer time in core and increase the performance in case of accident, has been demonstrated. The Fukushima Dai-chi event further fostered the research on this direction. Among different possible solutions, silicon carbide (SiC) is one of the materials worldwide under investigation as cladding with enhanced accident tolerance (Accident Tolerant Fuel – ATF). SiC exhibits many positive features that make it an attractive candidate for a new fuel-cladding system. In particular, SiC shows an outstanding behavior in corrosive atmosphere due to the protective silica scale, which forms on its surface in the case of passive oxidation. Even though many studies have been already conducted on SiC, further work is required to characterize SiC behavior in case of accident in a LWR.

In order to investigate the chemical behavior, first oxidation of silicon carbide composites in dry and wet atmosphere was experimentally studied up to 2000 °C at different steam and oxygen partial pressures. The volatilization of the silica was modeled by means of computational thermodynamics. Using experimentally determined equilibrium reaction constants available in the literature, the analytical Gibbs energy descriptions of $Si(OH)_4$ and $SiO(OH)_2$ gas species were developed using the CALPHAD method. These new descriptions were included into an existing thermodynamic database covering the Si-O-H-C-Ar system. Thermodynamic equilibrium calculations performed with the new database were carried out in order to define the equilibrium vapor pressures of the produced gas species. These vapor pressures were then used to model the mass loss of silicon carbide due to the volatilization of the silica scale developed during interaction with steam. The influence of parameters such as temperature, total pressure, and the ratio of the reactants on the silica volatilization, was studied in relation to the effective mass loss of silicon carbide.

One of the proposed silicon carbide matrix composite (SiC/SiC$_f$) designs foresees the presence of a metal liner between two silicon carbide composite layers, in order to ensure the tightness of the cladding. The current proposed metal by the CEA French laboratories in the so-called "Sandwich design" is tantalum. In this work, to predict the performance of tantalum under prototypical conditions, its oxidation behavior was studied at temperatures between 600 and 1100 °C. The hydrogen uptake in the metal was measured and compared with the theoretical values according to the literature.

Along with the chemical reaction, the mechanical behavior of the SiC cladding in operational and under accident conditions is a key aspect that still needs to be investigated. A finite elements analysis code (ADINA) was employed to calculate the stresses occurring in the SiC cladding. These stresses were calculated using a 2D model, which carefully accounted for the material's properties. Using the Weibull model, the failure probability of the cladding was calculated in case of operational conditions and during the loss of coolant accident (namely blowdown and reflood conditions). The use of prestress was also evaluated as method to mitigate the tensile stresses occurring in the cladding thickness. This model was applied to the experimental quench tests performed in an induction furnace at the Karlsruhe Institute of Technology (KIT) using SiC/SiC$_f$ received from Ceramic Tubular Products (CTP Llc). The samples were heated in steam atmosphere up to 2000 °C and quenched by water. The hydrogen production was measured in the case of isothermal oxidation, as well as during the heating phase, and compared with the hydrogen produced by zirconium alloys in the same conditions.

As a result, silicon carbide composites turned out to be applicable up to 64 hours at 1600 °C, and up to few hours at 1700 °C and 1800 °C. The presence of bubbles was detected on the SiC surface at high steam partial pressures. The bubbles, which may degrade the protecting SiO_2 scale, did not appear detrimental for the SiC composites under the studied conditions. The volatilization could not be measured. According to the thermodynamic calculations, more sensitive methods than those used in this work would have noted the volatilization products, which have low partial pressures in the exhaust gases. The tantalum showed a strong oxidation over all the temperatures tested. Thus, it may be a concern in a SiC composite cladding design in the case it came in contact with water. According to the FEA analyses, the tri-layered SiC cladding experiences very high stresses in case of accident conditions. The swelling proved to be a determining factor for the stress generation in the SiC thickness. In particular, the swelling combined with the thermal expansion of each layer should be carefully tuned to

lower the probability of failure of the cladding. Test simulating an accident were performed on the SiC composite. Although the results are conservative due to the absence of some loads, such as the inner and external pressure, and the irradiation of the materials, it can be concluded that SiC composite cladding survived without shuttering quench tests at up to 2000 °C.

Overall an evaluation of the mechanical and chemical performance of the SiC/SiC_f composites has been done. New results are presented and recommendations for further investigations are provided too.

Zusammenfassung

Hochtemperaturwerkstoffe finden heutzutage Anwendung in vielen Bereichen, insbesondere auch in der Energietechnik. Der Schwerpunkt dieser Arbeit liegt auf der Untersuchung des Hochtemperaturverhaltens von Siliziumkarbid als Hüllrohrmaterial in Kernkraftwerken.

Zirkoniumlegierungen werden seit mehr als 50 Jahren als Hüllrohrmaterialien in Leichtwasserreaktoren eingesetzt. Sie haben sich im Betrieb aufgrund ihrer Neutronendurchlässigkeit sowie ihrer sehr guten mechanischen und Korrosionseigenschaften bewährt und wurden für hohe Abbrände weiter optimiert. Bei nuklearen Störfällen und den damit verbundenen hohen Temperaturen führt die Oxidation der Hüllrohre in Wasserdampf allerdings zur Freisetzung beträchtlicher Mengen an Wasserstoff und Wärme, wie nicht zuletzt die katastrophalen nuklearen Unfälle in Fukushima gezeigt haben. Weltweit wird deshalb Forschung zur Entwicklung von störfalltoleranten Materialien (ATF – Accident Tolerant Fuels) für den Reaktorkern betrieben. Siliziumkarbid ist ein erfolgversprechender Kandidat für den Einsatz als Hüllrohr und anderer Strukturelemente. Diese Arbeit wurde begonnen vor dem Hintergrund langjähriger Erfahrungen des betreuenden Instituts bei der Untersuchung des Verhaltens von metallischen Reaktorwerkstoffen am KIT, insbesondere von Zirkoniumlegierungen, und mit dem Willen, neue Lösungen für unfalltolerante Hüllrohre voranzutreiben. Der Fokus liegt auf der tiefgehenden Untersuchung offener Fragestellungen für das Verhalten von Siliziumkarbid bei schweren nuklearen Störfällen.

Generell zeichnet sich Siliziumkarbid durch hervorragende Oxidations- und Korrosionseigenschaften bei hohen Temperaturen aus, die durch die Bildung einer oberflächlichen Siliziumoxidschicht bestimmt sind. Allerdings ist das Korrosionsverhalten stark von dem Herstellungsmethoden der Materialien und von der Zusammensetzung der umgebenden Atmosphäre abhängig. Deshalb wurde in dieser Arbeit die Oxidation von prototypischen SiC/SiC$_f$ Hüllrohren aus keramischen Faserverbundwerkstoffen bis 1600°C in Atmosphären mit variierenden Wasserdampf-Partialdrücken untersucht. Die Schutzwirkung der passivierenden oberflächlichen Siliziumoxidschicht kann in Dampf z.B. durch die Bildung von flüchtigen Hydroxiden beeinträchtigt werden. Im Rahmen dieser Arbeit

wurden deshalb thermodynamische Berechnungen zum Abdampfungsverhalten von SiO_2 durchgeführt. Gibbs Energiefunktionen für $Si(OH)_4$ und $SiO(OH)_2$ wurden mit Hilfe der CALPHAD Methode entwickelt und in die thermodynamische Datenbank für das System Si-O-H-C-Ar implementiert. Die Gleichgewichtspartialdrücke der gasförmigen Spezies wurden mit dem erweiterten Datensatz berechnet und zur Modellierung des Masseverlustes bei der Oxidation von SiC in Dampf genutzt. Der Einfluss von Temperatur, Druck und Gaszusammensetzung auf den effektiven Masseverlust wurde bestimmt.

Tantal wird als gasdichte Zwischenschicht in sogenannten SiC Sandwich Hüllrohren verwendet. Deshalb wurde auch das Oxidationsverhalten von Tantal in Dampf untersucht. Die Untersuchungen haben gezeigt, dass die Tantalschicht schon bei vergleichsweise niedrigen Temperaturen (600-900 °C) unter Bildung von porösen Oxidschichten stark oxidiert und deshalb im Betrieb der Kontakt mit Dampf vermieden werden muss. In der Arbeit wurden die kinetischen Reaktionskonstanten der Oxidation von Tantal in Dampf in Abhängigkeit von Temperatur und Dampfpartialdruck ermittelt. Darüber hinaus wurde die Wasserstoffaufnahme durch das verbliebene Ta Metall bestimmt.

Neben Oxidation und Korrosion bei sehr hohen Temperaturen ist auch das mechanische Verhalten der Hüllrohre bei Betriebs- und Störfallbedingungen von Bedeutung und bisher noch nicht hinreichend erforscht. Das Finite-Element-Programmsystem ADINA wurde für die Berechnung des Spannungsverlaufs über die Schichten der SiC Komposithüllrohre genutzt. Die mechanischen Spannungen wurden unter Verwendung eines 2D-Modelles und bestmöglich verfügbarer Materialdaten berechnet. Die Versagenswahrscheinlichkeit bei Betriebsbedingungen und für Kühlmittelverluststörfälle (Blowdown und Wiederfluten) wurden mit der Weibull-Verteilung berechnet. Darüber hinaus wurde auch der Einfluss von aufgebrachten Vorspannungen auf die Abschwächung von Zugspannungen im Hüllrohr bei Betrieb und unter Störfallbedingungen analysiert. Die Rechnungen wurden durch Abschreckexperimente mit SiC/SiC$_f$ Hüllrohren der Amerikanischen Firma CTP (Ceramic Tubular Products) in der Einzelstab-QUENCH-Anlage des KIT validiert. Dafür wurden die Hüllrohre von Temperaturen bis zu 2000 °C mit Wasser abgeschreckt. Zusätzlich wurde die Wasserstofffreisetzung bei diesen extrem hohen Temperaturen gemessen und mit dem Wasserstoffquellterm bei der Zirkoniumoxidation unter vergleichbaren Bedingungen verglichen.

Zusammenfassend kann festgestellt werden, dass im Rahmen der vorliegenden Arbeit die Datenbasis für das chemische und mechanische Verhalten von unfalltoleranten SiC/SiC Hüllrohren beträchtlich erweitert werden konnte.

Table of Contents

List of Figures

List of Tables

List of Symbols

α	Linear Thermal Expansion Coefficient
a	Activity
β	Volumetric Thermal Expansion Coefficient
b	Prescribed Temperature
C	Concentration
C_{Hext}	Effective hydrogen Concentration
C_{Heff}	Expected Hydrogen Concentration
$\Delta_r G_T^o$	Molar Standard Gibbs Energy of Reaction (kJ/mol)
$\Delta_r H_0^o$	Molar Standard Enthalpy Energy of Reaction (kJ/mol)
$\Delta_f H$	Enthalpy of Formation
$\Delta_f S$	Entropy of Formation(J/mol·K)
Δt	Time Step
Δm	Mass Change (g)
δ	Density (g/cm³)
d	Distance
ϵ_v	Volumetric Swelling
ϵ_l	Linear Swelling
ϵ_{swe}	Swelling
ε_{th}	Thermal Strain
E_a	Activation Energy (kJ/mol)
fef	Gibbs Free Energy Function
f_s	Number of Spacial function
f	Fugacity
g	Gravitational Acceleration (m/s)
G_T^o	Molar Gibbs Energy (kJ/mol)
G_m^{gas}	Gibbs Free Energy (for one mole of gas)
H_0^0	Standard Molar Enthalpy of Production (kJ/mol)
I	Intensity of Photons Transmitted Across a Distance
Io	Initial Intensity of Photons
J	Flux (g/m²s)
k_l	Linear Reaction Constant
k_{lin}	Linear Constant
k_p	Thermal Conductivity (W/(m·K))
k_{par}	Parabolic Constant
K_p	Reaction Constant
K_s	Sieverts Constant
λ	Wavelength
ln	Natural Logarithm
log	Logarithm Base 10

L	Length (m)
μ	Linear Attenuation Coefficient
M	Molar Mass (g/moles)
m	Weibull Modulus
m_s	Molar Fraction of the Species s
m_o	Initial Mass (g)
n	Positive Integer
N	Moles
n_t	Steps
P_i	Partial Pressure (Pascal)
P	Pressure (Pascal)
P_f	Probability of Failure
R	Gas Constant (J/(mol·K))
r_i	Inner Radius
r_o	Outer Radius
Re	Reynolds Number (-)
σ	Stress (Pa)
σ_c	Stress Below no Failure Occurs (Pa)
σ_o	Characteristic Stress (Pa)
σ_r	Radial Stress (Pa)
σ_z	Axial Stress (Pa)
σ_θ	Hoop Stress (Pa)
S	Surface (m^2)
S^o_{298}	Molar Entropy (J/(mol·K))
Sc	Schmidt Number (-)
θ	Molar Ratio Between the SiO_2 and the H_2O
ϑ	Ratio between the measured and the theoretical concentration of hydrogen in the metal
t	Time (s)
T	Temperature (K for calculation, °C for experimental work)
T_{ref}	Reference Temperature
T_f	Final Temperature
U	Conversion Coefficient
$\dot{V}$	Volumetric flow (l/h)
v	Velocity (m/s)
V	Volume (m^3)

List of Abbreviations

ATF	Accident Tolerant Fuel
BOL	Beginning of Life
CHext	Effective hydrogen Concentration
CEA	Commissariat à l'Énergie Atomique et aux Énergies Alternatives
CMC	Ceramic Matrix Composite
CTE	Coefficient of Thermal Expansion
CTP	Ceramic Tubular Products
CVD	Chemical Vapor Deposition
CVI	Chemical Vapor Infiltration
DOE	Department of Energy
DPA	Displacement per Atom
EBC	Environmental Barrier Coating
ECCS	Emergency Core Cooling System
ECR	Equivalent Clad Reacted
EDX	Energy Dispersive X-ray Spectroscopy
EMF	Electronic Force Method
EOL	End of Life
FEA	Finite Element Analysis
GDMS	Glow Discharge Mass Spectrometry
HPBR	High Pressure Burner Rig
HTGR	High Temperature Gas Reactor
IAEA	International Atomic Energy Agency
IGA	Instrumental Gas Analysis
LB-LOCA	Large-Break Loss of Coolant Accident
LHGR	Linear Heat Generation Rate
LOCA	Loss of Coolant Accident
LWR	Light Water Reactor
MIT	Massachusetts Institute of Technology
MS	Mass Spectrometry
NIST	National Institute of Standards and Technology
NRC	Nuclear Regulatory Commission
PDF	Powder Diffraction File
PWR	Pressurized Water Reactor
RIA	Reactivity Insertion Accident
SEM	Scanning Electron Microscope
SGTE	Scientific Group Thermodata Europe
TGA	Thermo Gravimetric Analysis
TMC	Thermo Mechanical Coupling
UTS	Ultimate Tensile Strength

XRD X-ray Diffraction

1. Introduction

This work was started from the objective to investigate refractory materials as part of nuclear power plants. An emphasis was given to the role of the fuel cladding. The nuclear technology is included in the so-called extreme technologies, which embrace conditions such as ultrahigh temperature, ultrahigh pressure, ultralow temperature and ultra-vacuum. During the last decades, the need for resistant materials which could withstand extreme conditions lead to the development of high performance materials, such as (Kumashiro 2000):

- High-purity materials: electronic, optical and atomic nuclear grade materials
- Perfect crystals
- New material phases
- Composites.

Depending on the function of these materials, some characteristics have to be fulfilled. For nuclear fission reactors, nuclear fusion reactors, and their high-temperature structural components, resistance to corrosion, as well as mechanical, thermal, and radioactive resistances, are required. These characteristics are in common with other applications (e.g., lubricant, abrasive polishing, high-temperature structural components), as summarized in Figure 1.1.

In this chapter a general overview of the refractory materials will be given, with a particular attention to those that are currently under consideration for nuclear applications. Moreover, the state of the art of the cladding materials will be analyzed and finally the thesis objective and outline will be described.
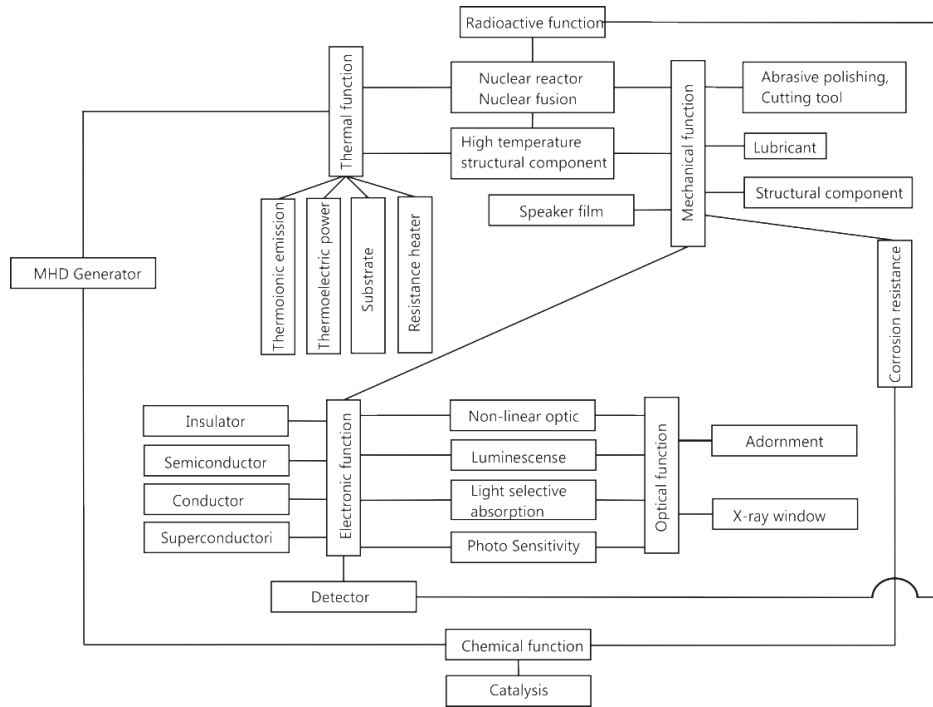
Figure 1.1: The relationship between various functions in refractory materials (Kumashiro 2000).

1.1 Refractory materials and accident tolerant fuel concepts

The functions of refractory materials are widely spread. They embrace electronic, optical, mechanical, chemical, thermal, and nuclear fission and fusion functions. ASTM C71 defines refractories as "non-metallic materials having those chemical and physical properties that make them applicable for structures or as components of systems, which are exposed to environments above 538 ℃". However, it is common to include some metals in the refractory materials group.

One cross-cutting material, which is present in all the applications mentioned above, is silicon carbide (SiC). SiC, along with silicon nitride (Si_3N_4), have been widely applied as high-temperature structural materials due to their strength, high thermal shock, and oxidation resistance (Narushima 1990; Jacobson 1993; Narushima 1997).

Silicon nitride exists in two crystalline phases: α and β-Si_3N_4. These are both based on SiN_4 tetrahedral units connected at the corners. A survey conducted by Sangster (2005) addressed that silicon nitride was mainly studied as bulk material until the mid-90. In the last two decades, the research on Si_3N_4 concentrated on thin films and its use in composites (Sangster 2005).

Silicon carbide is a crystalline compound well known for its excellent resistance to oxidation and corrosion, as well as for its good heat transfer coefficient, low expansion coefficient, and high strength at normal and elevated temperatures. Silicon carbide was discovered in the 19th century by Jöns Jakob Berzelius, who published in 1824 the discovery of a new compound, which was named "Kohlensilicium". The first who realized the potential of silicon carbide was Edward Goodrich Acheson, who started a large-scale synthesis procedure in the late 19th century. α-SiC can be found in 200 different crystal modifications (i.e., polytypes), which can differ in the basic unit or in the connection of these units. Two nomenclatures can be used to classify the different polytypes:

- Ramsdell (1947) notation: is the most commonly used notation and consists of two characters: a digit n which is derived by the smallest periodicity of the stacking order, and a letter which represents the Bravais lattice type, i.e., cubic (C), hexagonal (H), rhombohedral (R). In this nomenclature, a hexagonal crystal with the stacking order "abcacb" is named as 6H-SiC

- Jagodzinski (1949) notation: this notation considers that any layer in the stacking sequences can be described as having a local cubic (k) or hexagonal (h) environment. In this nomenclature, a hexagonal crystal with the stacking order "abcacb" is named as $(hkk)_2$

The general convention is to name β-SiC the cubic polytypes and α-SiC all other polytypes. Despite the driving forces for the occurrence of so many polytypes are still unclear (Presser 2008), it is proved that growth conditions and thermodynamic considerations play a role in the development of the structure. A systematic study of the different properties and behavior according to the different polytypes, such as for example the oxidation rate of the different crystal structure, is still missing. A summary of the SiC and Si_3N_4 properties is reported in Table 1.1.

Among the metals, the following ones can be classified as refractory: niobium (Nb), molybdenum (Mo), tantalum (Ta), tungsten (W), and rhenium (Re). Some of the common properties are the following: melting point higher than 2000 °C, high hardness at room temperature and high density. General properties of these materials are reported in Table 1.2. Tantalum, which is of major interest in this work, is a metal largely used in different applications, due to its excellent corrosion resistance, refractory character, high density, good thermal and electrical conductivity (Table 1.2).

Table 1.1: Properties of silicon nitride and silicon carbide.

	Silicon Nitride (Ziegler 1987)	Silicon Carbide (Snead 2007)
Density (21 °C)	3.1-3.2 g/cm³	3.21 g/cm³
Thermal Conductivity	15-50 (W/(m·K))	2-500 (W/(m·K))
Electrical resistivity	$\approx$1013 (Ω cm)	1 to 10^5 (Ω cm)
Young's modulus	300-330 (GPa)	460 (GPa)
Thermal expansion	$\approx$3.3 10^{-6} (K^{-1})	$\approx$4 10^{-6} (K^{-1})

Table 1.2: Properties of Nb, Mo, Ta, W, Re.

	Nb	Mo	Ta	W	Re
Density (g/cm³)	8.57	10.2	16.4	19.25	21.02
Melting point (°C)	2477	2623	3017	3422	3186
Thermal conductivity (27 °C) (W/(m·K))	53.7	138	57.5	173	48
Electrical conductivity (20 °C) (S/m)	$6.6 \cdot 10^6$	$1.9 \cdot 10^7$	$7.7 \cdot 10^6$	$1.7 \cdot 10^7$	$5.1 \cdot 10^6$

Among the current applications of Ta, which are mainly related to electronics and fabrication of chemical and mechanical equipment, tantalum is nowadays under investigation in the nuclear industry as a part of the cladding for generation IV High-Temperature Gas Reactors (Brachet 2014; Bansal 2015) and it could be considered in future as material for nuclear fuel claddings for light water reactors.

Although its melting point is 1852 °C, zirconium (Zr) is also included into the refractory metals group, along with hafnium (Hf), osmium (Os), and iridium (Ir) in a wider definition. General properties of these materials are reported in Table 1.3.

Table 1.3: Properties of Zr, Hf and Os, Ir.

	Zr	Hf	Os	Ir
Density (g/cm³)	6.52	13.31	22.57	22.56
Melting point (°C)	1855	2233	3033	2446
Thermal conductivity (27 °C) (W/(m·K))	22.6	23	87.6	147
Electrical conductivity (20 °C) (S/m)	2.4 x 10^6	3.02 x 10^6	1.2 x 10^7	2.1 x 10^7

Zirconium alloys have very low absorption cross-section of thermal neutrons[1], and they are resistant to corrosion. For these reasons, Zr has been preferred as cladding material for the fuel in commercial nuclear power plants (Light Water Reactors and Candu) in the last fifty years. Zr exhibits a hexagonal phase (α-phase) which undergoes allotropic transformation to cubic β-phase at 865 °C. Alloying elements, such as Sn, Nb, Fe, and Cr are usually added to optimize its performance. The non-metal refractory group includes transition metal carbides, nitrides and diborides.

1.2 State of the art of the nuclear fuel cladding

Since the early days of nuclear industry, efforts have been done to improve the fuel's accident tolerance as well as its economic performance in Light Water Reactors (LWR). The actual cladding material made of zirconium-based alloys (Zircaloy, Zry), was chosen in the 1950s as replacement for stainless steel. Zry was selected for its advantageous properties during operation and safety, including lower neutron absorption. As defined by the US Nuclear Regulatory Commission (US NRC), one of the "design basis accidents" concerning the pressurized water reactors involves the break in a cold leg between the reactor coolant pump and the reactor vessel. In the blowdown period, which lasts for about 30 seconds, a loss of coolant inventory occurs along with strong pressure reduction.

The cladding becomes dry due to the loss of coolant and heats up until the refill period (30-40 s), where water is injected by the Emergency Core Cooling System (ECCS) into the system.

Between 40 and 200 seconds the reflood period occurs and the water is injected into the core (OECD 2009). In order to face the eventuality of a Loss of Coolant Accident (LOCA) event, NRC defined the "acceptance criteria for emergency core cooling systems for light water nuclear reactors" (§ 50.46), which, among others, includes the following points:

- The peak cladding temperature shall not exceed 2200° F (1204 °C)
- The Equivalent Clad Reacted (ECR) including both operational corrosion and transient oxidation should not exceed the 17%

---

[1] The cross-section of Zircaloy-2 is reported to be 0.22 to 0.24 barn. Pure zirconium has a 0.18 barn cross section. The difference is attributed to the alloying agents and impurities from metal (Whitmarsh 1962).

- The change in geometry shall be so that the core remains coolable for long term.

Zirconium alloys have been facing some limitations for longer residence in the LWRs due to both corrosion and embrittlement. Indeed, the Zry critically worsened the situation during the Fukushima Dai-ichi accident by producing heat and hydrogen, causing explosions in the upper portion of different units, with significant damage to the top floors and exposure of the spent fuel pools to the environment. This highlighted the need for a cladding, which could allow for longer residence time in the reactor and could tolerate the loss of coolant for a more extensive period decreasing the hydrogen and heat production.

Currently, many cladding-fuel system designs with enhanced accident tolerance (ATF) are under consideration for deployment in PWRs. The envisioned solutions can be grouped in three categories: improved zirconium cladding, non-zirconium cladding, and alternative fuel-cladding forms (Zinkle 2014). Among the most popular ATF designs, three metal claddings (advanced stainless steel, FeCrAl alloys, molybdenum) are being investigated (Pint 2013), since their reactions with water at high temperature (1200 °C) are milder than those of zirconium (Sukjai 2013; Bragg-Sitton 2014; Park 2015). However, these metal claddings come at the expense of neutronic absorption penalty that will increase the cost of the nuclear fuel. Further options are currently different coatings solution on the Zircaloy cladding to prevent the steam to Zr metal contact (e.g., MAX Phases). However, recent research effort implies requiring a thick enough coating that would result in the same neutronic penalty as the steel alloys (Pantano 2014). While the cost of an alternative cladding could be accommodated, changing the fuel form in some ATF concepts such as TRISO fuel in SiC matrix would require larger economic investment. In addition, this solution can accommodate only small fraction of fuel compared to a standard UO_2 pellet in PWRs, which will dramatically increase the cost of fuel and could have implications for reducing the current fuel reload cycle length. Replacing the cladding with another material, namely the silicon carbide cladding, has perhaps the most potential benefit of all the ATF concepts.

Silicon carbide had been proposed with the primary purpose of improved neutronics[2] and safety (Yueh 2010; Katoh 2014; George 2015). The monolithic SiC structures behave as ceramic materials,

---

[2] The SiC microscopic thermal neutron absorption cross section is 0.086 barn.

thus undergoing brittle fracture, whereas the combination of monolithic SiC with SiC fibers in a fiber/matrix composite (SiC/SiC$_f$) has a pseudo-ductile response. For this reason, the combination of monolithic SiC and fibers is very attractive. The SiC fibers have been improved during the last years, going through three different fibers generations, in order to reach as close as possible stoichiometric composition (Bunsell 2006). Indeed, the presence of the siliconoxycarbide phase, which was typical in the first fiber generation, caused the instability of the material, in particular at high temperatures and under irradiation. The second generation overcame this problem. However, the presence of a large amount of free carbon was still affecting the oxidation and creep resistance (Bansal 2015). The third generation of SiC fibers produced was nearly stoichiometric and therefore their behavior was comparable to the SiC bulk material. To date, Hi-Nicalon Type-S and Tyranno SA SiC fibers are known to be stable under irradiation (Bansal 2015).

Many of the SiC benefits for use as cladding in LWRs have been already shown through experimental and computational works (Carpenter 2006; Snead 2007; Lee 2013). These include lower neutronic absorption of the cladding and orders of magnitude lower oxidation kinetics at possible post LOCA conditions compared to zirconium-based claddings. Many SiC cladding designs are nowadays proposed by different entities, but an early suggestion which remains promising thus far, consists of a three layers tube (Figure 1.2). In this design, an inner layer acts as a barrier for fission products. The composite layer gives the cladding the required ductility to withstand possible impacts during fuel handling, operation and safety related events. The composite layer alone is typically a porous structure that cannot stop the fission product transport to coolant (or vice versa) and thus the cladding design requires at least one monolith layer. As external layer, an environmental barrier coating (EBC) prevents coolant ingress into the strands that make up a composite middle layer. A second design proposed by the Commissariat à l'énergie atomique et aux énergies alternatives in France (CEA) has been also investigated in this work. This consists of three layers, two made of SiC/SiC$_f$ and an intermediate metal layer (tantalum or niobium) necessary to maintain the fission gas retention (Figure 1.3). This concept was mainly thought for the application in High-Temperature Gas Reactors (HTGR). However, the potential use of this cladding architecture in LWRs is also under evaluation.
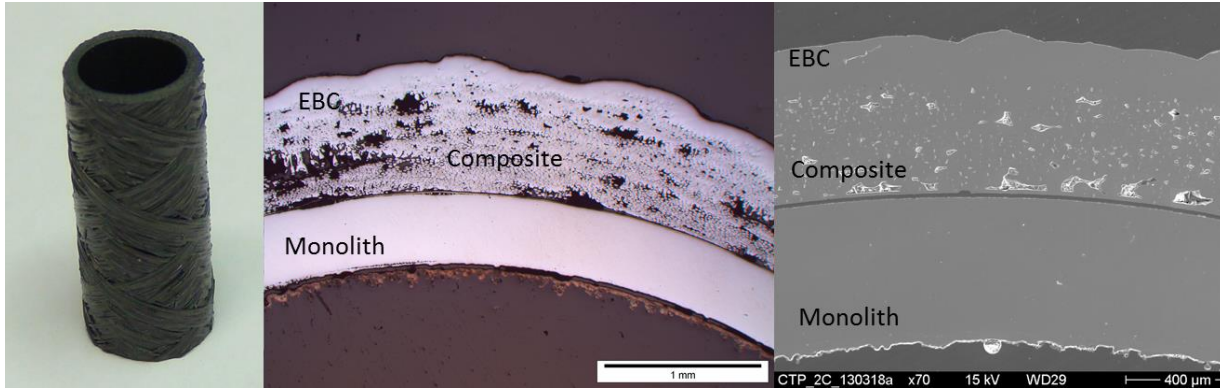
Figure 1.2: Macrograph and micrographs of a tri-layered sample's section. On the left, macrograph of a TRIPLEX sample. In the center picture, a micrograph of the section of a TRIPLEX sample made by means of optical microscopy, on the right a SEM image of the section of a TRIPLEX sample.
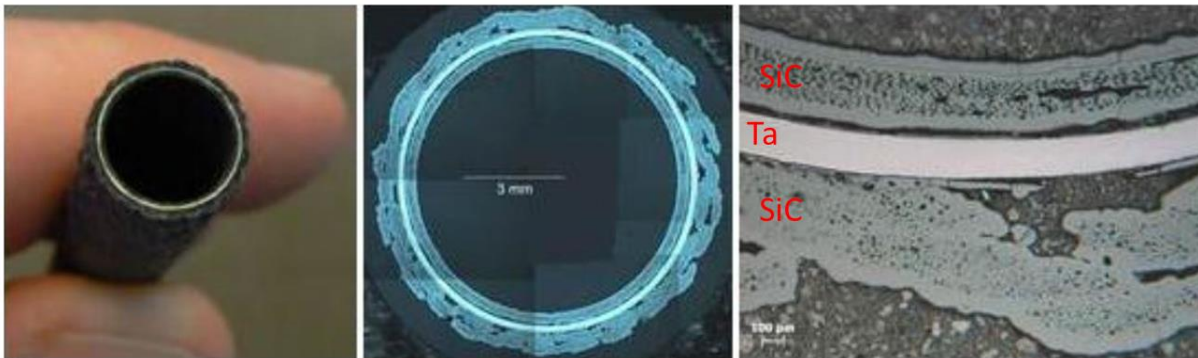
Figure 1.3: Macrograph and micrographs of a CEA sample's section (Courtesy of CEA). On the left, macrograph of a sandwich sample. In the center picture, a micrograph of the section of a sandwich sample made by means of optical microscopy, on the right a micrograph of the section of a sandwich sample at higher magnification.

Despite the SiC cladding promise, many issues still need to be resolved for its commercial deployment. The designs proposed as nuclear cladding still require assessments under operational conditions and in case of accident. This is intended under a chemical point of view, which includes the resistance to the oxidative environment, as well as the strength required to survive the strain due to thermal and mechanical stresses in the reactor's life. All these conditions are severely worsened in case of a nuclear

accident's occurrence. Other fundamental issues, which still need to be solved, are the ability to manufacture SiC cladding at the same dimensions as the current Zircaloy cladding, and the ability to join different SiC parts, in order to meet the dimension required for the nuclear core.

1.3 Thesis objective and organization

The objective of this work, which is schematized in Figure 1.4, is to evaluate the performance and safety aspect of possible accident tolerant fuels, with an emphasis on SiC cladding. In order to perform this study, two most important phenomena have been identified and explored. First, high-temperature steam reaction of SiC under representative accident conditions at temperature as high as 2000 °C has to be studied. In order to investigate this chemical issue, experimental work should be performed with cladding designs provided by two nuclear cladding producers: CEA and CTP (Ceramic Tubular Products, Llc). These prototypical designs have been oxidized and some of them have been also quenched under conditions as close as possible to a LOCA accidents.
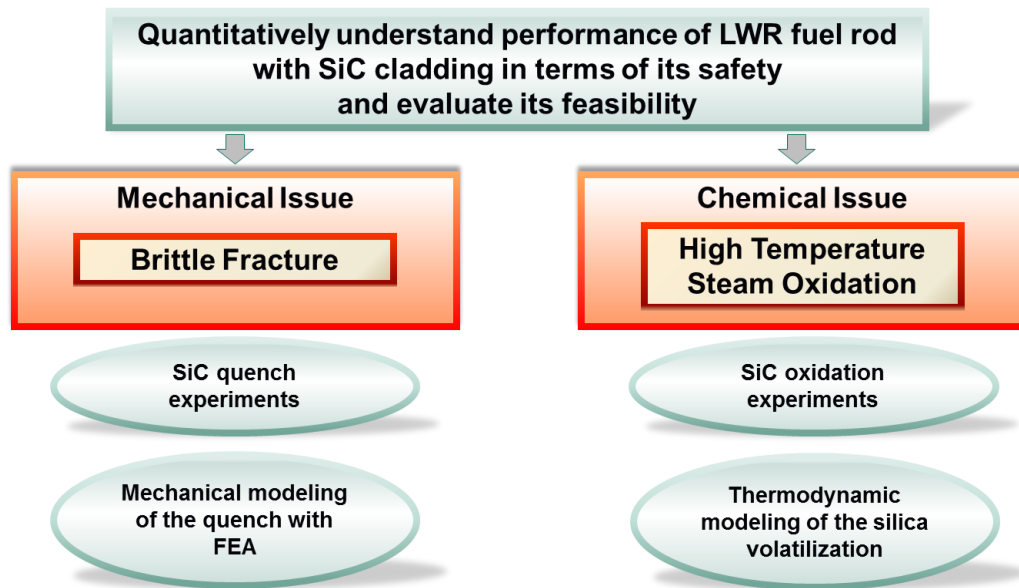
Figure 1.4: Structure of the thesis.

The second issue considered in this work is the mechanical behavior of the cladding structures. In this frame, the stresses in each layer of the SiC cladding have been calculated. During both steady state operation as well as transient scenarios, thermal shocks arising from the blowdown and subsequent

reflood could cause high thermal stresses, which may lead to a breakdown of the SiC structure. Therefore, accurate prediction of the occurring stresses is necessary to assess the SiC feasibility as fuel cladding. For this purpose, finite element analyses (FEA) will be employed in this work to deduce the stress response under case of accident conditions. Along these two main issues, work has to be done in order to study the materials related to the new cladding concepts. Indeed, the lack of data for the CEA design in the case of oxidation at high temperatures in steam environment, suggested performing separated test effect on tantalum.

Further step beyond this thesis is the study of the oxidation effect on the mechanical properties of the SiC composites. Some trials have been performed by the author in collaboration with CEA but are not presented in this work.

This thesis is divided in six parts, each of them covering a different topic faced during the work. After chapter one, which is an introduction to the refractory materials related to high-temperatures applications and nuclear technology, other five chapters are part of this manuscript.

Chapter 2 regards the experiments conducted at Karlsruhe Institute of Technology on silicon carbide in corrosive environments. These include tests in different atmospheres, such as dry oxygen and water vapor. In the dry oxidation experiments, the transition between passive and active oxidation is discussed. The oxidation experiments in steam involve the passive oxidation of silicon carbide and the bubbles formation. Thus the chapter mainly discusses this phenomenon and an explanation for the formation of bubbles on the surfaces at different temperatures is presented.

Chapter 3 deals with the modeling of the silica volatilization using the CALPHAD approach. This model determines whether the volatilization of the silica, developed on the silicon carbide surface in the case of passive oxidation, has an impact on the kinetics of the silicon carbide oxidation.

Chapter 4 analyzes the behavior of tantalum, a refractory material candidate as part of the cladding design considered by the CEA. In particular, tantalum tubes and plates have been tested under oxidizing conditions typical of LWRs accidents using thermal gravimetric analysis.

Chapter 5 analyzes the silicon carbide mechanical performance in case of nuclear accident conditions (LOCA) using a commercial finite element analysis software (ADINA). In particular, the importance of material properties, such as thermal expansion and swelling, has been addressed and studied. This work has been done in collaboration with the Massachusetts Institute of Technology (MIT).

Chapter 6 describes unique experiments performed at the Karlsruhe Institute of Technology (KIT) on the quench of silicon carbide from 2000 °C. The effect of quench on the samples has been evaluated and the stresses occurring on the cladding thickness during the occurrence of the quench procedure at lab-scale has been calculated using the ADINA code.

Chapter 7 summarizes the findings of the previous chapters and suggests future work on accident tolerant fuels.

2. SiC oxidation in dry and wet atmospheres: experiments

In this chapter, a study of the performances of silicon carbide, both monolithic and composite designs, is presented. The conditions investigated include high-temperatures and corrosive atmospheres, such as dry oxygen and wet atmospheres respectively. In particular, SiC made by means of sintering and CVD processes was respectively investigated. Among the sintering processes, several categories based on the sintering agents used, consolidation mechanisms and methods of pressurization are usually adopted to fabricate SiC bodies (Snead 2007). These methods imply the presence of additives in the final products which can cause acceleration of the oxidation (Singhal 1976), thus compromising the performance of the material. This deterioration is enhanced at high temperatures and in applications that require high purity materials. Therefore, in applications such as electronic and nuclear ones, the chemical vapor deposition is preferred to produce SiC. A wide variety of organo-metallic precursors, which contain Si and C source, are available to produce SiC CVD bodies. The deposition rate of CVD is rather small, up to several hundred μm/h (Liao 2003; Gao 2008), therefore this technique is usually employed for thin films. The employment of the CVD technique for the production of thick films and monolithic bodies is also possible (Riedel 2011), resulting in the most convenient method for nuclear applications.

2.1 Literature review

In this chapter, previous studies of oxidation of SiC in oxygen and wet atmosphere are reported. The reaction of silicon carbide with oxygen has been widely studied in the last century, in order to understand and predict the materials behavior at high temperatures in corrosive environment (Adamsky 1959; Jorgensen 1960; Gulbransen 1966; Hinze 1975; Singhal 1976; Costello 1986).

Depending upon oxidant concentration and temperature, SiC oxidation may be either passive or active. In the case passive oxidation occurs, a dense and protective oxide scale of SiO_2, amorphous at temperatures below 1673 K (Snead 2007), forms according to Eq. (2.1).

$$SiC_{(s)} + \frac{3}{2}O_{2(g)} \rightarrow SiO_{2(g)} + CO_{(g)} \tag{2.1}$$
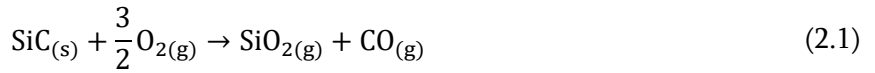
In this case, the silicon carbide's oxidation behavior follows the linear-parabolic model of Deal and Grove (Deal, 1965; Costello, 1986; Presser, 2008). The model from Deal and Grove is expressed in Eq. (2.2), where x is the oxide thickness, t is the time, A, B and τ are empirical constants.

$$x^2 + Ax = B(t + \tau) \tag{2.2}$$

In particular, B is the parabolic rate constant, and B/A is the linear rate constant, typical for the initial stage of the oxidation. However, little significance has been given to the linear constant, which varied erratically. As it is known in the literature, the oxidation rate is higher for C-face silicon carbide at temperatures lower than 1350 °C. Above this threshold, the oxidation rates reported in the literature follow two branches, which are not caused by the material's polarity (Presser 2008). In Figure 2.1 literature data concerning the parabolic constant of SiC oxidation collected by Presser (2008) are presented.

In the case Eq. (2.1) occurs, the volume ratio of the oxide formed to the consumed substrate volume is ≈1 (Pilling-Bedworth ratio), resulting in a good bond at the interface. In the case of very fast oxidation (30 °C/s), the presence of different Si oxidation states have been detected ("Si_2O_3" and "SiO") using XPS analysis (Park 2014).

The primary rate-controlling process is diffusion of oxygen through the oxide scale (Snead 2007), which can be explained by means of two mechanisms (Kalen 1991; Lamkin 1992):

- Interstitial (molecular) oxygen diffusion

- Oxygen ion diffusion through the SiO_2 tetrahedral network.
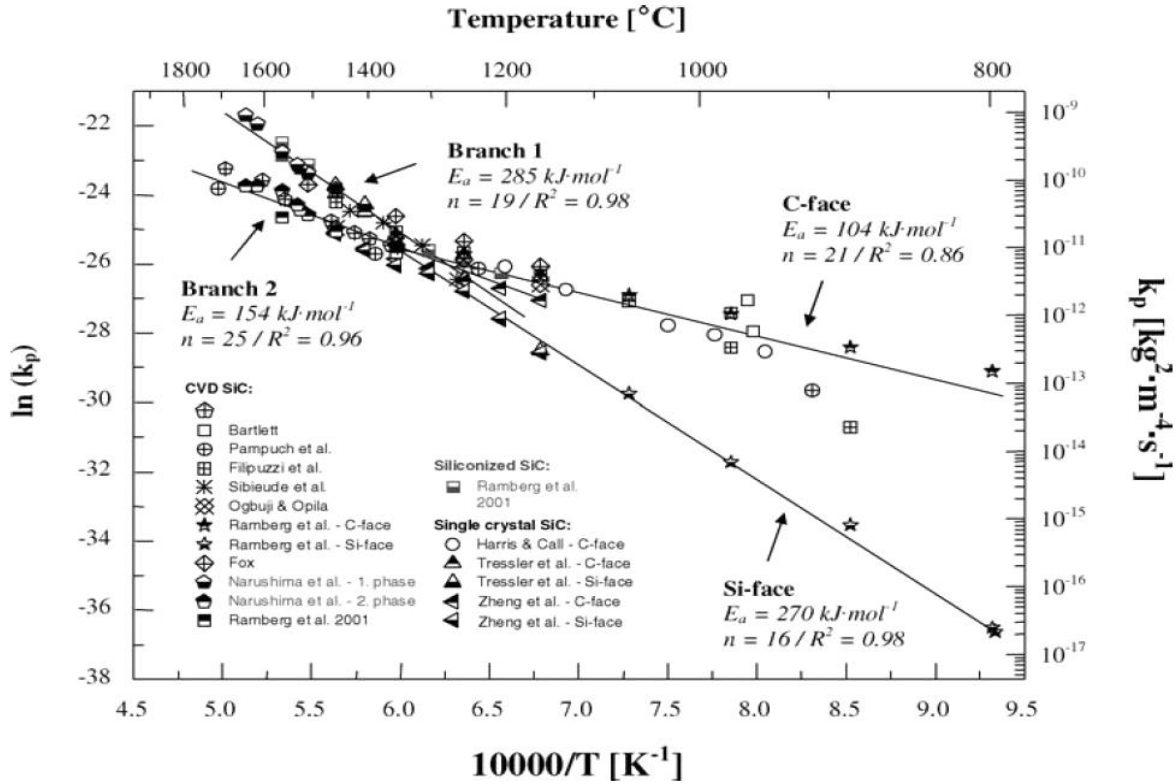
Figure 2.1: Arrhenius-plot of various parabolic rate-constants of SiC oxidation reviewed by Presser (2008).

According to calculations performed in the literature (Hoshino 2003), the diffusion of molecular oxygen is the favorite.

The second oxidation type, so-called active oxidation, occurs at higher temperatures and lower oxidant partial pressures. In this case, SiC decomposes into SiO and CO gas, as described by Eq. (2.3), without forming any protective oxide scale.

$$SiC + O_2 \rightarrow SiO + CO \tag{2.3}$$

The transition between passive and active oxidation on the silicon surface was first studied by Wagner (Wagner 1958). Wagner's theory is based on the decomposition of the SiO_2. The SiO gas partial pressure (P_{SiO}) was hypothesized being the determining factor of the transition: as long as the SiO vapor pressure at the silicon surface is less than the equilibrium pressure necessary for the condensation given in Eq. (2.4), SiO_2 will not form. In this case, Eq. (2.5) is expected.

$$SiO_{(g)} + \frac{1}{2}O_{2(g)} \rightarrow SiO_{2(s)} \tag{2.4}$$

$$Si_{(s)} + \frac{1}{2}O_{2(g)} \rightarrow SiO_{(g)} \tag{2.5}$$

Once the P_{SiO} reaches the equilibrium partial pressure, a protective layer is formed. Therefore, in the Wagner's theory the partial pressure of SiO is the critical value that determines whether passive or active oxidation occurs. This theory has been extended by other investigators to explain the passive-active transition for SiC (Gulbransen 1972; Singhal 1976; Hinze 1976).

Turkdogan (1963) developed an oxidation model which can be used for the silicon oxidation as well as for the metals. This theory predicts the formation of a so-called "fog" made of silicon oxide or silicon dioxide, as some investigators had modified. With increasing P_{O_2} in the bulk gas stream, the fog collapses on the silicon surface until the balance of the steady state is broken, and then the direct oxidation occurs on the silicon surface (Gao 2008). The difference between the theory of Wagner and that of Turkdogan can be explained as following: whilst the first is dependent on the equilibrium conditions, the second depends on kinetics and mass transport. Thus, the Turkdogan's theory has been rarely adopted due to a lack of knowledge of the detailed kinetics and transport (Riedel 2013).

Gulbransen (1966) investigated the transition between active and passive oxidation with a micro-balance, and identified the transition at 1300 °C between $1.3 \cdot 10^{-4}$ and $5.3 \cdot 10^{-5}$ bar and at 1400 °C above $1.3 \cdot 10^{-4}$ bar (Gulbransen 1966). Further work made by the same author (Gulbransen 1972) employed thermodynamic data to plot the partial pressures of the different gas species involved in the reactions between Si, O and C. Gulbransen (1972) hypnotized that the presence of pores in the silica is necessary to explain the transition between active and passive oxidation. The CO produced during the oxidation fills the pores, and the O_2 and SiO gas species diffuse through the CO. The oxygen reacts with SiO forming SiO_2 particles that deposit into the pores. The CO partial pressure in the pores defines the chemical potential of carbon and oxygen at the oxide-SiC interface. At the interface of SiC and SiO_2 the following reaction equations are established:

$$SiC_{(s)} + 2SiO_{2(s)} \leftrightarrow 3SiO_{(g)} + CO_{(g)} \tag{2.6}$$

$$SiC_{(s)} + SiO_{2(s)} \leftrightarrow 2SiO_{(g)} + C_{(g)} \tag{2.7}$$

$$2\text{SiC}_{(s)} + \text{SiO}_{2(s)} \leftrightarrow 3\text{Si}_{(s)} + 2\text{CO}_{(g)} \tag{2.8}$$
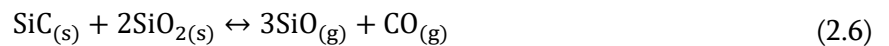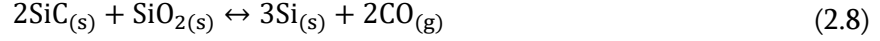
In the case the oxygen partial pressure is lowered, the CO partial pressure decreases, thus moving the Eq. (2.8) toward solid silicon. Additional decrease of oxygen partial pressure causes the instability of SiC in contact with SiO_2, thus forming Si with CO release.

Hinze formulated a two-steps model (Hinze and Graham, 1976) to explain the oxidation of Si and SiC and the transition between the passive and active oxidation. The first step consists in the formation of oxide islands and subsequent whiskers on the Si surface. Further increasing the oxygen partial pressure causes the passivation, which involves the formation of a dense oxide layer.

Heuer (1990) used the volatility diagrams to explain the passive-to-active transition of Si and SiC. He stated that this phenomenon occurs when the oxygen partial pressure is lowered enough to cause the evaporation of the solid silica, forming gaseous SiO. When the evaporation rate is faster than the diffusion of oxygen through the condensed oxide film, the oxide gradually volatilizes until the SiC is completely exposed to the atmosphere and the active oxidation starts. For the active to passive transition, the mass balance of Eq. (2.9) should be respected. Assuming ideal gas behavior and equal diffusivity of all gaseous species, Eq. (2.9) implies that in case of active oxidation, for each oxygen molecule that arrives at the Si surface, two SiO molecules are produced. This criterion is expressed in Eq. (2.10), and it corresponds to the isomolar line in the volatility diagram (Lou 1985). At the intersection of the isomolar line with the line expressing the transition between $\text{SiO}_{(g)}$ and $\text{SiO}_{2(l)}$ in the volatility diagram, the SiO_2 smoke starts to form. From this point, increasing the oxygen partial pressure, the SiO_2 begins to condense, hence the transition between active and passive oxidation occurs.

$$\text{SiO}_{2(s)} = \frac{1}{2}\text{O}_{2(g)} + \text{SiO}_{(g)} \tag{2.9}$$

$$P(\text{O}_2) = 0.5P(\text{SiO}) \tag{2.10}$$

Nickel (1992) considered the possibility of the development of SiO condensed phase at the oxide/SiC boundary. In his paper Nickel proposed the presence of two layers in the silica oxide: the first of liquid SiO and an outer layer of condensed SiO_2. In this case, Eq. (2.11) is the governing equilibrium condition.

16

$$SiC_{(s)} + SiO_{(l)} = 2Si_{(l)} + CO_{(g)} \qquad (2.11)$$

In oxygen atmospheres, most materials are unstable and tend to undergo oxidation, which is controlled by the diffusion of ions or the conduction of electrons through the oxides. Being a thermally activated phenomenon, the rate at high temperatures is greater than at low temperatures. Nevertheless, even at room temperature, a thin oxide film develops on the surface, which protects the underlining material from further oxidation. Under wet conditions, the corrosion rate is usually higher and degrades strongly the material.

As well as in oxygen, passive oxidation of SiC is observed in steam atmosphere. The active oxidation occurs for very low water vapor partial pressures (<10 Pa at 1427 °C) (Opila 1995). In the case of higher oxidant partial pressure, the SiC undergoes Eq. (2.12) developing a dense protective layer of silica (SiO_2).

$$SiC + 3H_2O = SiO_2 + 3H_2 + CO \qquad (2.12)$$

This dense oxide layer decreases the ease of oxidation of the substrate material. Combined with silica growth, silica volatilization takes part in the process via the following reactions:

$$SiO_{2(s)} + 2H_2O_{(g)} \rightarrow Si(OH)_{4(g)} \qquad (2.13)$$

$$SiO_{2(s)} + H_2O_{(g)} \rightarrow SiO(OH)_{2(g)} \qquad (2.14)$$

$$SiO_{2(s)} + \frac{1}{2}H_2O_{(g)} \rightarrow SiO(OH)_{(g)} + \frac{1}{4}O_{2(g)} \qquad (2.15)$$
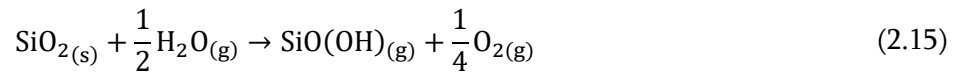
The volatilization can theoretically occur at a wide range of temperatures, and it is enhanced at high temperatures and high gas velocity. However, at 1300 °C and under gas velocity conditions of less than 1 m/s, the silica hydroxide species production is already negligible (Opila 2003). The volatilization is described by a linear constant, which is combined with the parabolic constant in the so-called paralinear behavior, formulated for Cr_2O_3 by Tedmon (1966) and applied for the first time to model the oxidation of SiC by Opila (1997). This is defined by the paralinear equation (Eq. (2.16)), where k_{par} is related to the parabolic oxidation of the SiC, whilst k_l describes the volatilization.

$$\frac{dx}{dt} = \frac{k_{par}}{2x} - k_l \qquad (2.16)$$

In this relation x is the oxide thickness and t the time. The parabolic constant k_{par} has been demonstrated to be proportional to $P(H_2O)$ with a power law exponent of one, whilst the linear constant k_l is proportional to the velocity (v) and the total pressure P_{tot}, according to Eq. (2.17) (Opila 1997).

$$k_l \sim \frac{v^{1/2}P(H_2O)^2}{P^{\frac{1}{2}}_{tot}} \tag{2.17}$$

Different authors have investigated the oxidation of SiC in steam. Jorgensen (1961) tested SiC in water up to 1514 °C using a thermobalance (TGA). In his work, he stated that the oxidation rate of silicon carbide depends on the water vapor partial pressure. Narushima (1990) tested CVD-SiC also with a TGA up to 1650 °C in wet oxygen (10 kPa steam) and suggested, based on the activation energy, that the rate-controlling step in the parabolic regime is the oxygen diffusion. Opila (1999) developed the paralinear kinetic model and mapped out the conditions to apply it, elucidating the strong dependency of the volatilization on the external conditions (Opila 2003; Opila 2004). Oxidation tests under 2 MPa total pressure and at temperatures as high as 1700 °C were performed by the Oak Ridge National Laboratory (ORNL), testing different gas velocities as external conditions (More 2000; Terrani 2014; Farmer 2014). The finding was that at high steam partial pressures, the oxide scale develops porosity due to the formation of CO gases, degrading the silica protective properties. This non-protective porous layer increased with the time, leaving vitreous silica with constant thickness on the SiC.

Agreement has been achieved on the diffusion mechanism for the SiC oxidation, despite no agreement has been found regarding the species diffusing. Many authors stated that the presence of water vapor enhances the oxidation rate. This was explained considering the smaller molecular diameter of a H_2O molecule compared to O_2 (276 versus 320 pm at 700 °C), which reacts with the silicon-oxygen network, forming immobile SiOH groups (Doremus 2001). Moreover the H_2O alters the SiO_2 by modifying and opening the SiO_2 network and increasing the diffusion of oxidant species (Irene 1977). Plotting the logarithm of the parabolic rate constant k_{par} versus the logarithm of the partial pressure of water Eq. (2.18), it is possible to derive information about the oxidant species.

$$\log k_{par} \propto \log(P_{H_2O})^n \tag{2.18}$$

In the case of SiC oxidation in oxygen atmosphere, the slope indicates diffusion of molecular oxygen ($n=0.5$). Concerning Si in steam, a power-law exponent ($n=1$) indicates that molecular water controls the oxidation. In the case of oxidation of silicon carbide in water, experimental results are leading to values of the n coefficient between 0.5 and 1. The most reliable explanation yields to parallel diffusion of a molecular and an ionic hydrogen-containing species (H_2O and OH^-) (Opila 1999).

Degradation of the silica scale, consisting of pitches, cracks and pores, was observed in precedent studies depending on the steam partial pressures (Opila 1999; Li 2010). The production of bubbles implies the degradation of the protective silica scale. Bubbles formation was frequently detected in the case of both dry and steam oxidation in the literature. Mieskowski (Mieskowski 1984) tested single crystal and polycrystals of α and β-SiC in air and oxygen at temperatures between 1200 and 1400 °C and bubbles were detected only on the polycrystalline samples. Kim (1990) studied the effects of oxygen partial pressure on the oxidation behavior of α-SiC at 1400 °C, where the presence of large pits suggested the eruption of bubbles. Schneider (1998) performed experiments on CVD SiC as coating on a graphite substrate under low total pressures (100-800 Pa) and temperatures between 1300 and 1600 °C using a microbalance. It affirmed that two major parameters influence the development of the bubbles: the outside pressure and the silica properties. Schneider inferred the external pressure threshold for the bubble formation calculating the gas pressures at the SiC – SiO_2 interface considering the different possible reactions, for both pure CVD and for the case of carbon inclusions. This would also explain the behavior found in the Mieskowski (1984) work. Indeed, since polycrystals are more likely to have carbon inclusions, these are thought to be the cause of the pressure build-up in the SiO_2 – SiC interface. Considering his approach, a gas pressure higher than atmospheric pressure would be necessary at the interface SiO_2 and SiC to develop such bubbles. Opila (1999) investigated the SiC oxidation at different steam partial pressures up to 1400 °C, with O_2 and argon as carrier gases. Bubbles were observed in the amorphous silica scale at 1100 °C and 1200 °C, increasing with increasing temperatures, exposure time and steam partial pressure. At 1400 °C the silica scale appeared fully crystalline and no bubbles were detected. Ogura (2002) observed the bubbles production in CVD SiC coating oxidized under low total pressure (0.8-440 Pa) between 1250 and 1700 °C in oxygen. By means of a mass spectrometer, he indicated the sharp rise of the channel 28 (CO) at the start of bubbles formation.

Goto (Goto 2002; Goto 2006) investigated CVD SiC using thermogravimetry at temperature as high as 1717 °C in Ar-O_2 and N_2-O_2 atmospheres. The output signal showed a zig-zag mass change, due to the production and eruption of silica bubbles. In a more recent paper by the same author, the bubbles were detected at 1600 °C after oxidation of CVD material for 42 h in oxygen. In this case the samples did not exhibit the zigzag-shaped behavior, due to the smaller size of the bubbles (Katsui 2014). ORNL (Terrani 2014) tested high purity CVD SiC and SiC/SiC composites[3] in steam at temperatures between 1200 °C and 1700 °C, with environmental pressure in the range of 0.1 – 2 MPa for different flow velocities. Bubbles were detected at 1700 °C in atmospheric pressure.

2.2 Oxidation of SiC in oxygen and steam: experimental details

This section reports experimental details of oxidation of silicon carbide specimens, including the materials tested, the facilities used at Karlsruhe Institute of Technology, the test conditions and the post-tests analyses.

2.2.1 Samples

In order to investigate the silicon carbide behavior in dry oxygen atmospheres, sintered cylinders of α-SiC made by the ESK (Elektroschmelzwerk Kempten) company were purchased (d=10mm, h=10mm), as shown in Figure 2.2. The production process is usually done without pressure in inert gas atmosphere or in vacuum at temperature between 1900 °C and 2200 °C with some additives (boron, aluminum and compounds, beryllium and compounds). The elemental analysis of this material was performed by the analytical lab of KIT-IAM-AWP, and results are given in Appendix A.

---

[3] SiC/SiC composite resulted to behave identically to CVD SiC as long as the fiber-matrix interphase remains protected.
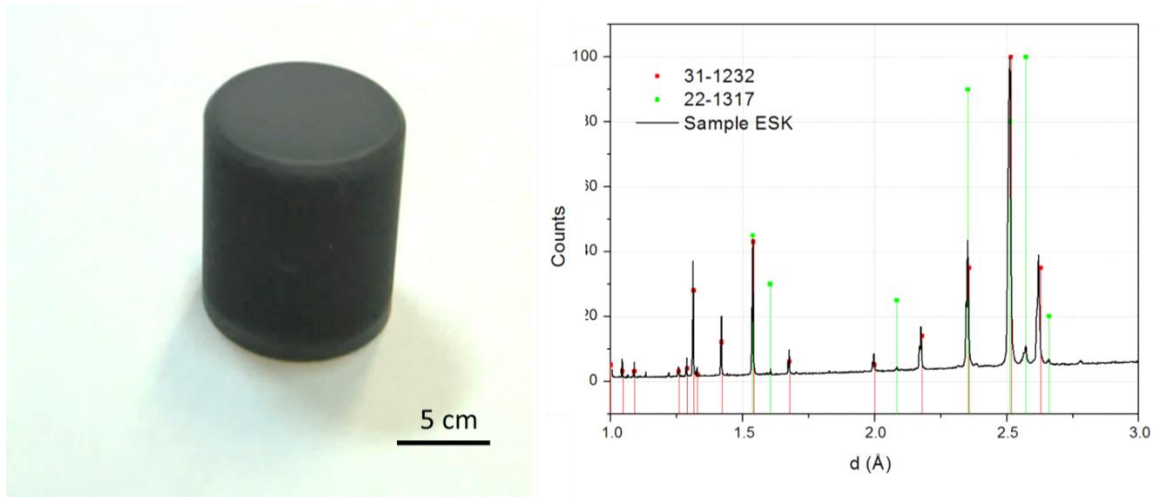
Figure 2.2: ESK sample and XRD analysis of the as-received sample.

This analysis confirmed the presence of impurities (0.6665 percent in weight): boron and oxygen turned out to be the 68 % of the total amount. In order to recognize which kinds of polytypes were present in these samples, XRD technique has been employed. Results are shown in Figure 2.2. The hexagonal polytypes 6H and 4H were detected according to the PDF 31-1232 (Bind 1978) and to the PDF 22-1317 (Hannam 1969) respectively, which are in agreement with the fabrication technique. An analysis of a sample's section has shown that the porosity is enhanced near the edge of the sample, probably due to the fabrication method. In Figure 2.3 micrographs of the SiC surface made by means of optical microscope and SEM are presented. The EDX analysis showed that the black spots are boron impurities.

For the experiments in steam, samples of Ceramic Matrix Composite (CMC) silicon carbide/silicon carbide fibers (Hi-Nicalon) by CEA were used to perform oxidation and quench tests (Table 2.1). The cladding design developed by the CEA laboratories (Buet 2012; Bansal 2015) consists of three braided layers (with 45° degrees of orientation) Hi-Nicalon S fibers from Nippon Carbon, reinforced with a SiC Chemical Vapor Infiltration (CVI) matrix. In order to maximize the mechanical performance of the composite material, a braided angle of 45° was chosen for the fibers, and a layer of ≈20-30 nm was deposited on the SiC fibers prior to the matrix infiltration (Figure 2.4). The last procedure allows optimizing the matrix-fiber bonding. As protection of the whole cladding, an external 50 μm thick CVD layer was applied and ground. A sketch of the braided fibers is given in Figure 2.4.
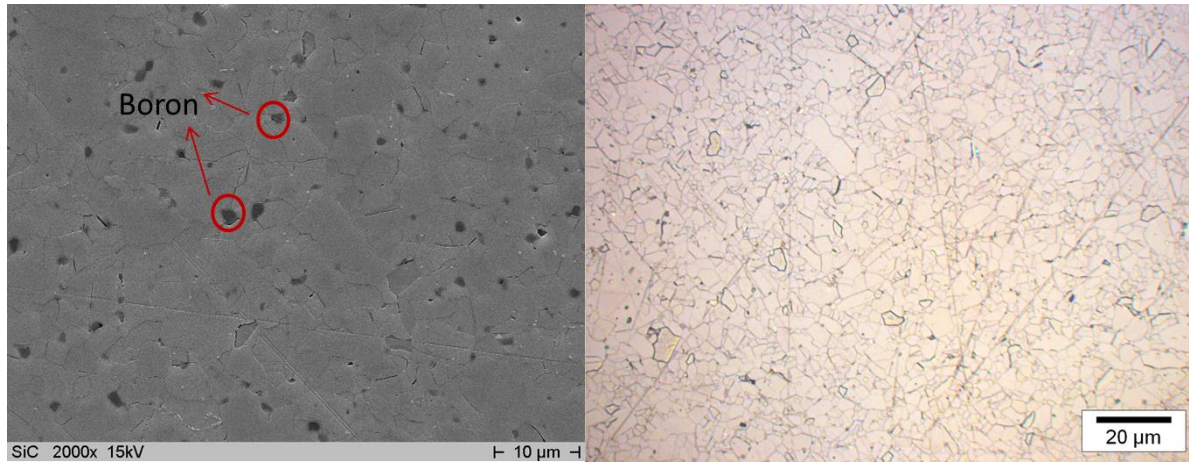
Figure 2.3: Optical and SEM micrographs of the ESK sample after etching.
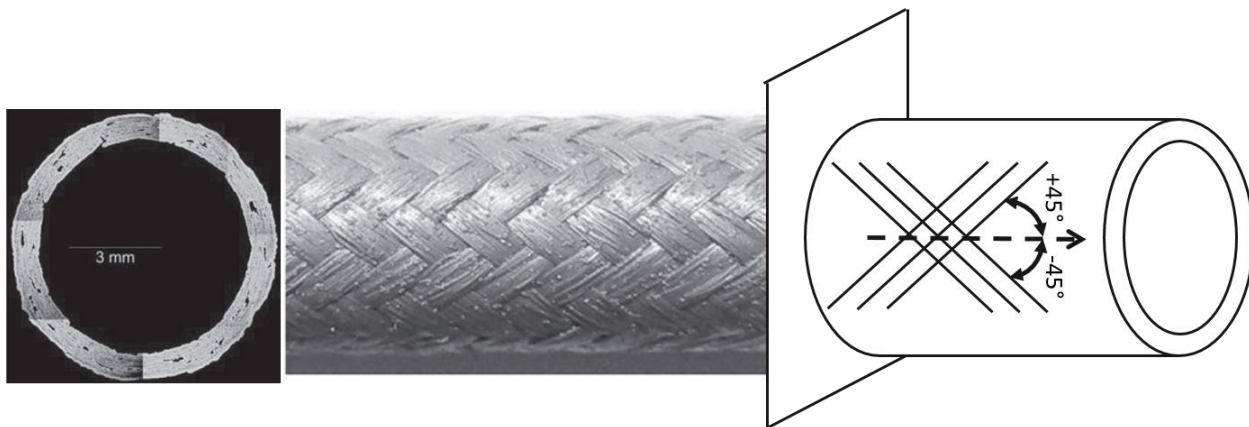
Figure 2.4: Sketch of the braided fiber in the CEA samples (macrographs and SEM from the literature (Bansal 2015)).

21 tube samples of a length of 20 mm, an external diameter of 9.5 mm and a wall thickness of 0.89 mm have been provided by the CEA (Table 2.1). The typical major impurities are Si, C, O, Al, and usually a carbon excess is present (C/Si at. % 1.07) (Bansal 2015). CEA laboratories provided the elemental analysis for the fibers and the matrix as well (Appendix B). The C, N, O and H elements have been measured by means of Instrumental Gas Analysis (IGA) whilst the other elements were measured by Glow Discharge Mass Spectroscopy (GDMS).

Table 2.1: Samples received from CEA and oxidized at the given test temperatures.

	Samples number	Temperature (°C)
	10	1600
	5	1700
	6	1800

2.2.2 Facilities

The oxidation experiments were performed in different setups, which were modified for the silicon carbide materials. The mass gain of SiC during oxidation in dry oxygen was measured by a thermobalance (Netzsch STA 409) able to reach 1550 °C with a readability of 50 μg (Figure 2.5). Digital mass flow controllers purchased from Bronkhorst High-Tech BV[4] were used to define the oxygen partial pressure in the argon flow.
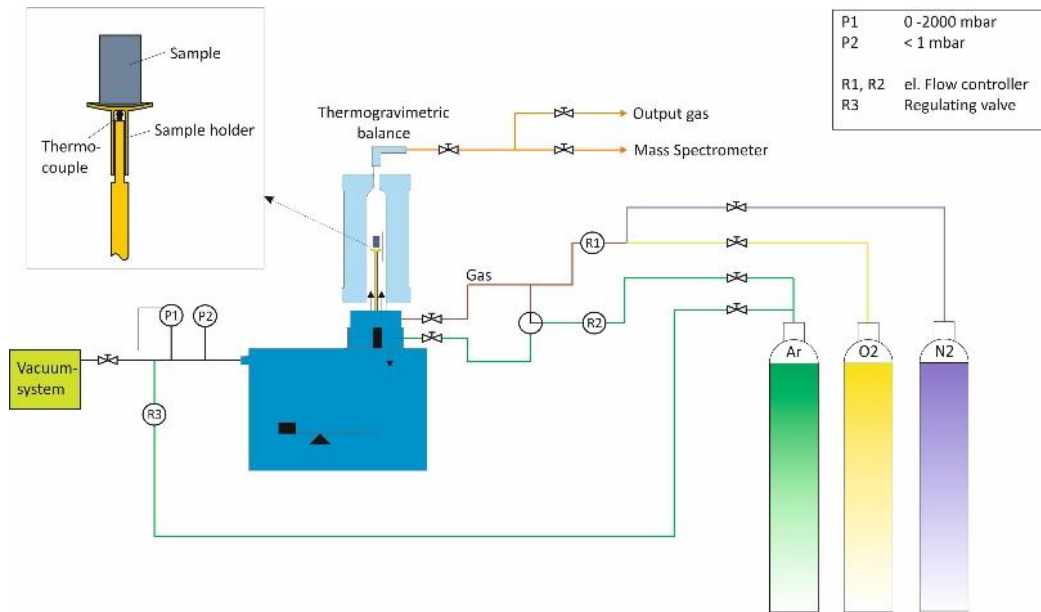
Figure 2.5: Sketch of the thermal gravimetric analysis test setup.

---

[4] F-200CV-002-AAD-33-V (0.7 ml/min O_2), F-200CV-005-AAD-33-V (5 ml/min O_2), F-201CV-050-AAD-33-V (50 ml/min O_2).

The tests in steam were carried out at 1600 °C in a horizontal alumina tube furnace (BOX) (Figure 2.6). A suspended sample holder was used to test the samples with hollow cylindrical shape, whilst the bulky samples were tested in an alumina boat. A study conducted by Opila (1995), highlighted the influence of the impurities contained in the alumina furnace tube. Such impurities, in particular sodium, increase the oxidation rate constant by about one order of magnitude, with respect to the same conditions in a quartz furnace. In the BOX facility, the water was stored in a vessel under pressure. The gas supply system for steam and argon consisted of two gas flow controllers, one liquid flow controller and a so-called controlled evaporator mixer unit (CEM), where the liquid water was evaporated and mixed with the non-condensable gas. The whole system was delivered by Bronkhorst High-Tech BV.

At temperatures higher than 1600 °C, the samples were tested in a vertical quartz furnace (QUENCH-SR) heated by induction coils (Figure 2.7). The power to the coil was supplied from a 20 kW oscillator, at a frequency of up to 700 kHz. The rig allowed quenching the sample by water heated between 30 and 90 °C. The samples' temperature was controlled by means of a two-color pyrometer connected to a controller, which adjusted voltage and current accordingly.
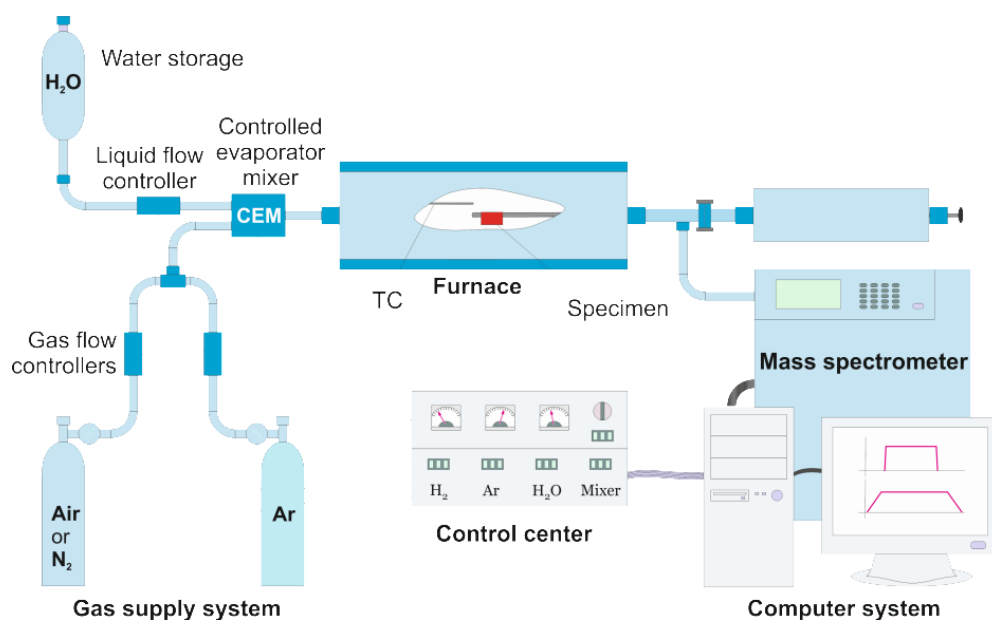
Figure 2.6: Sketch of the BOX facility.

24
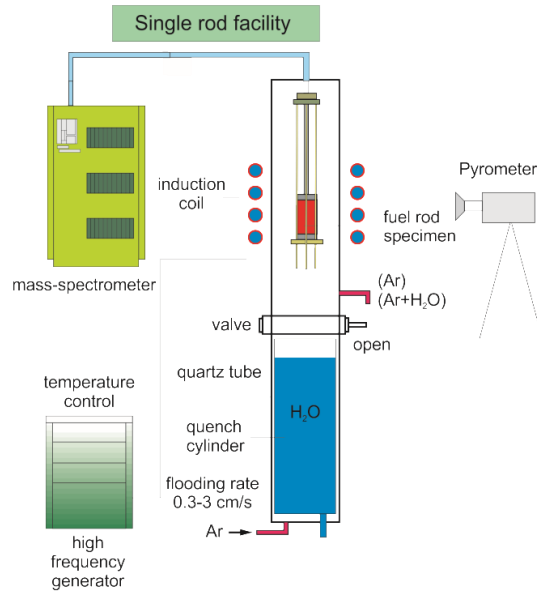
Figure 2.7: Sketch of the Single-Rod facility (QUENCH-SR).

The device allowed the use of different gas mixtures, such as argon and steam. The samples were hold by an alumina or a zirconia sample holder. In the induction furnace a susceptor was needed to heat the sample, since the resistivity of the SiC/SiC$_f$ composite was not high enough to allow the self-heating. Thus, a graphite pellet was used as susceptor, as shown in Figure 2.8. In Table 2.2 the technical specifications of all the devices described in this section are presented.
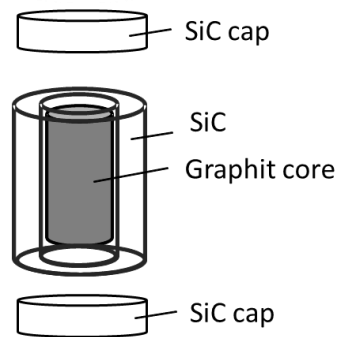
Figure 2.8: Sketch of the silicon carbide plus the graphite stick used as susceptor.

Table 2.2: Technical data of the devices described in this section.

	TG	BOX	Quench-SR
Temperature (°C)	300 - 1550	300 - 1600	500 - 2000 °C
Heater	Silicon carbide	Molybdenum	Inductive
Reaction tube material	Alumina	Alumina	Quartz
Inner diameter (mm)	25	32	40.5

Since the SiC lids on the SiC cylinder were not tight, and they could not prevent the oxidation of the graphite itself, alumina high-purity/high-temperature glue (Polytec PT - Resbond 989) was used to cover the graphite extremities. The data sheet of this glue is in Appendix C.

The flow-rate of the argon and steam gas mixture and the steam partial pressure were also controlled by a Bronkhorst evaporator and mixing system. The steam partial pressures were calculated considering the amount of moles of water and argon respectively. This approach was checked by means of thermodynamic calculations: the equilibrium water dissociation in the test rig was calculated at the experimental temperatures using Gibbs energy minimization techniques implemented in the Thermo-Calc software with the SGTE database (Scientific Group Thermodata 2014). Agreement has been found comparing the results with the reviewed data in the work by Jellinek (1986). As a result of the calculation presented in Figure 2.9, significant dissociation of water according to Eq. (2.19) starts only at temperatures above 1200 °C, i.e., it is 0.1% at 1357 °C. The water dissociation increases further with temperature and it is about 0.5% at 1600 °C and 3.5% at 2000 °C.

$$H_2O_{(g)} = H_{2(g)} + \frac{1}{2}O_{(g)} \tag{2.19}$$

Ionization of water is not expected at these temperatures. The water dissociation causes the presence of hydrogen and oxygen in the gas mixture. At 1600 °C, considering a dissociation of 0.5% (as shown by the dashed lines in Figure 2.9), the following partial pressures are in the gas mixture: $P_{H2} = 2/3 \cdot 5 \cdot 10^{-3}$ atm $= 337$ Pa and $P_{O2} = 1/3 \cdot 5 \cdot 10^{-3}$ atm $= 170$ Pa. This amount of oxygen may play a role in the oxidation of silicon carbide. According to the Ellingham diagram (Gaskell 2003), in the case of silicon in the presence of oxygen gas, SiO_2 forms at the surface of Si at 10^{-9} Pa of O_2 at 1600 °C.
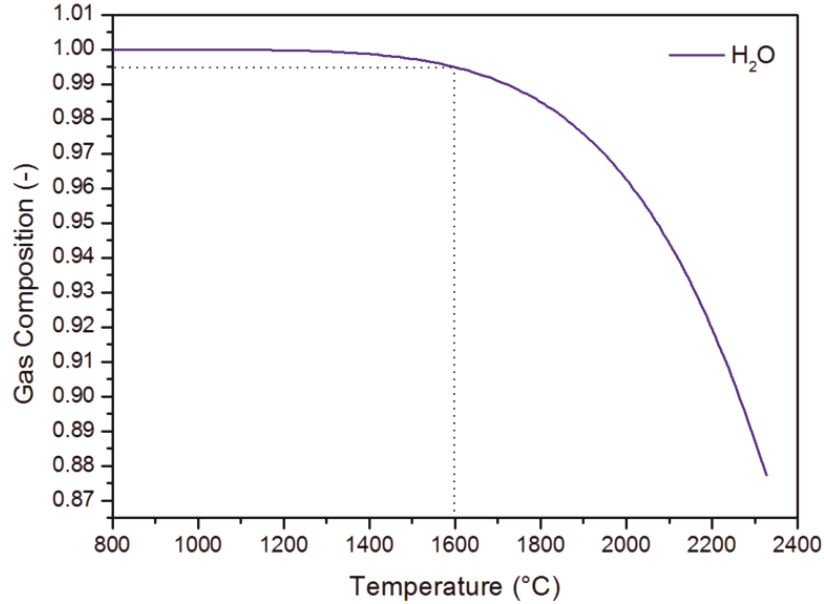
Figure 2.9: H_2O dissociation at temperature between 800 and 2300 °C calculated with Thermo-Calc (SGTE dataset).

Therefore, the P_{O_2} generated by the water dissociation should foster the passive oxidation reaction since the calculated pressure of O_2 in the atmosphere at 1600 °C (170 Pa) is much higher.

Other studies (Balat-Pichelin 2010) have shown that at 170 Pa oxygen partial pressure, CVD silicon carbide undergoes passive oxidation. However, under the conditions studied in this chapter, the amount of water vapor is considerably higher than the amount of oxygen and H_2O can be considered the main reacting species.

Both furnaces (BOX and SR-Quench) were connected with a quadrupole mass spectrometer (MS, Balzers GAM 300), which monitored the exhaust gases. All the facilities were already used for other experiments before starting the tests campaigns presented in this work. In order to avoid contamination from previous tests, blank tests were run before starting the experiments with silicon carbide specimens.

The volumetric flow rates were calculated using argon as reference gas. The hydrogen production in l/h, which is produced for example via Eq. (2.12), was calculated referring to the measured H_2 concentration to the known argon mass flow rate, according to (2.20):

$$\dot{V}_{H_2} = \frac{C_{H_2}}{C_{Ar}} \cdot \dot{V}_{Ar} \tag{2.20}$$

where $\dot{V}_{H_2}$, $\dot{V}_{Ar}$ are the volumetric flows of hydrogen and argon per unit of time, whereas C_{H_2} and C_{Ar} are the concentrations of the same species measured by the mass spectrometer. The production for unit of area is calculated dividing the $\dot{V}_{H_2}$ by the oxidized area of the sample.

2.2.3 Test conditions

The first series of experiments in dry oxygen with the ESK samples was a transient: the heating up phase was followed by the cooling phase as soon as the temperature of 1550 °C was reached. This experiment was repeated at different oxygen partial pressures (10, 50 and 100 Pa): these different oxygen partial pressures should allow addressing the transition between passive and active oxidation. However, in the first experimental conditions tested, the time at high temperature was too short (once the temperature was reached the cooling down phase started) to detect the oxidation with the thermobalance. Therefore, the second test oxidation series was performed with a longer isothermal phase, which was between 20 min and 8 h. The total flow was fixed at 10 l/h.

Isothermal experiments were conducted at 1600 °C in the BOX furnace. 10 samples shown in Table 2.1 were loaded in the furnace already heated at the prescribed temperatures and were held in the reaction chamber for time periods up to 64 h. The mass of the samples was measured before and after the test using a bench-top balance. By means of a sample lock connected to the furnace, the samples' masses were measured during the experiments at different times without including significant interference in the experiments.

Experiments at temperature beyond 1600 °C were conducted in the QUENCH-SR with the rest of the samples shown in Table 2.1. In this facility, the heating phase was run under inert atmosphere condition, up to 1400 °C (argon 40 l/h), with a heating rate of 10 °C/min. Once the temperature of 1400 °C was reached, the steam was injected. In this chapter, oxidation tests at 1700 °C and 1800 °C are presented, whereas in chapter 6 the quench tests are described. In order to study the SiC behavior in the case of quenching, the temperature was raised up to 2000 °C and the samples were quenched by water at 90 °C from the bottom of the facility with a velocity of 1 mm/s.

2.2.4 Post-test analysis

After the tests, the samples' appearance was documented by taking photos before embedding in epoxy (Bühler Epoxicure). Some samples have been analyzed with X-ray Computed Tomography (GE v/tome/xs), a nondestructive technique which allows visualizing interior features within solid object. This technique was used to check the integrity of the inner layer after quench of the tri-layered samples. The identification of different materials inside the sample using X-ray radiography depends on the total mass attenuation of chemical composition, as shown in Eq. (2.21)

$$I = I_0 e^{-\mu x} \tag{2.21}$$

where I is the X-ray signal after passing through the material with total mass attenuation μ and thickness x, I_0 is the incident X-ray beam. In this work, the following parameters were used: beam energy of 120 kV, a spatial resolution of 0.024 mm and a 360 °C as angle of rotation.

After the embedding procedure, the samples were ground and polished using a series of diamond plates with different coarseness. Details of the polishing procedure are reported in Table 2.3. This allows analyzing the samples using optical microscopy (MeF3 Reichert-Jung), and scanning electron microscopy (SEM) (Philips XL305). These two techniques enable to investigate the surface of the sample. The optical microscope employs visible light to detect and magnify small object.

The SEM uses a focused beam of high-energy electrons to generate a variety of signals at the surface of the solid specimen. An electron gun produced a beam of electrons, which travels in vacuum through electromagnetic fields and lenses in order to reach the sample.

Table 2.3: Polishing and grinding procedure.

Step	Disc / support	Grain size (GRIT)	Speed (U/Min.)	Pressure (bar)	Time (min)
Grinding 1	Diamant disc	220	150	3	3-5
Grinding 2	Diamant disc	600	150	2	5
Grinding 3	Diamant disc	1200	150	2	10
Polish 1	Perforated Synthetic rubber	15µm	150	2	20
Polish 2	Perforated Synthetic rubber	6µm	150	2	20
Polish 3	Perforated Synthetic rubber	3µm	150	2	15
Polish 4	Silk Cloth	1µm	150	2	5

Once the beam hits the sample, it emits characteristic electron and X-rays, which are collected and converted in a signal, which is representative for any element. The signals are converted into images by specific software. In this work, DIPS software was used for the SEM images.

XRD measurements were also performed in the Bragg–Brentano geometry, using a CuKα radiation, in order to identify the phases formed on the SiC surface. The X-rays in the instrument are generated in a cathode tube by heating a filament to produce electrons, which are accelerated by the application of a voltage. When the electrons hit the target (Cu in this case) with enough energy to dislodge inner shell electrons of the target material, X-ray spectra with a wavelength characteristic of the target material are produced. The X-rays are filtered, collimated, and directed onto the sample. When the Bragg law (Eq. (2.22)) is satisfied, constructive interference occurs forming a peak, which depends on the sample.

$$n\lambda = 2d\sin\theta \tag{2.22}$$

In Eq. (2.22) n is an integer, λ is the wavelength, d is the distance between the lattice planes, and θ in the incident angle.

Raman spectroscopy analysis was also conducted on some specific samples. This technique relies on inelastic scattering from a monochromatic light (i.e., laser) on a sample. The frequency of photons of the monochromatic light changes upon interaction with the sample. The shift of the frequency provides information about the vibrational, rotational and other low frequency transitions in the molecules, allowing determining the material's composition. The Raman spectra were measured in this work between 100 and 2000 cm^{-1}, with a Renishaw 1000 micro spectrometer using an argon ion laser at 514.5 nm (Modu-Laser, Type Aries-163). The software WIRE V.1.3.18 was used to acquire the spectra, applying extended continuous mode. The spot size was 1-2 μm in diameter and the laser power was 2 – 3 mW at the sample spot. For each sample, two or three spectra were recorded at different positions: no significant differences among the single spectra of the same sample were observed.

Finally, some specimens were etched using a Murakami solution made of 3 g of sodium hydroxide (NaOH) and 30 g of potassium hexacyanoferrate III ($K_3[Fe(CN)_6]$) diluted in 60 ml of distilled water. The etching solution preferentially attacked boundaries as shown in Figure 2.3.

2.3 Results

In this section, the results obtained through the experiments in dry oxygen and steam are presented, including the mass gain data and the post-test analysis.

2.3.1 Results of oxidation in dry oxygen

The first series of SiC oxidation experiments was performed at 1550 °C in a 10 l/h oxygen-argon mixture. The oxygen partial pressure was set between 10 Pa to 100 kPa, which corresponds to a range of oxygen from 0.01% to 100%. Usually thermogravimetric measurements are affected by the buoyancy effect: each sample exhibits a temperature dependent increase in weight not related to the oxidation phenomenon. The buoyancy effect can be evaluated comparing the oxidation curve of the reference sample to the SiC samples oxidation curve.

An inert material made of magnesium stabilized zirconia (Mg-PSZ FRIALIT FZM from FRIATEC) was used to run a blank test (Figure 2.10): in the initial stage, the gas temperature is higher than the sample's temperature due to the different thermal conductivity. The buoyancy of the gas itself decreases during time due to the differences in thermal conductivity, density and heat capacity and therefore the sample appears to gain weight. According to Figure 2.10, the buoyancy is about 0.05 % of the sample's initial mass. The buoyancy effect is enhanced by the quantity of argon: when the oxygen concentration is higher in the gas mixture, the weight of the gas is lower, thus the force applied on the sample decreases, causing less weight gain. According to NIST (Stewart 1989), the density of the argon is 0.03263 mol/dm³ at 22 °C whereas is 0.00802 mol/dm³ at 927 °C. Considering a molar mass of 39.948, the density of argon at the two temperatures can be written as 1.3035 g/dm³ and 0.3204 g/dm³.

The buoyant force on the weight is expressed as in Eq. (2.23) (Gupta 2012), where V is the volume of the weight, δ is the density of the gas (air or argon), and g the gravitational acceleration.

$$F_C = V\delta g \tag{2.23}$$

The derivative of the buoyant force is expressed in Eq. (2.24), with α the thermal expansion coefficient of the SiC. Therefore, the change in mass due to buoyancy is given by Eq. (2.25):

$$\frac{\partial F_C}{\partial T} = \left(\delta\frac{\partial V}{\partial T} + V\frac{\partial \delta}{\partial T}\right)g = \left(\delta 3\alpha V + V\frac{\partial \delta}{\partial T}\right)g \tag{2.24}$$

$$\Delta m = -\left(3\alpha\delta + \frac{\partial\delta}{\partial T}\right)V\Delta T \tag{2.25}$$

being $\frac{\partial\delta}{\partial T}$ negative, Eq. (2.25) can be rewritten as Eq. (2.26), where $\frac{\partial\delta}{\partial T}$ is the positive value of the change in density of the gas per unit temperature.

$$\Delta m = \left(-3\alpha\delta + \frac{\partial\delta}{\partial T}\right)V\Delta T \tag{2.26}$$

Plugging the values shown in Table 2.4 in Eq. (2.26), the change in mass due to the buoyancy is $1.7 \cdot 10^{-3}$ g. This value is comparable to the mass change noted in Figure 2.10 (e.g., the 0.05 % of 2.5 g is $1.25 \cdot 10^{-3}$ g). In Figure 2.11 the net mass gain of the samples heated up to 1550 °C and immediately cooled down is presented in percent. This was calculated subtracting the reference measurement performed with the zirconia sample from the SiC measurement.
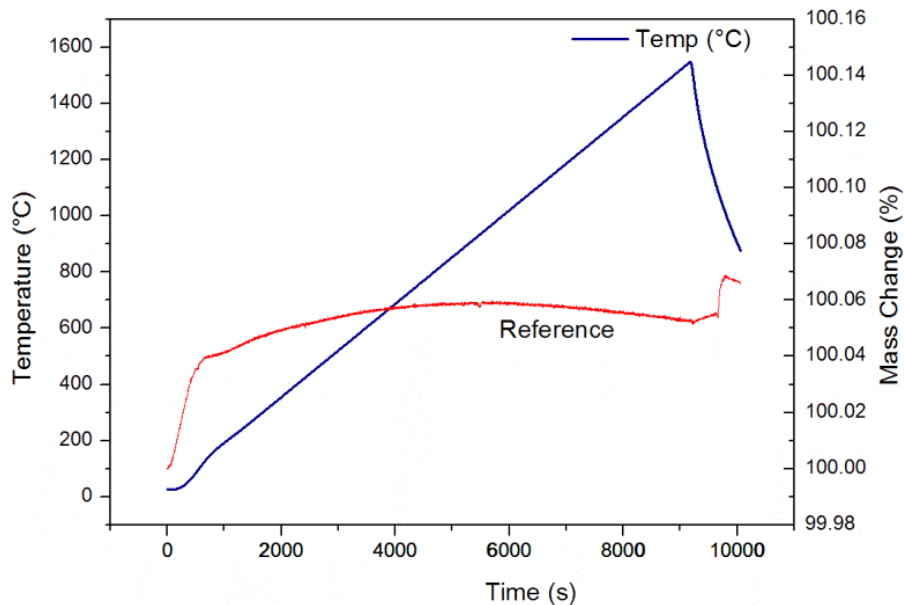
Figure 2.10: Mass change of the reference samples registered with the thermobalance in the case of transient experiments.

As a result, the mass gain of the SiC samples is between 0.02 % and 0.04 % of the initial mass, which is equal to about 10^{-4} g. This mass change was beyond the sensitivity of the bench-top balance, thus no mass change was detected apart from the TG measurements. In Figure 2.11, all the curves show mass gain, with the exception of the sample tested in argon and 10 Pa oxygen partial pressure[5], which is showing a mass loss. In order to have a more significant reaction, longer tests have been performed between 20 min and 8 h. The oxygen partial pressure was set between 10 and 100 Pa. Description of the tests are provided in Table 2.5.
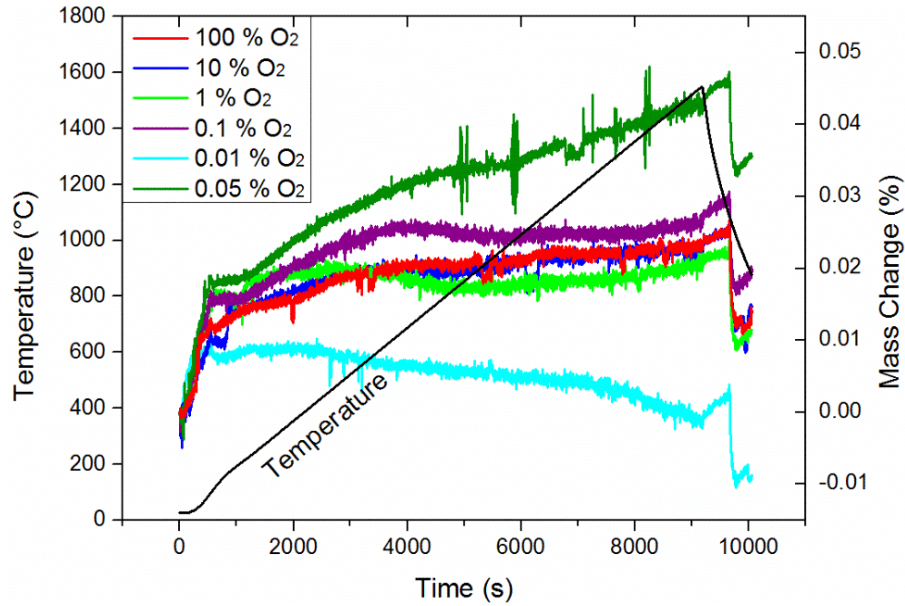
Figure 2.11: Mass change of the SiC samples tested in argon with different oxygen quantity with the thermobalance in the case of transient experiments.

Table 2.4: Values used for calculating the mass change due to the buoyancy.

Property	Value
δ (g/dm³) (Argon T=22 °C)	1.65
α (1/K) (SiC)	$4 \cdot 10^{-6}$
V (dm³) (Sample)	0.000785
ΔT (Experiments)	1528
$\partial\delta/\partial$T (Argon)	$1.36722 \cdot 10^{-4}$

---

[5] 10 Pa ≈ 0.01% ≈ 100 ppm

Table 2.5: SiC oxidation experiment in dry oxygen and argon, where m_i is the initial mass and m_f is the final mass of each sample.

Sample	P_{O2} (Pa)	Temperature (°C)	Time (min)	m_i (g)	m_f (g)	Δm (g)
ESK2	50	1550	20	2.3151	2.3147	-0.0004
ESK3	10	1550	20	2.4459	2.4445	-0.0014
ESK4	10	1550	20	2.4370	2.4350	-0.0020
ESK5	100	1550	20	2.4567	2.4572	0.0005
ESK6	10	1550	480	2.4786	2.4644	-0.0142
ESK7	10	1550	480	2.5708	2.5508	-0.0200
ESK8	50	1550	480	2.5700	2.5710	0.0010
ESK9	50	1400	120	2.3845	2.3845	0.0000
ESK10	50	1550	300	2.3943	2.3936	-0.0007

Some oxide pieces stuck onto the sample holder preventing to have accuracy in the bench-top balance measurements. The TG curve, along with the microscopy analysis, characterize with more precision the reaction occurred during the tests. The sections of the samples ESK5 and ESK10 investigated with SEM are shown in Figure 2.12. A silica layer in the order of 0.6 μm after 20 min and about 0.8 μm after 5 h was detected. In Figure 2.13 the surfaces of the samples oxidized in 50 Pa oxygen partial pressure (ESK10) and in 10 Pa oxygen (ESK7) are presented.
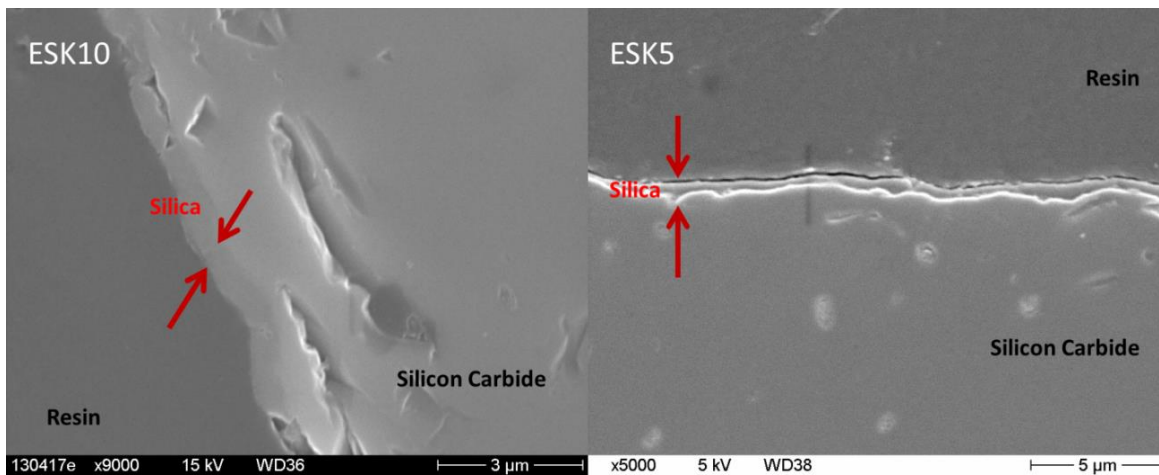
Figure 2.12: SEM macrographs of SiC sample section after oxidation (ESK10 and ESK5).
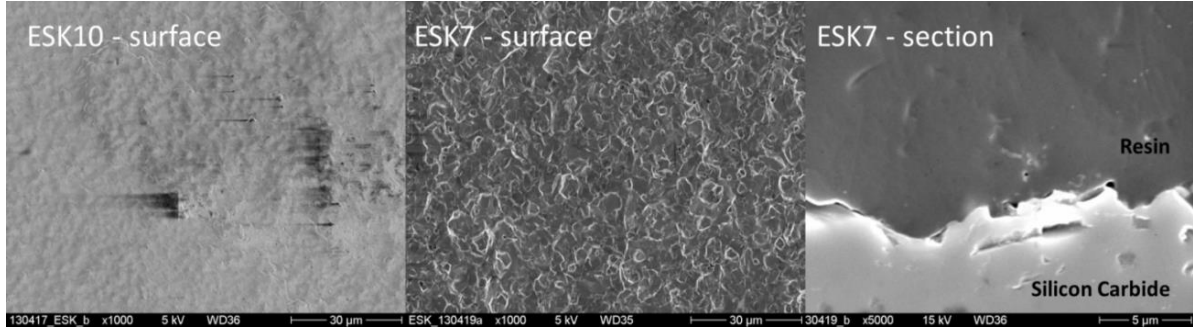
Figure 2.13: SEM analysis of the surface of samples ESK10 and ESK7 and section micrograph of sample ESK7.

The first figure shows a dense oxide layer whereas no silica layer is recognized on the sample ESK7 oxidized at 10 kPa oxygen (Figure 2.13). This is also confirmed by the micrograph of the section of sample ESK7. Indeed, no oxide layer is visible between the silicon carbide and the epoxy in the section micrograph. In order to calculate the mass change from the thermal gravimetric analysis, Eq. (2.27) was used.

$$\Delta m \left(\frac{g}{m^2}\right) = \frac{\Delta m \ (\%) \cdot m_o \ (g)}{100 \ \cdot \ A \ (m^2)} \tag{2.27}$$

where m_o is the initial mass, A is the sample's area, and Δm is the mass change. According to Eq. (2.27), the mass change has been plotted for the samples ESK6, ESK7, ESK8 and ESK10 in Figure 2.14. The mass gain of ESK10 in the graph is comparable with the silica thickness detected by electron microscope in Figure 2.12. The difference between passive (grey and light blue lines) and active (red and purple line) can be noticed. The threshold oxygen partial pressure is identified between 50 and 10 Pa, which agrees with the literature data. The parabolic constant was calculated fitting the highlighted data plotted in Figure 2.15. According to the experimental data, the parabolic constant is $8.5 \cdot 10^{-3}$ mg/(cm^{2}s$^{1/2}$) for the oxidation at 1550 °C in 50 Pa oxygen partial pressure.
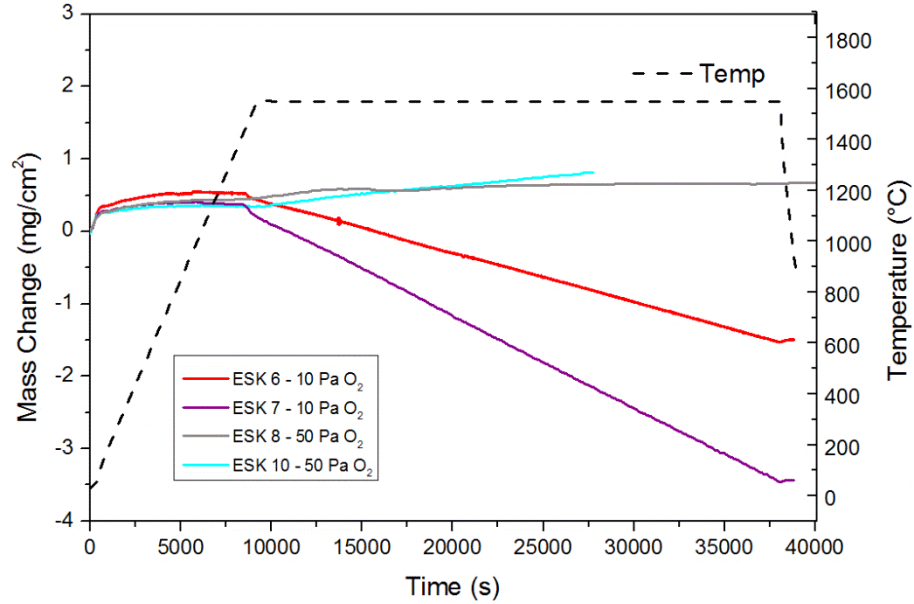
Figure 2.14: Temperature profile and thermal gravimetric online measurement of SiC oxidation in dry oxygen.
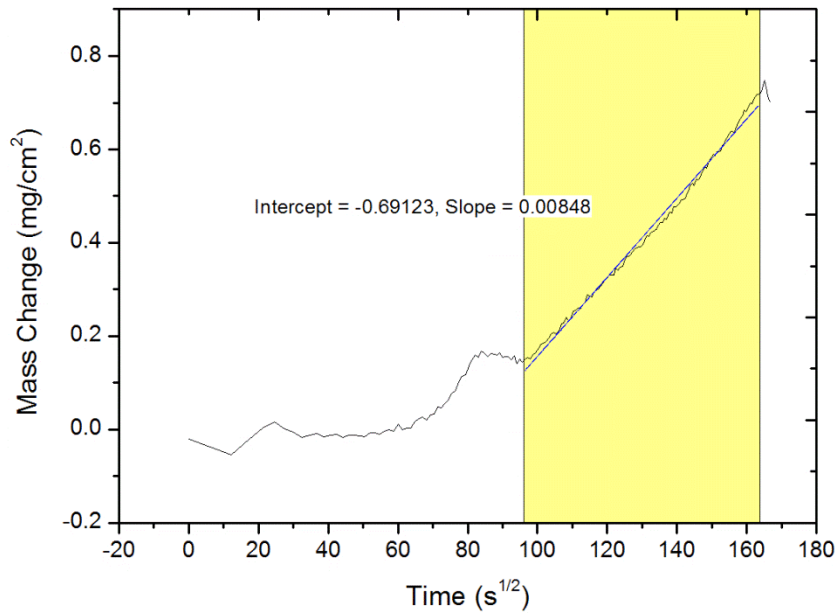
Figure 2.15: Fitting of the experimental data (ESK10).

2.3.2 Results of experiments in steam

Isothermal oxidation tests were performed at 1600 °C up to 64 h in pure argon (6.0) and different steam partial pressures (10, 30 and 60 kPa). The oxidation experiments are summarized in Table 2.6.

36

One sample has been kept as a reference. The maximal temperature and flow allowed by the furnace was chosen for these experiments. Three different steam partial pressures (10, 30 and 60 kPa) in argon atmosphere were chosen to investigate the influence of the steam partial pressure on the samples. Figure 2.16 shows an overview of the external surface of the samples oxidized at 1600 °C in different steam partial pressures.

Table 2.6: SiC oxidation experiments in argon and steam.

Sample	P_{H2O} (kPa)	Temperature (°C)	Time (h)	Total Flow (l/h)
S1	10	1600	5	66
S2	10	1600	16	66
S3	60	1600	22	64
S4	30	1600	22	64
S5	60	1600	22	133
S6	30	1600	25	133
S7	60	1600	22	133
S8	60	1600	64	64
S9	60	1600	22	133

S2 — Time: 16 h / Tot Flow: 66 l/h / PH_2O: 10 kPa

S3 — Time: 22 h / Tot Flow: 64 l/h / PH_2O: 60 kPa

S4 — Time: 22 h / Tot Flow: 64 l/h / PH_2O: 30 kPa

S5 — Time: 22 h / Tot Flow: 133 l/h / PH_2O: 60 kPa

S6 — Time: 25 h / Tot Flow: 133 l/h / PH_2O: 30 kPa

S7 — Time: 22 h / Tot Flow: 133 l/h / PH_2O: 30 kPa

S8 — Time: 64 h / Tot Flow: 64 l/h / PH_2O: 60 kPa

S9 — Time: 22 h / Tot Flow: 133 l/h / PH_2O: 60 kPa

Figure 2.16: Post-test appearance of samples oxidized at 1600 °C at different steam partial pressures.

Some samples have the surface covered by bubbles, in particular samples S8 and S9. Samples S5 and S7 also show bubbles, but those appear to be developed within the SiO_2 layer. For shorter time and lower steam partial pressures, such bubbles were not detected. Sample S2 shows lighter spots consisting in different coloration of the surface.

The oxide scale produced during the oxidation is not visible by optical analysis. Indeed, no significant differences can be noted by means of optical microscope on the samples before and after oxidation tests, as can be seen in Figure 2.17.

The steam partial pressure during oxidation plays a role in the mass gain of the samples. This can be noted in Figure 2.18, where the mass change per unit of area is presented considering the experiments at 10 and 30 kPa already shown in Table 2.6. The surface specific oxidation rate constant (k_{par}) was determined, although the points are scattered in the graph since the oxidation of SiC was weak, in particular for shorter time. For longer time the uncertainties are due to the scattering produced by the bubbles formation. Indeed, once the bubble reaches its maximum diameter, it explodes letting some oxide scale falling apart. The fit of the data issues a parabolic rate constant of $4.8 \cdot 10^{-4}$ mg/(cm²s$^{1/2}$) and $1.2 \cdot 10^{-3}$ mg/(cm²s$^{1/2}$) at 10 kPa and 30 kPa steam partial pressure, respectively.

At higher steam partial pressures, the oxidation behavior is different, as it can be seen in Figure 2.19. The calculation of k_{par} was not possible due to the scattering of the data. Considering the oxidation tests carried out for longer periods of time, the samples underwent severe mass loss and degradation due to the presence of bubbles (see S8 in Figure 2.16).

The mass spectrometer output signal highlighted the correlation between the steam partial pressure and the oxidation rate (Figure 2.20). In this graph, the hydrogen production of different samples during the oxidation is presented. The mass spectrometer data at 60 kPa are more scattered due to the strong formation of bubbles on the silica surface.
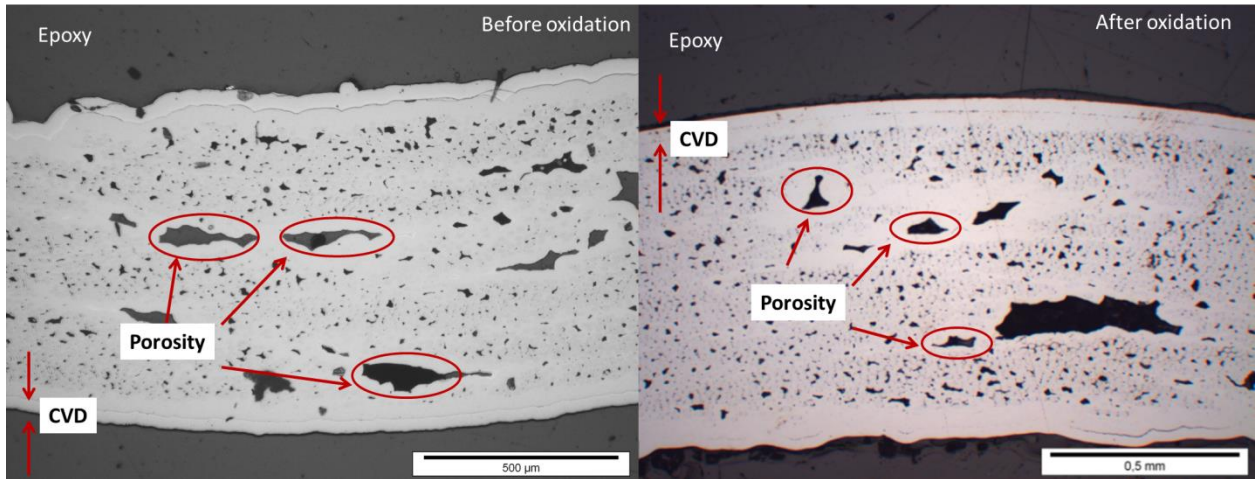
Figure 2.17: A typical overview of the SiC cross section (Sample S5).
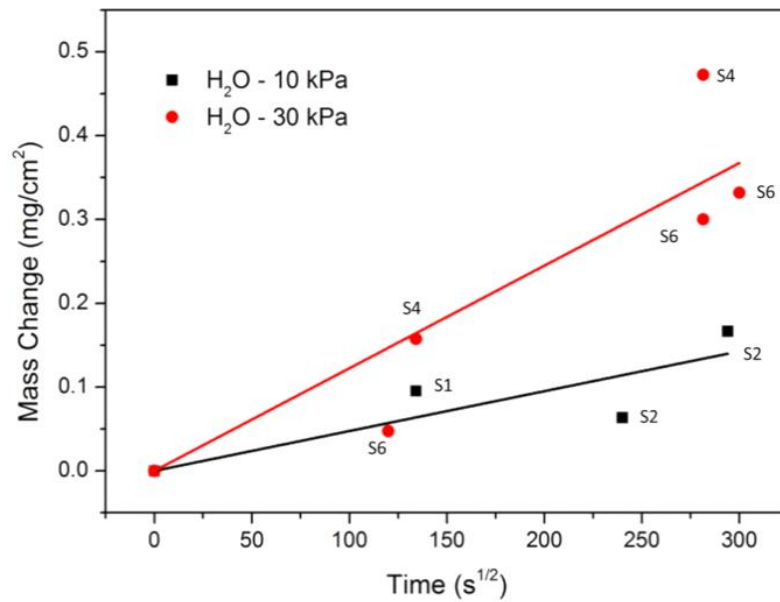
Figure 2.18: Mass gain of samples oxidized at 1600 °C under 10 kPa and 30 kPa steam partial pressure in argon.
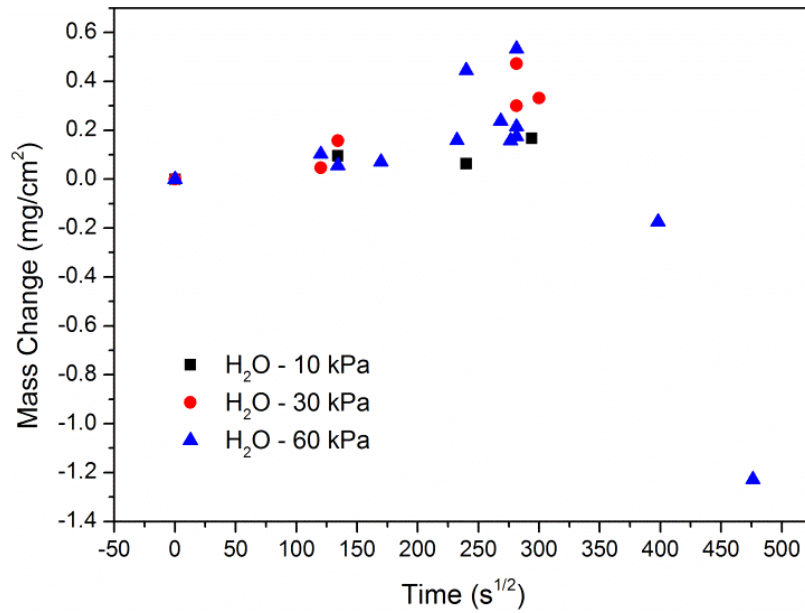
Figure 2.19: Mass gain of samples oxidized at 1600 °C under 10, 30, and 60 kPa steam partial pressure in argon.
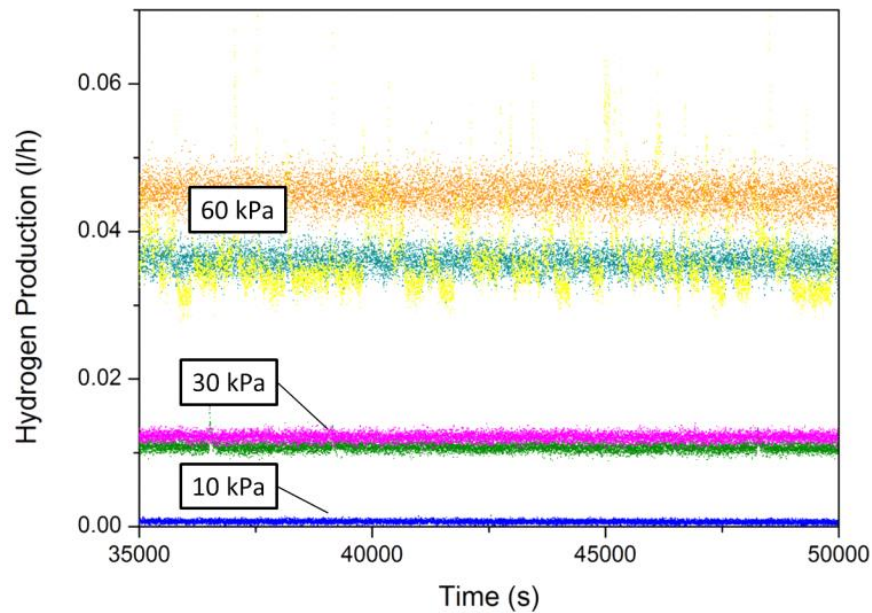
Figure 2.20: Hydrogen production during the oxidation phase at 1600 °C of SiC samples at different steam partial pressures. Each color corresponds to a sample: S1, S2 at 10 kPa, S4 and S6 at 30 kPa, S3, S5, S7 and S8 at 60 kPa. The time interval was chosen since no extraction of the sample was done during this time.

The hydrogen production was integrated over the time and the hydrogen production for unit of surface was calculated. As example, the hydrogen produced by the sample S4 after 10 h oxidation in

40

steam was almost 0.01 kg/m^2, whilst the hydrogen produced by Zry calculated using the Prater-Courtright correlation (Prater 1987) is 100 times higher (1.17 kg/m^2). The SEM sections of the samples S2, S4, S5 and S8 are presented in Figure 2.21 and in Figure 2.22 respectively. The samples oxidized at 10 kPa steam partial pressure have a dense, compact silica layer of about 5 μm (Figure 2.21). Figure 2.22 shows how the silica scale changes after being oxidized in 30 kPa steam partial pressure and at 60 kPa steam partial pressure, and how the oxidation time influences the bubbles formation in the silica layer. During the experiments, the samples oxidized at 30 kPa (Figure 2.22a) have developed traces of bubbles on the surface, but those are not visible in the section. Whereas on the section of the samples oxidized at 60 kPa steam partial pressure, bubbles with a diameter of almost 200 μm are visible (Figure 2.22b and Figure 2.22c). In Figure 2.23, the XRD measurement of the section of the sample S6 is presented. The XRD pattern of the uncoated Hi-Nicalon Type S SiC fibers can be recognized. It consists of 5 reflections around 2Θ of 35.7°, 41.4°, 60.4°, 71.8° and 76° (Singh 2012), despite the second and the last ones are quite weak.
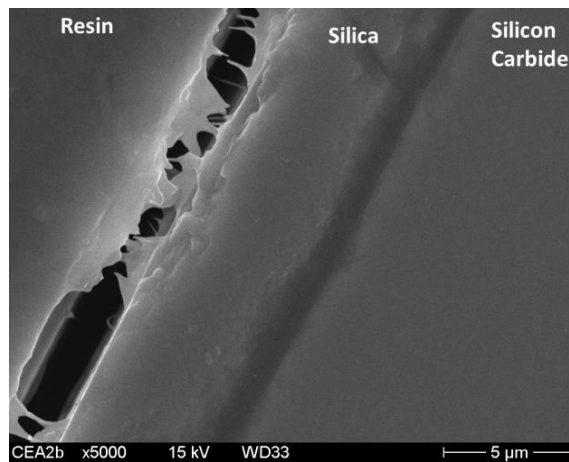
Figure 2.21: SEM micrograph of sample S2 showing the silica scale developed on silicon carbide samples oxidized at 1600 °C at 10 kPa steam partial pressure.
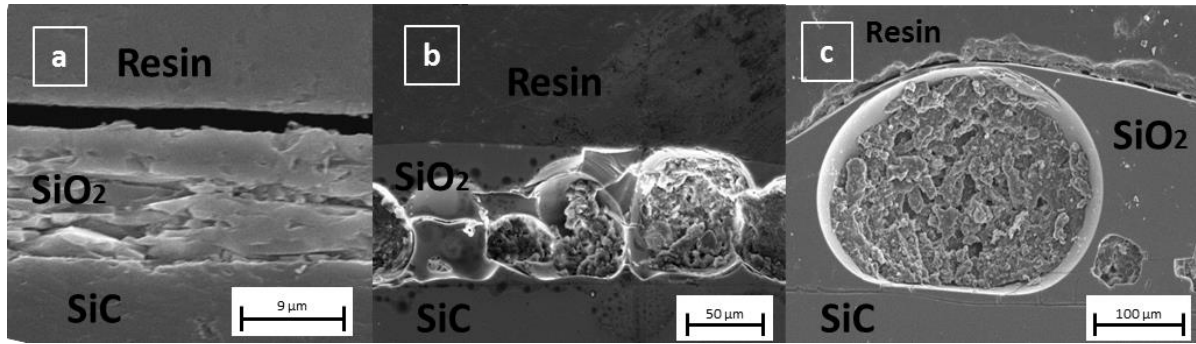
Figure 2.22: SEM micrographs showing the silica scale developed on silicon carbide samples oxidized at 1600 °C at different steam partial pressures; (a) steam 30 kPa after 22 h (Sample S4); (b) steam 60 kPa after 22 h (Sample S5); (c) steam 60 kPa after 64 h (Sample S8).

Even if the initial sample is β-SiC, a small amount of α-SiC in the XRD analysis can be due to micro-twins and stacking in the β-SiC crystalline core. This diffraction pattern is in line with the one measured by CEA (Buet 2012). A broad peak at $2\theta \approx 20°$ reveals the amorphous nature of the silica. This shows a different behavior of the silica depending on the temperature, since a study of SiC oxidation by Park (2014) highlights the formation of crystalline silica already after 2 h at 1200 °C. After 25 h, bubbles of about 70 μm diameter develop at the interface between the silica and the silicon carbide, onto a thin layer visible for example in Figure 2.24 of the sample S5. This layer turned out to be carbon, as shown by the EDX analysis in Figure 2.24. The inner surface of the bubble in Figure 2.24 looks jagged and rough. Backscattering images did not highlight the presence of impurities, which could have enhanced the bubble formation. A 10 μm thick carbon layer is also clearly visible at the interface between the SiC and the SiO_2 in Figure 2.25.
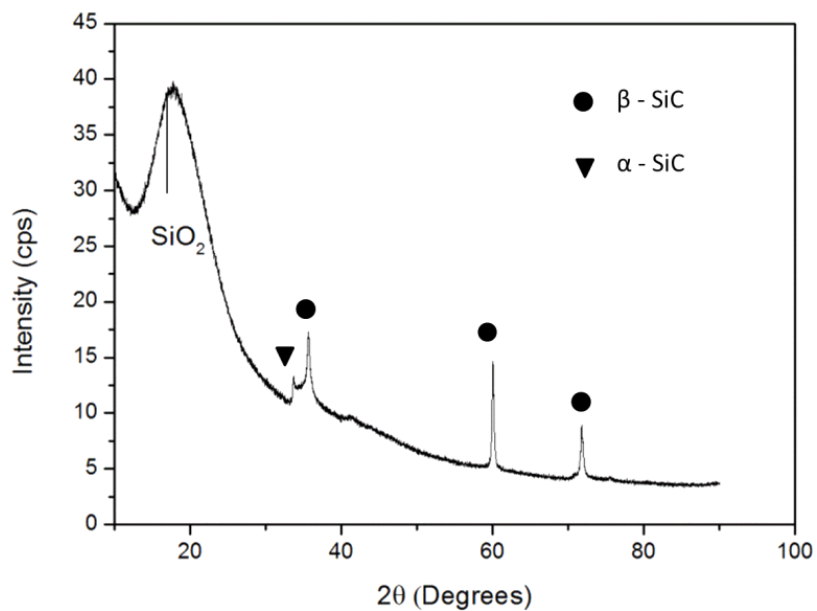
Figure 2.23: XRD measurement of S6 SiC oxidized for 25 h at 1600 ℃.
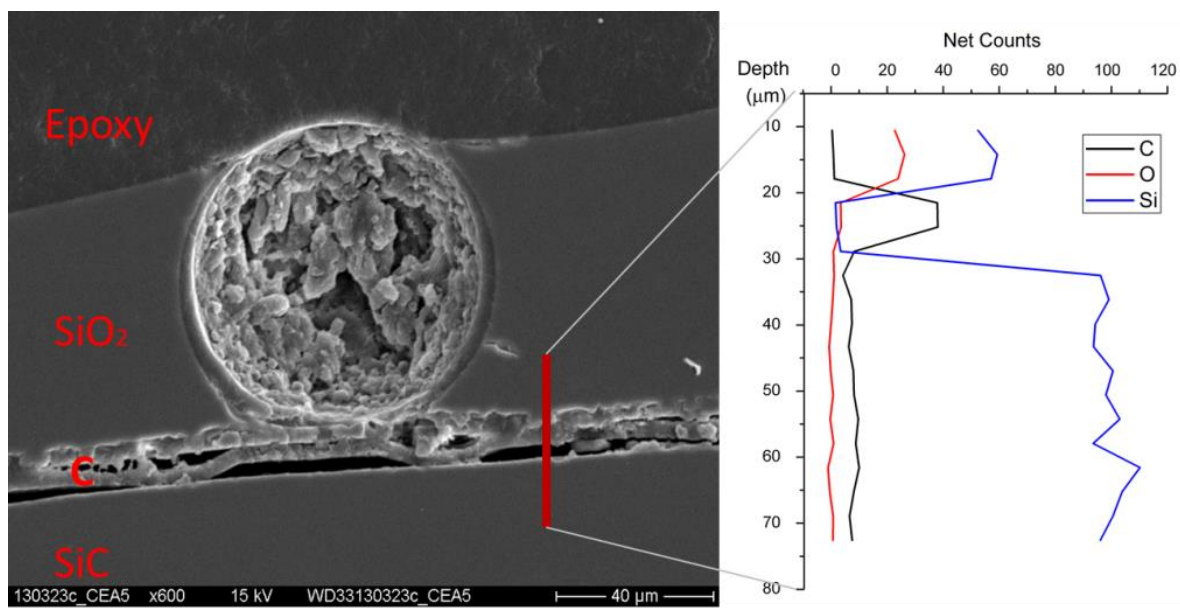
Figure 2.24: SEM micrograph and elemental mapping of the section of the sample S5 oxidized at 1600 ℃.
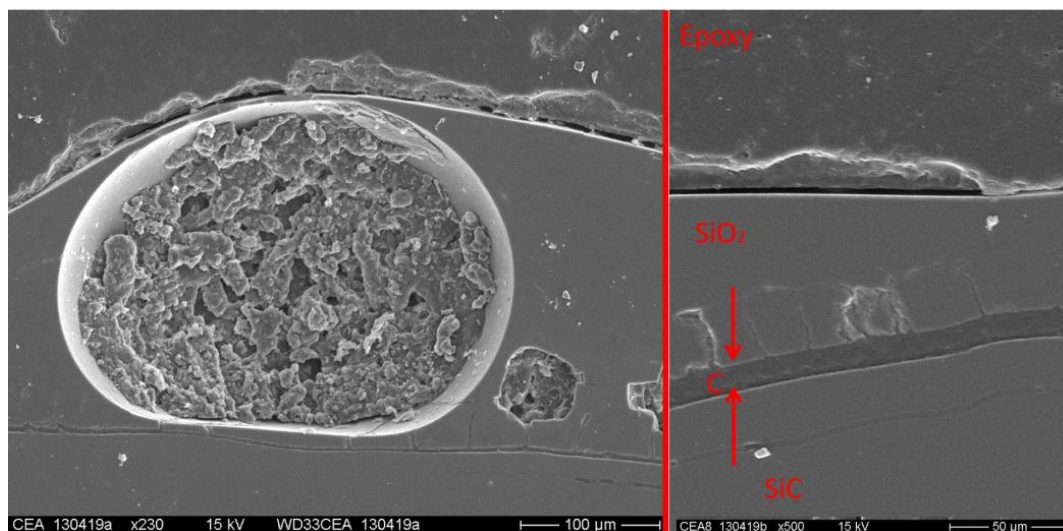
Figure 2.25: SEM micrograph of the interface between the silicon carbide and the silicon oxide of the sample S8. The carbon layer is visible and pointed by the arrows.

Micro Raman spectroscopy was conducted on the sample S8 to further characterize the layer and to confirm the presence of the carbon layer between SiC and SiO_2. Five measurements have been undertaken for each area as outlined in Figure 2.25. The peaks have been compared with the literature (Zabinski 1995; Hodkiewicz 2010) and with the RRUFF database. The sample in Figure 2.25 can be outlined as in Figure 2.26.

The spectra of the silicon carbide and the crystalline SiO_2 have been identified in Figure 2.26(a) and (c). Spectrum (b) presents many narrow peaks, which have not been completely identified. The literature (Zabinski 1995) reports one narrow peak for crystalline carbon (cubic 1332 cm^{-1} (diamond), hexagonal 1578 - 1585 cm^{-1} (graphite)), whereas two broad peaks are detected in the case of the amorphous carbon (1350 cm^{-1} / Disorder band and 1586 cm^{-1} graphite band) (Reich 2004). One peak in Figure 2.26b can be assigned as the G carbon band, confirming the EDX analysis. Different possible chemical elements have been taken into account in order to identify the peaks which were not identified in the spectra (b) in Figure 2.26. Beside the presence of Si, O, and C, possible impurities from the tubes (Al, Na, Zr, Mo) or from the water (Cu) have been taken into account. Comparison with the following compounds ($AlSiO_5$, Al_2O_3, $NaAlSiO_4$, Cu) have been performed without success. Spectrum (d) confirms the amorphous structure of SiO_2.
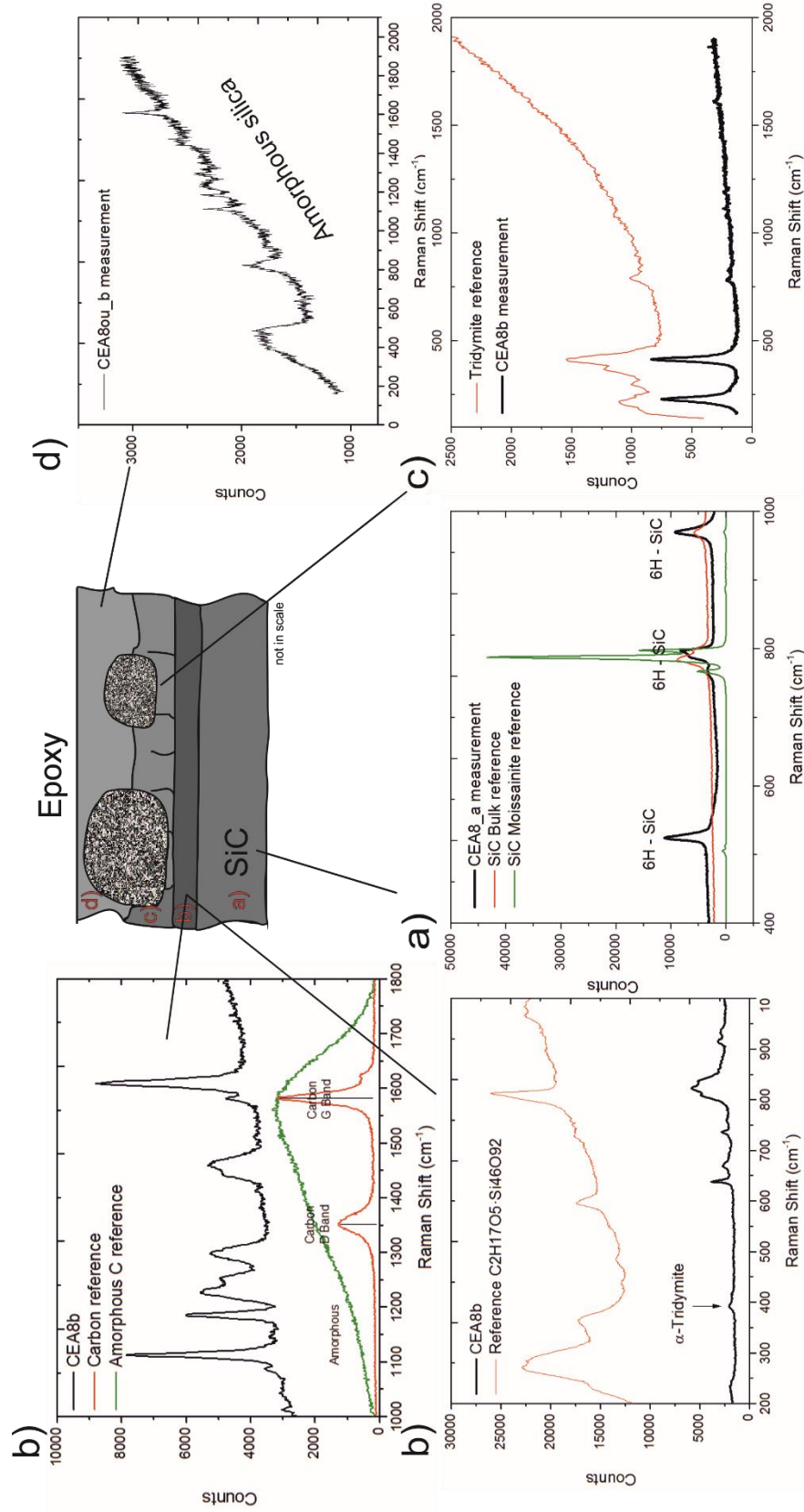
Figure 2.26: Micro Raman spectra of the silicon carbide (a) and carbon (b) and silica layers (c, d).

Tests at higher temperatures (1700 °C and 1800 °C) were performed for 1 hour in the QUENCH-SR furnace described previously (see Table 2.7 for tests' details). On the samples tested at these temperatures, it was not possible to measure the mass before and after the test, due to the inclusion of Al_2O_3 glue on the surface. According to the mass spectrometer's measurement, the hydrogen generation rate increased with increasing temperature. In addition, the hydrogen generation fluctuated to a greater degree at 1800 °C than at 1700 °C. The average hydrogen flow rate for each sample during the isothermal period was calculated by means of Eq. (2.20). Considering the temperature dependence, at 1600 °C the maximum values measured were between 0.35 and 1.7 $g/(m^2 \cdot h)$. At higher temperatures, the hydrogen production was measured between 12 and 61 $g/(m^2 \cdot h)$. The values were scattered, maybe due to contamination by different materials, such as the graphite used to heat up the samples. The silica thickness was measured using SEM techniques. Figure 2.27 shows a dense silica layer. Comparing to the measurements done at 1600 °C, the silica layer at higher temperatures is considerably thinner, and no traces of bubbles in the interlayer between SiO_2 and SiC are noted. This can be due to the high temperature, which is close to the softening point of the silica and can lead to the relocation of the excess silicon dioxide to the bottom of the samples or volatilization.

Table 2.7: Testing parameters of the silicon carbide's samples tested at 1700 and 1800 °C.

Sample	Temperature (°C)	Time (min)	Steam rate (g/h)	Argon rate (l/h)
DM a	1800	30	60	40.00
DM b	1800	60	60	40.00
DM c	1700	30	60	40.00
DM d	1700	60	30	87.60
DM f	1700	60	60	50.10
DM g	1700	60	60	50.10
DM h	1800	60	60	40.00
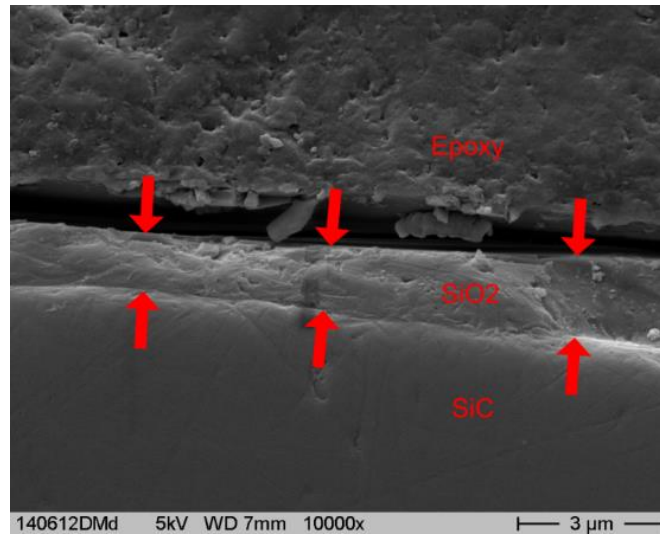
Figure 2.27: SEM macrograph of the cross section of sample DMd at 10000X magnification of a sample oxidized at 1700 °C. The arrows show where the silica layer begins and ends.

2.4 Discussion

The work done on the sintered SiC samples (ESK) samples in dry atmosphere was conducted in order to identify the transition between the passive and active oxidation and to quantify the parabolic constant for this material. Comparing with literature data collected by Presser (2008) and shown in Figure 2.1, the parabolic rate constant measured at 1600 °C in this work ($8.5 \cdot 10^{-11}$ kg/ (m²s^½)) is consistent with the data in the literature. As already discussed, the oxidation tests performed in this work were conducted in an alumina furnace. According to Opila (1995), the impurities contained in the alumina could raise the parabolic constant by one order of magnitude. Being the value calculated in this work already in the lowest range of the values shown in Figure 2.1, it is reasonable to affirm that the oxidation resistance of this specific silicon carbide is higher than the average.

In previous works, the influence of the steam partial pressure on the oxidation kinetics of CVD-SiC was studied at up to 1400 °C (Opila 1999). The finding was that the log k_{par} increased with increasing steam partial pressure. One given explanation is that the water weakens the SiO_2 original structure replacing the Si-O-Si bonding by the weaker Si-OH OH-Si (Wagstaff 1969) increasing the oxidation velocity. In Opila's work, the k_{par} derived from TG measurements oxidation of CVD SiC is

47

4.98 · 10^{-4} mg/(cm² s$^{1/2}$) in steam-oxygen atmosphere for 10 kPa and 6.07 · 10^{-4} mg/(cm² s$^{1/2}$) at 25 kPa and 1400 °C. These values are comparable with the result obtained in this work at 10 kPa, while at 30 kPa the value calculated in this work is one order of magnitude higher (4.7 · 10^{-4} mg/(cm² s$^{1/2}$) for 10 kPa steam partial pressure and 1.2 · 10^{-3} mg/(cm² s$^{1/2}$) for 30 kPa). This can be explained considering the difference of temperature and the alumina impurities in the furnace.

In this work, the presence of bubbles was detected on the oxidized silicon carbide surface at every temperature tested, depending on the exposure time and steam partial pressure, according to Opila (1999). Considerations on bulk materials can be applied on the samples investigated in this work, since the external layer of the composite is made of CVD silicon carbide. Therefore, as long as the underlying composite layer is untouched, the theory expressed by Goto's group (Katsui 2014) can be used to explain the development of the bubbles on the samples used in this work. In case a dense SiO_2 layer develops on the SiC external surface, the gas produced from the interaction between the SiC and the steam remains entrapped in the interface between the SiC and the SiO_2. When the gas pressure exceeds the external pressure, bubbles are formed. This can occur when these three criteria are met:

-   Development of a dense silica scale

-   Presence of higher gas pressure than external pressure at the interface

-   Sufficiently low viscosity of the SiO_2.

Considering the first requirement, the silica, at the temperatures studied in this work, appears in three modifications: tridymite, cristobalite and amorphous. The transition between tridymite and cristobalite occurs at 1470 °C, therefore at 1600 °C cristobalite is expected. Among the forms in which silica appears, its formation on SiC results in a first vitreous layer and in a subsequent porous non-protective cristobalite scale (Tortorelli 2003). It has been proven that the steam, as well as the impurities coming from the reaction chamber, decrease the SiO_2 crystallization temperature and enhance the crystallization process. Indeed, the crystallization follows a diffusion model in case of dry oxidation and a linear one in the case of steam oxidation. Despite the faster oxygen diffusion in vitreous silica than in beta-cristobalite (Rodríguez-Viejo 1993), the oxidation itself can be fostered in the case of the formation of crystalline silica. This is caused by the cracks developed in the protective oxide scale, which may act as

shortcuts for oxidant transportation (National Research Council 1970). XRD investigations of the samples oxidized in this work have shown the presence of amorphous silica, which supports the bubbles formation.

The second condition necessary for explaining the bubbles is the presence of gases at the interface of SiO_2 and SiC. They can come either from the oxidation of SiC or from the interaction between SiC and SiO_2. The first hypothesis implies that the gases accumulate at the interphase, requiring that the permeability of the CO through the SiO_2 scale is lower than that of H_2O. Another source of CO production is the reaction between SiO_2 and SiC (Narushima 1994; Goto 2002). Figure 2.28 shows the vapor pressure of CO and SiO_2 at the interface between SiC and SiO_2 calculated with the CALPHAD method, with the database from SGTE (Scientific Group Thermodata 2014). In case that C is present, (which can come from the CVD-SiC impurities) at standard pressure, the bubbles can start to be produced at around 1507 °C, when the gas internal pressure is equal to the external pressure (10^5 Pa in our experiments). This is supported by the diffusion coefficient of the two species CO and H_2O in silica. Data provided by Doremus (2001) stated that the values of the diffusion coefficients of molecular water behaves according to Eq. (2.28), which yields to $3 \cdot 10^{-7}$ cm^2/s as diffusion coefficient at 1100 °C. The diffusion coefficients of molecular water can be compared to the value presented in the work by Pongráz (2009) at the same temperature for carbon monoxide ($D_{CO} = 1.8 \cdot 10^{-9}$ cm^2/s).

$$D = 1.3(10)^{-4} \exp\left(-\frac{8360}{T}\right) \quad \left(\frac{cm^2}{s}\right) \qquad (2.28)$$

According to the two values, it is reasonable to assume that the CO accumulates at the interface and can be the oxidation limiting species. Regarding the presence of carbon in the material, a significant carbon excess was detected in the external layer of the oxidized samples by the elemental analysis (Appendix B). Besides, a possible explanation for the carbon layer could also be the migration of carbon towards the silica. The presence of carbon can be correlated with the flux of oxidant and products to explain the bubbles formation.
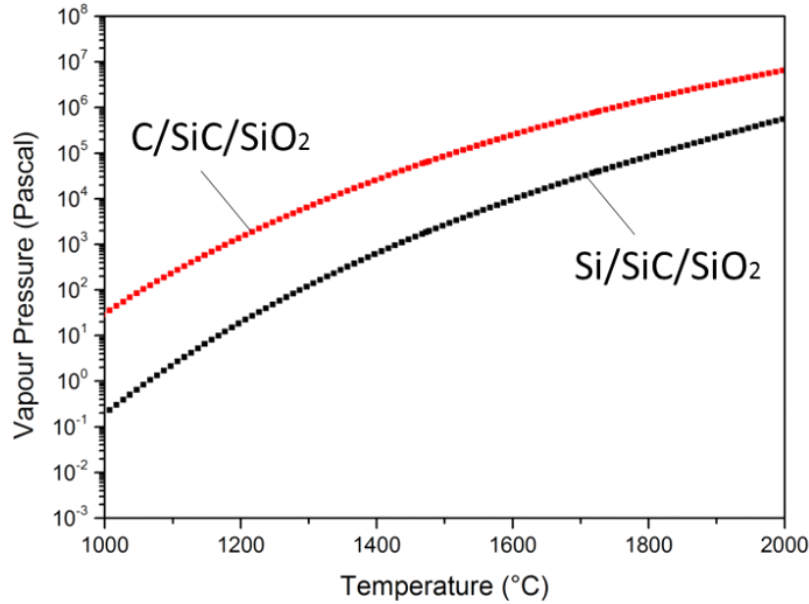
Figure 2.28: Vapor pressure of the gas species (SiO and CO) in equilibrium with C-SiC-SiO$_2$ and Si-SiC-SiO$_2$ calculated with Thermo-Calc.

Schneider (1998) modeled three possible cases regarding the trend of the gases fluxes during SiC oxidation (Figure 2.29). In case 1, the flux of oxidant and products is the same, hence an equilibrium is established; in case 2 the CO and the H$_2$ diffuse faster than H$_2$O, leading to further oxidation; case 2 occurs when the oxidant diffuses faster than the products. Case 3 is the case where CO and H$_2$ accumulate at the interface and, therefore, pressure build-up occurs. This is probably the situation that occurred during the experiments at 30 kPa and 60 kPa steam partial pressure in this work. Indeed, the stability diagram of the Si-C-O states that the carbon solid phase can exist with SiO$_2$ solid and SiC solid when $a_c=1$. At 1873 K, this corresponds to $P_{CO} = 2.3 \cdot 10^5$ Pa and $P_{O_2}= 2.3 \cdot 10^{-10}$ (Katsui 2014). This indicates that the outward diffusion of CO is the rate-limiting process of the oxidation of SiC.

The last criterion for bubbles formation is easily fulfilled, considering that the logarithm of the SiO$_2$ viscosity in poise at 1600 °C is 10.6 using the Urbain correlation shown in the paper by Doremus (2002). This value of viscosity is close to the softening point, as shown in Figure 2.30 (Guy 1976). This means that the SiO$_2$ can easily expand producing bubbles.
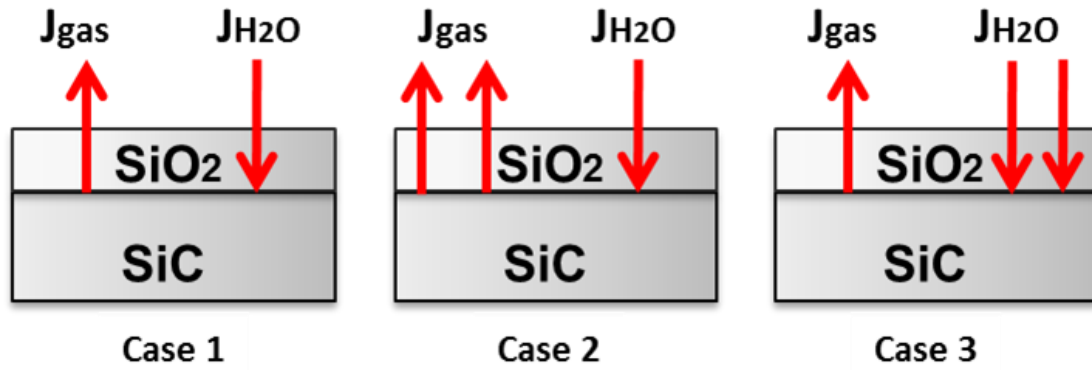
Figure 2.29: Depiction of various fluxes during SiC oxidation in steam (Schneider 1998).
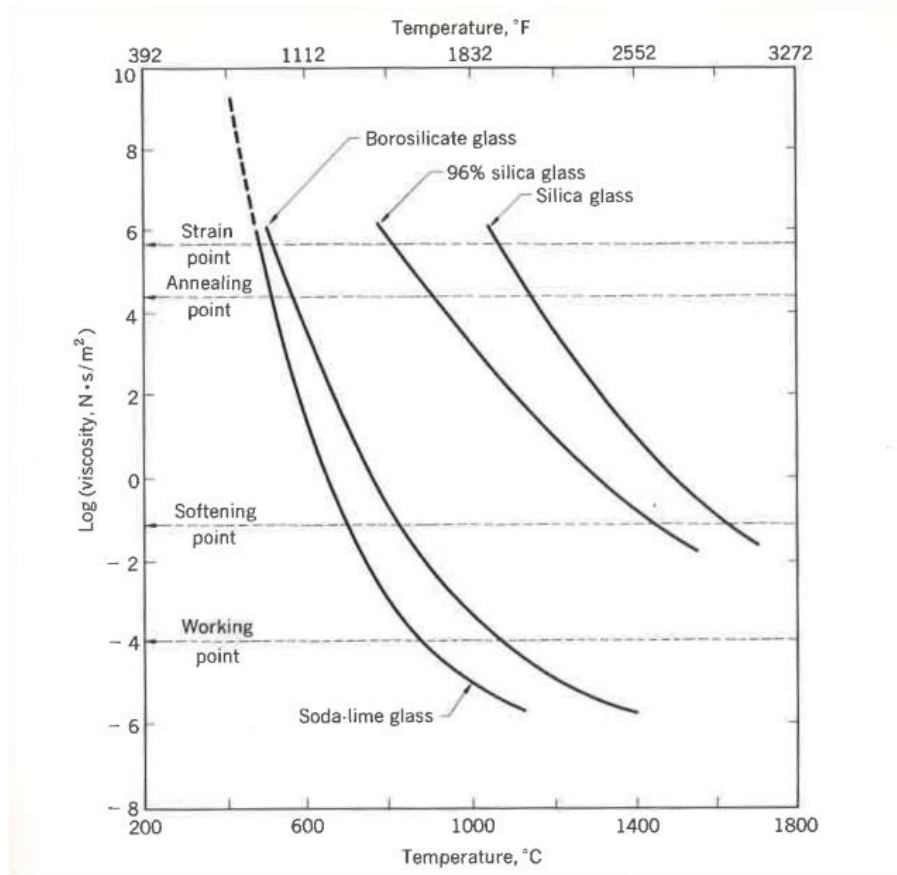
Figure 2.30: Important temperatures for the fabrication of silicate glasses shown in relation to the curves of viscosity versus temperature (Guy 1976).

2.5 Conclusions of the SiC oxidation tests in dry oxygen and steam

Oxidation in dry atmosphere of commercial SiC samples was performed at 1550 °C. The transition between passive and active oxidation was registered occurring at the oxygen partial pressure in the range of 10 to 50 Pa. The parabolic constant was calculated for the passive oxidation and compared with the data in the literature, showing good agreement.

Ceramic matrix composites tube segments from the CEA laboratories were oxidized at 1600 °C up to 64 h at different steam partial pressures, 10, 30 and 60 kPa. For the lower steam partial pressures, the values of the k_{par} are in agreement with the data in the literature, presented at lower temperatures. At 60 kPa, the mass gain becomes irregular and the k_{par} cannot be calculated. This is mainly due to the formation of bubbles, which increases with exposure time and steam partial pressure. Bubbles formation was observed at 1600 °C only at 30 and 60 kPa steam partial pressure. At higher temperatures, bubbles were detected during the experiments, but no traces were found in the silica scale in the post-analysis. The bubbles formation can be explained considering that an amorphous silica layer develops on the silicon carbide surface, and this has been confirmed by the EDX measurement. The raising of the carbon activity at the interface between the SiC and the SiO_2 increases the gas pressures at the interface, thus promoting the formation of bubbles. The bubbles formation suggests that under these conditions, the carbon monoxide accumulates at the interface and results in the rate-limiting step.

Oxidation tests at 1700 and 1800 °C were performed for as long as 1 hour. In these experiments, the silica layer was found to be 2 μm thick. Bubbles were also noted during the experiments, but the post-test analysis shows a dense silica layer. This can be explained considering that the temperature is close to or above the silica melting point. Therefore, during the cooling phase, it relocates and solidifies again.

Overall the silicon carbide performs very well at temperatures up to 1800 °C: during all experiments, the samples maintained a coolable shape and did not present severe degradation caused by the oxidation. From the oxidation experiments, it can be stated that SiC tri-layered samples can give an additional safety margin regarding the beyond LOCA margin, maintaining the coolability in steam atmosphere for up to three days at 1600 °C, and in the order of hours at 1700 °C and 1800 °C.

3. Thermodynamic modeling of the silica volatilization in steam

In the previous chapter the oxidation of silicon carbide and experimental tests performed in oxygen and steam at high temperatures were presented. Throughout the experimental tests described in this work, the volatilization has not been quantified. In order to give a quantification of the volatilization rate, this phenomenon was studied in this chapter using thermodynamic modeling. The reaction of silica with water has been investigated as fundamental process in different fields, such as geological and astrophysical processes (Hashimoto 1992), as well as for understanding the behavior of silica-based coatings and silica-forming ceramics such as silicon carbide (Robinson 1999). In corrosive atmospheres, the capability of producing compact SiO_2 layers at the solid-gas interface is often employed as a protection from further oxidation for the underlying material. However, deterioration of the protective coating can occur under conditions favorable to the volatilization of SiO_2, which takes place throughout the production of silica hydroxide species, developed in case of reaction of the silica with water vapor.

Thermodynamic calculations and kinetic simulations performed using thermodynamic descriptions and kinetic models of the multi-component systems are important tools, which can be used to understand and predict degradation mechanisms under different conditions. The aim of the work described in this chapter is to calculate the erosion rate of the SiO_2 scale occurring during volatilization by developing analytical expressions of the Gibbs free energies of the gas species produced during volatilization of SiC with the CALPHAD method. Since previous experimental work (Jacobson 2005) has shown that these $Si(OH)_4$, $SiO(OH)_2$ gas species are formed during the reaction of SiO_2 with water vapor at high temperatures, only these two species have been considered. Zhang (2014) recently developed thermodynamic descriptions of the Gibbs energy functions of $Si(OH)_4$, $SiO(OH)$, and

SiO(OH)$_2$. However, a comprehensive review of the experimental data, which were selected to optimize the thermodynamic parameters of the free energy functions, was not presented and the analytical expressions themselves were not published.

3.1 Thermodynamic data on silicon-hydroxide species in the literature

Thermodynamic descriptions of the gaseous products of the volatilization of SiO$_2$ in steam atmospheres are required to be able to model the thermodynamics and kinetics of SiC oxidation. At high steam partial pressures (P>10^{-4} bar at 1700 K (Opila 1995)), passive oxidation of silicon carbide occurs, resulting in the formation of a protective silica scale as in Eq. (2.12) and Eq. (3.1).

$$SiC + 3H_2O \rightarrow SiO_2 + CO + 3H_2 \tag{3.1}$$

Simultaneously, the SiO$_2$ scale undergoes volatilization due to the reaction of SiO$_2$ with H$_2$O. According to Opila (1999), the volatilization of silica at atmospheric pressure in water vapor occurs through the following reactions, mainly resulting in the formation of three different silicon hydroxide species (Si(OH)$_4$, SiO(OH)$_2$, SiO(OH)) (as in Eqs. 3.13, 3.14, 3.15):

$$SiO_{2(s)} + 2H_2O_{(g)} \rightarrow Si(OH)_{4(g)} \tag{3.2}$$

$$SiO_{2(s)} + H_2O_{(g)} \rightarrow SiO(OH)_{2(g)} \tag{3.3}$$

$$SiO_{2(s)} + \frac{1}{2}H_2O_{(g)} \rightarrow SiO(OH)_{(g)} + \frac{1}{4}O_{2(g)} \tag{3.4}$$
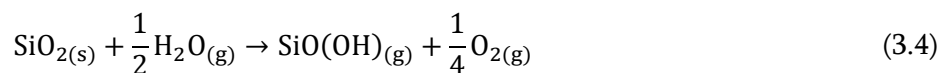
Both experimentally determined and theoretical estimates of the equilibrium constants for the Si-containing hydroxide species are available in the literature (Krikorian 1970; Hashimoto 1992; Hildenbrand 1994; Hildenbrand 1998) and are analyzed in the following section.

In the literature, the second and third thermodynamic law methods are used to calculate the thermodynamic state functions based on the equilibria of the involved gas species (Drowart 2005).

The second law method is used to determine the enthalpy of reaction $\Delta_r H_T^o$ in small temperature ranges. By applying the Van't Hoff equation:

$$\frac{\text{dln}K_p}{\text{dT}} = \frac{\Delta_r H_T^o}{RT^2} \tag{3.5}$$

$\Delta_r H_T^o$ is obtained as the slope of the graph of $\ln K_p$ against $1/T$, where K_p is the reaction constant, and T the temperature. The advantage of the second law method is that it does not require the thermodynamic data at a reference temperature. However, $\Delta_r H_T^o$ is only calculated for the average temperature in the temperature range considered.

The reaction enthalpy $\Delta_r H_0^o$ can be determined with more accuracy using the third law method (Darnell 1968). According to the third law method, the molar Gibbs energy at temperature T can be determined as in Eq. (3.6):

$$\tag{3.6}$$
$$\Delta_r G_T^o = -RT\ln k_p = \Delta_r H_0^o - T\Delta_r \left(\frac{G_T^o - H_0^o}{T}\right)_{prod}$$
$$= \Delta_r H_0^o - T\sum\left(\frac{G_T^o - H_0^o}{T}\right)_{prod} - \sum\left(\frac{G_T^o - H_0^o}{T}\right)_{react}$$

where G_T^o is the molar Gibbs energy at temperature T, H_0^o is the standard molar enthalpy at a reference temperature (either 0 K or 298 K), and $\left(\frac{G_T^o - H_0^o}{T}\right)$ is the tabulated free energy function (fef) for product and reactant species. The fefs of condensed phases are mostly based on experimental determination of heat capacity down to low temperatures. For gaseous molecules, the fef is generally calculated using statistical mechanical formulae from molecular parameters, i.e., geometry (interatomic distances, bond angles), vibrational frequencies, excitation energies, and multiplicities of electronic data. This method is convenient since the free energy functions for reactants and products have much smaller variations with temperature than G_T^o.

Thermodynamic descriptions of the gaseous products of the volatilization of SiO_2 in steam atmosphere are required to be able to model the thermodynamics and kinetics of SiC oxidation. Therefore, a review of the experimental and theoretical data for the reaction of water vapor with SiC is given in the following section.

Krikorian (1970) reviewed the experimental work in the silica-steam system up to 1970 K. The equilibrium constants for reactions between SiO_2 and H_2O at the given temperatures were used in order

to identify the complex Si-O-H gas species ($Si_m(OH)_{2n}O_{2m-n}$). According to this method, the reaction between SiO_2 and H_2O is written as Eq. (3.7):

$$mSiO_2 + nH_2O = Si_m(OH)_{2n}O_{2m-n} \tag{3.7}$$
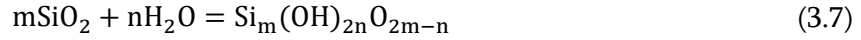
with the equilibrium constant expressed as:

$$K_{eq} = -\frac{f_{complex}}{(a_{s,l})^m (f_{H_2O})^n} \tag{3.8}$$

where $f_{complex}$ is the fugacity of the different Si-O-H gas species, $a_{s,l}$ is the activity of the components in the solid or liquid condensed phase, and f_{H_2O} is the fugacity of water. Krikorian also calculated the free energy functions of different species from the estimation of the vibrational frequencies. The third law method was then used to calculate the enthalpies of formation of the gas species at 0 K. $Si(OH)_4$ was found to be at ambient pressure the dominant gas species up to 1970 K.

Hashimoto (1992) used the transpiration method to study the reaction of water vapor with crystalline SiO_2 (transparent alpha quartz) at temperatures between 1373 K and 1773 K. In these experiments, mixtures of O_2 and H_2O were allowed to react with crystalline SiO_2 in a noble-metal reaction cell, saturating the atmosphere with silicon hydroxide species. According to the Si-content of the condensate from the gas, the main product of the reaction was $Si(OH)_4$. From these measurements, the equilibrium partial pressure of $Si(OH)_4$ could be calculated assuming ideal gas behavior. The enthalpy of formation of the hydroxide gas species was also calculated using data from the JANAF tables (Chase 1998).

Hildenbrand and Lau (Hildenbrand 1994; Hildenbrand 1998) measured the partial pressure of $SiO(OH)_2$ and $SiO(OH)$ from the reaction of silica and H_2O at 1963, 2041 and 2065 K using a Knudsen effusion cell source. The gas species were identified by means of a magnetic deflection spectrometer. The enthalpies of formation of $SiO(OH)_2$ and $SiO(OH)$ from SiO and OH gas species were calculated using the third law method, in which thermodynamic data for $SiO(OH)_2$ and $SiO(OH)$ available in the literature (Krikorian 1970) were used to calculate the free energy functions. In contrast to other works, the $Si(OH)_4$ species was not detected.

Allendorf (1995) combined ab initio electronic structure calculations and empirical correlations to derive the enthalpies of formation at 0 and 298 K and the Gibbs energy of formation from 298 to 2500 K for many gas species, including $Si(OH)_4$, $SiO(OH)$, $SiO(OH)_2$. In particular, electronic structure calculations were performed to calculate the equilibrium geometries and harmonic vibrational frequencies of the gas species (Ho 1990). Calculations of electron correlation effects coupled with empirical bond additivity corrections for the equilibrium geometries were subsequently performed. This was done in order to accurately determine the heat of formation at 0 K. Thermodynamic properties such as entropies, heat capacities, and heat of formation at other temperatures were further calculated using the heat of formation data at 0 K, the calculated geometries and scaled frequencies and equations derived from statistical-mechanics.

Opila (1997) investigated the formation of volatile species from the reaction of fused quartz frit in an oxygen stream saturated with water vapor at ambient pressure using high pressure sampling (supersonic sampling) mass spectrometry. Since the most intense peak was observed for the $Si(OH)_3^+$ species, it was concluded that $Si(OH)_4$ was the dominant silicon hydroxide gas species in accordance with Hashimoto (1992). A small peak was also observed for $SiO(OH)^+$, suggesting the presence of $SiO(OH)_2$. $SiO(OH)$ could not be measured because its partial pressures were below the detection limit of the instrument (10^{-6} bar).

The work of Opila (1997) was followed by that of Jacobson (2005), in which the transpiration method was used to study the interaction of SiO_2 (cristobalite) with water vapor at temperatures between 1073 and 1728 K. At temperatures below 1673 K, formation of $Si(OH)_4$ was confirmed since the slope of the graph of $logP(Si-OH)$ against $logP(H_2O)$ was 2, as expected for the reaction according to Eq. (3.2). At higher temperatures, formation of mixtures of $Si(OH)_4$ and $SiO(OH)$ or $SiO(OH)_2$ was detected since the slope of the graph of $logP(Si-OH)$ against $logP(H_2O)$ was less than 2. In order to clearly identify the other gas species, experiments with two different oxygen partial pressures in the reaction chamber were performed. Using this method, the specific gas species could be identified since formation of $SiO(OH)$ is suppressed by oxygen, as shown in Eq. (3.4), whereas the amount of $SiO(OH)_2$ is independent of the oxygen partial pressure, remaining constant at different oxygen partial pressures. The results did not show any oxygen partial pressure dependency, so that the formation of $SiO(OH)$

could be ruled out. The enthalpies and entropies of formation of Si(OH)$_4$ were determined using the second law method. Additionally, the enthalpies of formation of Si(OH)$_4$ and SiO(OH)$_2$ at 298 K were calculated with the third law method using free energy functions from the data of Allendorf (1995). Moreover, Jacobson performed third law calculations employing the experimental data from Hashimoto at 1673 K and the data at reference temperature from Allendorf (1995).

Recently, Plyasunov (2011) analyzed the available experimental data for the reaction of SiO$_2$ with H$_2$O to produce Si(OH)$_4$. In this work, 102 data points from seven literature sources were analyzed and the assessed thermodynamic functions for Si(OH)$_4$ are given in Table 3.1 of this work (Plyasunov 2011). Rutz and Bockhorn (2007) used ab initio and density functional theory calculations to derive the standard enthalpy of formation, entropy and heat capacity for many Si-O-H species. The values for Si(OH)$_4$ are in agreement with other values in the literature. The enthalpies and entropies of formation of Si(OH)$_4$, SiO(OH)$_2$ and SiO(OH) from the literature are summarized in Table 3.1, Table 3.2, and Table 3.3.

Table 3.1: Thermodynamic data for Si(OH)$_4$ from the literature.

References	$\Delta_f H$ (kJ/mol)	$\Delta_f S$ (J/mol K)	S^o_{298} (J/mol K)	Comments
Krikorian	-1348	563		Estimation (0 K)
Hashimoto	-1342.7±2.7	592.5±1.0		Experimental (1600 K)
Allendorf	-1342.2±3.3		342.5	Ab initio calculation (298 K)
Jacobson	-1344.6±2.7	544.1±2.1		Experimental (1200 K)
Plyasunov	-1340.7±3.5		347.8±6.2	Calculation
Rutz & Bockhorn	-1333.1		333.9	Ab initio calculation

Table 3.2: Thermodynamic data for SiO(OH)$_2$ from the literature.

References	$\Delta_f H$ (kJ/mol)	S^o_{298} (J/mol K)	Comments
Hildenbrand & Lau	-893±4		Third-law
Allendorf	-804.6±6.2	292	Ab initio (298 K)
Jacobson	-836±40		Transpiration

Table 3.3: Thermodynamic data for SiO(OH) from the literature.

References	$\Delta_f H$ (kJ/mol)	S°_{298} (J/mol K)	Comments
Krikorian	-494		Estimation (298 K)
Hildenbrand & Law	-494±4		Third law (298 K)
Allendorf	-312.5±1.5	271	Ab initio (0 K)

The enthalpy of formation of $Si(OH)_4$ at 298 K from Krikorian (1970), Hashimoto (1992), Allendorf (1995), and Jacobson (2005), are in good agreement with each other. However, there is a deviation in the enthalpies of formation at 298 K for $SiO(OH)_2$ and SiO(OH). This can be explained considering that $SiO(OH)_2$ was not directly measured by Jacobson, but was indirectly determined from the gas mixture as the difference between the total amount of gases produced and the contributions given by $Si(OH)_4$. The $\Delta_f H$ value lies between that measured by Hildenbrand and the one calculated by Allendorf. The enthalpy of formation values for the SiO(OH) species are scattered, due to the difficulty encountered in measuring the species.

In the following section, the data from the literature are compared with each other in order to be able to select the experimental data which will be used for the thermodynamic optimization.

3.2 Development of a thermodynamic description of silicon-hydroxide gas species

In this chapter, the data in the literature of the silicon hydroxide gas species are reported and compared.

3.2.1 Si(OH)₄ species

The works of Hashimoto (1992) and Jacobson (2005) show that $Si(OH)_4$ is the main product of volatilization of solid silica with water vapor. Hashimoto gave an analytic expression of $\log_{10}(K_P)$ for the reaction of solid SiO_2 with gaseous H_2O to produce $Si(OH)_4$ as expressed in (3.2), whereas Jacobson listed their results as $\ln(K_P)$ values. Allendorf (1995) calculated the Gibbs energy of formation of $Si(OH)_4$ from the elements at 1000, 1500, 2000 and 2500 K. Eq. (3.9) was therefore used in our work to

be able to compare the reaction constants K_p for Eq. (3.2) from Hashimoto (1992) and Jacobson (2005) with that calculated from the data of Allendorf (1995).

$$\Delta_r G^o_{(Si(OH)_4))} = \Delta_f G^o{}_{(Si(OH)_4)Allendorf} - \Delta_f G^o_{(SiO_2)} - 2\Delta_f G^o_{(H_2O)} \tag{3.9}$$

In Eq. (3.9), $\Delta_f G_{(SiO_2)}$ and $\Delta_f G_{(H_2O)}$ are the Gibbs energy of formation of condensed SiO_2 and gaseous H_2O at 1 bar from the elements respectively (Scientific Group Thermodata 2014), and $\Delta_f G_{(Si(OH)_4)Allendorf}$ is the Gibbs energy of formation of $Si(OH)_4$ from the elements taken from Allendorf (1995). The data from Allendorf (1995), Hashimoto (1992), and Jacobson (2005) are presented in Figure 3.1 as $\ln(K_p)$ against temperature. The data from Krikorian (1970) are not shown since the $\ln(K_p)$ values are much lower than that of Allendorf (1995), Hashimoto (1992), and Jacobson (2005). The Gibbs energy of reaction, along with the equilibrium constants measured by Jacobson (2005) and Hashimoto (1992) are presented in Table 3.4. Hashimoto (1992) gave a numerical expression for the reaction constant of Eq. (3.2), which is Eq. (3.10).

$$\log(K_p)_{Hashimoto} = (-0.2963 \pm 0.0087) \times 10^4 \left(\frac{1}{T}\right) + (-3.45632 \pm 0.0545) \tag{3.10}$$

From this numerical expression the values in Table 3.4 including the relative error were calculated. These data were used to optimize the thermodynamic parameters of the Gibbs free energy description of $Si(OH)_4$.
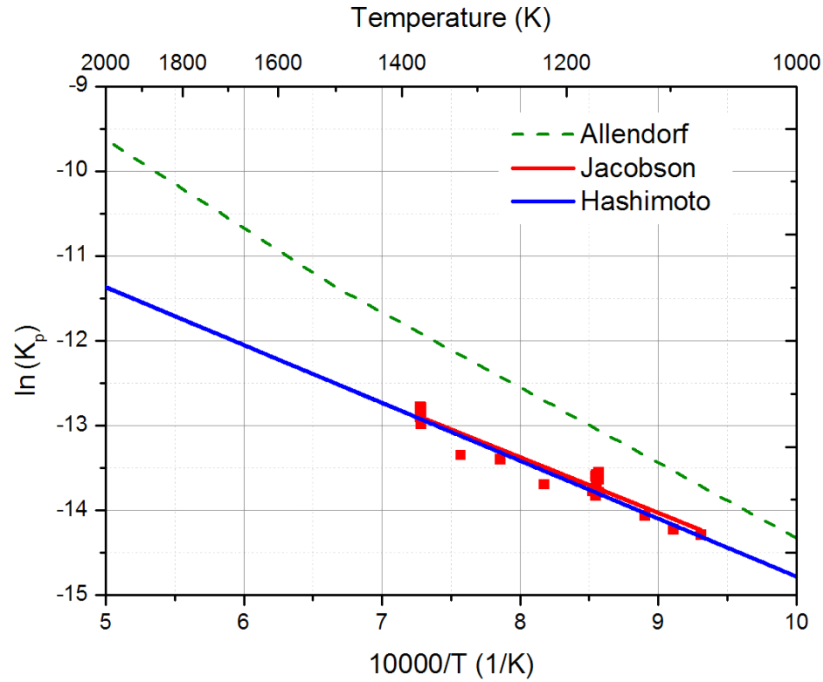
Figure 3.1: Reaction constants for Eq. (3.2) from Allendorf, Hashimoto and Jacobson. Each symbol is an experimental value from (Jacobson 2005).

Table 3.4: The Gibbs energy of reaction and the equilibrium constants employed in this work for $Si(OH)_4$ (a) Jacobson (b) Hashimoto.

Temperature (K)	ln K_p	$\Delta G_r^o(Si(OH)_4)$ $(J \cdot mol^{-1})$
1098 [a]	-14.23	129840
1074 [a]	-14.293	127564
1169 [a]	-13.686	132951
1373 [a]	-12.926	147481
1200 [b]	-13.591±0.063	135535±630
1300 [b]	-13.171±0.063	142282±683
1400 [b]	-12.810±0.063	149028±735
1500 [b]	-12.497±0.063	155775±788
1600 [b]	-12.223±0.063	162522±840
1700 [b]	-11.982±0.063	169269±893
1800 [b]	-11.767±0.063	176015±945
1900 [b]	-11.575±0.063	182762±998

3.2.2 SiO(OH)₂ species

Allendorf (1995) calculated the Gibbs energy of formation of SiO(OH)₂ from the elements at 1000, 1500, 2000 and 2500 K. In order to compare data from Hildenbrand (1994; 1998), Jacobson (2005) and Allendorf (1995) with each other, the reaction constants K_P for the reaction of condensed SiO₂ with gaseous H₂O at 1 bar to form SiO(OH)₂ were calculated according to Eq. (3.3). Since Allendorf (1995) presented the Gibbs energy of formation of SiO(OH)₂ from the elements, Eq. (3.11) was used to calculate the Gibbs energy of reaction of SiO₂ and H₂O to SiO(OH)₂, expressed as $\Delta_r G^o_{(SiO(OH)_2)}$

$$\Delta_r G^o_{(SiO(OH)_2)} = \Delta_f G_{(SiO(OH)_2)}\text{Allendorf} - \Delta_f G^o_{(SiO_2)} - \Delta_f G^o_{(H_2O)} \tag{3.11}$$

where $\Delta_f G_{(SiO(OH)_2)\text{Allendorf}}$ is the Gibbs energy of formation of SiO(OH)₂ from the elements according to Allendorf (1995) whereas $\Delta_f G_{(SiO_2)}$ and $\Delta_f G_{(H_2O)}$ are the Gibbs energies of formation of SiO₂ and H₂O respectively taken from the SGTE database (Dinsdale 1991). Hildenbrand (1994; 1998) presented the equilibrium constants for the reaction:

$$SiO_{(g)} + 2OH_{(g)} = SiO(OH)_{2(g)} \tag{3.12}$$

Eq. (3.13) was therefore used to calculate the Gibbs energy of reaction of solid SiO₂ and vapor H₂O to SiO(OH)₂ ($\Delta_r G^o_{(SiO(OH)_2)}$) from the data of Hildenbrand (1994; 1998) using the following reaction Eqs. (3.13),(3.14),(3.15) to form the thermodynamic cycle:

$$\Delta_r G^o_{(SiO(OH)_2)} = \Delta_f G_{(SiO(OH)_2)} - \Delta_f G^o_{(SiO_2)} - \Delta_f G^o_{(H_2O)} + \Delta_f G^o_{(SiO)} + 2\Delta_f G^o_{(OH)} \tag{3.13}$$

$$Si_{(s)} + O_{2(g)} \xrightarrow{\Delta_f G^o_{(SiO2)}} SiO_{2(s)} \tag{3.14}$$

$$H_{2(g)} + O_{2(g)} \xrightarrow{\Delta_f G^o_{(OH)}} 2OH_{(g)} \tag{3.15}$$

$$Si_{(s)} + \frac{1}{2}O_{2(g)} \xrightarrow{\Delta_f G^o_{(SiO)}} SiO_{(g)} \tag{3.16}$$

$$H_{2(g)} + \frac{1}{2}O_{2(g)} \xrightarrow{\Delta_f G^o_{(H_2O)}} H_2O_{(g)} \tag{3.17}$$

In these equations, $\Delta_f G_{(SiO2)}$, $\Delta_f G_{(H_2O)}$, $\Delta_f G_{(SiO)}$, and $\Delta_f G_{(OH)}$ are the Gibbs energies of formation of SiO₂, SiO, OH and H₂O from the elements, which were taken from the SGTE database (Dinsdale 1991). The

$\ln(K_p)$ against $1/T$ plots from the data of Allendorf (1995), Hildenbrand (1994; 1998), and Jacobson (2005) are shown in Figure 3.2.

The data of Allendorf (1995) were not used to optimize the thermodynamic parameters of the Gibbs energy description of $SiO(OH)_2$ since they are significantly lower than the data of Hildenbrand (1994; 1998) and Jacobson (2005). Table 3.5 lists the Gibbs energy of reaction, along with the equilibrium constants experimentally determined by Jacobson (2005) and Hildenbrand (1994). These data were used to develop the Gibbs energy description of $SiO(OH)_2$.

3.2.3 SiO(OH) species

The SiO(OH) species was not modeled in this work since experimental data are only available at one temperature (2065 K) from Hildenbrand and Lau (1994; 1998) and the calculations from Allendorf (1995) and Krikorian (1970) do not agree with each other.
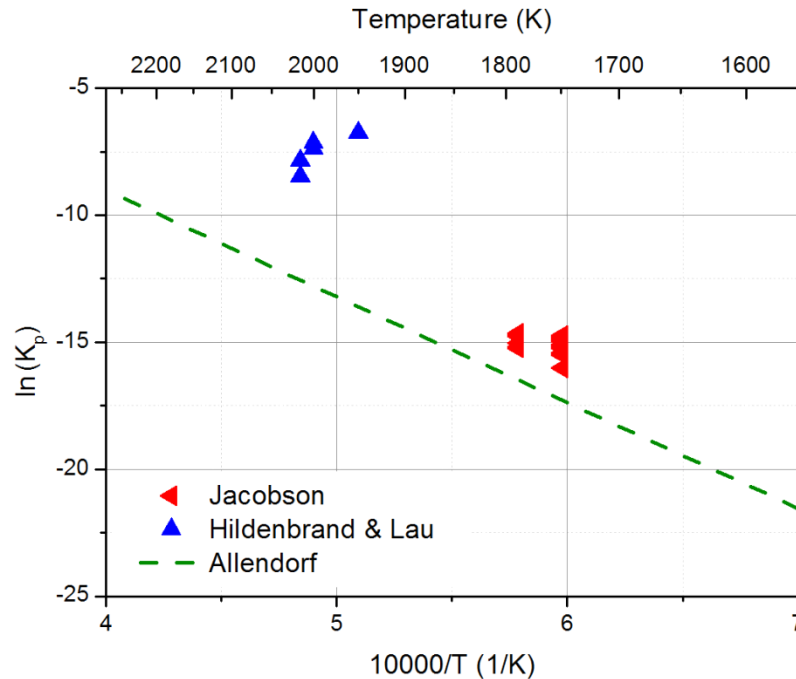
Figure 3.2: Reaction constants for Eq. (3.3) from Hildenbrand and Lau (1994; 1998), Jacobson (2005) and Allendorf (1995).

Table 3.5: The Gibbs energy of reaction and equilibrium constants of $SiO(OH)_2$, from Jacobson (2005) (a), from Hildenbrand and Lau (1994; 1998) (b).

Temperature (K)	$\ln K_P$	$\Delta G_r^o(SiO(OH)_2)$ $(J \cdot mol^{-1})$
1673 [a]	-15.407	214301
1673 [a]	-15.087	209846
1673 [a]	-14.737	204981
1673 [a]	-14.812	206031
1673 [a]	-15.243	212023
1673 [a]	-15.495	215520
1673 [a]	-14.879	206954
1673 [a]	-16.009	222681
1673 [a]	-15.250	212114
1673 [a]	-15.141	210604
1673 [a]	-15.430	214621
1673 [a]	-14.988	208476
1728 [a]	-15.237	218904
1728 [a]	-15.181	218094
1728 [a]	-15.042	216099
1728 [a]	-14.777	212298
1728 [a]	-14.704	211247
1728 [a]	-14.66	210633
1963 [b]	-9.12	110553
2041 [b]	-7.90	121405
2041 [b]	-8.12	125055
2065 [b]	-8.76	145587
2065 [b]	-8.15	135082

3.3 Thermodynamic optimization of $Si(OH)_4$ and $SiO(OH)_2$

The analytical Gibbs energy functions for the $Si(OH)_4$ and $SiO(OH)_2$ gas species were developed based on the available experimental data. The total Gibbs free energy of one mole of an ideal gas G_m^{gas} is expressed as:

$$G_m^{gas} = \sum_i y_i G_i^o(T, P_o) + RT \sum_i y_i \ln y_i + RT \ln P \tag{3.18}$$

where y_i is the site fraction of species i, so that $\sum_i y_i = 1$ and the site fraction of species i is identical to the ratio of the partial pressure of species i to the total pressure P. Additionally, $G_i^o(T, P_0)$ is the Gibbs

64

energy of species i at the reference pressure P_0, which is expressed as an analytical function of temperature as:

$$G^o(T, P_0) = a + bT + cT\ln T + dT^2 + eT^3 + \frac{f}{T} \qquad (3.19)$$

where a, b, c, d, e, and f are the temperature coefficients (Lukas 2007).

The analytical Gibbs energy functions for the $Si(OH)_4$ and $SiO(OH)_2$ species were optimized independently of each other since the gas phase is assumed to be ideal and there are no interactions between gas species. To reduce the number of thermodynamic parameters used to model the Gibbs energies of the $Si(OH)_4$ and $SiO(OH)_2$ species, the following equations were used:

$$G^o{}_{SiO(OH)_2} = G^o{}_{SiO_2} + G^o{}_{H_2O} + v_1 + v_2T \qquad (3.20)$$

$$G^o{}_{Si(OH)_4} = G^o{}_{SiO_2} + 2G^o{}_{H_2O} + v_3 + v_4T \qquad (3.21)$$

where $G^o{}_{SiO_2}$ and $G^o{}_{H_2O}$ are the analytical expressions of the Gibbs energy functions of SiO_2 and H_2O gas species taken from the SGTE database (Scientific Group Thermodata 2014) and v_1 to v_4 are the thermodynamic variables which were optimized.

In Figure 3.3 the equilibrium constants for Eq. (3.2) and Eq. (3.3) are plotted before the optimization ($v_1=v_2=v_3=v_4=0$) and are compared with the experimental data from the literature. The v_1, v_2, v_3, and v_4 parameters were optimized by means of the PARROT module of Thermo-Calc software (Andersson 2002) using a least-squares fitting method which minimizes the sum of the squares of the error between the calculated and experimental data (Lukas 2007). The values of the optimized parameters are given in Table 3.6.

As it can be seen in Table 3.6, the variables v_3 and v_4 for the $SiO(OH)_2$ species are one order of magnitude lower than the values v_1 and v_2 for $Si(OH)_4$. This can be due to the different binding energy between the constituent molecules, namely Si-O (807 kJ/mol), O-H (424.9 kJ/mol) (Madou 2002). According to Mills (2010) the total bonding energy of $Si(OH)_4$ is 3644 kJ/mol. The Si-OH binding energy can be accounted as $\approx$ 490 kJ/mol. According to these data, the $SiO(OH)_2$ has a total binding energy of 2631 J/mol, 30% lower than the $Si(OH)_4$.
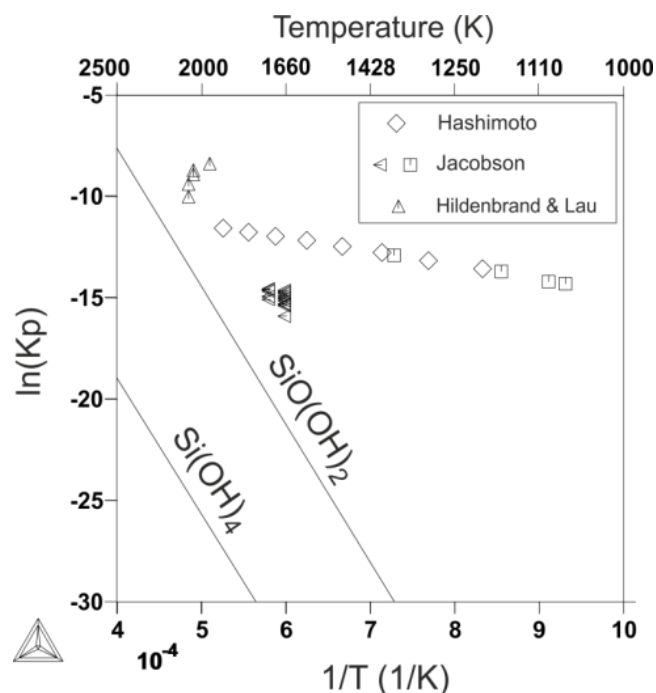
Figure 3.3: Calculation of equilibrium constants for $Si(OH)_4$ and $SiO(OH)_2$ for the reactions as given in Eqs. (3.2) and in (3.3), before optimization. The triangle symbols represent experimental data for $SiO(OH)_2$ (from Jacobson (2005) and Hildenbrand and Lau (1994; 1998)) and the squares are those for $Si(OH)_4$ species (from Jacobson (2005) and Hashimoto (1992)).

Table 3.6: Optimized values of the variable v_1 to v_4.

v_1 (J/mol)	v_2 (J/mol · K)	v_3 (J/mol)	v_4 (J/mol · K)
-518786.4	236.9	-87631.8	7.4

The entropies at the reference temperature (298 K) for the two species $Si(OH)_4$ and $SiO(OH)_2$ calculated with the new database are in reasonable accordance with the values presented in Table 3.1. The value for $SiO(OH)_2$ ($S°_{SiO(OH)2_{(g)}} = 410.125 \frac{J}{mol \cdot K}$) from our calculations is higher than the value from Allendorf (1995) shown in Table 3.2. This is not surprising since the data from Allendorf were not taken into account for the modeling of the $SiO(OH)_2$ species.

It is important to note that v_1 and v_3 are related to the enthalpy of formation of the gas species, whereas v_2 and v_4 are related to the entropy of formation, accordingly respectively to the following equations (DeHoff 2006).

$$\Delta H(T) = -T^2 \left(\frac{\partial (\Delta G/T)}{\partial T} \right)_p \tag{3.22}$$

$$\Delta S(T) = - \left(\frac{\partial \Delta G}{\partial T} \right)_p \tag{3.23}$$

The relation between the optimized variables in Table 3.6 and the entropy of formation can be demonstrated as followed. The entropy of formation of $Si(OH)_{4(g)}$ from $SiO_{2(g)}$ and $H_2O_{(g)}$ according to Eq. (3.2) can be calculated by means of Eq. (3.24), whereas Eq. (3.25) can be used to calculate the entropy of formation of $SiO(OH)_{2(g)}$ from $SiO_{2(g)}$ and $H_2O_{(g)}$ according to equation Eq. (3.3).

$$\Delta_f S^o_{Si(OH)_4(g)} = S^o_{Si(OH)_4(g)} - S^o_{SiO_2(g)} - 2S^o_{H_2O(g)} = -236.94 \frac{J}{mol\ K} = -v_2 \tag{3.24}$$

$$\Delta_f S^o_{SiO(OH)_2(g)} = S^o_{SiO(OH)_2(g)} - S^o_{SiO_2(g)} - S^o_{H_2O(g)} = -7.43 \frac{J}{mol\ K} = -v_4 \tag{3.25}$$

where $S^o{}_{SiO_2(g)}$ and $S^o{}_{H_2O(g)}$ are from the Janaf table (Chase 1998).

The calculation of the equilibrium constants for $Si(OH)_4$ and $SiO(OH)_2$ for the reactions given in Eqs. (3.2) and (3.3), after optimization are shown in Figure 3.4. The calculated line for the $Si(OH)_4$ species shows a slight curvature. It is important to note that according to the Van't Hoff equation the graph of lnK_P versus $1/T$ is a straight line. However, this is true only when the enthalpy of reaction $\Delta_r H$ is independent of temperature. Indeed, in this work the enthalpy of reaction is not independent of temperature. This can be explained considering Eq. (3.19), which allows expressing the Gibbs free energy of reaction as following:

$$\Delta_r G_T = \Delta a + \Delta bT + \Delta cTlnT + \Delta dT^2 \tag{3.26}$$

where $\Delta a, \Delta b, \Delta c$, and Δd are the differences in the respective temperature coefficients between reactants and products. Combining the Van't Hoff expression in Eq. (3.5) and the Gibbs energy expression in Eq. (3.18), the following equation can be derived.

$$\Delta_r H_T = \Delta a - \Delta cT - \Delta dT^2 \tag{3.27}$$

67
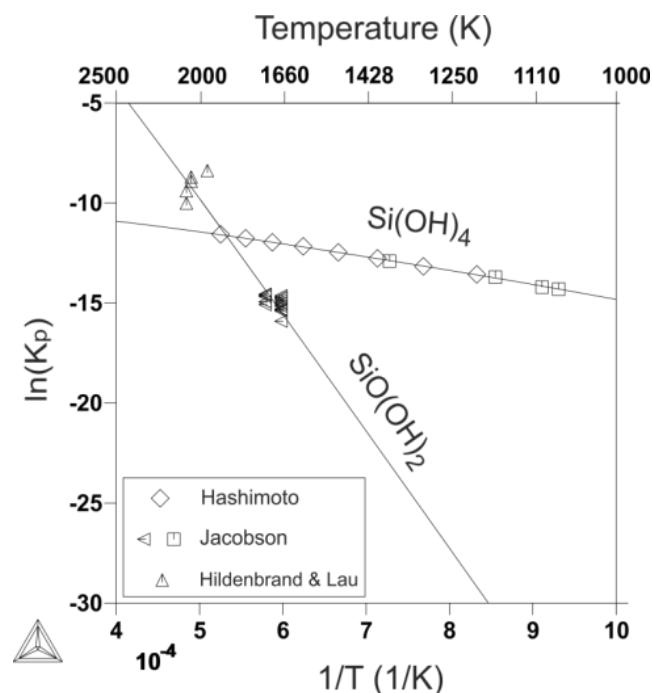
Figure 3.4: Calculation of equilibrium constants for Si(OH)$_4$ and SiO(OH)$_2$ for the reactions given in Eqs. (3.2) and (3.3), after optimization using data of Table 3.6. The triangle symbols represent experimental data for SiO(OH)$_2$ (from Jacobson (2005) and Hildenbrand and Lau (1994; 1998) and the squares are those for Si(OH)$_4$ species (from Jacobson (2005) and Hashimoto (1992)).

Therefore, using our Gibbs free energy functions for the phases in the multi-component system, the graph of ln(K$_P$) versus 1/T (Figure 3.4) should have a very slight curvature because the enthalpy of reaction is not independent of temperature. After optimization of the Gibbs energy expressions of Si(OH)$_4$ and SiO(OH)$_2$, a thermodynamic dataset for the Si-O-H multi-component system was developed including the thermodynamic descriptions of the Si(OH)$_4$ and SiO(OH)$_2$ gas species and other phases taken from the SGTE (Scientific Group Thermodata 2014). These species are liquid SiO$_2$, liquid silicon, tridymite, quartz (beta, normal), solid silicon and gas. The following gas species were also included: H, OH, HO$_2$, HSi, H$_2$, H$_2$O, H$_2$O$_2$, SiO(OH)$_2$, SiH$_2$, SiH$_3$, Si(OH)$_4$, SiH$_4$, Si$_2$H$_6$, O, SiO, O$_2$, SiO$_2$, Si$_2$O$_2$, O$_3$, Si, Si$_2$, Si$_3$.

Different descriptions for the silicon carbide species exist in the literature. The thermodynamic database for SiC developed by the SGTE employed the data published in the Janaf table (Chase 1998). In this description, two different sets of data are included, one for the α phase and one other for the

β phase. According to the Janaf table (Chase 1998), α-SiC is less stable than β-SiC up to 2200 K. However in the literature, the Gibbs energy of formation was also measured by Kleykamp (1998) using electronic force method (emf) and a higher thermodynamic stability for α-SiC than β-SiC has been found. An additional description of β-SiC was presented by Gröbner (1996). The Gibbs free energy description of the alpha and the beta modifications of SiC in the SGTE dataset and the description of SiC by Gröbner (1996) are presented Table 3.7 and plotted in Figure 3.5. According to Figure 3.5, no significant difference can be noted between the description provided by Gröbner and the SGTE.

Using this dataset, selected thermodynamic calculations of phase equilibria in the multi-component and heterogeneous Si-O-H system were performed using 1 mole of Si, 2 moles of H and 3 moles of O, which correspond to the stoichiometry of the elements for the reaction between SiO_2 and H_2O as expressed in Eq. (3.3).

Multi-component calculations relating to the development of $Si(OH)_4$ and $SiO(OH)_2$ gas species at different conditions were performed in an open system. At a total pressure of 1 bar, condensed phases such as liquid silica, cristobalite and tridymite are produced depending on the temperature, along with the gas phase. Figure 3.6 shows the logarithm of the calculated partial pressures of the species in the gas phase.
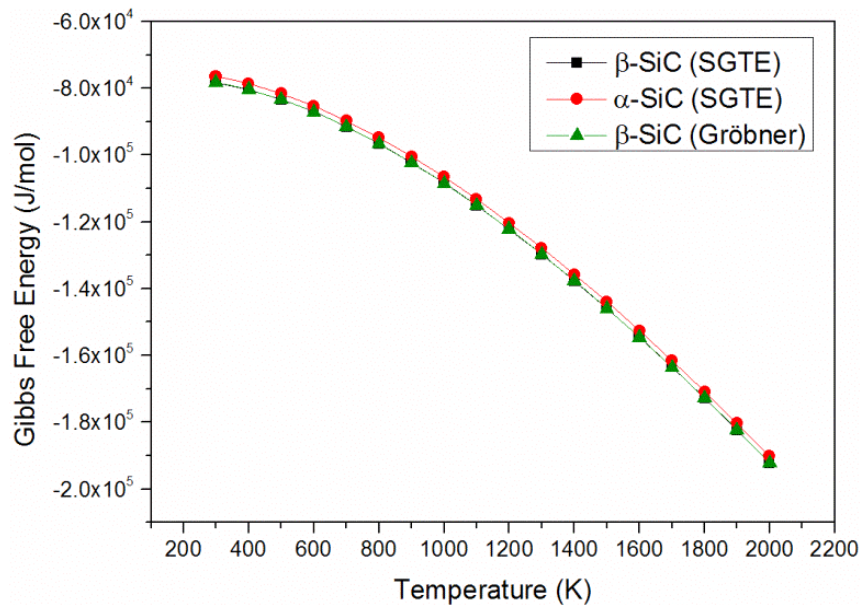
Figure 3.5: Gibbs free energy of the α-SiC and of the β-SiC according to the SGTE.

Table 3.7: Binary parameters of SiC phase with parameter = A+BT+CTln(T)+DT²+E/T+FT³. The function considered for the SGTE is between 298 – 800 K.

Parameters	A	B	C	D 10^3	E 10^{-6}	F 10^6
SiC-α (SGTE)	-84137.15	177.39	-26.50	-20.34	3.08	0.4
SiC-β (SGTE)	-85598.6	173.63	-25.92	-20.99	3.19	0.44
SiC (Gröbner)	-88584.0	271.15	-41.28	-4.36	0.8	0.2
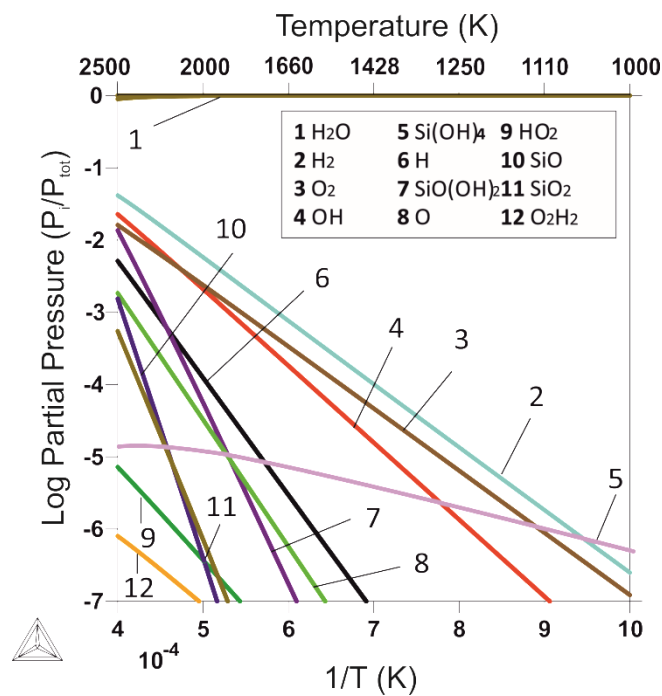
Figure 3.6: Calculated partial pressures of gas species for $n_{Si}:n_H:n_O$=1:2:3 at P=1 bar. Either liquid silica, cristobalite, or tridymite is in equilibrium with the gas phase depending on the temperature.

According to the calculations, $SiO(OH)_2$ production starts to become significant only at temperatures above 2000 K. The ratio between hydrogen and steam, along with oxygen partial pressure, can be compared to the thermodynamic equilibrium shown in the Ellingham diagram (Gaskell 2003). For example at 1873 K, the calculated partial pressures of P_{O2} and P_{H2} are P_{O2} = 1.2·10^{-3} bar, P_{H2} = 3 · 10^{-3} bar, thus $P_{H2/H2O}$ ≈ 3 · 10^{-3} (Figure 3.6). According to the Ellingham diagram shown in Figure 3.7, an oxygen partial pressure of P_{O2} = 1.2 · 10^{-3} bar at 1873 K is associated with a $P_{H2/H2O}$ ratio of 3 · 10^{-3} (the green line

connects the intersection with the temperature). This is in excellent agreement with the $P_{H2/H2O}$ ratio at 1873 K calculated in Figure 3.6.

Figure 3.8 shows only the partial pressures of $Si(OH)_4$, $SiO(OH)_2$, SiO, and SiO_2 versus $1/T$ for the same calculations. The trend suggests that the partial pressures of all the species increase with increasing temperature. This change is less pronounced for $Si(OH)_4$ than for the other gas species, which is expected based on the experimental data shown on the $\ln(K_p)$ vs $1/T$ curves in Figure 3.4. The results show that the partial pressure of $Si(OH)_4$ is higher than that of $SiO(OH)_2$ at $T<1936$ K, whereas for higher temperatures, the opposite occurs.
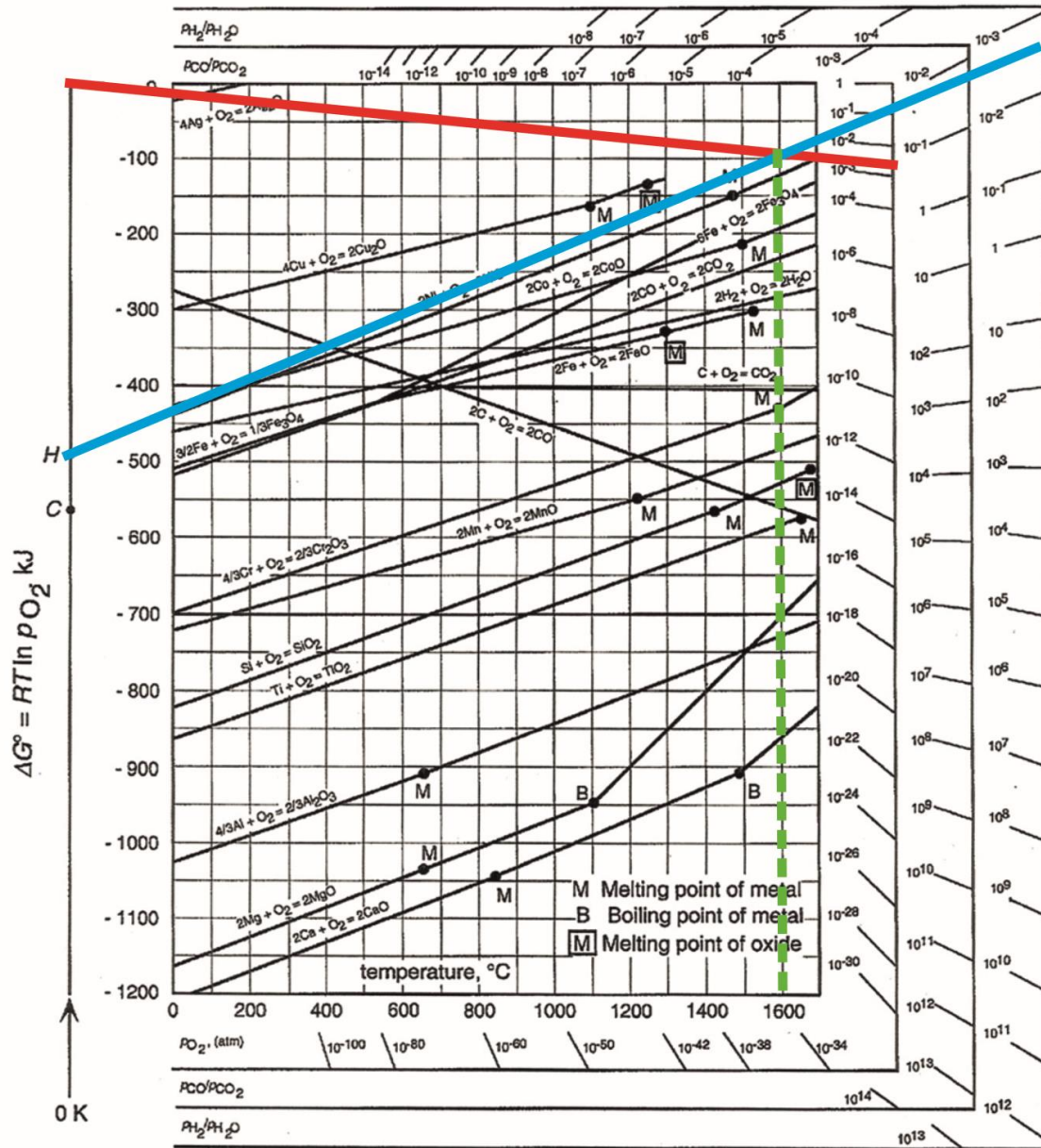
Figure 3.7: Ellingham diagram (Gaskell 2003). The red and the blue lines indicate respectively the P_{O2} and the $P_{H2/H2O}$ at 1873 K, from the partial pressures calculated in Figure 3.6. The intersection of these two lines is connected to the temperature lines through the green line. The temperature indicated by the green line, shows the temperature of equilibrium according to the Ellingham diagram, which corresponds to the temperature at which the P_{O2} and the $P_{H2/H2O}$ were considered in Figure 3.6.
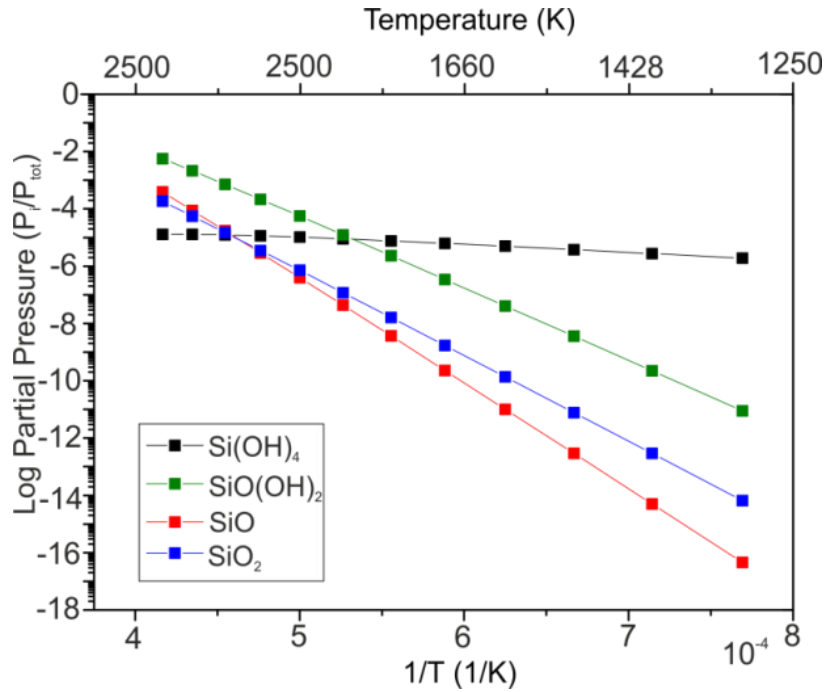
Figure 3.8: Partial pressures of the gaseous species Si(OH)$_4$, SiO(OH)$_2$, SiO$_2$ and SiO as function of the temperature.

The same calculations were performed by adding 1 mole of argon in order to check the influence of the presence of an inert gas. The results are presented in Figure 3.9, where the logarithm of the partial pressure of Si(OH)$_4$ and SiO(OH)$_2$ gas species is compared considering n_{Si}:n_O:n_H:n_{Ar}=3:2:1:0 (lines with lighter colors) and n_{Si}:n_O:n_H:n_{Ar}=3:2:1:1 (lines with darker color). The calculation shows that the partial pressures of SiO(OH)$_2$ and Si(OH)$_4$ decrease due to the presence of argon. The decrease is proportional to the amount of argon moles. This behavior can be explained considering that the different gas pressures change according to the Dalton's law of partial pressure.
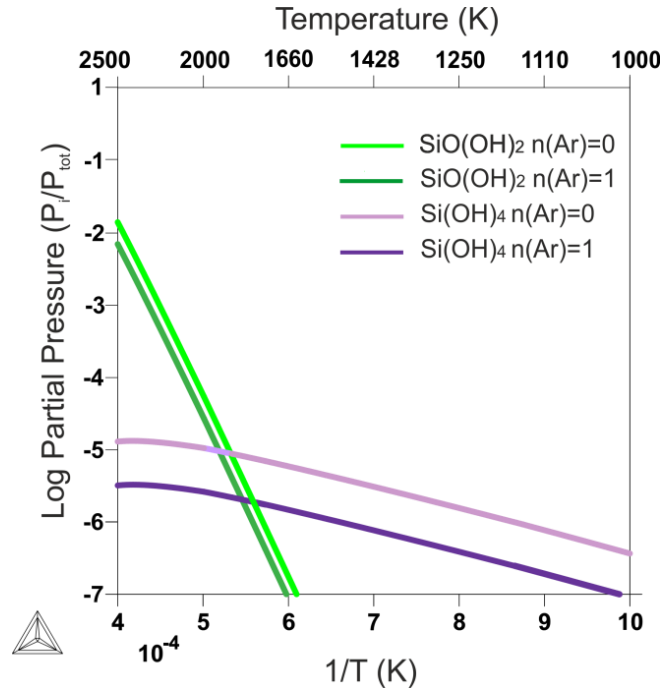
Figure 3.9: Comparison of the calculated partial pressures of $Si(OH)_4$ and $SiO(OH)_2$ species for $n_{Si}:n_H:n_O=1:2:3$ and $n_{Ar}=0$ and $n_{Ar}=1$ at P=1 bar.

The Dalton's law can be expressed as Eq. (3.28), where P_{tot} is the pressure of the system, n are the gas species present in the system, P_i the partial pressure, and x_i is the mole fraction of the i-th component in the total mixture of n components.

$$P_{tot} = \sum_{i=1}^{n} P_{tot} \cdot x_i = \sum_{i=1}^{n} P_i \tag{3.28}$$

According to this law, in case the total pressure of the system is kept constant, the partial pressures of the different species change. In Figure 3.10, the trend of the $\ln(K_p)$ for the two gas species ($Si(OH)_4$ and $SiO(OH)_2$) is plotted for two different temperatures: solid line at 1900 K and dashed line at 2300 K. As shown in Figure 3.10, the K_p is independent of the total pressure. The calculated partial pressures of the silicon hydroxide species against the water vapor pressure at 1673 K are compared to the data from Jacobson (2005) in Figure 3.11. In his work, Jacobson (2005) measured the total pressure of Si-containing species as a function of water vapor pressure. Moreover they calculated the

expected partial pressure of Si(OH)$_4$ at 1673 K (Figure 3.11a). These calculations are based on extrapolations of their experimentally determined equilibrium constants for the formation of Si(OH)$_4$ from SiO$_2$ and H$_2$O vapor, which were obtained at temperatures below 1375 K.
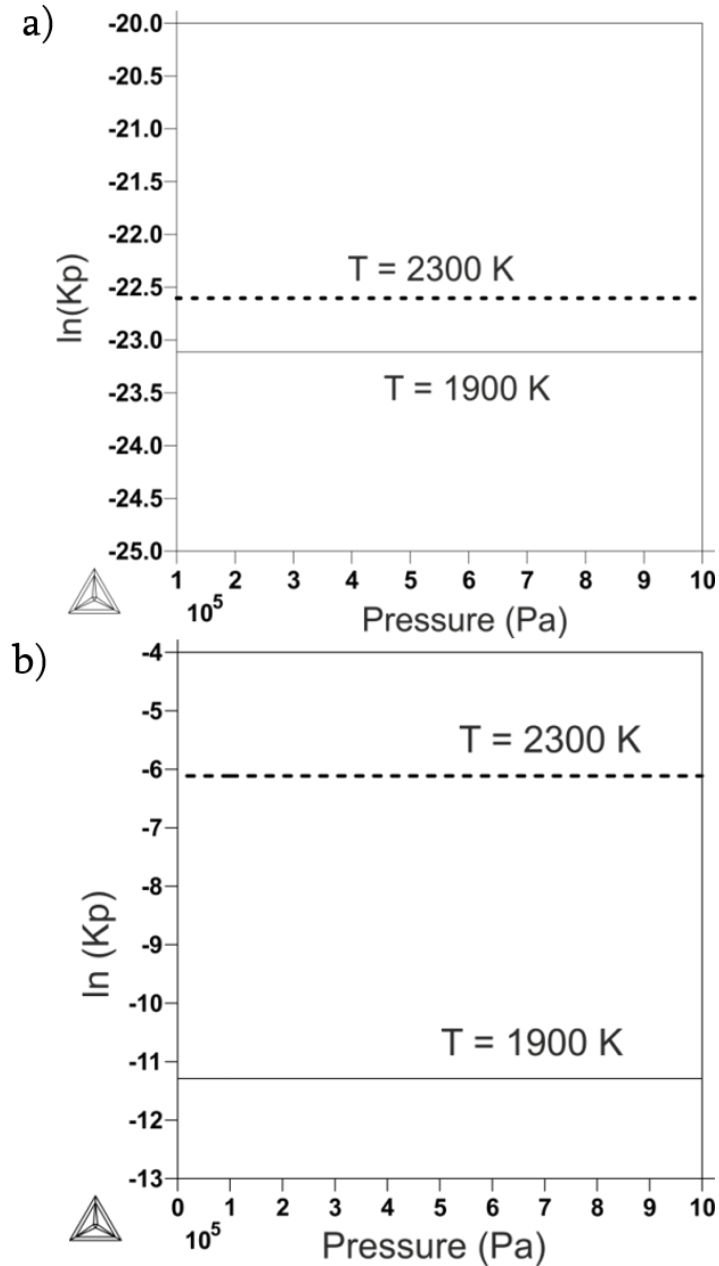
Figure 3.10: Pressure dependence of the equilibrium constant of the two gas species: graph (a) Si(OH)$_4$, graph (b) SiO(OH)$_2$.
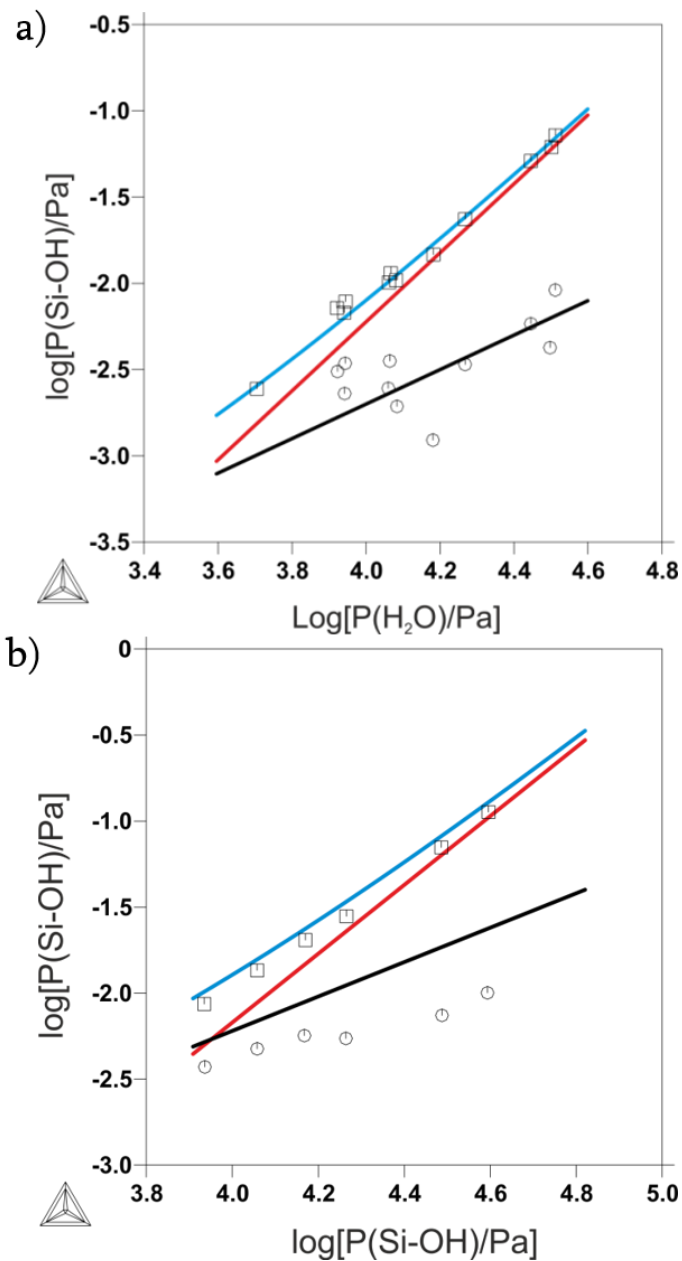
Figure 3.11: Pressure of the Si-containing species against water pressure (a) at 1673 K (b) at 1728 K. From the literature (Jacobson 2005), the squares are the total pressures of Si-containing species, whilst the circles are the experimental points for the assumed partial pressures of $SiO(OH)_2$ determined by subtracting the extrapolated partial pressures of $Si(OH)_4$ from the total measured pressure of Si-containing species. The lines represent the data calculated in this work: black line is the calculated partial pressure of $SiO(OH)_2$, the red line is the calculated partial pressure of $Si(OH)_4$ and the blue line is the sum of the two partial pressures.

The difference between the total pressure and the extrapolated $Si(OH)_4$ pressure is assumed to be the partial pressure of $SiO(OH)_2$. The new thermodynamic description well reproduces the total pressure of Si-containing species and the extrapolated partial pressures of $Si(OH)_4$ and $SiO(OH)_2$ determined by Jacobson at 1673 K (2005). At 1728 K, the total pressure of the Si-containing species calculated using the thermodynamic description in this work is only slightly higher than that measured by Jacobson (2005) as shown in Figure 3.11b. This can be explained considering that our calculated $SiO(OH)_2$ partial pressures are higher than those expected by Jacobson (2005), based on subtracting the extrapolated partial pressures of $Si(OH)_4$ from the measured total pressure.

3.4 Influence of external parameters

In order to study the influence of H_2O partial pressure on the heterogeneous equilibria, thermodynamic equilibrium calculations were performed for a one-mole system in which the ratio of the input mole fractions of SiO_2 to H_2O (θ) was allowed to vary between 10^{-8} and 10. These calculations were performed for T= 1900 and 2300 K and at total pressures of P_T= 1, 3 and 6 bar. Figure 3.12, Figure 3.13, and Figure 3.14 show the calculated mole fractions of H_2O, $Si(OH)_4$, $SiO(OH)_2$, SiO, and SiO_2 as a function of θ at the different total pressures at 1900 K (Figure 3.12a and Figure 3.13) and 2300 K (Figure 3.12b and Figure 3.14). In Figure 3.15, the calculated amount of moles of condensed SiO_2 is presented. The mole fractions of H_2, OH, and O_2 in the gas phase at the same conditions are shown in Figure 3.16. Generally, the calculated mole fractions of H_2O are higher at 1900 K than at 2300 K (Figure 3.12) because the extent of dissociation of water vapor to H_2, OH, and O_2 is greater at higher temperatures. This observation is confirmed in Figure 3.16, which shows that the calculated mole fractions of H_2, OH, O_2 are higher at 2300 K than at 1900 K.

The calculations show that for $\theta \leq 10^{-4}$ at both 1900 and 2300 K at P_T=1, 3 and 6 bar with increasing SiO_2 mole fraction, the mole fractions of gaseous $Si(OH)_4$, $SiO(OH)_2$, SiO, and SiO_2 increase, that of H_2, OH, and O_2 remain constant, whereas the mole fraction of gaseous H_2O decreases. In these θ ranges, no condensed SiO_2 is formed. Thus, all input SiO_2 reacts with H_2O to produce $Si(OH)_4$, $SiO(OH)_2$, SiO, and SiO_2 gases. For $\theta \geq 10^{-4}$, condensed SiO_2 is stable and the mole fractions of all gas species remain constant. At these θ values, the equilibrium partial pressures of all gas species are calculated when H_2O

vapor is in contact with stable SiO_2, and the amount of condensed SiO_2 increases with increasing θ, as can be seen in Figure 3.15.

The calculations also show that an increase in the total pressure results in an increase in the mole fraction of $Si(OH)_4$ and a decrease in the mole fractions of SiO and SiO_2 in the gas. The influence of the total pressure on the composition of the gas phase was experimentally investigated by Opila (1997) using mass spectrometry techniques. In that work, the main species at one bar total pressure was $Si(OH)_4$, which was confirmed by the presence of the fragment ion $Si(OH)_3^+$. Small peaks were also observed for $SiO(OH)^+$, which suggested the presence of $SiO(OH)_2$. On the other hand, Hildenbrand (1994; 1998) did not detect any $Si(OH)_4$ formation in his experiments which were performed at lower total pressures. These experimental observations from independent works confirm the results of the calculations which show that an increase in the total pressure results in an increase in the amount of $Si(OH)_4$ in the gas phase.

At both 1900 K ($\theta > 10^{-4}$) and 2300 K, the partial pressure of $SiO(OH)_2$ is independent of the total pressure. This behavior is in agreement with the calculations shown in Figure 3.10, where the equilibrium constant of $SiO(OH)_2$ for the reaction in Eq. (3.3) does not depend on the total pressure. The exception at 1900 K for $\theta < 10^{-4}$ can be due to the low initial SiO_2 presence. At 2300 K, the partial pressure of $SiO(OH)_2$ is always higher than that of $Si(OH)_4$, which is also in agreement with the calculated equilibrium constants of these two species for the stoichiometric reaction equations Eqs. (3.2) and (3.3), shown in Figure 3.4 in the temperature range 1000-2500 K.
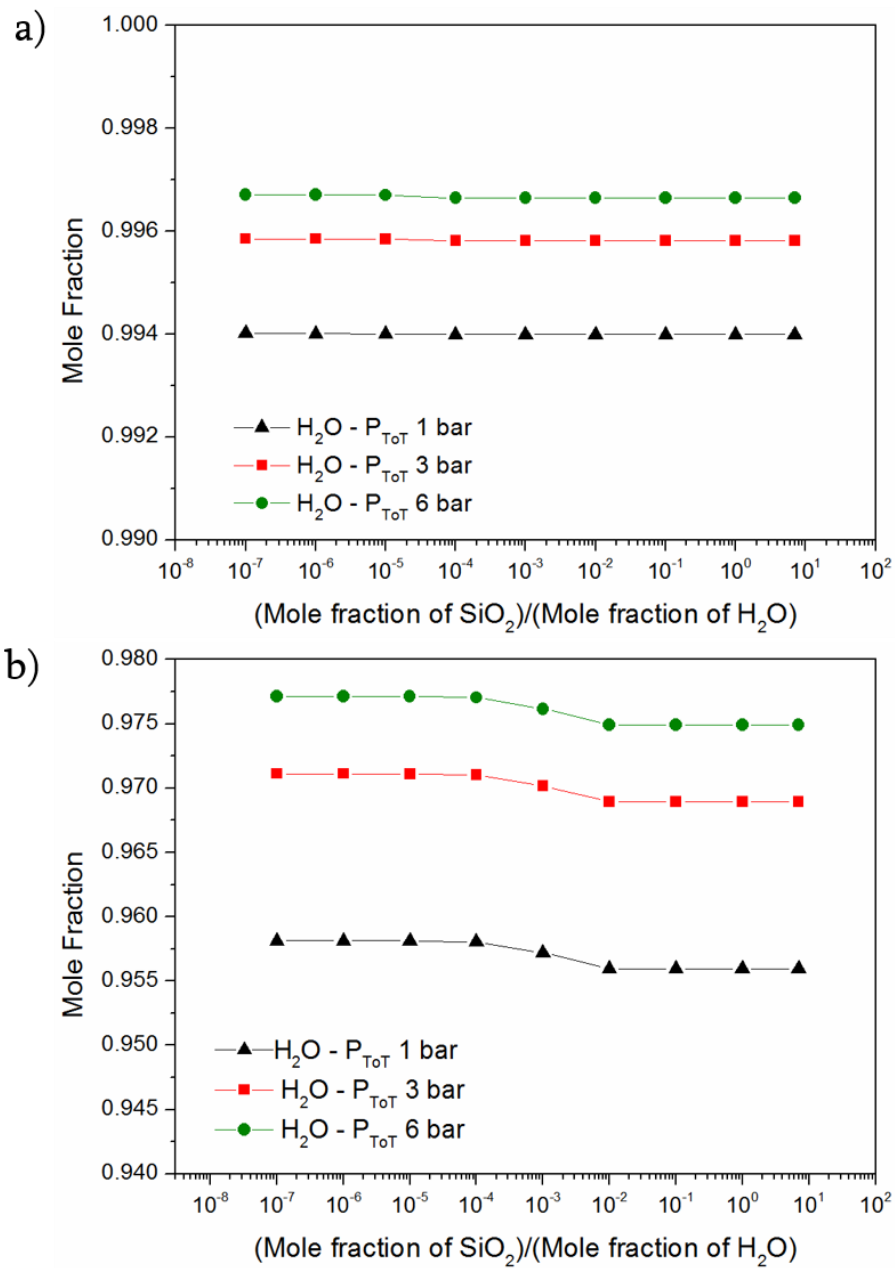
Figure 3.12: Mole fractions of H2O in the gas phase at (a) 1900 K and (b) 2300 K calculated for different values of Θ (Mole fraction of SiO2 / Mole fraction of H2O).
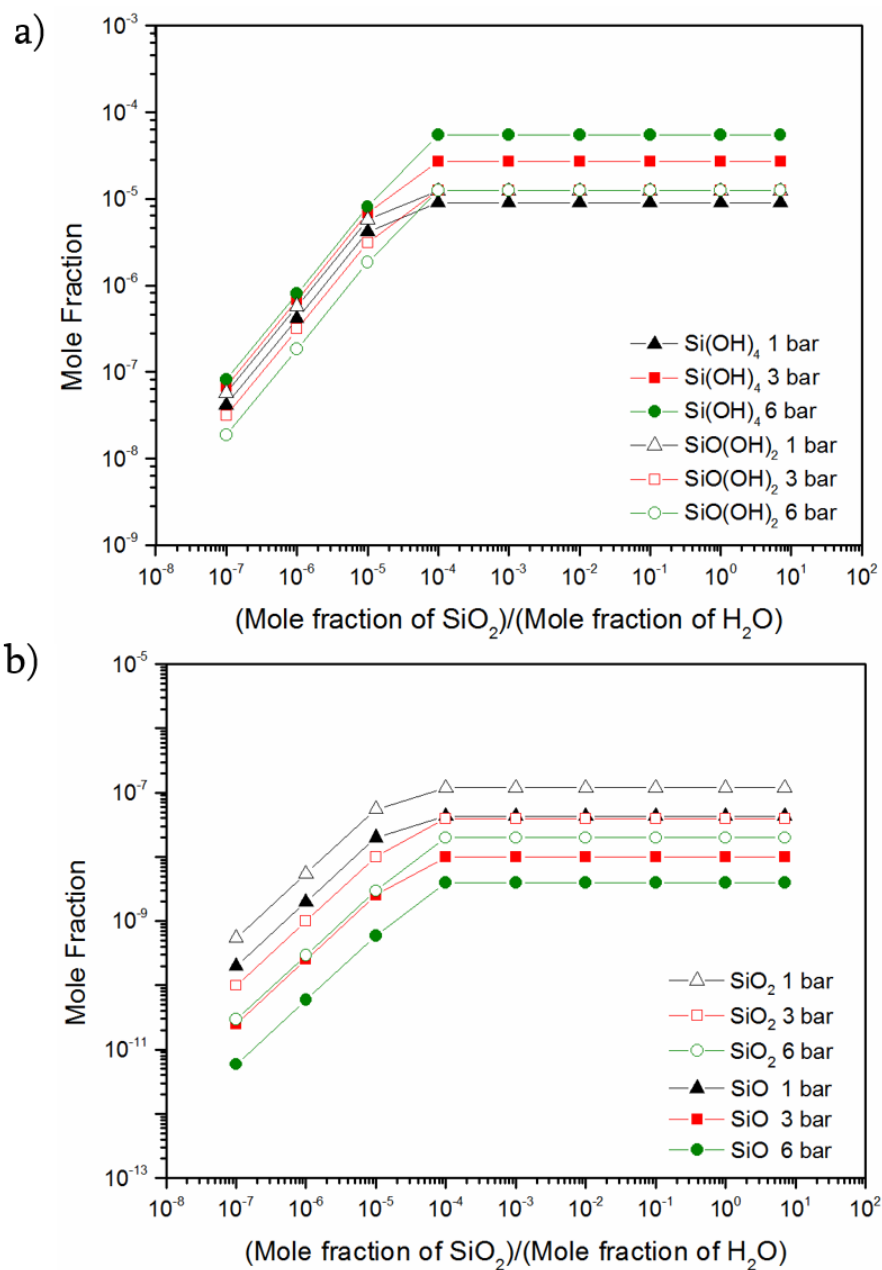
Figure 3.13: Mole fractions in the gas phase of (a) $Si(OH)_4$ and $SiO(OH)_2$ and (b) SiO_2 and SiO at 1900 K calculated for different values of Θ (Mole fraction of SiO_2 / Mole fraction of H_2O).
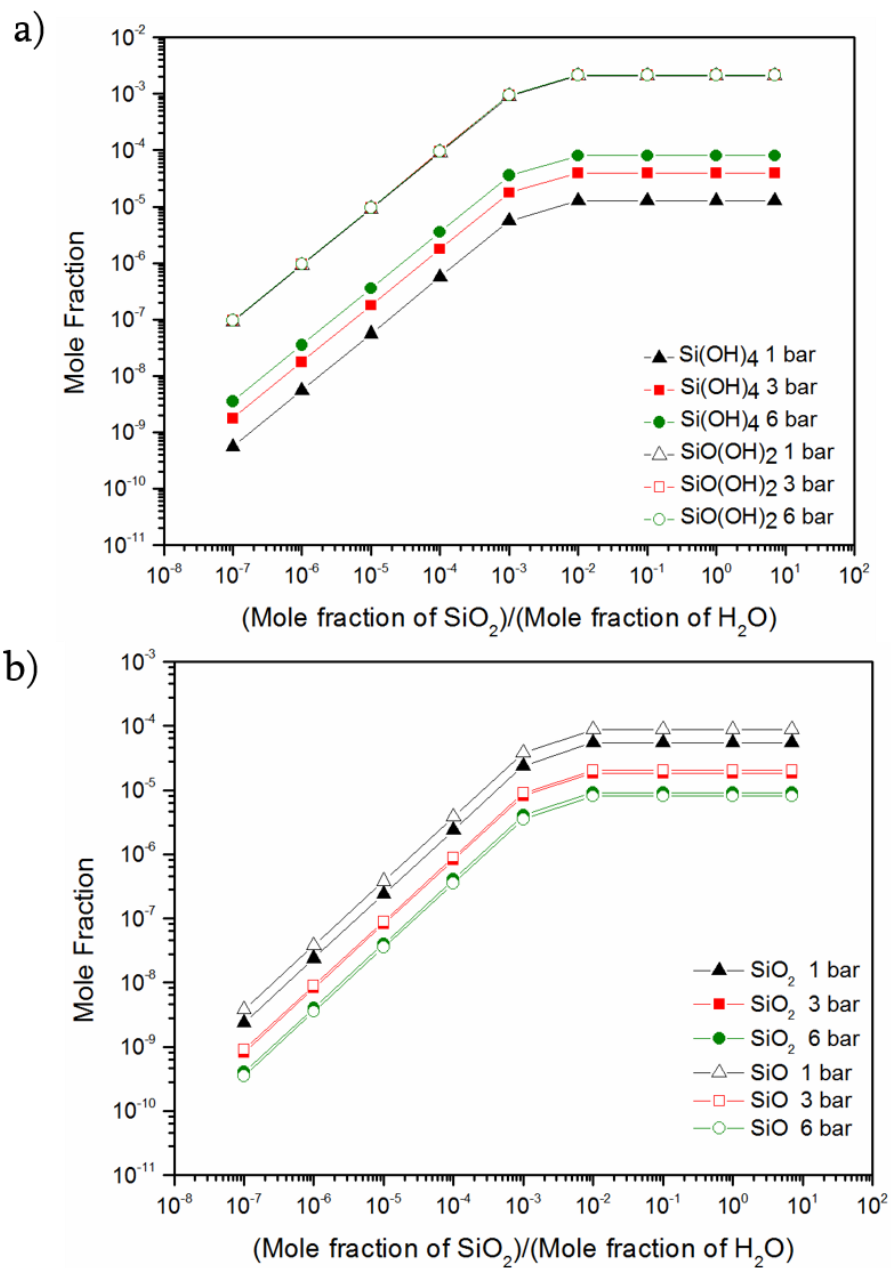
Figure 3.14: Mole fractions of $Si(OH)_4$ and $SiO(OH)_2$ (a) and SiO_2 and SiO including H_2O (b) in the gas phase at 2300 K calculated for different values of Θ (Mole fraction of SiO_2 / Mole fraction of H_2O).
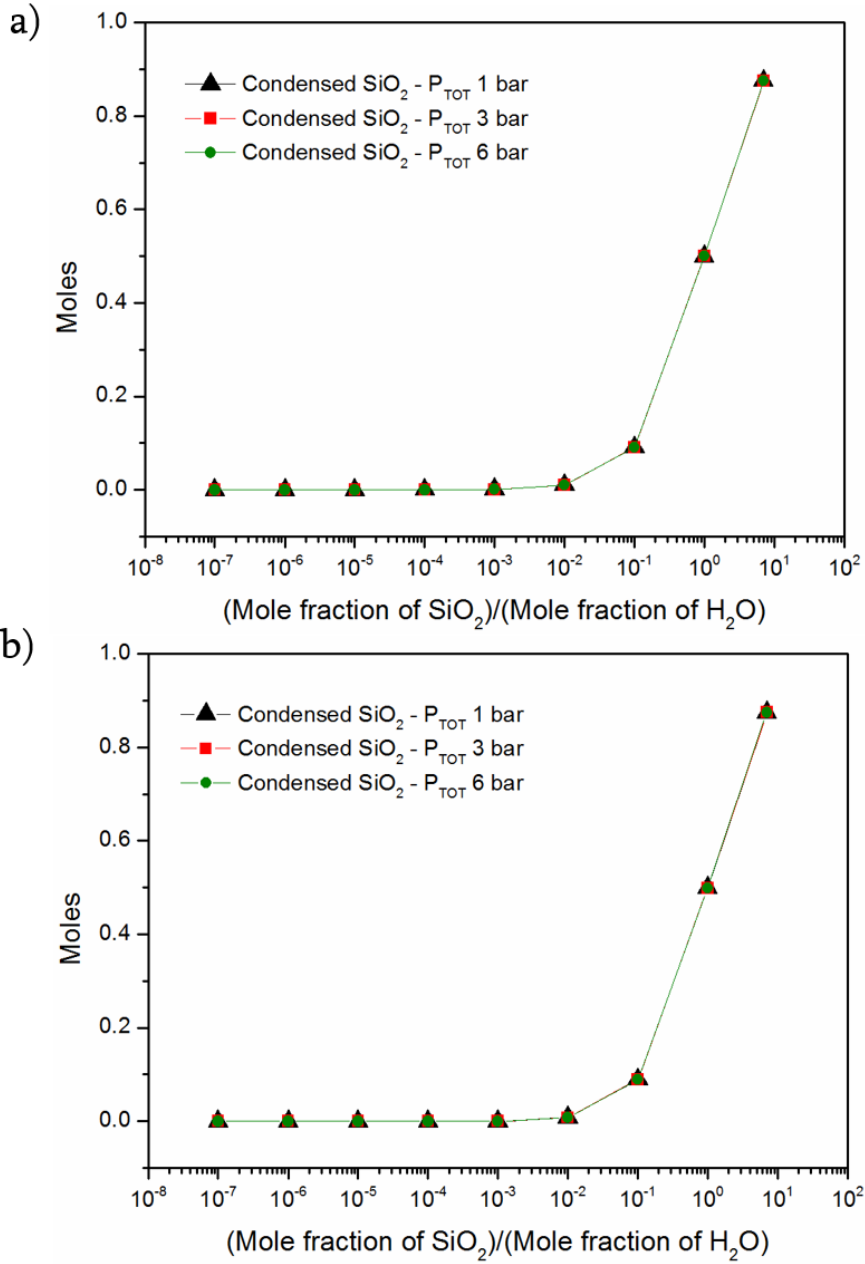
Figure 3.15: Trend of condensed silica molar fraction at (a) 1900 K and (b) 2300 K at the different total pressures calculated for different values of Θ (Mole fraction of SiO_2 / Mole fraction of H_2O).
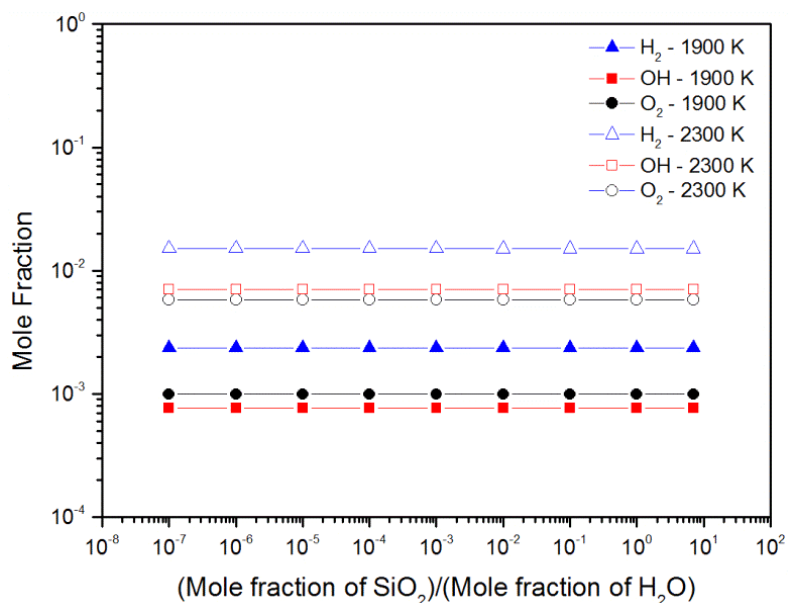
Figure 3.16: Mole fractions of H_2, OH and O_2 in the gas phase at 3 bar total pressure and 1900 K and 2300 K calculated for different values of Θ (Mole fraction of SiO_2 / Mole fraction of H_2O).

3.5 Application to silica volatilization

The amount of gas produced during the reaction of SiO_2 with water vapor at high temperatures can be used to derive the rate of reaction and its influence on the SiO_2 volatilization. The erosion of silica occurs through Eqs. (3.2), (3.3), and (3.4), respectively. During SiC oxidation, it is assumed that silica growth occurs at the same rate as silica evaporation. In a previous work by Robinson (1999), the SiO_2 growth rate was not taken into account because it is negligible in comparison to the rate of silica volatilization, and SiC recession is commensurate with SiO_2 evaporation. The degradation of silicon carbide due to silica volatilization can therefore be modeled by referring to Eq. (3.1), where 1 mole of SiC results in 1 mole of SiO_2 which eventually volatilizes. This 1 to 1 molar relation between SiC and SiO_2 allows one to compare the results obtained in this work with the literature.

The calculations performed in the previous section give the partial pressures of the silicon hydroxide species developed during the SiO_2 volatilization process. In order to clarify the kinetics of SiO_2 volatilization, a model is required that takes into account conditions such as temperature, pressure, and gas flow rates. Nickel (Hack 2008) simulated corrosion in gas atmospheres starting from the equation

of state for the ideal gas, assuming that in a static atmosphere, the equation of state for the ideal gas at equilibrium describes the maximum material loss to the atmosphere. Therefore, the ideal gas equation can be used to express the mass of volatilized material in the reaction equation:

$$N = \frac{PV}{RT} = \frac{\Delta m\,u}{M} \qquad (3.29)$$

where N is the maximum number of moles which may enter the reactor chamber, P is the pressure, V is the volume, Δm is the material loss, u is a factor related to the stoichiometric equation for the reaction of SiO_2 with H_2O, and M is the molecular weight of the gas species produced. Maximum erosion would take place if all the vaporized species are swept away from the surface at their equilibrium partial pressures. The linear reaction constant k_l can be calculated using Eq. (3.30) as:

$$k_l = \sum_{s}^{n} \frac{P_s VM}{SRTu} \qquad \left(\frac{g}{m^2}\right) \qquad (3.30)$$

where S is the exposed surface area and P_s is the partial pressure of the gas species. If the gas flow rate is known, then the corrosion depth rate Eq. (3.31) can be calculated as:

$$\dot{X}_l = \frac{MP_s Vv}{S\delta uRT} = \frac{MP_s \dot{V}}{S\delta uRT} \qquad \left(\frac{m}{s}\right) \qquad (3.31)$$

where $\dot{X}_l$ is the corrosion depth per time unit, v is the number of exchanges of molecules per time, $\dot{V}$ is the flow rate and δ is the density. In order to calculate the flux, Eq. (3.32) can be used.

$$J = \sum_{s}^{n} \frac{MP_s Lv}{RTu} \qquad \left(\frac{g}{m^2 s}\right) \qquad (3.32)$$

Another approach has been formulated by Opila (2003), assuming that the rate of volatilization is limited by the transport of the volatile species. In this model, a plane surface with a laminar gaseous boundary layer is taken into account. In order to model SiO_2 volatilization, the density and the inter-diffusion coefficients of the volatile species are required. Moreover, thermo-hydraulic conditions are taken into account by means of the Reynolds (Re) and Schmidt (Sc) numbers, as well as the inter-diffusion coefficients (D) of the volatile species in the boundary-layer Eq. (3.33). Additionally, L is the characteristic length of the test specimen parallel to the direction of the gas flow.

$$J = 0.664 Re^{0.5} Sc^{0.33} \frac{D\delta_{v_i}}{L} \qquad \left(\frac{g}{m^2 s}\right) \tag{3.33}$$

In this equation, δ_{v_i} is the gas density which is expressed for each volatile species ($Si(OH)_4$, $SiO(OH)_2$) as in Eq. (3.34):

$$\delta_{v_i} = \frac{P_i M_i}{RT} \qquad \left(\frac{g}{m^3}\right) \tag{3.34}$$

The experimental data published by Robinson (1999) were used to validate the thermodynamic descriptions of the silicon hydroxide gas species developed in this work and to compare the two different models discussed above to predict the silica volatilization from the volatile species. The experiments in (Robinson 1999) were conducted under gas turbine combustor conditions. Opila (1999) defined the gas compositions, total pressure, and gas velocity (Table 3.8) for fuel lean conditions in a high pressure burner rig (HPBR). In order to consider this gas composition in the database, the thermodynamic descriptions of all stable phases and species containing C and Ar from the SGTE SSUB 4.0 database supplied with Thermo-Calc® were additionally included. The parameters required to solve Eq. (3.33) are from the literature (Opila 1997). In Figure 3.17, the SiC mass loss calculated using the Opila model is presented and compared to experimental data and to the original calculations from Opila (1999). The empty dots show the experimental data from the work of Robinson and Smialek (1999) and the blue dots show the results of own calculations using the Opila model and the partial pressures of the gas species calculated using the thermodynamic description developed in this work.

In order to reproduce the gas composition in Table 3.8, the carbon and the argon species were added to the database. The black lines were calculated by Opila (1999) using two different data sets (A and K) for the Si-O-H gas species. In order to understand the differences between the results, the sources of the original data for the Si-O-H gas species used by Opila (1999) should be considered.

Table 3.8: Conditions for the calculation of the volatilization from the literature (Opila 1999).

	Total Pressure	Gas velocity	Gas composition (Vol%)
HPBR fuel lean	6.3 (bar)	21 (m/s)	11.0 CO_2, 2.1 O_2, 12.3 H_2O, 74.6 N_2

In both A and K datasets, the thermodynamic descriptions for $Si(OH)_4$ are developed from the data of Hashimoto. However, in dataset A, the thermodynamic data for $SiO(OH)_2$ are from Allendorf (1995) whereas the thermodynamic data from Krikorian (1970) are used in dataset K. Figure 3.17 shows that the predicted SiC weight losses calculated using dataset K are much higher than the experimentally observed results. Since both datasets (A and K) use the same thermodynamic data for $Si(OH)_4$, the higher SiC weight losses predicted by dataset K can only occur because dataset K calculates too high $SiO(OH)_2$ partial pressures in the temperature range of interest. On the other hand, dataset A well reproduces the experimental data at temperatures below 1550 K. A good agreement between the SiC weight loss predicted using database A and that predicted using the thermodynamic descriptions of $Si(OH)_4$ and $SiO(OH)_2$ developed in this work can be found at temperatures between 1500 and 1750 K.
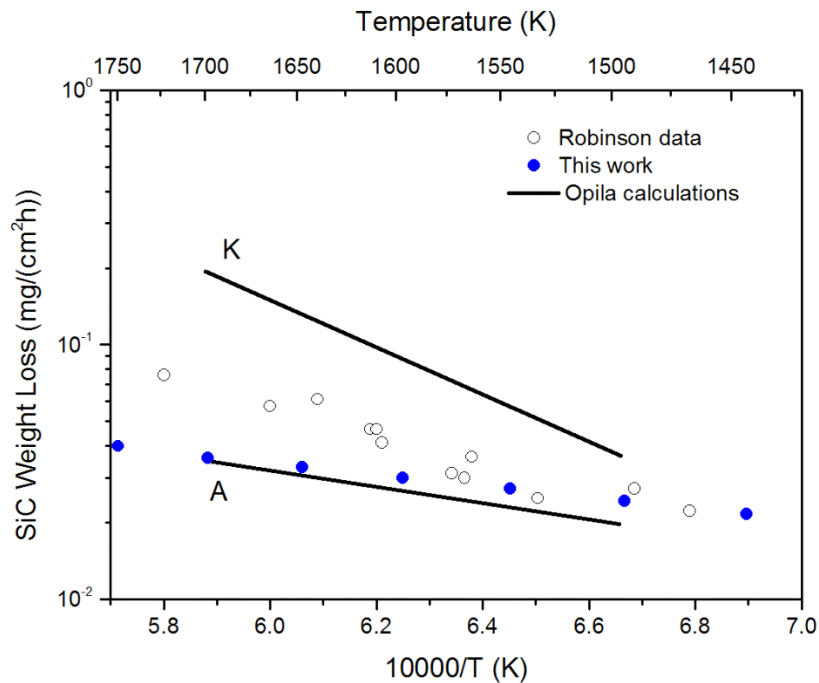
Figure 3.17: SiC weight loss calculated by Opila (black line using Allendorf thermodynamic data (A) and Krikorian thermodynamic data (K)). The experimental data (empty dots) are from the work of Opila and Robinson (1999). The blue circles indicate the recession rate calculated in this work using the thermodynamic database developed in this work and the model from Opila.

In Figure 3.18, the SiC weight losses calculated in this work using the model from Nickel (model 1 in the figure) are compared to those calculated using the Opila model (model 2 in the figure) along with the experimental data from Robinson (1999). As shown in Figure 3.18 the SiC weight losses occurring at temperatures lower than 1650 K are overestimated by the model of Nickel (Hack 2008). At higher temperatures, both curves increase rapidly due to the increasing production of $SiO(OH)_2$.

A combination of the models developed by Opila (1999) and Nickel (2008) can, however, be used to estimate SiC mass losses since the real system behavior is found between the two extremes. Calculations using the model from Opila fit closer at lower temperatures whereas calculations using the model of Nickel are preferable at higher temperatures. An explanation for this result can be given considering the nature of the two models: whilst that from Opila includes the diffusivity data of the gases, Nickel analyzes the mass loss reactions considering only thermodynamic equilbrium.
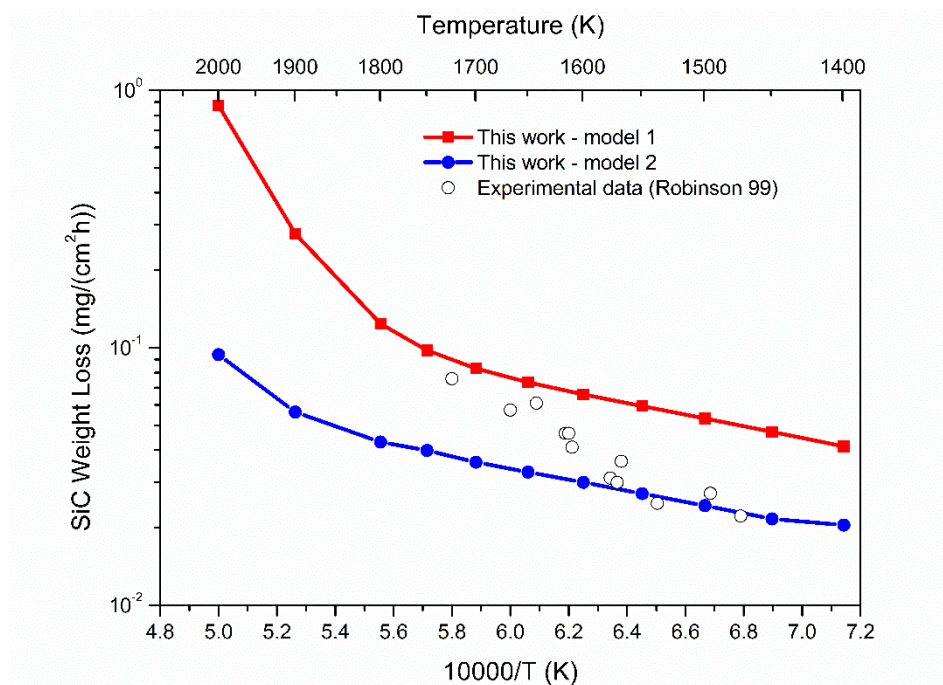
Figure 3.18: Experimental data from the work of Robinson (1999)(empty dots) compared to the recession rate calculated in this work using the model from Opila (blue dots) and from Nickel (red dots).

Diffusion kinetics play a much smaller role at higher temperatures, and the partial pressures of the gas species used to calculate the SiC weight losses can be determined by assuming ideal gas behavior. Additionally, since the diffusivity data used in the Opila model are only valid at 1573 K (the temperature dependence of the diffusivities of $Si(OH)_4$ and $SiO(OH)_2$ was not taken into account) SiC weight loss calculations using the model of Opila are in good agreement with the experimental data between 1500 and 1600 K. This further emphasizes the importance of accurate determinations of the diffusivities of the gas species to be able to predict SiC mass loss at temperatures at which ideal gas behavior cannot be assumed.

Comparing to the work performed by Zhang (2014), the calculated values shown in Figure 3.19 fit closer the experimental data measured by Robinson (1999) at the temperature from 1538 K to 1666 K. In the paper from Zhang (2014), the experimental data used for the optimization are not shown and the thermodynamic descriptions of the gas species were not presented; moreover, the data from Krikorian are used. The use of a different set of data could explain the difference behavior compared to our calculation shown in Figure 3.18.
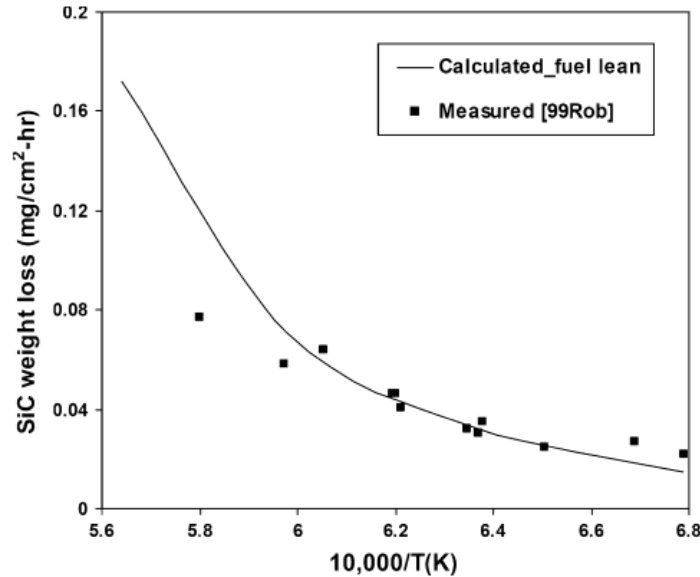
Figure 3.19: Comparison between the calculated and measured weight loss rate of SiC under fuel lean condition at 6 atm (Zhang 2014).

3.6 Conclusions of the thermodynamic modeling of SiC erosion

The good corrosion resistance of silicon carbide stems from the development of a protective silica layer on the surface when the material is in contact with an oxidant. On the other hand, material degradation through volatilization of the silica layer occurs depending on the boundary conditions and on possible reactions with the oxidant. In this chapter, the Gibbs energy descriptions of the $Si(OH)_4$ and $SiO(OH)_2$ silicon hydroxides which are produced by the reaction between silica and steam were developed to be able to calculate the erosion rates due to SiO_2 volatilization. Additionally, a study of the influence of parameters such as temperature, total pressure and ratio between the reactants was performed. In order to model the kinetics of the volatilization of silica, the SiC mass loss was predicted using the calculated partial pressures of the silicon hydroxide species. Two kinetics models were employed: the first from Opila (1997) and the second from Nickel (Hack 2008). The calculated SiC recession rates were compared to the values calculated by Opila (1999) and measured by Robinson in the temperature range between 1500 and 2100 K. The calculations performed in this work using both the models presented, show agreement between calculations and experiments. According to these results, the model of Opila is closer to the experimental data at lower temperatures, whereas the model of Nickel is closer to the experimental data at higher temperatures.

4. Oxidation of SiC potential cladding related materials: tantalum

Tantalum is a refractory metal considered as component in the future cladding designed by the CEA. The original cladding concept consists of three layers, as already shown in Figure 1.3: the external one made of SiC, an intermediate liner of tantalum, important to retain the fission gas products, and an inner SiC layer.

Tantalum in contact with SiC forms a silicide and carbide. As it can be thermodynamically determined, Ta reacts during the annealing phase, and a rough layer of intermixed Ta carbide and Si carbide is formed. Tantalum corrosion at high temperatures has been previously studied in dry atmospheres such as air and oxygen (Cowgill, 1960; Kofstad, 1963a; Kofstad, 1963; Stringer, 1967; Stringer, 1968; Voitovich, 1995; Bouzouita, 2002; Chandrasekharan, 2005) but there is still a lack of knowledge of tantalum behavior in wet atmospheres. In this chapter, the oxidation of tantalum at temperatures between 600 and 1100 °C at different steam partial pressures with argon as carrier gas is presented. Thermal gravimetric analysis was used to monitor mass gain during the oxidation tests. The hydrogen uptake at different temperatures was measured and compared with the theoretical values.

The present chapter has the following structure: first, the available literature on tantalum oxidation is discussed. Next, the experimental procedure followed in this work, including samples, devices, and experimental parameters, are described. The results of the tantalum oxidation in steam at temperature up to 1100 °C followed by the discussion on the kinetics results and hydrogen uptake are presented.

4.1 Literature review

Tantalum reacts in contact with oxygen or steam forming an oxide layer, mainly according to Eqs (4.1) and (4.2).

$$4\,\text{Ta} + 5\,\text{O}_2 \rightarrow 2\,\text{Ta}_2\text{O}_5 \tag{4.1}$$

$$2\,\text{Ta} + 5\,\text{H}_2\text{O} \rightarrow \text{Ta}_2\text{O}_5 + 5\,\text{H}_2 \tag{4.2}$$
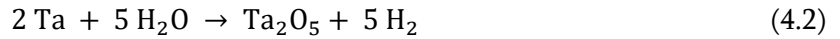
According to the Ta-O phase diagram (Figure 4.1) the solubility limit of O in Ta is 1.5, 2.2, 3.2, 4.2 and 6.4 at. % O at 700, 900, 110, 1300 and 1650 °C respectively (Garg 1996). Ta_2O_5 is the only well-established tantalum oxide phase at equilibrium, and exists in its alpha phase up to 1320 °C (Garg 1996). The presence of many Ta-O metastable phases such as TaO, TaO_y, TaO_z was reported in the literature in the case of Ta powder or bulk material oxidation (Vaughan 1960; Norman 1962 Kofstad 1963; Garg 1996). At low temperatures, a first formation of the orthorhombic TaO_y (Norman 1962) is followed by the presence of tetragonal TaO_z, which grows as platelets between 500 °C and 800 °C. At temperatures higher than 800 °C, TaO forms rather than TaO_z (Kofstad 1963). In order to perform well as a stable and protective oxide layer, the oxide scale should present high density and good adhesion to the underlying metal. The presence of lateral stresses, which can arise due to the misfit between the oxide and the underlying metal, can turn the oxide in a non-protective scale. This phenomenon is of great interest in tantalum oxide films, since the Pilling-Bedworth ratio is one of the highest (>2) (Bürgel 2011), thus developing large compressive stresses in the oxide scale.
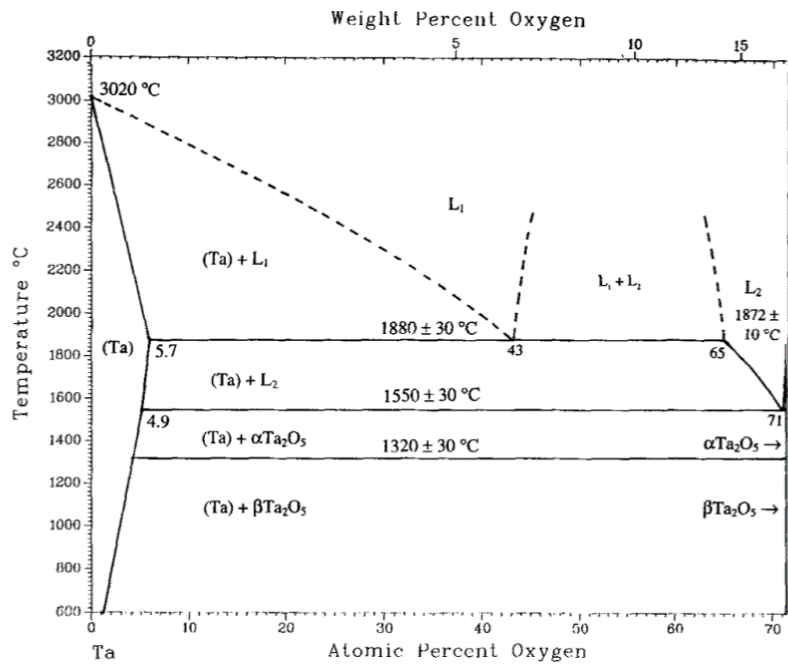
Figure 4.1: Partial Ta-O phase diagram (Garg 1996).

91

These stresses cause cracks or fractures in the oxide scale, which loses in this case its protective function (McCafferty 2010). Cowgill (1960) studied the influence of oxygen partial pressure (between 133 and 101325 Pa) on the oxidation of Ta sheets between 600 °C and 860 °C. The results indicated that at low oxygen partial pressures, the rate-controlling step depends on the square root of the oxygen partial pressure, meaning that the adsorbed oxygen molecules dissociate rapidly into atoms.

When the partial pressure increases, the process varies linearly, addressing the increased importance of the absorption process rather than the dissociation process. Kofstad (Norman 1962; Kofstad 1962a; Kofstad 1962b; Kofstad 1963a; Kofstad 1963b) investigated the oxidation of Ta powder at different oxygen partial pressures (between 1 and 101325 Pa) at temperatures between 300 and 1300 °C using X-ray diffraction and thermal gravimetric analysis. At temperatures between 450 °C and 600 °C the kinetics was parabolic, with the activation energy of 121 J/mol, which corresponds to the activation energy of oxygen diffusion into the Ta-O solid solution. The parabolic stage describes the oxygen dissolution in tantalum and the nucleation of sub-oxides, which creates platelets at the metal-oxide interface (Adelsberg 1968). The transition from parabolic to linear is due to the formation of Ta_2O_5, which cracks continuously as it is formed, causing breakaway conditions. The parabolic stage length decreases with increasing temperature: from a duration of 400-800 min at 450 °C to complete disappearance at 600 °C. At 800 °C the mechanism changes and the oxide produced is not anymore TaO_z but more likely traces of sub-oxides and TaO. For oxidation temperatures between 1000 and 1300 °C the oxidation can be divided into three stages (Kofstad 1962a):

- Pre-parabolic: the oxygen dissolves interstitially in the body-centered cubic lattice of tantalum, and the oxide starts to form on the metal surface
- Parabolic: the surface is completely covered by oxide and the rate-limiting step is the diffusion of oxygen through the Ta_2O_5 scale, according to the Wagner mechanism
- Post-parabolic: a linear behavior starts, caused by the oxide layer breakaway. At temperature between 1050 and 1300 °C the oxidation rate ceases to be linear and decreases with time, due to the higher ductility of the oxide.

Kofstad (1962a) studied also the electrical conductivity of the tantalum oxide and stated that the oxide behaves as a n-type at low oxygen partial pressure, and as a p-type at higher oxygen partial pressure

value (at 900 °C this transition occurs at ≈100 Pa). According to the Wagner theory, this implies that, at lower partial pressure, the oxidation does not depend on the oxygen partial pressure, whilst it is affected at higher oxygen partial pressure.

Stringer (1967; 1968) formulated a model for the Ta oxidation in 50 kPa oxygen atmosphere at temperatures up to 900 °C. This can be divided into two different mechanisms: at temperatures between 500 °C and 800 °C, the oxidation is dominated by an interface reaction. At temperature higher than 800 °C, the oxidation starts developing a scale which detaches once it reaches a critical thickness due to compressive growth stresses; thus the metal underneath starts to develop a new oxide layer. Since the critical thickness is in the order of few micrometers, the sequence of small parabolic kinetics leads to an overall linear kinetics. Moreover, systematic studies in oxygen considering the influence of the curvature for cylindrical samples were performed, reporting that a sphere oxidized faster than a coupon-shaped specimen.

Voitovich (1995) investigated the oxidation of Ta ingots and single crystal, in dry air with thermal gravimetric analysis at temperatures between 600 and 1000 °C for different purity grades. The finding was that the samples with higher impurities oxidized with higher rate at temperatures between 600 and 800 °C. At temperatures higher than 900 °C the TaO starts to be an intermediate product and the materials with more impurities oxidized slowly.

Richards (1954) investigated oxidation of tantalum at different carbon dioxide partial pressures in the temperature range between 700 and 950 °C: below ≈830 °C the Ta_2O_5 was not protective, and a linear behavior was addressed. At higher temperatures, the linear kinetics was preceded by a non-linear kinetics.

Bouzuoita (2002) went further and used thermal gravimetric experiments to create a model for the Ta oxidation in CO_2 at temperatures between 720 and 880 °C. The model can be divided into three steps: dissolution of oxygen into metal, nucleation of the sub-oxide, formation of the Ta_2O_5 from the sub-oxide.

The oxidation of tantalum has been largely studied in dry atmospheres, whilst little work has been reported on the reaction between tantalum and steam.

Kilpatrick (1965) tested 1 cm length specimens cut from 5 mm and 10 mm diameter rod (99.9% purity) in saturated steam between 950 °C and 1300 °C in an induction furnace. The oxides found were β-Ta_2O_5 and α-Ta_2O_5. Despite the attempt to measure the ratio of the moles of hydrogen formed to the moles of oxide from the mass gain, an accurate measurement was not possible due to the interaction of tantalum with the alumina crucible. In the case the alumina was removed, this ratio was found between 2.5 and 2.6. The oxidation mechanism can be summarized considering a first step where the water vapor is adsorbed and dissociated. Once the oxygen is available, nucleation of the oxide starts.

Adelsberg (1968) reported a study on the oxidation of Ta sheets in wet atmosphere, in particular in H_2O - Ar - H_2 gas mixtures at temperature between 840 °C and 1250 °C. The oxygen partial pressure varied from 10^{-7} to 10 Pa at 840 °C and from 0.0002 Pa to 10000 Pa at 1250 °C. The mass change was monitored during the experiments with a balance. A paralinear oxidation behavior was measured for all the samples tested. The oxidation results were dependent on the H_2O partial pressure, whilst it was found independent on the flow and on the H_2/ H_2O ratio. At the temperatures tested, the oxidation in steam was modeled as follows: after the development of the first thin oxide scale, the water vapor diffuses through the oxide and it is adsorbed. The H_2O decomposes and the Ta_2O_5 lattice incorporates the oxygen. Subsequently, the H_2 is desorbed and the oxidation proceeds at the metal-oxide interface.

De Nicola (1995) investigated the oxidation of tantalum at 520 °C in pure dry oxygen, pure water vapor and a mixture of the two, at total pressure between 100 and 11000 Pa, using thermal gravimetric analysis. In this study, the kinetics was parabolic for some minutes and then a linear kinetics was found. Comparing the three atmospheres, the kinetics was faster in pure oxygen, and the presence of the steam did not modify the shape of the kinetics or the morphology of the oxide layer. The rate of oxidation in the gas mixture was found intermediate between the other two conditions. De Nicola proposed a model to explain the behavior in the atmosphere mixture depending on the partial pressure of the oxidants.

Arias (1981) investigated oxidation of tantalum in 2.3 kPa steam partial pressure using a thermo-balance between 500 and 1000 °C. The results showed linear regime at temperatures between 500 and 625 °C, whereas for higher temperatures the parabolic regime was detected. Since no sensitive change was found between the kinetics Arias' work and that measured in air by Kofstad, Arias concluded that the gaseous hydrogen does not change the surface of the oxide. Generally, the hydrogen produced can

reach the metal and dissolve into it, causing hydrogen embrittlement, which can induce brittle behavior of tantalum (Baboian 2005).

According to the phase diagram Ta-H (Figure 4.2), considerable amount of hydrogen could be absorbed by the metal. At atmospheric pressure, the solubility of hydrogen in tantalum has a maximum at room temperature and decreases with increasing temperature. The description of the equilibrium between the hydrogen concentrations in the tantalum and the partial pressure of H_2 is given by the Sieverts' law (Eq. 4.3):

$$\left(\frac{H}{Ta}\right)_{at} = K_s \cdot p_{H_2}^{\frac{1}{2}} \tag{4.3}$$

Where $\left(\frac{H}{Ta}\right)_{at}$ is the atom ratio between H and Ta, p_{H_2} is the hydrogen partial pressure and K_s is the Sieverts constant, which can be written as:

$$K_s = \exp\left(\frac{\Delta_f S}{R} - \frac{\Delta_f H}{RT}\right) \tag{4.4}$$

Since the dissolution reaction is exothermic, the hydrogen uptake is expected to decrease with increasing temperature. The standard thermodynamic functions, which are the relative change in enthalpy and the relative change in entropy for the reaction of hydrogen from gas to solid solution in tantalum, and the analytical expression of K_s can be found in the literature (Franzen 1977; Taxak 2013). Franzen (1977) experimentally measured the equilibrium hydrogen pressure and the atomic fraction of hydrogen in pure tantalum. According to these experiments, the following expression was formulated for the Sievert´s constant values:

$$\log K_s = 2.98 - \frac{1781}{T} \tag{4.5}$$

where the T is the temperature in K. The K_s results in Torr. The K_s values converted in Pa are presented in Table 4.1.
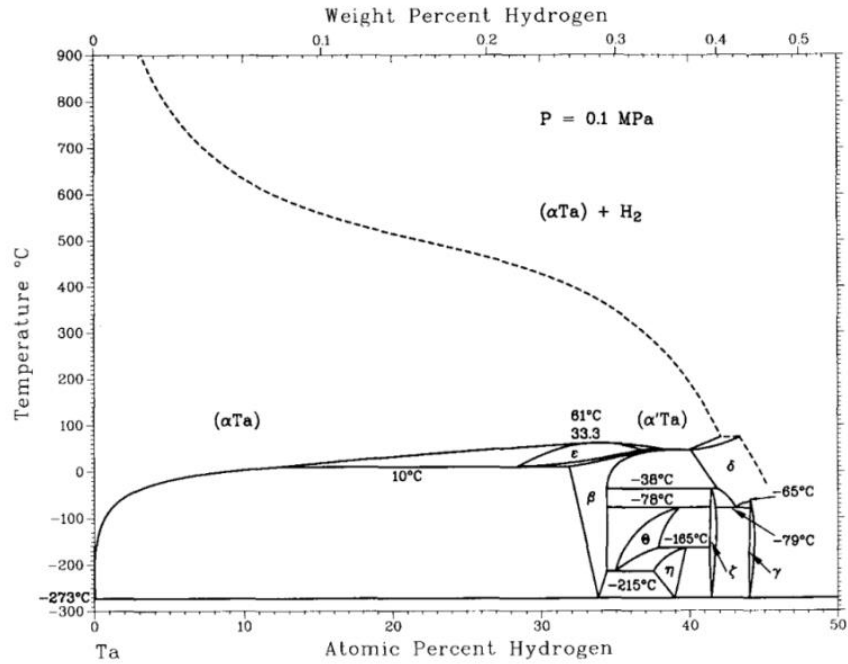
Figure 4.2: Ta-H phase diagram (San-Martin 1991).

Table 4.1: Ks constants values at different temperatures.

Temperature	600 °C	700 °C	800 °C	900 °C	1000 °C
K_s (1/Pa)	$8.61 \cdot 10^{-4}$	$5.31 \cdot 10^{-4}$	$3.59 \cdot 10^{-4}$	$2.59 \cdot 10^{-4}$	$1.97 \cdot 10^{-4}$

4.2 Experimental details

In this chapter experimental details of the oxidation of tantalum in steam are given. In particular, samples tested, devices, test conditions, and the post-test analysis used to characterize the sample after the test are reported.

4.2.1 Samples

Two different tantalum geometries and compositions were tested in this work. One set of samples had hollow-cylindrical shape with an inner diameter of 8.6 mm, 0.15 mm wall thickness, and 10 mm height. These specimens were cut from a longer tube received from CEA. The second set of samples was made of 10x10 mm² squared coupons 0.7 mm thick, cut from a sheet plate purchased from Alpha

Material. Table 4.2 lists the impurities in the Ta samples. Before each experiment, the samples were cleaned in an ultrasonic bath with isopropanol. Alumina sample holders were used to carry out the experiments in the thermobalance. Different holder's designs were adapted to the different samples: the cylindrical samples were placed on a plate, whilst the coupon samples were placed in a sample holder provided with a notch. In the case the samples were expected to crumble, a bigger sample holder was used and the powder was collected into it (Figure 4.3).

Table 4.2: Major impurities of the Ta samples.

Plate samples (Alpha Material)		Tube (Plansee Material)	
Elements	Detected impurities	Elements	Detected impurities
C	0.001	C	<0.005
O	0.001	O	<0.015
Mg	0.0002	H	<0.0015
Al	0.0024	W	<0.005
P	0.001	Mo	<0.005
Ca	0.0019	Fe	<0.005
Ti	0.0008	Ti	<0.001
Nb	0.0168	Nb	<0.01
		Ni	<0.005
		N	<0.005
		Si	<0.005
Total	0.0261		<0.05

Figure 4.3: Overview of the different samples and sample holders: left) holder for the plates, center) holder used in the case powder was produced; right) holder for tubes.

4.2.2 Facilities

The oxidation tests in steam were carried out in a thermobalance (TGA, Netzsch STA 409C), already shown in Figure 2.5, connected to a mass spectrometer (QMS 403 C Aëolos) for process control. DI water was used to produce the steam throughout an evaporator. Almost no thermal dissociation of the water is expected at these temperatures. As already discussed in Section 2.2.2, thermodynamic calculations show that dissociation of water according to Eq. (4.6) is negligible at the temperature of interest of this work.

$$2H_2O_{(g)} = 2H_{2(g)} + O_{2(g)} \tag{4.6}$$

The mass gain was detected before and after each experiment by means of a bench-top balance, and during the oxidation by means of the TGA.

Selected additional samples were oxidized in the TGA in 100 kPa steam in order to measure the hydrogen uptake at temperature between 600 and 1000 °C. The hydrogen uptake was measured using the hot extraction method: this procedure is reliable since the absorption-desorption of H_2 in tantalum does not show any hysteresis. The hot extraction was done in an induction furnace (LAVA), at temperatures up to 1500 °C in argon flow (20 l/h, 99.9999% purity). This furnace was flushed with a mixture of argon and H_2 before being used for the hydrogen extraction. In order to measure the hydrogen background, blank measurements of the exhaust gas without any sample loaded, were performed before and after the experimental campaign. The exhaust gases containing the H_2 released by the Ta samples were analyzed by the mass spectrometer especially calibrated for hydrogen (Balzers GAM 300). This allowed calculating the integral of the hydrogen absorbed by the samples. In Figure 4.4, the gas trend of the sample Ta3 (see Table 4.7) during the annealing phase is presented as an example. The impurities of the argon gas could raise concerns regarding the measurements of the hydrogen released. Indeed oxygen impurities could be as high as 0.1 Pa, and this oxygen amount could oxidize the hydrogen released, thus introducing a consistent error in the measurements. On the other hand, Figure 4.4 clearly shows that the hydrogen peak is two orders of magnitude higher than the oxygen and water vapor signal. Therefore, the error due to the argon impurities can be considered negligible.

4.2.3 Test conditions

The heating up phase in the TGA tests was performed in argon (99.9999% purity, 3 l/h) with 10 °C/min heating rate. The steam was produced by an evaporator and introduced in the reactor chamber 10 min after the isothermal experiment temperature was reached.

The influence of the steam partial pressure was investigated using three nominal partial pressures, 10, 50 and 100 kPa at temperatures between 500 and 1100 °C. Before the experiments, the samples were measured with a caliper and weighted.

The experiments' parameters are summarized in Table 4.3, whereas in Table 4.4 and Table 4.5 the experimental matrices for all the samples are presented. According to Eq. (4.2) and (4.7), the maximum mass gain due to the oxidation, assuming the complete conversion of tantalum in oxide, is 22% of the original mass.

$$\Delta m_{max}\ (\%) = \frac{m_{(Ta_2O_5)} - m_{(2Ta)}}{m_{(2Ta)}} \cdot 100\% = \frac{441.9\frac{g}{mol} - 2 \cdot 180.9\frac{g}{mol}}{2 \cdot 180.9\frac{g}{mol}} \cdot 100\% = 22.1\% \qquad (4.7)$$

In these experiments, the tests were stopped when the oxidation reached 10% of the original mass. Eq. (2.27) was used to calculate the mass change from the thermal gravimetric data. The parabolic constants were calculated in this work for all the experiments performed.

Table 4.3: Experimental parameters used for oxidation test of tantalum samples.

P_{H2O}	100 kPa	50 kPa	10 kPa
Steam	3 g/h	3.18 g/h	0.64 g/h
Argon	-	4 l/h	7.2 l/h
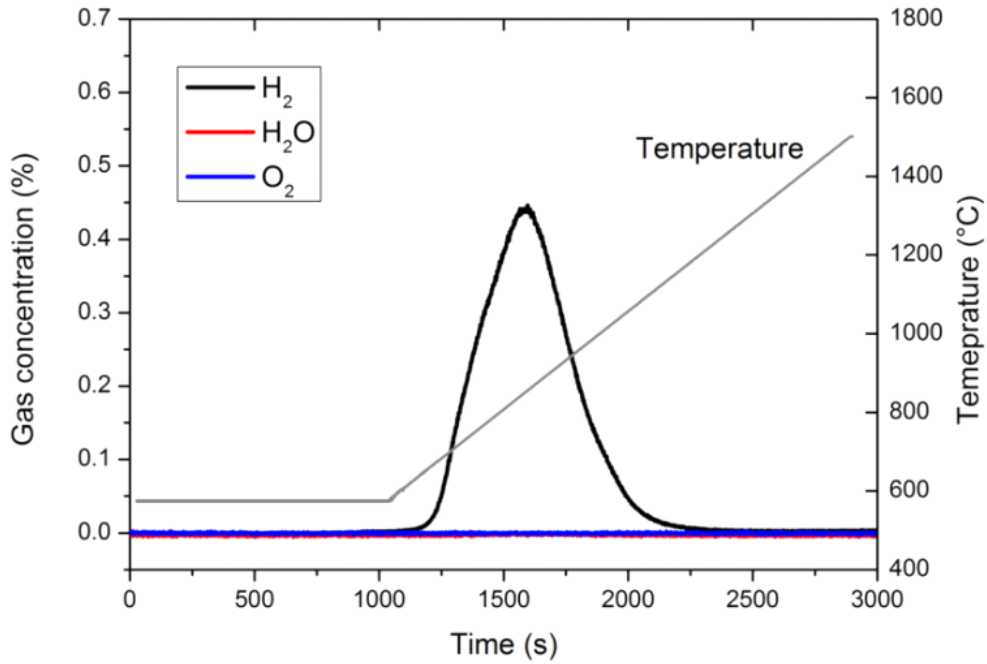
Figure 4.4: Mass spectrometer signal during the annealing of the Ta3 sample in the LAVA furnace.

Table 4.4: Experimental matrix used for the plate-shaped samples. The letter p indicates the plates samples, the first digit refers to the temperature (1 is the lower temperature up to 6 that indicates the higher temperature), and the second to the steam partial pressure (1 = 10 kPa, 5 = 50 kPa, 9 = 100 kPa).

Temperature	Steam Partial Pressure		
(°C)	10 kPa	50 kPa	100 kPa
600	p11	p15	p19
700	p21	p25	p29
800	p31	p35	p39
900	p41	p45	p49
1000	p51	p55	p59
1100	p61	p65	p69

Table 4.5: Experimental matrix used for the tube-shaped samples. The letter t indicates the tube samples, the first digit refers to the temperature (1 is the lower temperature up to 6 that indicates the higher temperature), and the second to the steam partial pressure (1 = 10 kPa, 5 = 50 kPa, 9 = 100 kPa).

Temperature	Steam Partial Pressure		
(°C)	10 kPa	50 kPa	100 kPa
600	t11	t15	t19
700	t21	t25	t29
800	t31	t35	t39
900	t41	t45	t49
1000	t51	t55	t59
1100	t61	t65	t69

The linear constant was determined by linear fit of the mass change versus the time $\left(\frac{g}{m^2 s}\right)$, and it is presented for each experiment in Table 4.8. Some samples presented two different linear trends. Hence, two linear constants have been calculated, namely kl_1 and kl_2.

4.2.4 Post-test analysis

After the experiments, the samples were embedded in epoxy resin, and were ground and polished. Details are reported in Table 4.6. The micrograph of the section of Ta sheet and tube acquired with optical microscope is shown in Figure 4.5. The samples were then etched in a mixture of 100 ml water, 50 ml HNO_3 and 20 g ammonium bi-fluoride. Post-analysis was carried out using optical microscope (MeF3, Reichert-Jung) and X-ray diffraction (in Bragg–Brentano geometry, with CuKα radiation). The hydrogen uptake was measured for 6 samples. The tests performed to measure the hydrogen uptake are presented in Table 4.7. Two samples were oxidized at 600 °C, in order to quantify the hydrogen uptake before the breakaway (2 min oxidation) and after the breakaway (62.5 min oxidation).

Table 4.6: Ta Polishing and grinding procedure.

	Disc / support	(GRIT)	Speed (1/min)	Pressure (bar)	Time (min)
Grinding 1	Diamant disc	220	150	2	3-5
Grinding 2	Diamant disc	600	150	2	5
Grinding 3	Diamant disc	1200	150	2	10
Polish 1	Perforated Synthetic rubber	6 μm	150	1.5	4
Polish 2	Perforated Synthetic rubber	3 μm	150	1.5	6
Polish 3	Perforated Synthetic rubber	1 μm	150	1.5	2
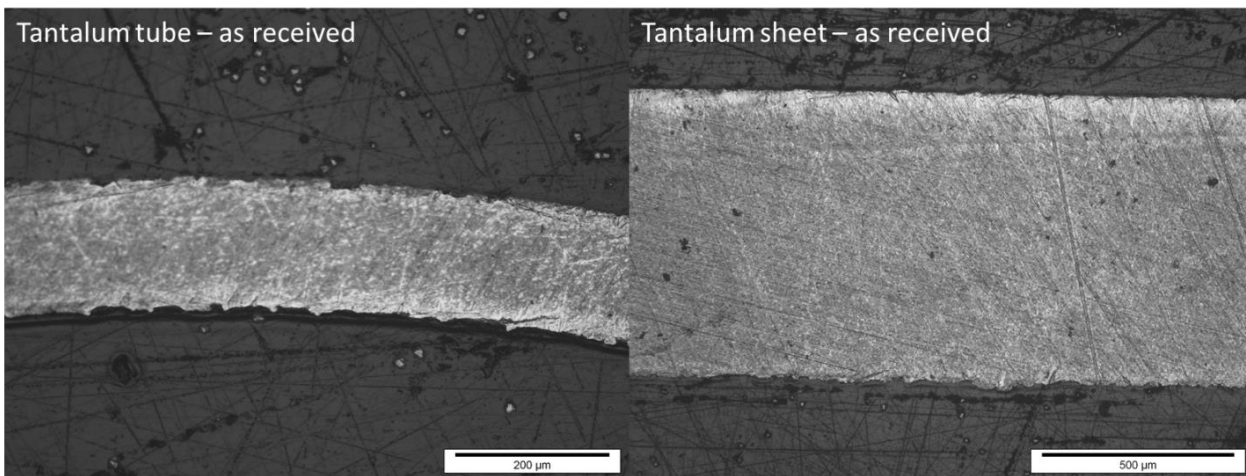
Figure 4.5: Micrographs of the section of tantalum sheet and tube with optical microscope.

Table 4.7: Experimental matrix used for H_2 uptake measurements.

Sample	Temperature (°C)	Steam (kPa)	Time (min)
Ta1	600	100	2
Ta2	600	100	62.5
Ta3	700	100	54
Ta4	800	100	210
Ta5	900	100	80
Ta6	1000	100	12

4.3 Results of Ta oxidation tests

In this section, the results achieved during the oxidation tests and the hydrogen uptake measurements are presented. After the tests, the optical analysis showed different surface color for the two types of samples: the cylinders maintained a grey color, close to the tone before oxidation, whereas the plates showed a white surface. As a second difference between the two shapes, the oxidation for the plate samples was favored at the edges of the samples, resulting in a rounding off of the previous rectangular shape. In Sections 4.3.1, 4.3.2, 4.3.3 the samples are presented at different temperatures with their macrographs and micrographs obtained by means of optical microscopy techniques. The kinetics is reported for each temperature in Section 4.3.4, as well as the activation energies in Section 4.3.5. Finally, in Section 4.3.6 and in Section 4.3.7 the results of the hydrogen uptake measurements and the XRD analysis are shown.

4.3.1 Temperature range: 600-700 °C

Macrographs of the samples oxidized at 600 and 700 °C, are in Figure 4.6 and Figure 4.7. The plates crumbled in a fine white powder, thus the remaining plates and the powder are both shown in the figures. The tubes mainly maintained their shapes.
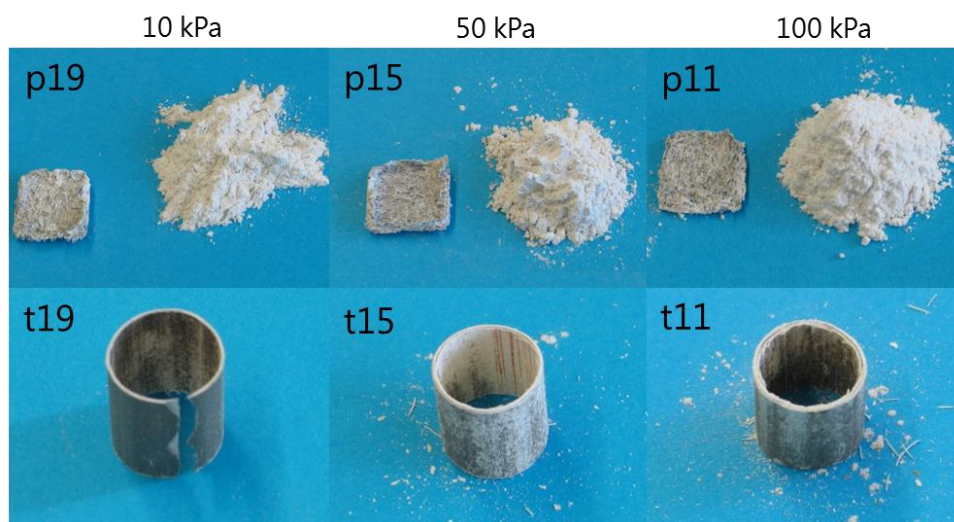
Figure 4.6: Macroscopic images of the samples after oxidation at 600 °C.
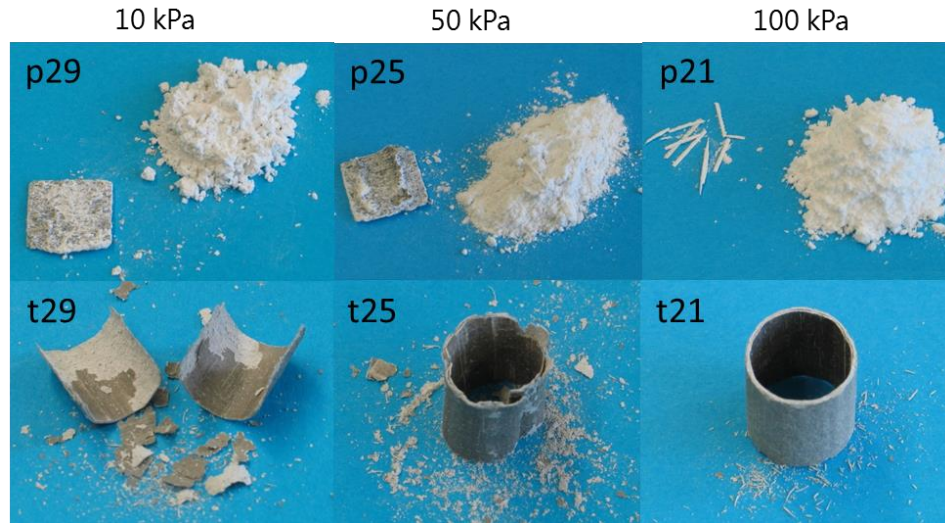
Figure 4.7: Macroscopic images of the samples after oxidation at 700 °C.

In Figure 4.8, the mass gain of the oxidation of plates and tubes is shown at 600 °C and 700 °C. At the lowest temperatures (600 and 700 °C), a considerable difference between the tubes and the plates can be noticed: generally, the plates oxidized faster, except for the oxidation at 700 °C in 10 kPa. A strong dependency on the steam partial pressure can be noted. At these temperatures, two linear constants can be calculated: the first considering the period between 300 s and 900 s and the second for the rest of the time. After the initial stage, an enhanced oxidation can be noted during the plate's tests depending on the steam partial pressure, whereas the tube oxidation is not affected by the steam partial pressure. The oxidation at 700 °C is somewhat slower than at 600 °C, and this is shown by the k_{12} values shown in Table 4.8. The post-test analyses carried out with optical microscope are not presenting significant difference between the two temperatures. In Figure 4.9 and in Figure 4.10 the cross sections of the samples oxidized are presented at 600 °C and at 700 °C respectively. For the plate-shaped samples, the oxide is easily detached, while in the tubes the oxide is still visible in the optical micrograph, and it shows a horizontal stratification.
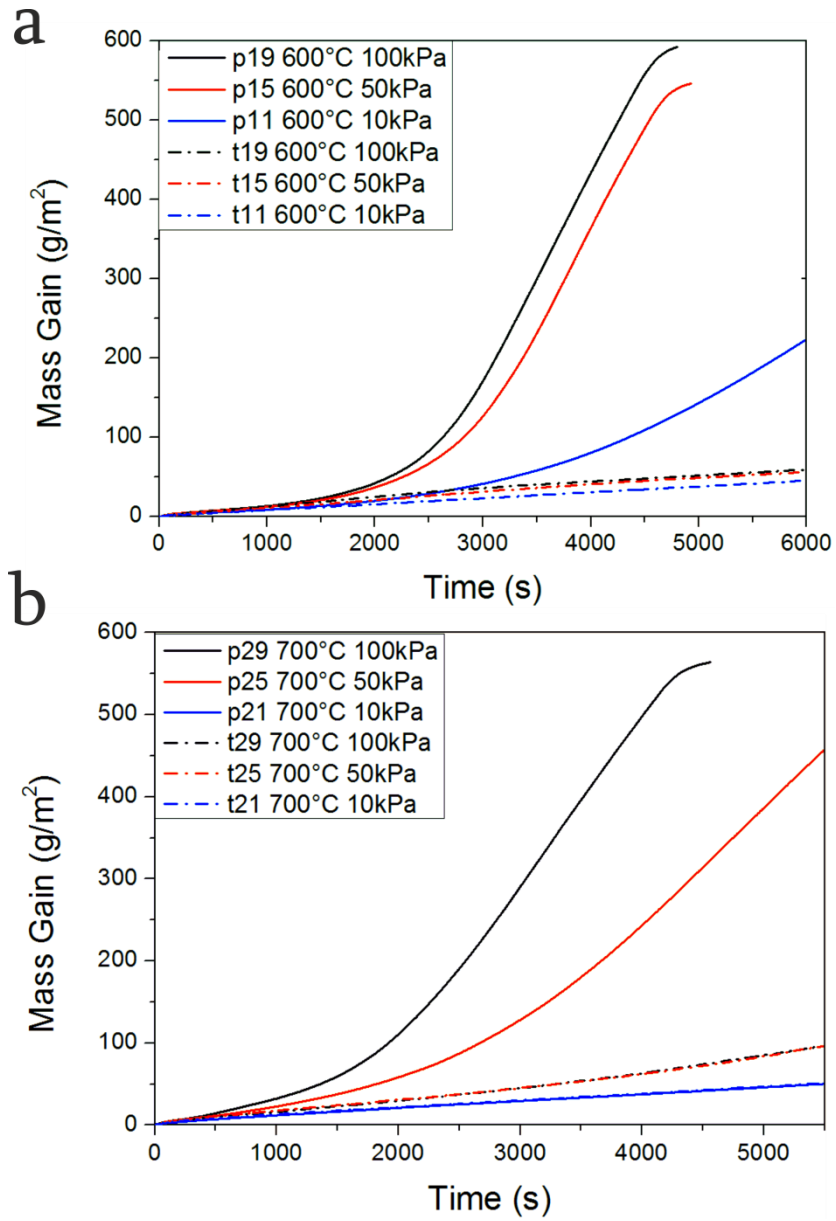
Figure 4.8: Mass gain of the tantalum samples oxidized at 600 °C and 700 °C.
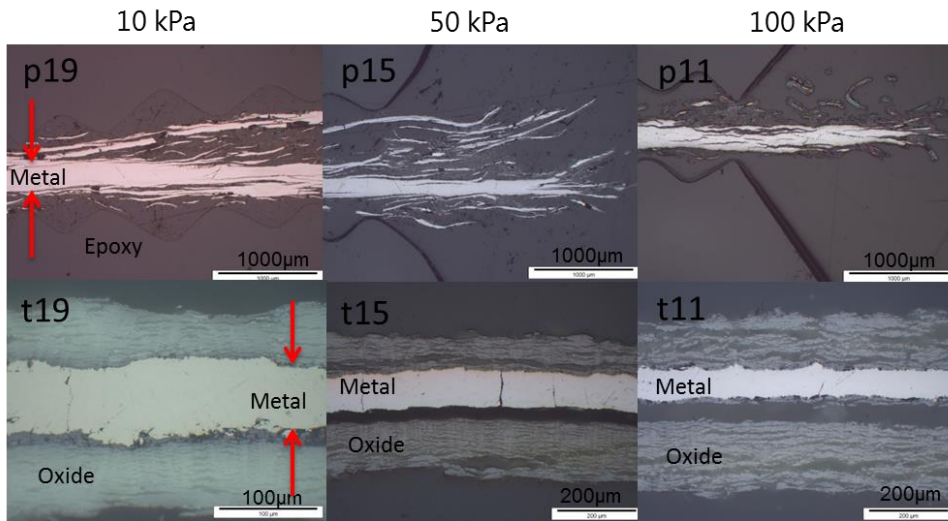
Figure 4.9: Cross section micrographs with optical microscope of the Ta samples at 600 °C.
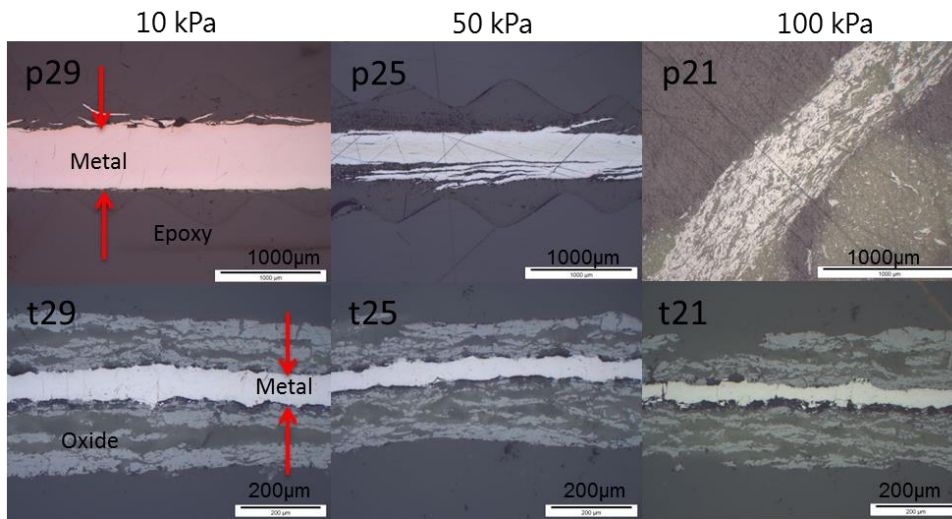
Figure 4.10: Cross section micrographs with optical microscope of the Ta samples at 700 °C.

4.3.2 Temperature range: 800-900 °C

In Figure 4.11 and in Figure 4.12 macrographs of the samples oxidized at 800 °C and 900 °C are presented. Comparing to the lower temperatures, the samples maintained their shapes and did not crumble, in particular the coupon-shaped samples.
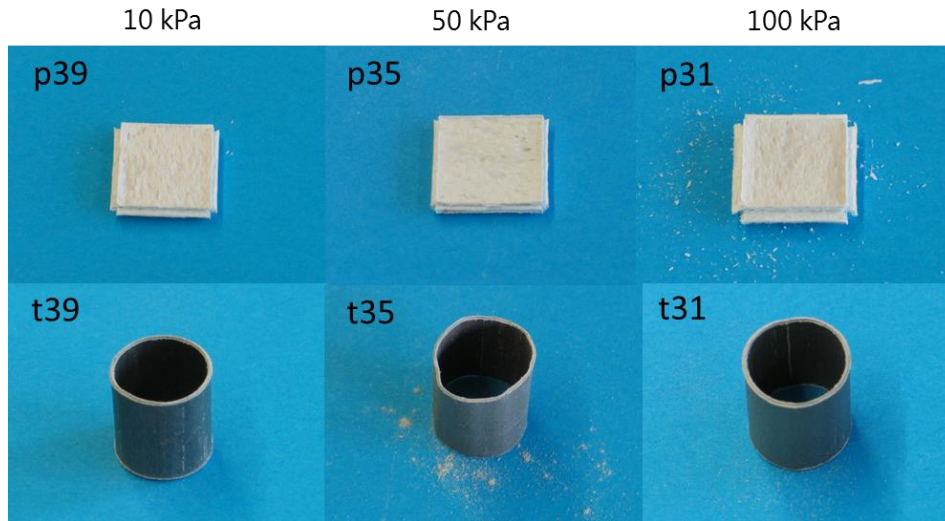
Figure 4.11: Macroscopic images of the samples after oxidation at 800°C.
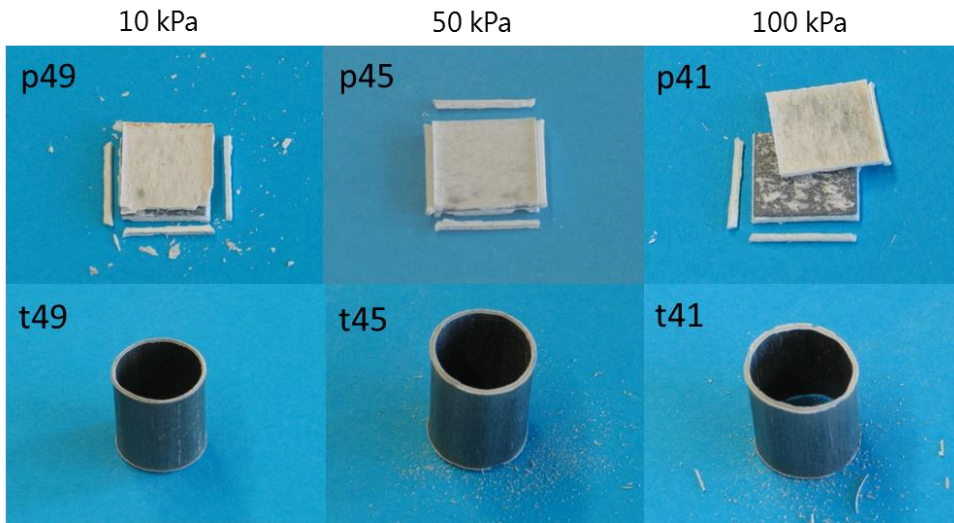
Figure 4.12: Macroscopic images of the samples after oxidation at 900 °C.

As can be noted in Figure 4.13, at 800 °C and 900 °C, no significant difference can be seen in the mass gain between the plates and the tubes. The oxidation performed in 10 kPa steam partial pressure results in a slower oxidation rate than at the other partial pressures. The steam partial pressure affects the oxidation behavior of plates and tubes in the same way. In Figure 4.14 and in Figure 4.15 the cross sections of the samples oxidized at 800 °C and 900 °C are presented. The oxide developed on the tubes is more compact than the oxide on the plate. Indeed, the oxide on the plates shows horizontal stratification. Some cracks are present on the tubes oxide scale. In correspondence of these cracks, the oxide

is thicker. As a result, the interface between the oxide and the metal is more jagged for the tubes samples.
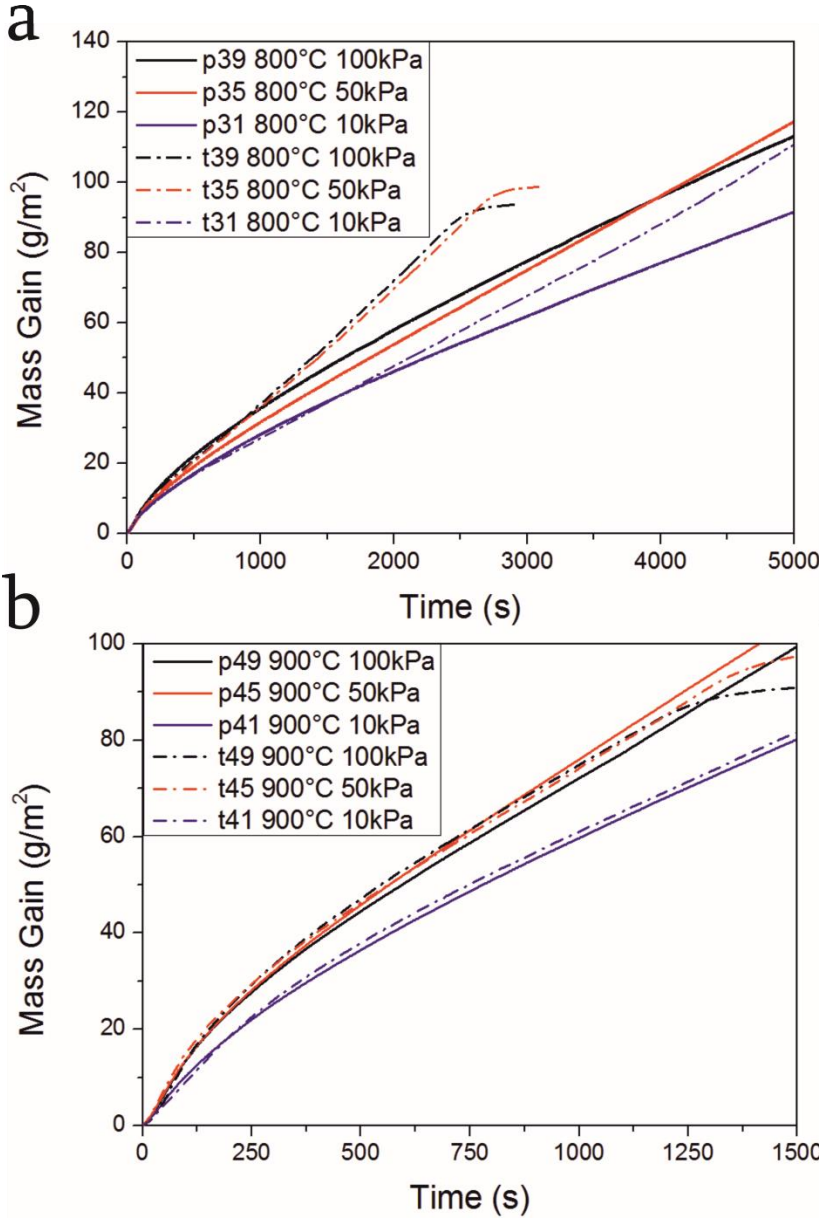
Figure 4.13: Mass gain of the tantalum samples oxidized at 800 °C and 900 °C.
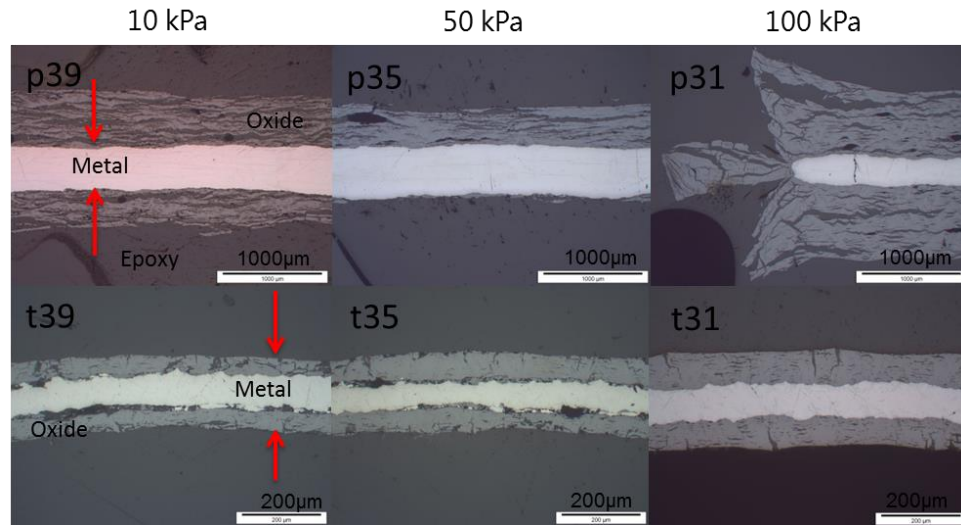
Figure 4.14: Cross sections with optical microscope of the Ta samples at 800 °C.
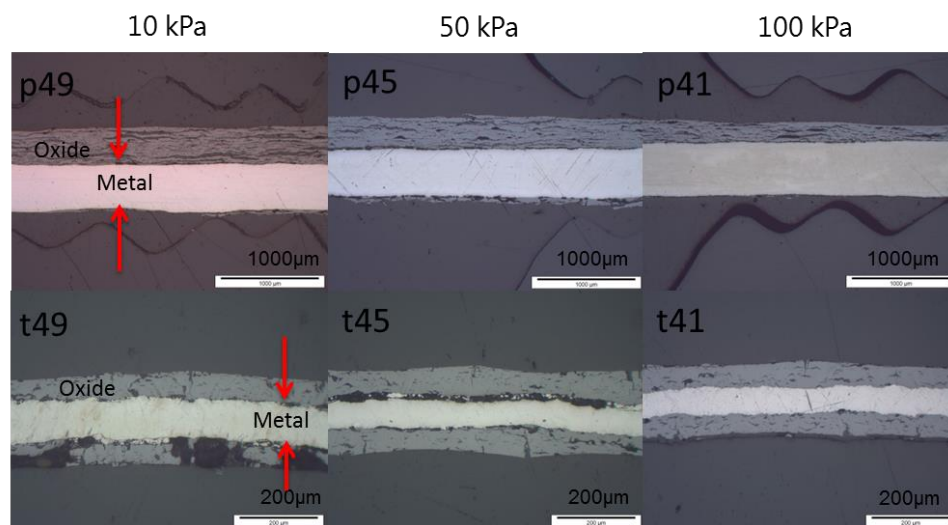
Figure 4.15: Cross sections with optical microscope of the Ta samples at 900 °C.

4.3.3 Temperature range: 1000-1100 °C

In Figure 4.16 and in Figure 4.17 macrographs of the samples oxidized at 1000 °C and 1100 °C are presented. The plates tested at 1000 °C have the same aspect of those tested at 900 °C: the samples are homogeneously oxidized, and they tend to separate, splitting in the central part. At 1100 °C the oxidation of the plates mainly occurs on the sides of the samples. The tubes deformed after tests at 10 kPa. In Figure 4.18, the mass gain curves show a rather linear kinetics. At 1000 °C and 1100 °C the steam partial pressure is affecting the oxidation rate. Moreover, at 1100 °C the tube oxidized faster than the

plates. In Figure 4.19 and in Figure 4.20 cross sections of the samples oxidized at 1000 °C and 1100 °C are presented. At the highest temperature, the oxide shows a different structure compared to the lower temperatures. The oxide appears denser and with a columnar morphology. The cracks in the oxide scale of the tube-shaped samples are more evident at this temperature.
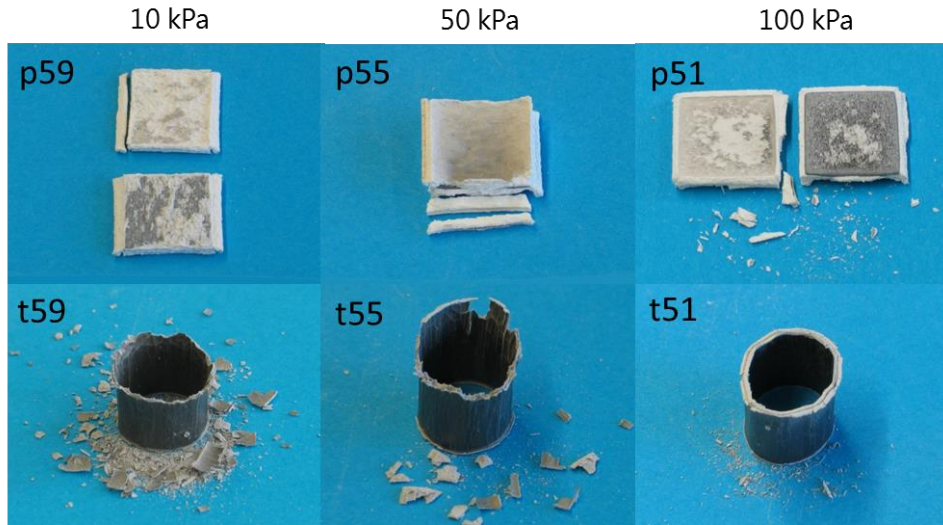
Figure 4.16: Macroscopic images of the samples after oxidation at 1000 °C.
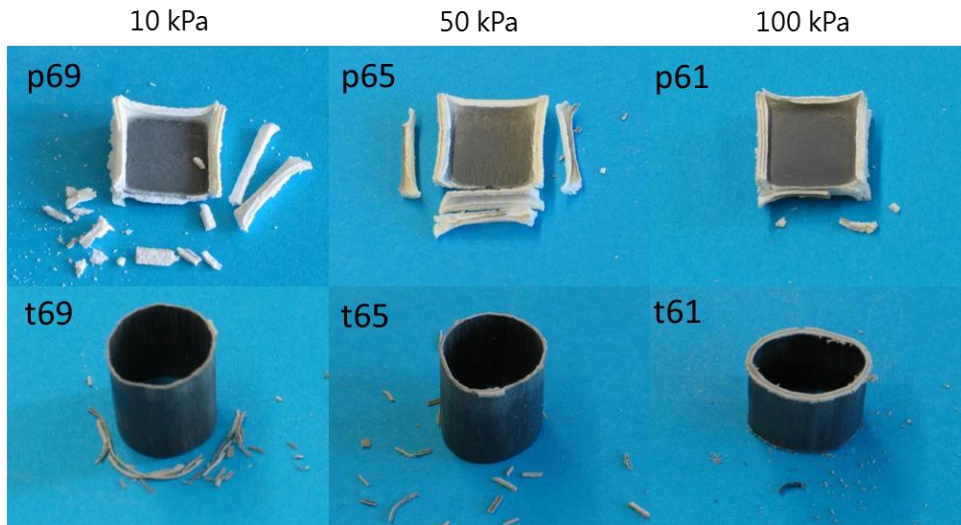
Figure 4.17: Macroscopic images of the samples after oxidation at 1100 °C.
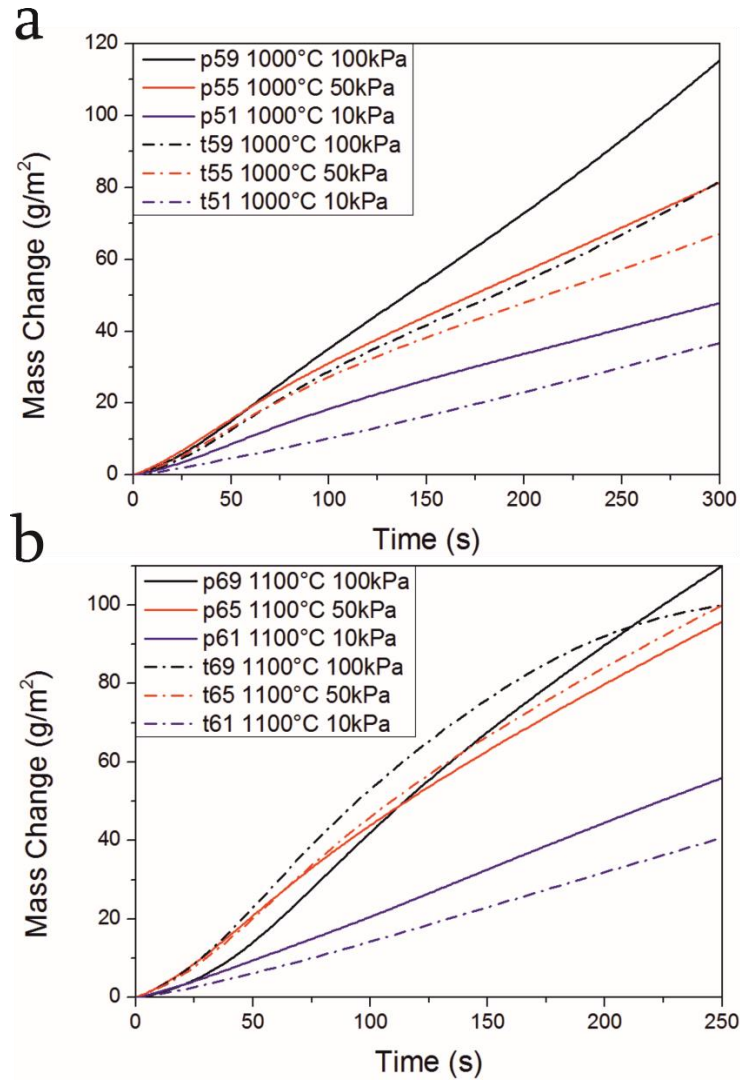
Figure 4.18: Mass gain of the tantalum samples oxidized at 1000 °C and 1100 °C.

4.3.4 Kinetics parameters

Linear oxidation behavior was detected for all the samples investigated in this work. A glimmer of parabolic oxidation can be noticed at the very beginning of the experiments, when the temperature is still not stabilized. The non-isothermal condition prevented to calculate the parabolic constant. For the samples that have shown two different slopes during the oxidation process, in particular at the lower temperatures (600 and 700 °C), the second linear constant was considered. This choice can be justified since k_{l2} has higher effect on the overall mass gain. In Table 4.8 the linear constants are shown for all the experiments performed.
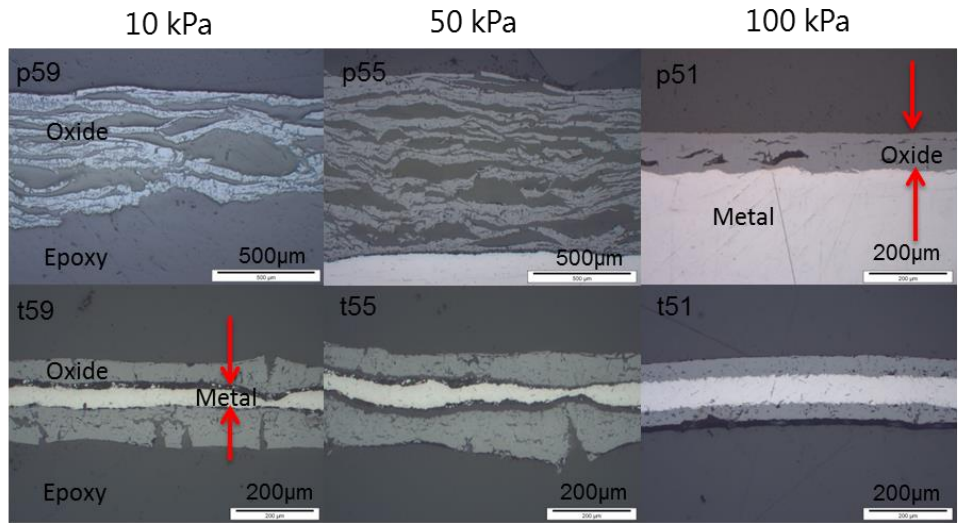
Figure 4.19: Cross sections with optical microscope of the Ta samples at 1000 °C.
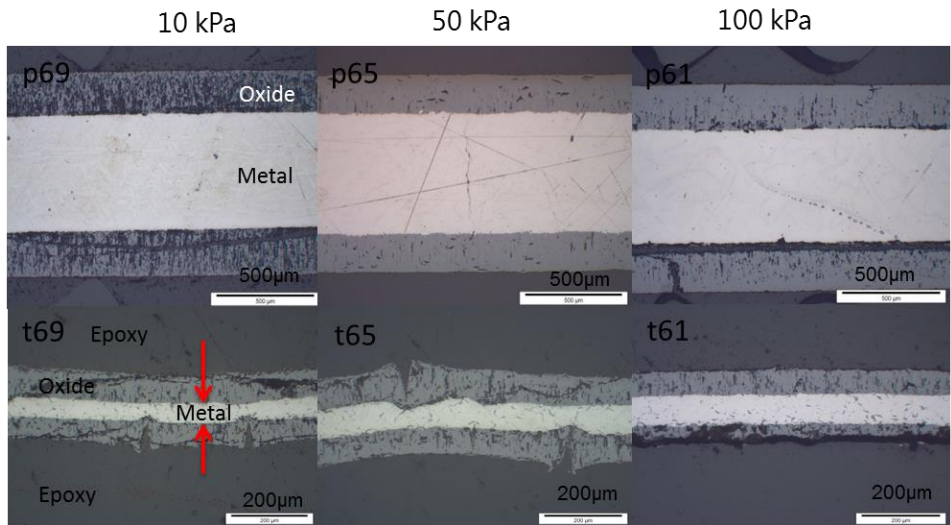
Figure 4.20: Cross sections with optical microscope of the Ta samples at 1100 °C.

Table 4.8: Overview of the linear rate constants calculated for each sample.

Temperature (°C)	Steam Partial Pressure (kPa)	Sample	k_{l1} (g/m²/s)	k_{l2} (g/m²/s)
600	100	p19	0.01148	0.26178
	50	p15	0.01025	0.26087
	10	p11	0.00786	0.09609
	100	t19	0.01213	0.00759
	50	t15	0.01035	0.00734
	10	t11	0.00758	0.00758
700	100	p29	0.03538	0.20748
	50	p25	0.02211	0.14225
	10	p21	0.00869	0.03578
	100	t29	0.01324	0.02222
	50	t25	0.01353	0.02266
	10	t29	0.0084	0.01388
800	100	p39	0.02366	
	50	p35	0.02095	
	10	p31	0.01361	
	100	t39	0.03441	
	50	t35	0.03352	
	10	t31	0.02054	
900	100	p49	0.05602	0.06065
	50	p45	0.05659	
	10	p41	0.03837	
	100	t49	0.06037	
	50	t45	0.05695	
	10	t41	0.04411	
1000	100	p59	0.66485	
	50	p55	0.26985	0.51826
	10	p51	0.16764	
	100	t59	0.258	
	50	t55	0.23795	
	10	t51	0.12007	
1100	100	p69	0.23706	
	50	p65	0.22578	
	10	p61	0.14458	
	100	t69	0.27871	
	50	t65	0.26923	
	10	t61	0.1589	

The linear rate constants have been plotted for experiments in the temperature range from 600 to 900 °C (Figure 4.21a) and up to 1100 °C (Figure 4.21b). In Figure 4.21a the values between 0.01 and 0.009 g/m²/s are shown, whereas in Figure 4.21b the values not visible in the previous graph are shown in the range from 0 to 0.7 g/m²/s. The linear constant values of the plates at 600 °C and at 700 °C are the same order of magnitude of the linear rate constant at 1000 °C and 1100 °C, therefore they are presented in Figure 4.21b.
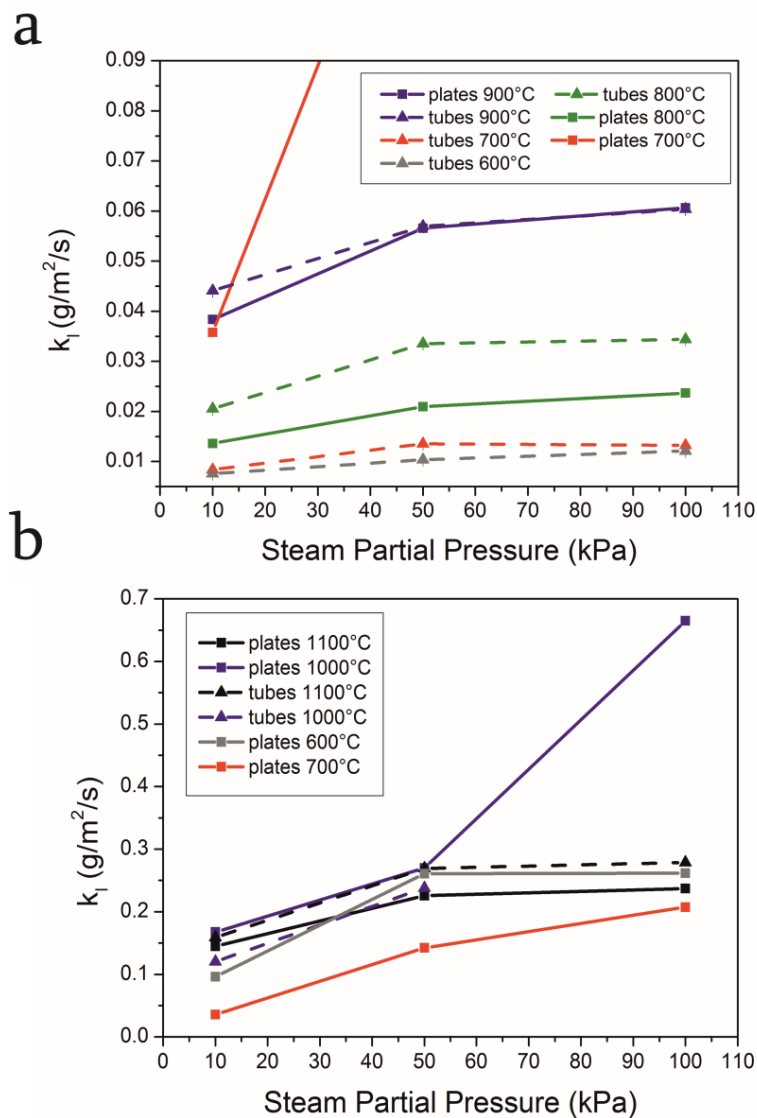
Figure 4.21: (a) Linear constants of the samples oxidized at 700, 800 and 900 °C (b) and at 600, 700, 1000 and 1100 °C.

4.3.5 Activation energy

The activation energy for the linear oxidation rate was outlined using the Arrhenius equation by determining the slope of $\ln(k_{ll})$ against 1/T. In these data, the activation energy is not significantly affected by the steam partial pressure. Only the values for the oxidation tests performed at 10 kPa steam partial pressure are presenting systematically lower ln(k). In Figure 4.22a and in Figure 4.22b the values for the plates and for the tubes are respectively plotted considering the k_{ll}. The activation energy was calculated accounting the constants calculated for each temperature tested (Table 4.9).

4.3.6 Hydrogen uptake

The content of hydrogen absorbed by the metal was determined by means of the hot extraction technique on selected samples as already shown in Table 4.7. In order to calculate the hydrogen concentration in the metal, the measured H_2 volume release of each sample was related to the amount of the non-oxidized metal using the TG data. These values correspond to the H_2 measured concentration in tantalum metal.

In Figure 4.23, the hydrogen uptake is presented at different temperatures in the range between 600 to 1000 °C. The early parabolic oxidation phase is still visible at 600 °C, whilst at higher temperature the parabolic oxidation is too short to be distinguished from the linear phase. In order to measure the hydrogen uptake before and after the transition between parabolic and linear oxidation, two experiments have been performed only at 600 °C. The first test measures the hydrogen uptake after 2 min oxidation, thus in the parabolic regime (k_{par}); the second sample is oxidized for 62 min, allowing measuring the hydrogen uptake during the linear regime, which occurs after the breakaway. Figure 4.23 shows that, before the breakaway, the hydrogen uptake is less than 50 ppm$_w$. In case of breakaway, the hydrogen uptake is almost 30 times higher. According to the Ta-H phase diagram shown in Figure 4.2 (San-Martin 1991, Predel 1996), the solubility of H at these temperatures is lower than at ambient temperature (800 ppm$_w$). This could cause the presence of precipitates. According to the data presented in Figure 4.23, the measured hydrogen fraction in the metal ($C_H)_{eff}$ can be calculated, as it is plotted in Figure 4.24.

Table 4.9: Activation energy of the Ta samples oxidized in argon and different steam partial pressure.

	E_a plates (kJ/mol)	E_a Tubes (kJ/mol)
10 kPa	+67.9	+85.3
50 kPa	+66.9	+88.2
100 kPa	+70	+83.3
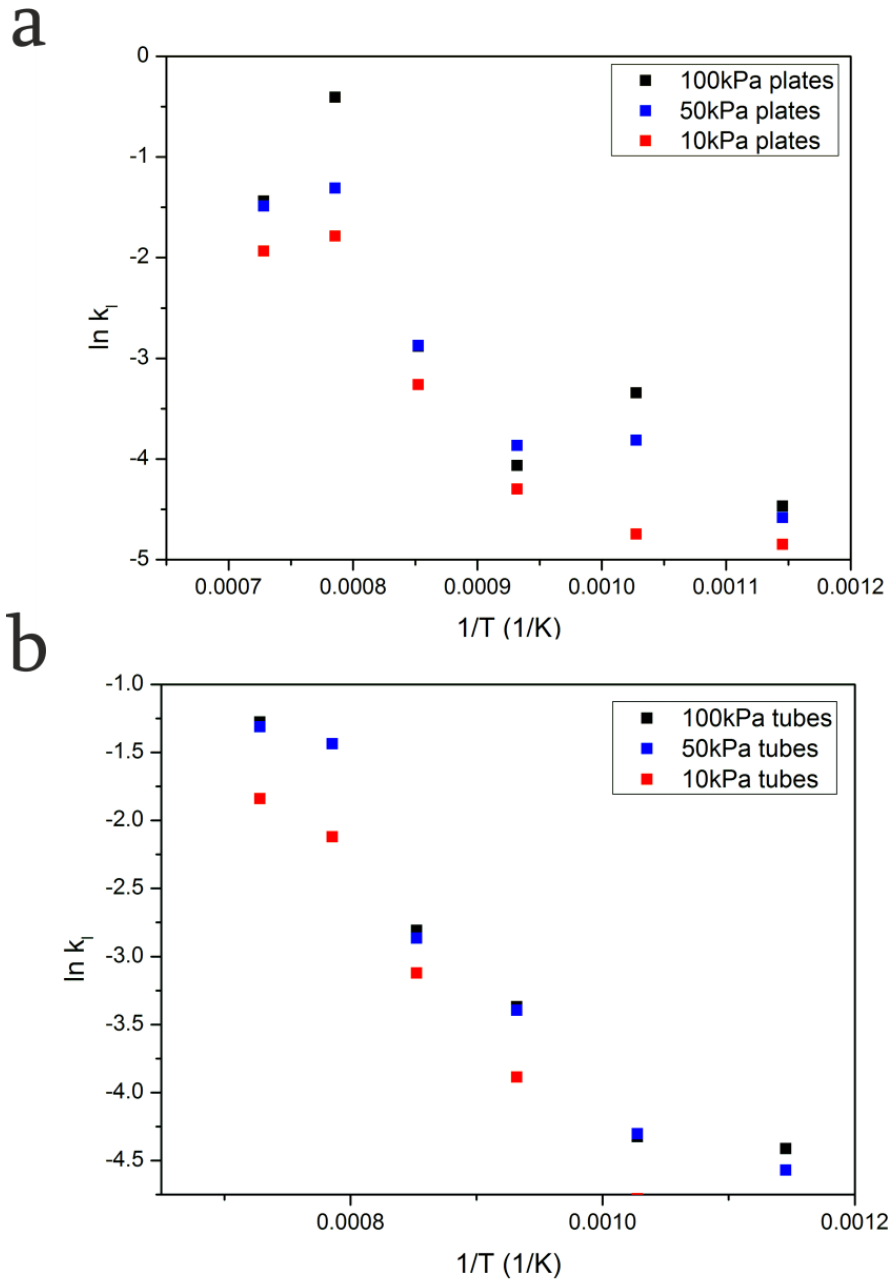
Figure 4.22: Graph of the $\ln k_l$ (a) for the plate samples (b) for the tubes.

These values are always beyond the maximum solubility of hydrogen in tantalum, which is, according to Figure 4.25, equals to about 1100 at 600 °C, 725 ppm at 700 °C, 450 ppm at 800 °C. This could cause precipitates that can explain the detachment of the oxide layer.
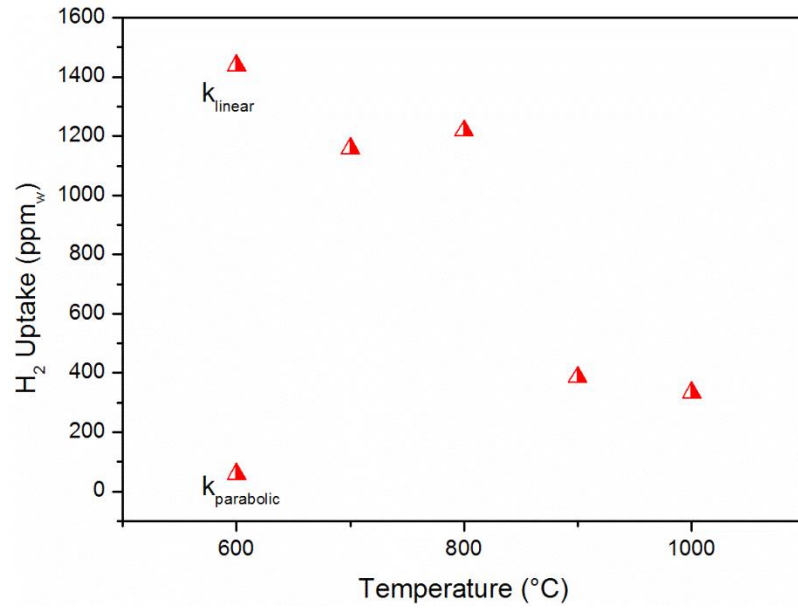
Figure 4.23: Hydrogen uptake in the tantalum metal.
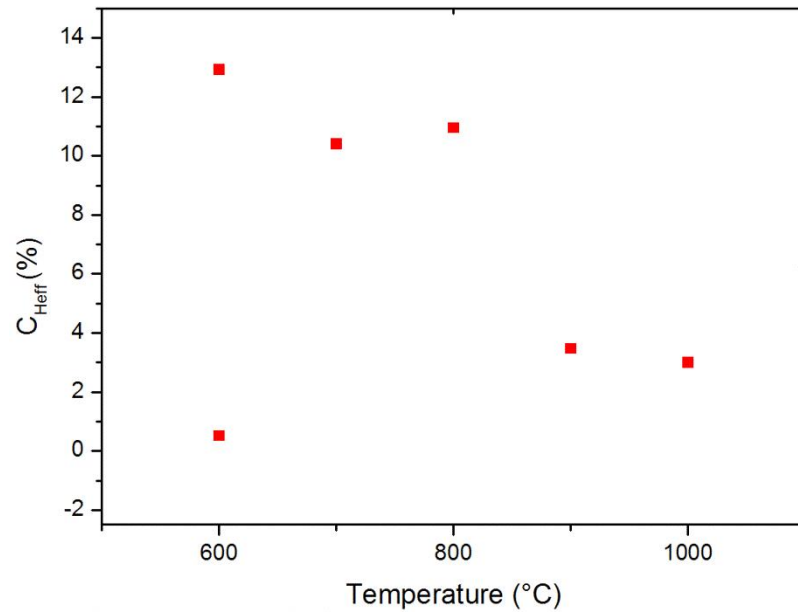
Figure 4.24: Concentration of hydrogen measured in the Ta metal.
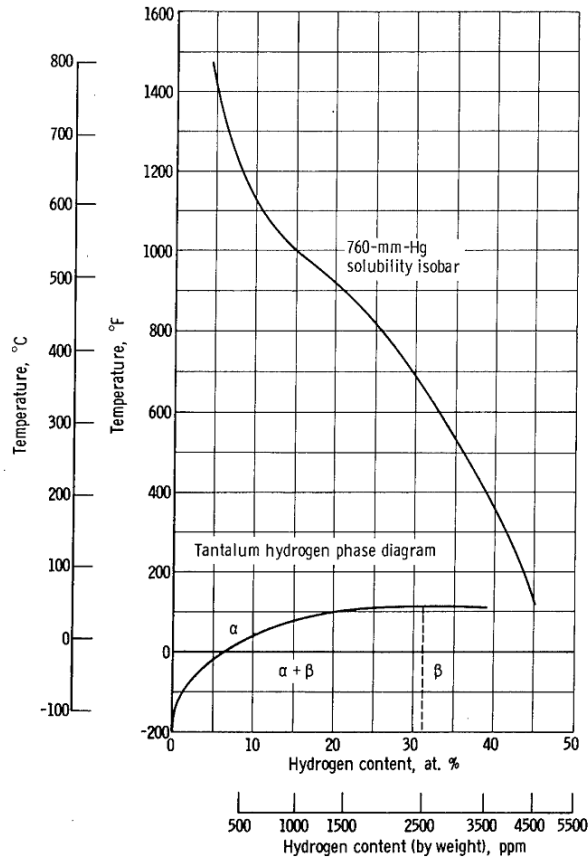
Figure 4.25: Tantalum-hydrogen phase diagrams and solubility isobars (Stephens 1966).

The theoretical hydrogen content in the metal can be determined by means of the Sieverts' relation, thus using the square root of the hydrogen partial pressure in the ambient atmosphere. The hydrogen partial pressure in the atmosphere can be estimated from the mass gain of the tantalum specimen due to the Eq. (4.2), and from the steam/Ar flow rate during the oxidation process.

Considering that the reaction in Eq. (4.8) occurs at the Ta/Ta₂O₅ interface, as already assumed by Adelsberg (1968), the mass gain detected by the TGA is considered to be entirely due to the oxygen absorption.

$$H_2O(\text{ads}) + \blacksquare_{O^=} + 2e^- \rightarrow H_2(\text{ads}) + O^= \tag{4.8}$$
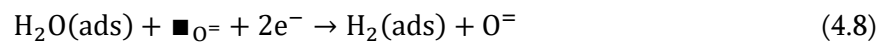
The hydrogen in the career gas at different temperatures can be calculated considering Eq. (4.8) (results are in Figure 4.26). The highest value for the hydrogen in the career gas was found at 1000 °C, decreasing at 800 and 900 °C and presenting again an increase at 600 and 700 °C.

The theoretical hydrogen concentration in the sample ($C_{H_{ext}}$) can be calculated based on the equilibrium with the H_2 partial pressure in the ambient atmosphere. The values of ($C_{H_{ext}}$) are plotted in Figure 4.27.

The ratio between the measured concentration and the theoretical concentration of hydrogen in the metal can be expressed with a coefficient (ϑ). A value of ϑ higher than 1 suggests that the hydrogen concentration in the metal is higher than the concentration expected from the Sieverts' law. Thus, a local hydrogen partial pressure at the metal-oxide interface rather than the hydrogen partial pressure in the gas bulk determines the hydrogen uptake.

$$\vartheta = \frac{C_{H_{eff}}}{C_{H_{ext}}} \tag{4.9}$$
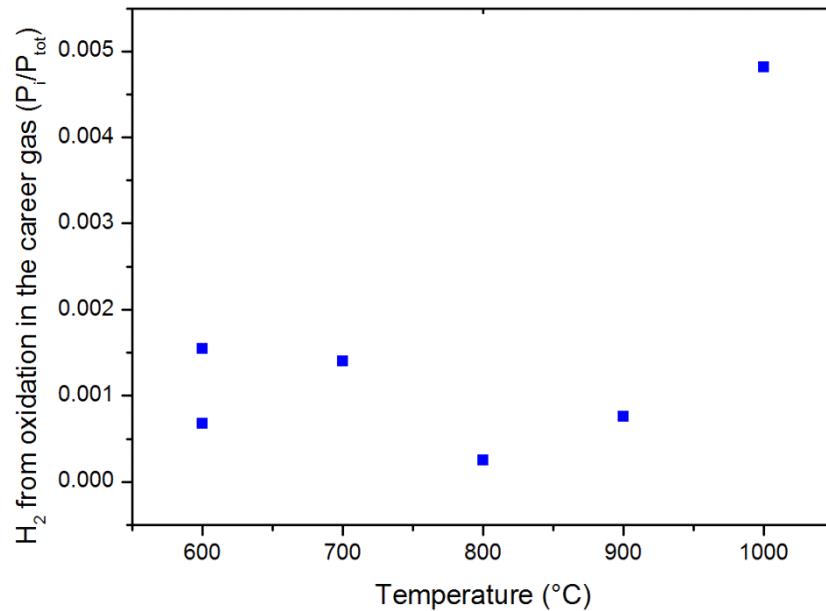
Figure 4.26: Hydrogen concentration in the carrier gas from the dissociation of H_2O due to the oxidation of tantalum.
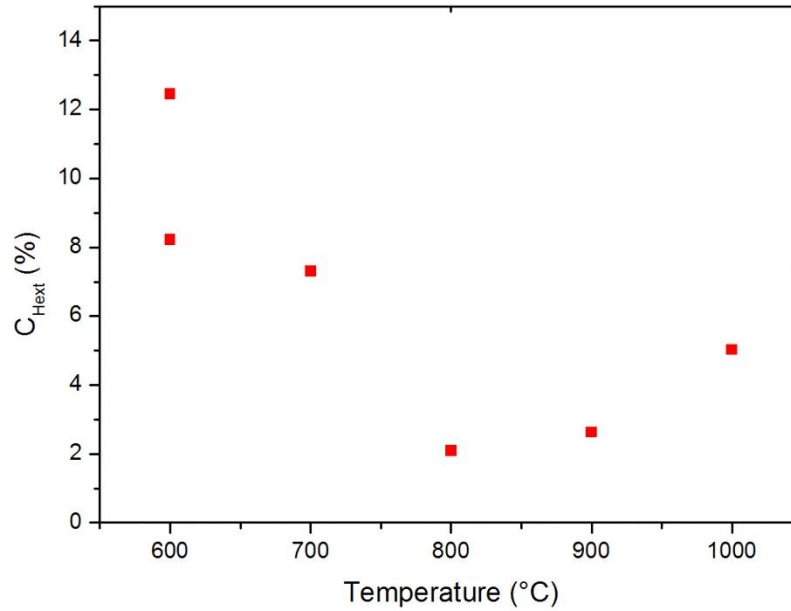
Figure 4.27: Theoretical concentration of hydrogen in the Ta metal.

The (ϑ) values calculated using Eq. (4.9) at different temperatures are plotted in Figure 4.28. The results of the measured hydrogen by hot extraction ($C_{H_{eff}}$) are slightly higher than the estimation of the hydrogen partial pressure in the ambient atmosphere ($C_{H_{ext}}$), as shown in Figure 4.28. In particular, at 800 °C, the local hydrogen partial pressure at the oxide-metal interface is 5 times the estimated H concentration in the metal.

4.3.7 XRD analysis

Powder of tantalum oxidized at 600 °C and 900 °C has been collected and analyzed by means of the XRD technique. The results in Figure 4.29 are mainly showing Ta_2O_5 related reflections. No evidence of sub-oxide was found in this analysis.
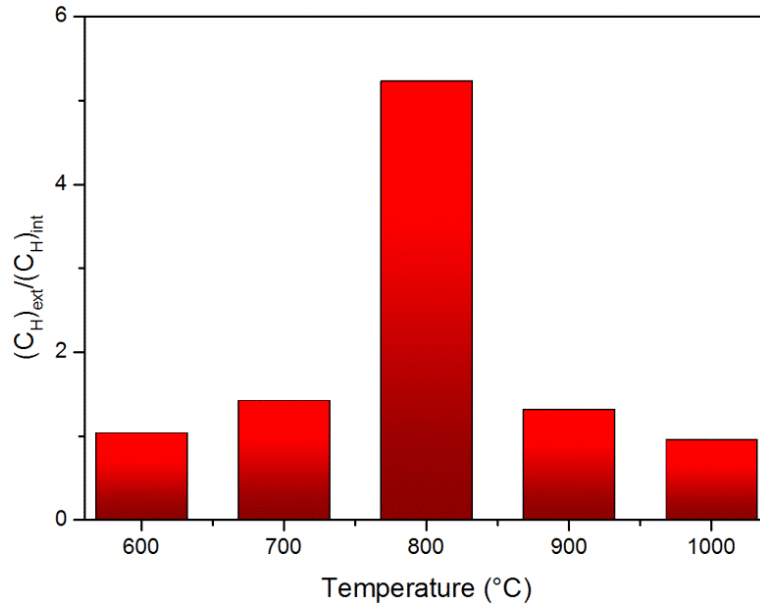
Figure 4.28: Ratio between the hydrogen uptake measured and the value expected from the estimation using ambient P_{H_2} and the Sieverts' law.
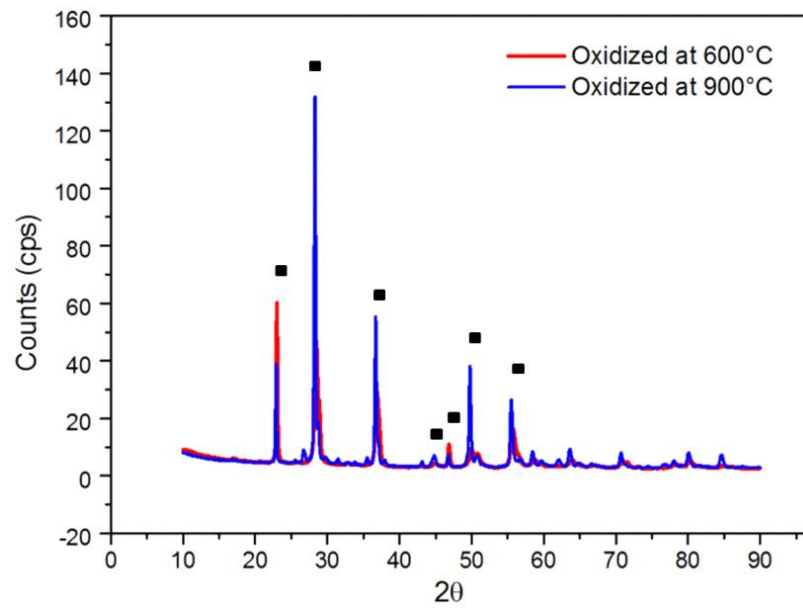
Figure 4.29: of Ta samples oxidized at 600 °C (red curve) and 900 °C (blue curve). The symbol ■ indicates the Ta_2O_5 peaks (Stephenson 1971).

4.4 Discussion

The oxidation experiments show a different behavior of the tantalum depending on the shape of the sample, the temperature and the steam partial pressure. As shown in Figure 4.30, the oxidation of the plates is stronger at the edges of the specimens. Considering that the oxidation is carried on by the oxygen saturation of the most external metal layer, this could justify the strong localized oxidation at the edges of the samples. The edges of the samples saturate faster due to the simultaneous diffusion from the intersecting surfaces, increasing the oxidation rate. The same results were found in the work from Kofstad (1963a). The deformation of the oxide layer can be explained considering that thick scales of alpha tantalum oxide have a tendency to deform due to the build-up stresses in the layer. As already said, the tube-shaped samples have shown different color from the plate samples. This difference can be due to different impurities in the samples' composition. The tests performed in this work have shown that thicker plate samples have higher oxidation rates for each temperature than the cylinder-shaped samples. Only at 1100 °C the tubes oxidized slightly faster than the plates. This could be explained considering that the rounded shape allows the oxide layer being more adherent to the metal surface, and therefore to be more protective.
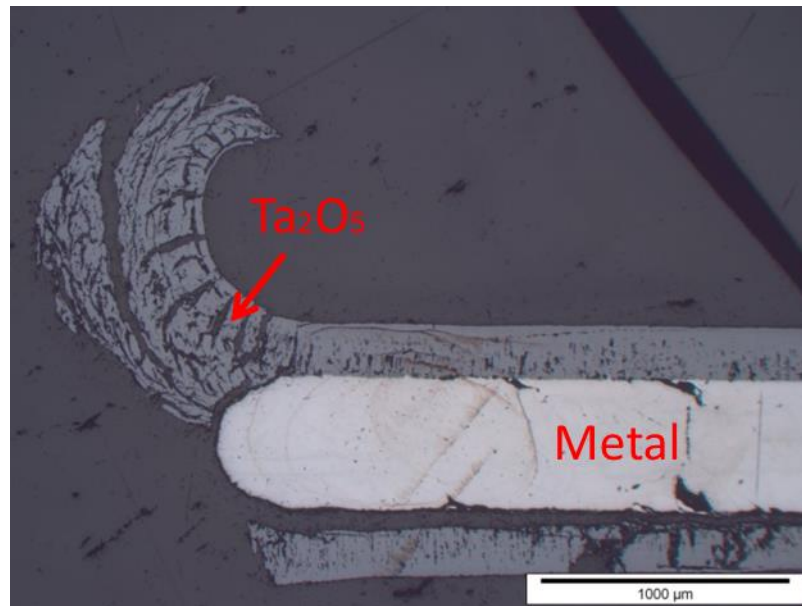
Figure 4.30: Optical microscope cross section of sample p61 oxidized at 1100 °C in 10 kPa steam partial pressure.

The presence of lateral stresses on a non-flat surface could fix the oxide tighter to the surface. The oxide growing on the convex surface develops tensile stresses, whilst compressive stresses are developed in the inner oxide surface. Deformation of the thinner tubes was observed in many experiments, thus relieving the oxide growth stresses (Davis 1997). This stress relief could have somewhat reduced the stress in the oxide, thus developing a more dense scale.

The degradation of the specimens is stronger at lower temperatures, as can be seen in the macrographs and in the optical micrographs of the sections. This can be caused by the morphology of the scale, which turns out to be more sintered and hard at temperature higher than 800 °C. A possible explanation can be found considering that at temperature lower than 800 °C, sub-oxides such as TaO_z develop at the interface of the metal oxide in platelets shape, as already detected in Kofstad's work (Kofstad 1963), leading to crack formation. The cracks generate stronger oxidation of the underlying metal inducing faster breakaway, which is very likely due to the high molar volume ratio between the tantalum and its stable oxide, which is equal to 2.31. This could also elucidate why the linear constants at 600 and 700 °C are comparable to the values measured at 1100 °C, as can be seen in Figure 4.21. At higher temperatures (1000 °C and 1100 °C) the kinetics can be related to the kinetics described by Cowgill (1960). This would indicate that the oxidant species is oxygen also in the case the reaction occurs in steam atmosphere.

The oxide scales not detached on the tube samples were slightly more oxidized on the outer (convex) surface than on the inner surface, as already noted by Stringer (1967). The dilatation of the tubes is higher at low temperatures, which can be seen in the stratification of the oxide scale highlighted at 600 °C and 700 °C. At these temperatures, a breakaway phenomenon occurs after a time period dependent on the steam partial pressure. At high temperatures, oxidation occurs in the metal close to the cracks, as it is shown in Figure 4.31, where two sections of cylindric-shaped samples oxidized at 700 and 1100 °C are presented. Moreover, large tensile fissures, which penetrate in the scale thickness, are observed in the cylindrical samples in correspondence to the cracks (Figure 4.31). At lower temperatures, the oxide scale is poorly adherent and circumferential separation occurs, which can be due to different contraction during cooling.
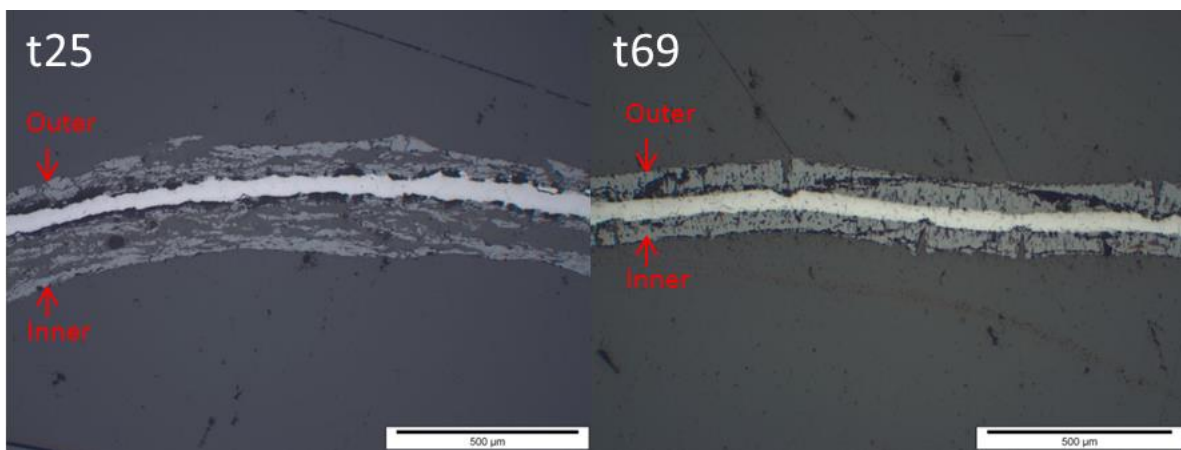
Figure 4.31: Cross section with optical microscope of cylinder-shaped tantalum samples oxidized at 700 °C in 50 kPa steam partial pressure (t25) and at 1100 °C in 100 kPa (t69).

The kinetics was found to be affected by the steam partial pressure. According to Kofstad (1963b), the tantalum oxide exhibits p-type conductivity at the oxygen partial pressures considered in this work, explaining how the oxide growth is dependent of the oxygen partial pressure. As already modeled by Adelsberg, the oxidation can occur in case of steam oxidation, through the incorporation of oxygen in the oxide layer. This is somehow confirmed comparing the oxidation rate measured by Kofstad (1963b), who measured an oxidation rate of at 900 °C $\approx$ 0.1 g/(m²s), whilst in this work the samples p49 and t49, oxidized in pure steam at 900 °C as well, have shown an oxidation rate of 0.06 g/(m²s). This can be an indication that the steam dissociates and the oxygen act as oxidant. The kinetic results have been compared with Adelsberg (1968). The comparison is reasonable since Adelsberg tested sheets of 0.5 cm thickness and 6 mm cylinders with impurities (see Figure 4.32) comparable to our samples.

According to Figure 4.33, the linear constants at 1000 °C have the same order of magnitude, being in our work almost doubled than those in Adelsberg's work. In this work, as well as in Adelsberg's work, oxidation dependence on the steam partial pressure has been noted. The difference can be due to the different treatment that the samples had before the oxidation in Adelsberg's tests, where the coupons were vacuum-annealed for 45 min at 1500 °C and polished before undergoing oxidation. The higher activation energy at higher steam partial pressure can be explained considering the oxygen from the dissociation of water in the metal is the actual oxidizing species.

Table I. Analyses of the Tantalum Used in This Study

Element	20-mil Sheet	40-mil Sheet	$\frac{1}{4}$-in. Rod
Tantalum	99.95 pct min	Balance	99.90 pct min
Oxygen	70 ppm	20 ppm	70 ppm
Carbon	50 ppm	20 ppm	50 ppm
Nitrogen	20 ppm	50 ppm	20 ppm
Hydrogen	–	–	5 ppm
Niobium	<100 ppm	10 ppm	500 ppm
Tungsten	<100 ppm	50 ppm	100 ppm
Silicon	<100 ppm	5 ppm	100 ppm
Titanium	<100 ppm	5 ppm	100 ppm
Zirconium	<100 ppm	5 ppm	100 ppm

Figure 4.32: Impurities of the samples tested by Adelsberg (1968).

As shown in the Ta-O and in the Ta-H phase diagrams (Figure 4.1 and Figure 4.2 respectively), the hydrogen can be absorbed by the metal, whereas the oxygen has comparatively low solubility and therefore diffuses throughout the oxide scale. This could justify the comparable linear rate constant for oxygen and steam oxidation, as already mentioned above in this text.
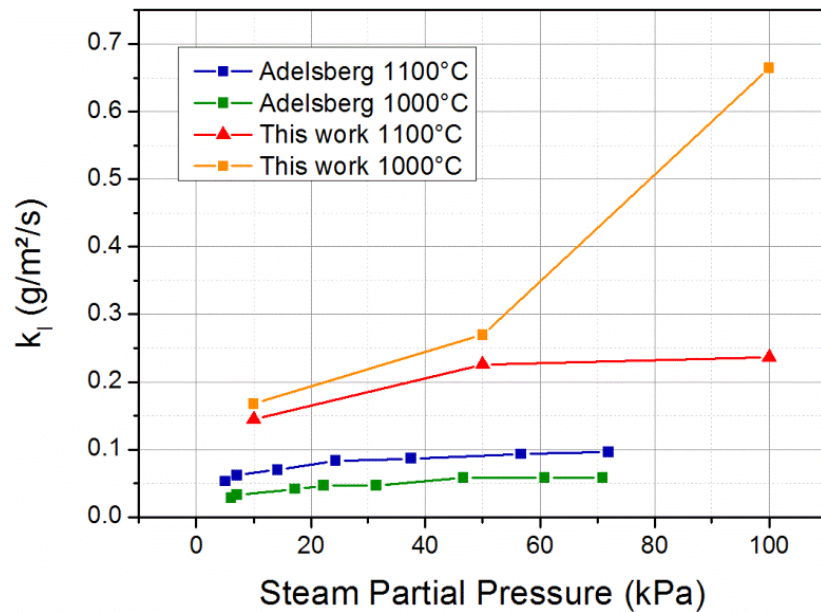
Figure 4.33: Comparison between the linear constants measured for plate-shaped samples at 1000 °C and 1100 °C by Adelsberg (1968) and those measured in this work.

Concerning the hydrogen uptake, as already mentioned in Section 4.3.6, the value should decrease with increasing temperature, which is partially in agreement with our results shown in Figure 4.23. As presented in Figure 4.28, the value of the hydrogen uptake measured is higher than the expected value from the Sieverts' law. This indicates that close to the metal, the hydrogen partial pressure exceeds the value calculated in the ambient considering the H_2 produced and the flow of the career gas. This surplus can be due to a local higher H_2 partial pressure at the interface between the metal and the oxide. This effect has a peak at 800 °C, as it can be noted in Figure 4.28. The oxide structure can explain the highest value at 800 °C: as it was reported in Figure 4.34, at this temperature, the oxide scale is dense enough not falling apart, but presents stratification and longitudinal cracks. Therefore, due to the micro channels generated in the oxide, a "pump effect" (Grosse 2009; Grosse 2010) could locally increase the H_2 partial pressure close to the metal, enhancing the hydrogen uptake. The local hydrogen partial pressure according to the Sieverts' law has been estimated between 170 and 700 Pa, depending on the temperature.
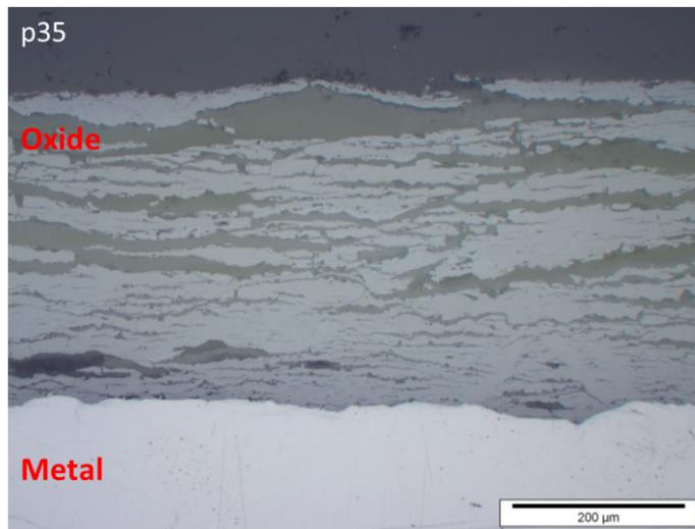
Figure 4.34: Cross section with optical microscope of the Ta plate p35 sample at 800 °C.

4.5 Conclusions of the tantalum oxidation tests in steam

In this chapter, oxidation tests of tantalum in steam atmosphere at temperatures between 600 and 1100 °C are presented and kinetics data are given. The samples showed different behavior depending on the shape: the plates underwent stronger oxidation than the cylinders. Since the coupons oxidized

strongly on the edges, whereas the cylinders developed a denser oxide layer due to the stresses developed on the convex surface, the different form could have played a significant role in the oxidation. Regarding the kinetics, three different stages can be recognized: at 600 and 700 °C, an initial parabolic stage is followed by two different linear stages. While the first parabolic stage follows the Wagner's law, the linear can be correlated to the start of the breakaway, which occurs due to the metastable sub-oxides, which foster cracks' formation. The transition between the first and the second linear regime can be due to the transition between two different sub-oxide, TaO_z to TaO_y.

At 800 and 900 °C the oxidation follows only the linear law. The scale proves to be dense enough not falling apart, probably due to the formation of TaO. However, the oxide presents stratification and longitudinal cracks. This structure supports the hypothesis of the hydrogen absorption due to the pump effect. The linear rate constants are lower than the ones measured at 600 and 700 °C.

At 1000 and 1100 °C the linear oxidation constants have the same order of magnitude as at 600 °C and 700 °C. The oxide scale shows columnar features, and especially at 100 kPa steam, the presence of high porosity can be noted.

Overall, the hydrogen uptake is higher than the theoretical value estimated by means of the Sieverts' law considering the equilibrium with the ambient hydrogen partial pressures. This has been explained considering the "pump effect", which affects the hydrogen concentration especially at 800 °C, due to the characteristic oxide scale.

5. Mechanical performance of SiC multi-layer cladding

In this chapter, the mechanical behavior of silicon carbide composite has been investigated. Monolithic silicon carbide presents a brittle behavior, and therefore the use as fuel-cladding is not recommended. Coupling SiC monolith with fibers improves the mechanical performance leading to the so-called pseudo-ductile behavior. However, an accurate analysis of the stresses occurring in particular cases along the SiC carbide thickness is of high priority in order to allow evaluating the feasibility of such a cladding design. In this work, the stresses in each layer of the SiC cladding are evaluated using finite element analysis (FEA) during both steady state operation as well as transient scenarios, such as a LOCA accident. In LOCA, thermal and pressure shocks caused by the coolant blowdown and subsequent reflood could cause high thermal stresses, which may lead to cracking of the SiC structure. FEA can be employed to deduce the stress response in the case of accident conditions. The magnitude of tensile stresses is the key indicator of the probability of failure in a three-layer SiC cladding type. In previous works by ORNL (Ben-Belgacem 2014), the single-layer stress under steady-state conditions was calculated. However, this is not sufficient to draw any conclusions on the multilayer performance of SiC under steady and transient conditions. Another study conducted at MIT modeled the stress in three layers under steady and quasi-steady transient conditions (Lee 2013; Shirvan 2014; Lee 2015;) but neglected the accident conditions. In this chapter, the detailed sensitivity of the fully thermally-mechanically coupled 2D steady state and axisymmetric Large Break LOCA (LB-LOCA) has been simulated, including tracking of the quench front in water. This work also accounts for the effect of pre-stressing of the cladding on the SiC transient response for possible improvements of its mechanical performance. The properties of the SiC material, such as thermal expansion, swelling, and thermal conductivity play a crucial role in the calculation of thermal stresses, as well as of stresses due to the

pressure difference between the inner and outer cladding surfaces. Hence, simulations with temperature dependence of these properties have been performed. The analysis has been carried out using the commercial finite element software ADINA (Bathe 2000).

Experimental work reproducing the quench procedure was also performed and results are presented in Chapter 6. The stresses occurring during the experiments were calculated by means of the FEA analysis.

5.1 Description of the model and the material properties used

A 2D R-Z model was drawn up in order to simulate the three-layer SiC cladding, with the typical PWR cladding thickness of 0.57 mm, an outer diameter of 95 mm and a thickness ratio among the three layers of 4.5/4.5/1 (Figure 5.1). The simulation modeled a length of 2 cm as was sufficient to avoid appreciable end effects on the mid-section and avoid unnecessary computational expenses, which would have arisen in case the entire clad length was modeled. Due to axi-symmetry, only a 2D segment instead of the 3D tube was modeled. This may be an important approximation depending on the manufacturing techniques used for the composite layer. For this work, only the stress in the axial center of the model is reported, and stresses at the ends of the tube are not considered since only 2 cm of the 360 cm long cladding is simulated. The monolithic inner part is held fixed in the y direction (in ADINA, a so-called fixity condition was applied). This model has been previously validated against analytical calculations performed in a work at MIT (Lee 2013). The geometry was analyzed imposing proper boundary conditions, which are discussed in the following sections. It is noted that this work does not predict pellets to clad hard contact throughout the life of SiC cladding design during operation, since the presence of fuel was neglected in this analysis.

Particular attention was paid to the material properties. Some of these properties, such as the thermal expansion coefficient and swelling dependence on temperature, have a significant role in the stress development along the cladding thickness, as shown in the literature (Ben-Belgacem 2014; Lee 2015). The temperature and dose dependence of conductivity and swelling were accurately incorporated into the model.
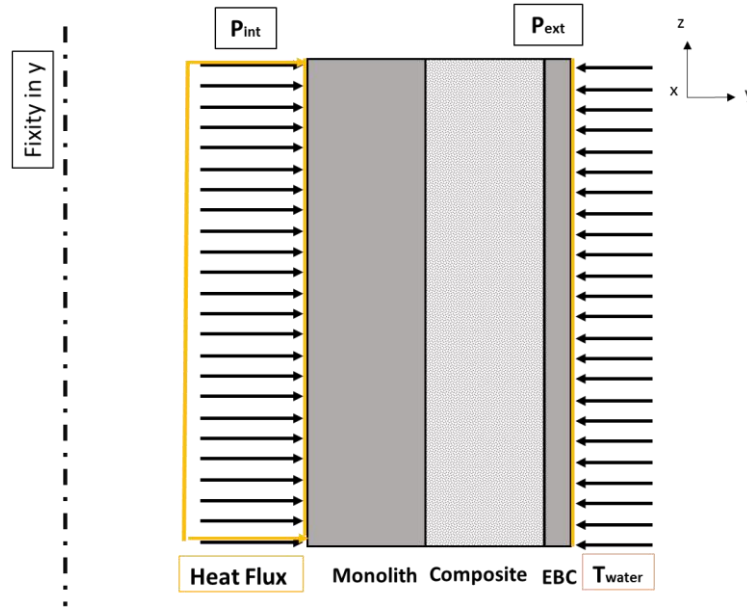
Figure 5.1: ADINA model forcladding section analysis, including loads and fixities.

In the following sections, the materials properties used to model the silicon carbide cladding are discussed. The density, the Young's modulus and the Poisson's ratio are regarded isotropic and constant during the simulation (Table 5.1). After significant neutron dose, a modest reduction of the Young's modulus for the CVD has been observed, whilst for the composite was insignificant (Katoh 2010; Katoh 2011). Therefore, this dependence was not taken into account in the simulations here reported. The thermal conductivity, the thermal expansion and the swelling are considered time and temperature dependent and are explained in the next sections. Unlike monolith, the composite fibers exhibit pseudo-ductility as experimentally shown by Katoh (2007). However, this pseudo-ductility is ignored in this work and all material is assumed to be elastic. This has been shown to be conservative for three-layer geometry by Shirvan and Kazimi, 2014 (Shirvan 2014) and have small impact on the stress distribution.

Table 5.1: Material properties used in the model.

Material property	Monolithic	Composite
Young's Modulus (Pa) (Snead 2007)	$4.60 \cdot 10^{11}$	$2.3 \cdot 10^{11}$
Poisson's ratio (Snead 2007; Nozawa 2012)	0.21	0.13
Density (mg/cm^3)	3200	2000

5.1.1 Thermal conductivity

The thermal conductivity (k_p) of the cladding strongly affects the fuel temperature: higher thermal conductivity reduces both the fuel temperature and the average cladding temperature. In the silicon carbide the electron-phonon transport is the dominant heat transmission mechanism due to the lack of conductive shells. This phenomenon depends on the following variables:

- Temperature: at operational and accident temperatures the thermal conductivity decreases with temperature
- Grain size effect: becomes negligible with increasing temperature
- Nature of grain boundaries: impurities reduce the thermal conductivity.

From these considerations, it can be deduced that a single crystal has a high k_p while the k_p drops down for hot-pressed materials. Indeed, impurities, micro-pores, departure form stoichiometry or multiplication of grains and grains boundaries, considerably reduce the thermal conductivity of the non-irradiated perfect crystal. Very pure materials, such as CVD, have a thermal conductivity very close to that of the single crystal, which can be modeled above 300 K and prior to irradiation by Eq. (5.1) (Snead 2007).

$$k_p = (-0.0003 + 1.05 \times 10^{-5}T)^{-1} \left(\frac{W}{K \cdot m}\right) \tag{5.1}$$

In nuclear applications, neutron irradiation induces defects in the material, producing scattering of phonons. Thus, the conductivity decreases until saturation is reached, which occurs after only few dpas.

Once the saturation dose is reached, the temperature dependence is reduced. Near-stoichiometric composition, as for example in β-phase SiC fibers, are considered to behave similar to high-purity CVD SiC. Conventional non-stoichiometric SiC-based fibers undergo volume contraction (Katoh 2014). The effect of irradiation was described by the defect thermal resistivity model proposed in the work by Snead (2007). The dependence of the hoop stress developed in the cladding upon different thermal conductivity (Table 5.2) under a heat flux of 684.6 kW/m² is presented in Figure 5.2. From Figure 5.2 it can be stated that the decrease in the thermal conductivity of CVD SiC leads to the increase in the hoop and radial stresses in each layer.

Table 5.2: Thermal conductivity of SiC used for stress calculation.

	Initial value	Intermediate value	Low value
Thermal conductivity (W/(K · m))	10	6	4
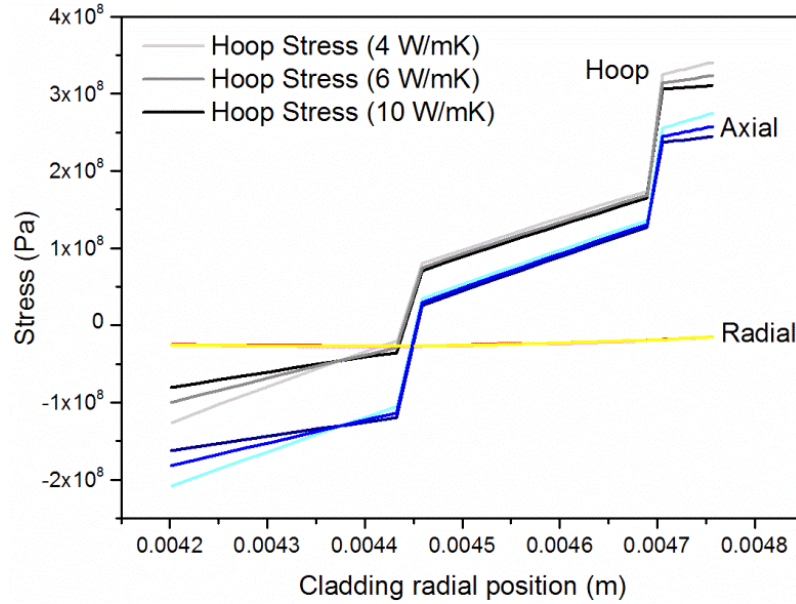
Figure 5.2: Sensitivity of hoop stress to thermal conductivity (4, 6, 10 W/(K · m)) with a heat flux of 684.6 kW/m² and an inner pressure of 25 MPa. The line colors become darker for higher thermal conductivity.

Considering the hoop and the axial stresses, the inner stress shows an increase of about 50 MPa, the composite stress is only slightly increased while the external EBC has an increment of 40 MPa. The difference between the stresses developed in the inner monolith and in the composite decreases with the increase in thermal conductivity. The inner monolith experiences the higher temperature values and gradients with lower thermal conductivity, resulting in a larger "push back" by the composite layer and therefore higher compressive stress. On the other hand, since there is no outer layer to provide a push back for the EBC, higher tensile stress is experienced with decreasing thermal conductivity.

5.1.2 Thermal expansion and swelling

One of the material properties related to thermal stresses is the thermal expansion. This property results from the interatomic spacing between the atoms of SiC, which is a function of temperature.

Thermal expansion is usually calculated to be linear with the thermal expansion coefficient. Two kinds of thermal expansions coefficients are generally considered: the linear thermal expansion coefficient (α), and the volumetric thermal expansion coefficient (β). The linear (α) is defined as the fractional change in length per unit change in temperature, while the stress on the material is kept constant, as shown in Eq. (5.2). The volumetric thermal expansion coefficient is defined as the fractional change in volume per unit change in temperature while the pressure is constant on the whole body, as shown in Eq. (5.3) (Barron 2012).

$$\alpha = \frac{1}{L}\left(\frac{\partial L}{\partial T}\right)_\sigma \tag{5.2}$$

$$\beta = \frac{1}{V}\left(\frac{\partial V}{\partial T}\right)_\sigma \tag{5.3}$$

These values are measured under zero applied stress conditions. The thermal expansion minimum value of zero is registered at the ground level temperature (0 K), and increases with temperature. This property is dependent on the material crystal structure: it exhibits anisotropic behavior for the hexagonal crystal. Evaluation of thermal expansion and swelling by means of experimental work for the CVD and composite material has been documented in the literature. For the CVD SiC, the thermal expansion can be expressed as a third-order polynomial (Snead 2007).

Considering the SiC/SiC composite, the thermal expansion has been measured for two different fiber designs: HNLS and SA3. The results have shown that these samples exhibited the same behavior as the CVD material (Katoh 2014). Eq. (5.4) was used in this work to calculate the thermal expansion, where T is the temperature (Snead 2007) in K. This expression is valid for the range of temperature between 125 K and 1273 K.

$$\alpha = -1.8276 + 0.0178\,T - 1.5544 \times 10^{-5}T^2 + 4.5246 \times 10^{-9}T^3 \left(\frac{10^{-6}}{K}\right) \tag{5.4}$$

Under irradiation, a second phenomenon occurs: the buildup of Frenkel defects in the lattice depending on the temperature yields to the swelling of the material. The silicon carbide swelling is temperature dependent until reaching a saturation point: increasing the temperature, the saturation point decreases. In this work, the swelling was considered at its saturation value. Experimental results in the

literature usually account for the swelling as volumetric percentage. From these values, the linear coefficient ϵ_l, which accounts for the longitudinal expansion, has been calculated considering the silicon carbide as an isotropic material, as shown experimentally by Katoh (2002), using Eq. (5.5)

$$\epsilon_v = 3\epsilon_l \tag{5.5}$$

where ϵ_l and ϵ_v are the linear coefficient and the volumetric swelling, respectively. The swelling for the CVD-SiC can be extracted from experimental work from Katoh (2002) and Newsome (2007) in the temperature ranges of 573-1173 K. From these data, saturation of swelling occurs within 0.1-1 dpa depending on the temperature. The experimental values were fitted into Eq. (5.6), where T is in K.

$$\epsilon_{mon}^{sw} = 0.07 - 1.2 \cdot 10^{-4}\, T + 5.4 \cdot 10^{-8} \cdot T^2 \tag{5.6}$$

Regarding the SiC-SiC composite, swelling values are scarce in the literature. Moreover, the addition of sintering agents in SiC (such as boron, yttrium or aluminum) has shown to impact the magnitude of induced-irradiation swelling (Koyanagi 2011). In this work, the author proposes a sensitivity analysis to assess the influence of the swelling. The values calculated for the monolith layers have been empirically changed, resulting in a modified first term constant value in Eq. (5.6), similarly as already done in the literature (Lee 2015).

$$\epsilon_{comp}^{sw} = 0.06 - 1.2 \cdot 10^{-4}\, T + 5.4 \cdot 10^{-8}\, T^2 \tag{5.7}$$

In order to include the swelling influence in the ADINA finite element code, the swelling has been assimilated with the thermal expansion. The thermal expansion coefficient measures the difference of the length of a specimen at an assumed reference temperature (T_{ref}) and the length of the specimen at the temperature T. Therefore, a simple form for the thermal strain in case the material is isotropic is given by Eq. (5.8).

$$\epsilon = \bar{\alpha}_{(T_{ref}, T)}(T - T_{ref}) \tag{5.8}$$

The $\bar{\alpha}_{(T_{ref}, T)}$ can be expressed as in Eq. (5.9) (Niffenegger 2012), where L is the length of the specimen at the specified temperature:

$$\bar{\alpha}_{(T_{ref}, T)} = \frac{\left(L_{(T)} - L_{(T_{ref})}\right)}{L_{(T_{ref})}\,(T - T_{(ref)})} \tag{5.9}$$

The thermal expansion coefficient and the derived swelling coefficient were summed and then incorporated in the total expansion coefficient (CTE), as shown in Eq. (5.10), in order to have a description of the material behavior after irradiation.

$$CTE = \frac{\left[(T - T_{ref})\alpha^{th} + \frac{\epsilon^{sw}}{3}\right]}{T - T_{ref}} \tag{5.10}$$

In Eq. (5.10) the superscript [th] indicates the thermal expansion while the [sw] indicates the expansion due to the irradiation swelling phenomenon. As already explained, the swelling is dose dependent below a saturation point, which usually occurs after 1 dpa[6]. The swelling values used in this analysis were taken from the literature. The experimental data are for an irradiation damage higher than 1 dpa, therefore, the analysis in this work was carried out for the case that swelling saturation occurs, this being also the limiting condition. During LOCA, the reactor fission reaction is assumed to be shutdown due to a SCRAM upon initiation of the transient. Therefore, the irradiation swelling strain during steady-state operation is preserved even though the cladding undergoes large temperature changes during LOCA.

In order to simulate this residual swelling strain in ADINA, swelling strains based on the average temperature experienced by the cladding are assigned to each layer. Since high temperature gradients exist in both the inner monolith and composite layer during operation, in order to accurately capture the dependence of swelling on the temperature, each layer is divided into three sections. Each section is characterized by discrete values of swelling strain based on the steady state average cladding radial temperature distribution in that section. This allows a more accurate simulation of the gradient of the swelling in the layers and at the same time preserves the residual strains induced by irradiation swelling during LOCA. In Table 5.3, the swelling values considered in the calculation are shown.

Combining the swelling values shown in Table 5.3 and the thermal expansion coefficient calculated as in Eq. (5.6), the total thermal expansion coefficient (CTE) values were calculated using Eq. (5.10).

---

[6] Considering a value of 10^{-7} dpa/s (Rosinski 2001) 1 dpa occurs after 115 days.

Table 5.3: Swelling values considered for each SiC cladding layer for the EOL and BOL cases.

Layer	Temperature (K) (EOL)	Swelling (EOL)	Temperature (K) (BOL)	Swelling (BOL)
Inner Monolith	726	0.0135	827	0.0101
Monolith	722	0.0137	818	0.0104
Outer Monolith	717	0.014	807	0.0107
Inner Composite	702	0.0082	775	0.0055
Composite	676	0.0093	721	0.0074
Outer Composite	650	0.0105	666	0.0098
EBC	635	0.0175	636	0.0175

The values in Table 5.3 assume a reference temperature of 560 K, since the reactor operates at about this temperature at hot zero power condition before heat generation increases to its design value.

The same calculation was run considering two other reference temperatures (300 K and 1200 K). The motivation behind assuming different reference temperatures arises from the possibility of existence of prestresses from the manufacturing process of the multi-layer cladding.

5.1.3. Stress at failure

Silicon carbide, due to its ceramic nature which enhances its brittle behavior, undergoes fracture-dominant failure. Statistical models, such as the Weibull model, are usually employed to describe the strength of silicon carbide. In this model, the probability of failure considering a uniform stress is given by Eq. (5.11).

$$P_f(\sigma) = 1 - \exp\left(-\left(\frac{\sigma - \sigma_c}{\sigma_o}\right)^m \frac{V}{V_o}\right) \tag{5.11}$$

Neglecting the stress below which no failure occurs ($\sigma_c = 0$), and considering the volume normalized (V=Vo) for simplicity, the equation reduces to:

$$P_f(\sigma) = 1 - \exp\left(-\left(\frac{\sigma}{\sigma_o}\right)^m\right) \tag{5.12}$$

where the parameter m is the Weibull modulus, σ_o the characteristic stress, V is the volume of the specimen, V_o the reference volume; m and σ_o are obtained by fitting experimental data.

In order to apply this model to the material and calculate the ultimate tensile strength (UTS), mainly two sets of data are necessary:

- The stress field

- The statistical parameters for the material, which need to be obtained experimentally.

In this work, values of the stress field have been predicted by finite element analysis, employing the ADINA code. Regarding the statistical parameters, data already published in the literature have been used. It is noted that the data in the literature are applicable to a certain volume and material quality (e.g., crack distribution). When SiC cladding is considered deployable, it is the author's expectation that the statistical parameters will be improved due to high quality assurance requirements of nuclear fuel. The probabilistic model can be applied both to the CVD monolith and to the composite. A recent work by Kim (2015) investigated the fracture behavior of the SiC triplex tube and concluded that the average ultimate hoop strength is 282.4 MPa with a Weibull modulus of 11.05. The CVD and composite layers can be also studied separately. The fracture strength for the CVD has been investigated in different studies in the literature and summarized in a paper by Snead (2007). For the current work, values derived from tubes loaded with internal pressure, and for a neutron dose equal to 1.9 dpa were used, which correspond to the characteristic strength of 369 MPa and a Weibull modulus of 4.4.

The analysis of the fiber-reinforced matrix failure can be divided into two steps. First, micro-cracks develop in the matrix, which turn into macro-cracks resulting in a shift in load onto the fibers. Under such circumstances, dispersed fracture replaces the ultimate failure. CVD and CVI matrix along with Hi-Nicalon™ Type-S and Tyranno™-SA3 SiC fibers have been investigated by ORNL (Katoh 2010). Experimental results lead to the following parameters: Weibull characteristic strength 290 MPa with a Weibull modulus of 17.5.

For a brittle solid material, an acceptable risk, which is the failure probability, can be assigned. The calculated failure probability shown in Figure 5.3 reveals that an applied stress of 200 MPa has a failure probability of 15% in the composite layer considering the Weibull parameters already addressed.
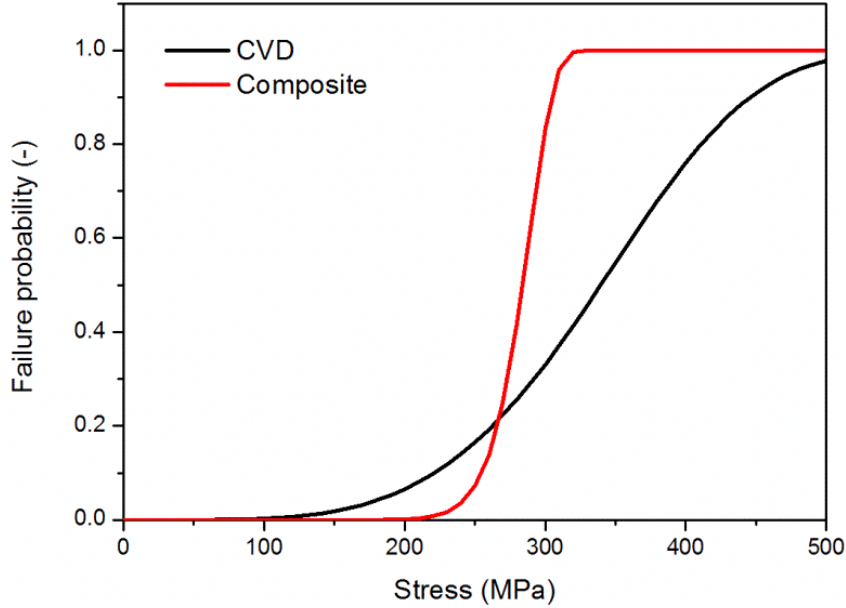
Figure 5.3: Failure probability of CVD with a Weibull characteristic strength of 369 MPa with Weibull modulus of 4.4 (black curve) and composite with a Weibull characteristic strength of 290 MPa with Weibull modulus of 17.5 (red curve).

Evaluation of the feasibility of the silicon carbide cladding requires a comparison between calculations and experimental data, in order to assess the cladding performance in case the of stress development. For this reason, tests have been performed in the literature (Carpenter 2010; Stempien 2011; CTP 2014) in order to evaluate the inner pressure which leads to the cladding failure. In these experiments, SiC tubes were loaded with an internal rubber plug, considered to be linearly elastic, homogeneous, and isotropic in order to treat it as an incompressible fluid. The plug was compressed with a measured force, which resulted in a pressure being applied to the internal cladding.

The compressive axial stress induced by the friction between the plug and the tube was considered negligible. The boundary conditions for the simulation are presented in Table 5.4. The pressure at failure was calculated considering the maximal force divided by the plug area. The hoop stress failure was calculated considering the Eq. (5.13) for a thick cylinder.

$$\sigma_\theta = \frac{r_i^2 P}{r_o^2 - r_i^2}\left(1 + \frac{r_o^2}{r_i^2}\right) \tag{5.13}$$

Table 5.4: Boundary conditions for experimental comparison.

Boundary conditions	
External pressure (Pa)	$1.0 \cdot 10^5$
Internal pressure (Pa)	$4.1 \cdot 10^6$
Environmental Temperature (°C)	22
Distributed heat flux (W/m²)	-

The internal pressure at failure P, was considered in an ADINA simulation in order to calculate the peak stress under these conditions, neglecting friction force between the plug and the sample.

The temperature load was not applied in this simulation; hence, the case was run without the use of thermal analysis in ADINA. The results are shown in Figure 5.4. The hoop stress in the inner monolith is between 235 and 292 MPa, which corresponds to the highest calculated values along the cladding thickness. Therefore, it is reasonable to assume that cracks start in the monolith layer and propagate in the rest of the sample. The stress in the composite material is ≈120 MPa for 41 MPa inner pressures and ≈160 MPa for 51 MPa, much lower than in the monolith. These specimens experienced hoop strength slightly less than 300 MPa, which corresponds to a 33% probability for a standard monolith layer to fail, considering the probability analysis shown in Figure 5.3.
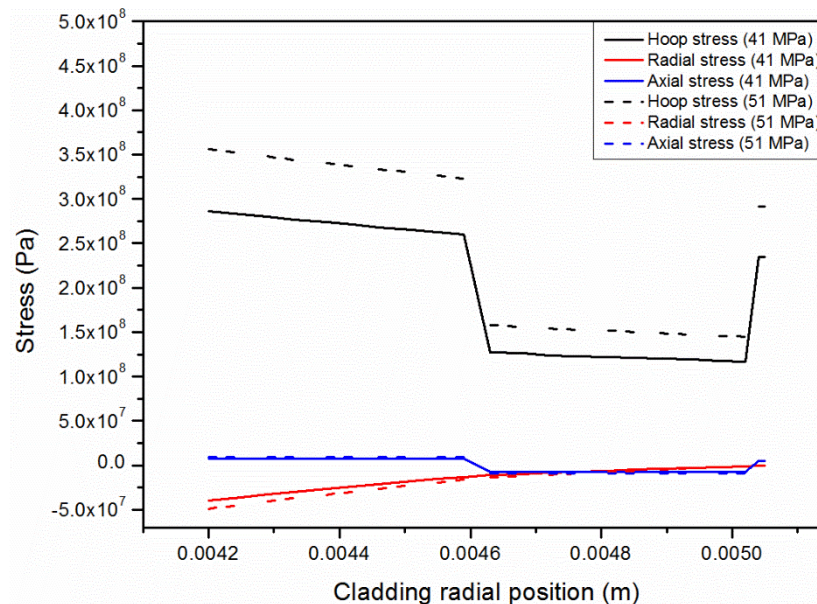
Figure 5.4: Stress results using internal failure pressure by Stempien (2011).

In the following sections, the stress field calculated by the FEA will generate failure probability values by means of this model. As a term of comparison, in the current cladding design, the failure rate is lower than 10^{-5} when considering all fuel rods in the operating US reactors. In this analysis, it is worth to take into account that the wide range of fracture strengths reported in the literature affects the results, which are very sensitive to the experimental parameters used. Hence, this large scatter has to be considered and further experiments are required to predict the failure probability with much higher accuracy and precision.

5.1.4 Boundary conditions used for the calculations

During steady-state operation, the SiC cladding experiences a total stress arising from internal and external pressure and temperature gradients. These were set as boundary conditions for the geometry represented in Figure 5.1. The material properties considered include the thermal expansion coefficient with the addition of irradiation-induced swelling, the thermal conductivity, and the heat capacity.

The thermal conductivity saturates quickly after 1 dpa of irradiation damage (Barron 2012). Therefore, the thermal conductivity after 1 dpa is used for this work. In a time-dependent study, this may lead to overrate the thermal stresses at the beginning of life, but only for a short while, whereas the mechanical stresses are generally compressive due to the excess outer pressure.

The specific heat can be approximately expressed between 200-2400 K, according to the expression presented in the work by Snead (2007) for nuclear-grade CVI SiC/SiC. Since the heat capacity is very similar to CVD (Katoh 2014) the same correlation was used in this analysis.

The nominal heat flux of a PWR, rated at 3.8 GW$_{th}$ with 193 assemblies of 17x17 pins (25 control rods) with each active fuel pin being 3.65 m long and an outer cladding diameter of 0.0095 m, is calculated as 684.6 kW/m^2 (Cladding outside heat flux). During in-core residence of the SiC cladding, different operating conditions are experienced by each pin. Thus, the stress level in the cladding changes mainly because of fuel rod pressurization over time and local power level changes. Hence, three different cases were investigated as summarized in Table 5.5. The peaking factor of 1.55 is used to increase this nominal average heat flux at the Beginning of Life (BOL), whereas 0.75 peaking factor is used at the End Of Life (EOL).

In all the cases, for steady state operation, an outer cladding temperature of 623 K was prescribed. As listed in Table 5.5, it is assumed that the BOL case has an initial pressure of 5 MPa to represent the initial fill gas pressure, which increases with time. The pressure increase at end of life is mainly due to the release of fission gases. The inner rod pressure is commonly designed to reach around 14 MPa at the EOL for common PWRs in order to maintain the cladding in compression (15.5 MPa coolant pressure). Here, the EOL pressure was assigned to 25 MPa due to the fact that the fuel temperature with SiC cladding would be much higher than the actual fuel temperature. This is due to two reasons: first the SiC thermal conductivity is lowered by the irradiation; second, the fuel-clad gap is not expected to close during the fuel cycle, increasing the resistance between the fuel and the coolant. At shutdown, residual power (decay heat) maintains a heat flux of 4% of its original value. As the fuel temperature significantly drops, the plenum pressure drops as well. Thus, no additional mechanical constraint was assumed under shutdown conditions.

The simulation of the SiC cladding stress distributions during LB-LOCA requires reactor system thermal hydraulic response during the accident. Specifically, system pressure, bulk coolant temperature, and heat transfer coefficient are the required inputs for the prediction of the SiC cladding stress and fracture analysis models. The RELAP5-3D developed by Idaho National Lab (INL 2005) for the transient simulation of LWR systems during postulated accidents was used to provide such boundary conditions.

The swelling was considered always at saturation conditions. Based on these premise, the hoop (σ_θ), radial (σ_r) and axial (σ_z) stresses were calculated considering the boundary conditions and material properties previously discussed.

Table 5.5: Simulation conditions for SiC cladding stress calculation.

Time in the core	Hot pin peaking factor	Heat flux (MW/m²)	Pin plenum pressure (MPa)
Beginning of life	1.55	1.06	5
End of life	0.75	0.51	25
Conservative	1.55	1.06	25

Particular attention should be paid to the magnitude of tensile stresses. Indeed, for the monolith SiC material, the strength under tensile stress is several times lower than under compression, due to the lower microstructure resistance to crack propagation (Ashby 2005). In the literature, the uniaxial compressive failure stress of SiC has been measured being between -4 GPa to -7 GPa (Forquin 2003; Sarva 2001).

5.2 FEA simulations in operation conditions

In this chapter, the calculations made using the swelling from Eqs. (5.6) and (5.7) are presented. Once the swelling was calculated, it was added to the thermal expansion according to Eq. (5.10). The composite and the inner monolith layer were discretized into three sections in the radial direction.

As discussed in Section 5.1.2, an average swelling value based on the steady state temperature distribution was assigned to each section while 10 finite element meshes were used within each section to achieve the desired accuracy. The results of the calculations under steady conditions are shown in Figure 5.5 for the limiting stress (hoop stress). In order to confirm that the division of the cladding to only 7 sections is valid, a second method to include the swelling was also tested. This strategy consists of using a continuous swelling value calculated using Eqs. (5.6) and (5.7) (Figure 5.5b).

The validity of the first method is confirmed as the two calculations (average swelling and continuous swelling) show comparable results, as presented in Figure 5.5a and Figure 5.5b during static conditions.

During LOCA events, the radiation turns off and the strain from the irradiation swelling remains according to the irradiation temperature. Therefore, having an average swelling depending on the irradiation temperatures is required for the LOCA simulations and the more accurate second method is not valid during the simulated transient. In Figure 5.5a, the stresses present discontinuity points in the composite and in the monolith layers, due to the different swellings considered in each sub-layer.
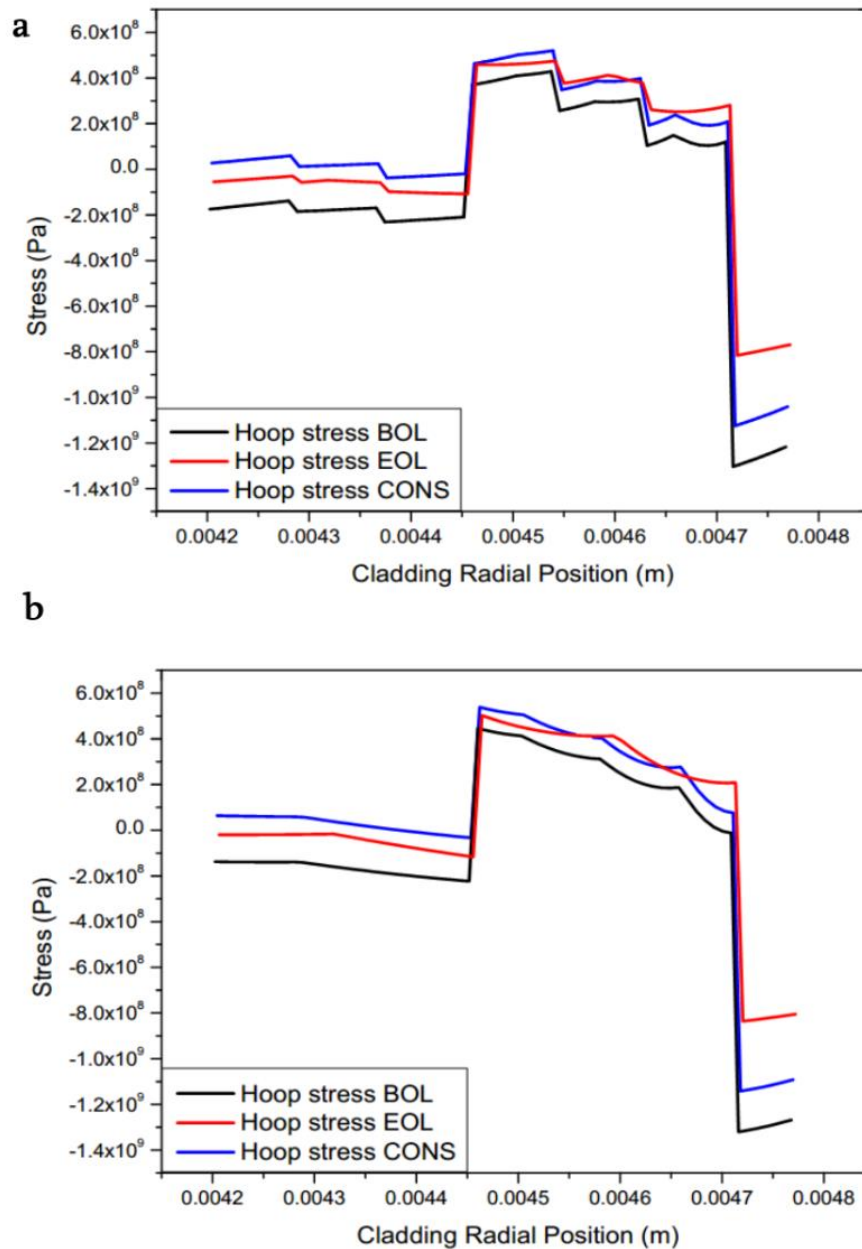
Figure 5.5: Hoop stress for different instants in lifetime considering Tref 560 K, (a) considering the swelling dependent only on the irradiation temperature (b) considering the swelling dependent on the temperature during the simulation.

In Table 5.6 the extreme values of the stress in different simulated cases are presented. The hoop stress in the monolith is compressive at BOL and turns into tensile up to 63 MPa under the conservative

conditions. The composite undergoes more severe stresses, reaching 490 MPa at the end of life. The EBC experiences strong compressive stresses in each case. The same calculations were performed considering different reference temperatures for both the composite and for the CVD (300 K and 1200 K). The results shown in Figure 5.6 show values comparable to the results obtained at 560 K, implying an insensitive performance to the assumed reference temperature.

Compressive prestresses in the monolith layer (and in the composite) are one possible way of preventing tensile stress. The application of prestresses involves placing the material under a residual compressive stress. Thus, as long as the ceramic is prestressed in compression, the probability of failure due to tension is zero. The prestresses could be physically applied during manufacturing, perhaps upon winding of the fibers around the inner monolith and while weaving the fibers themselves to form the composite, depending on the winding orientation. The calculations of the stress field under accident conditions were performed with the reference temperature of 560 K in the conservative case, which is the most conservative among the three cases analyzed.

Table 5.6: Hoop stress results shown in Figure 5.5 in steady state.

Hoop Stress	Monolith		Composite		EBC	
BOL (MPa)	-117	-231	103	428	-1270	-1316
EOL (MPa)	-108	-30	467	252	-810	-769
Conservative (MPa)	59	-37	514	192	-1164	-1050
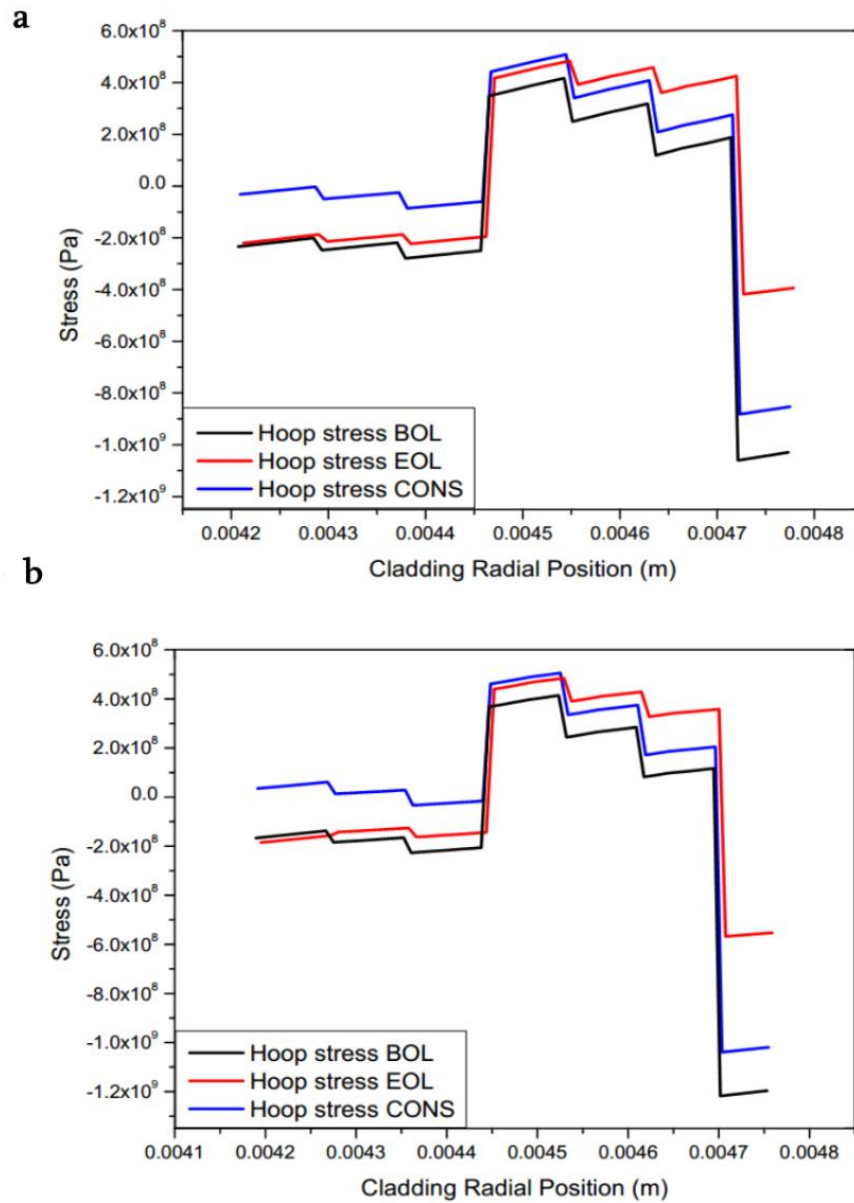
Figure 5.6: Hoop stress for different instants in lifetime considering the swelling dependent only on the irradiation temperature for (a) Tref 300 K, (b) Tref 1200 K.

5.3 Stress calculations during blowdown and reflood in LOCA accident

The simulation of the SiC cladding stress distributions during LB-LOCA requires defining the reactor system thermal hydraulic conditions during the accident. Specifically, the system pressure, bulk

coolant temperature, and heat transfer coefficient at the fuel surface are the required inputs for the SiC cladding stress and fracture analysis models. RELAP-3D was used for this purpose, which is widely used in safety assessment for transient simulation of LWR coolant systems during postulated accidents. The boundary conditions of pressure and steam temperature of a PWR during LB-LOCA were calculated with RELAP 5. The upper portion of the fuel was considered (z=2.49 m). The power level decays quickly as a function of time during LOCA (Figure 5.7). Figure 5.8 shows the cladding temperature and coolant pressure as a function of time. The transient, which simulates the blowdown in a LOCA accident, starts from the steady state solution for the conservative case. Three time functions were created to represent the LB-LOCA case: change of power, external pressure, and external temperature. The time was discretized with a finite time step $\Delta t = 0.1$ s, as shown in Eq. (5.14).

$$t_{tot} = \Delta t \cdot n_t \qquad (5.14)$$

where n_t is the number of steps (i.e., 1600). Considering these inputs, the restart has been done from the static condition presented in Figure 5.5a.
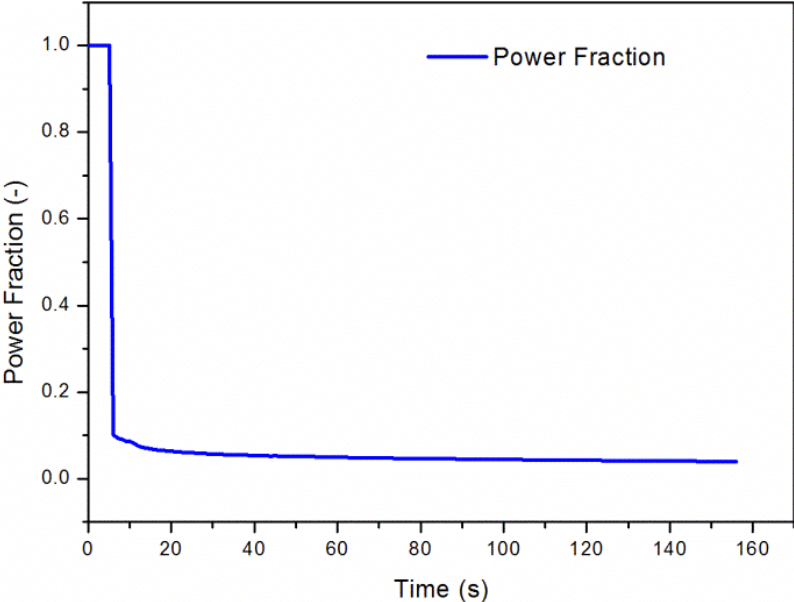
Figure 5.7: Calculated power fraction during LOCA.

146
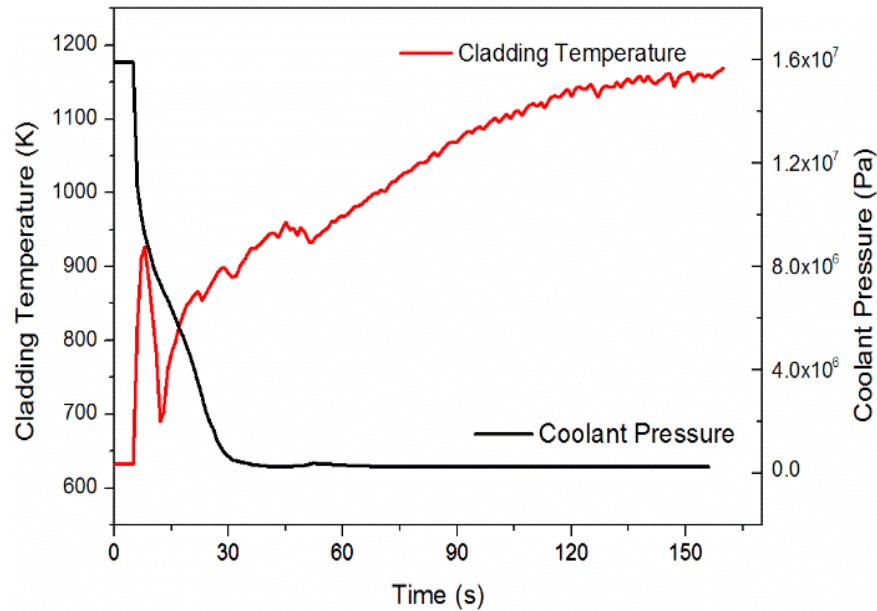
Figure 5.8: Calculated cladding outer temperature and outer pressure during LOCA.

In Figure 5.9, the hoop stresses are presented as a function of time and cladding radial position. The sharp decrease of the external pressure and the increase of the temperature cause an abrupt increase of each stress in the three layers during the first 20 seconds. In particular, the temperature influence can be noted in the small peak in the composite layer, which occurs after about 10 seconds, corresponding to the peak in the temperature profile. The drop of the pressure leads to a hoop tensile stress (340 MPa) in the inner monolith, which is the maximum value reached. After 50 seconds, the loadings are almost stable, due to the low power and the outside pressure stabilization. Indeed, after 50 seconds, the external clad temperature increases from 900 K to 1150 K, eventually causing the change of the stresses during the overall simulation time. The stresses at the start and at the end of each layer during LOCA blowdown are summarized in Table 5.7. The calculated stresses are within reason: the hoop stress in the monolith is the limiting stress, which is up to 340 MPa. In the composite, the σ_θ has the highest tensile value (560 MPa). In the EBC, the hoop stresses, as well as the axial stress, are highly compressive, as high as 1.3 GPa. The radial stress during LB-LOCA remains somewhat insensitive to these external conditions, and does not present concerns since the σ_r remains between -26 and 13 MPa.

147
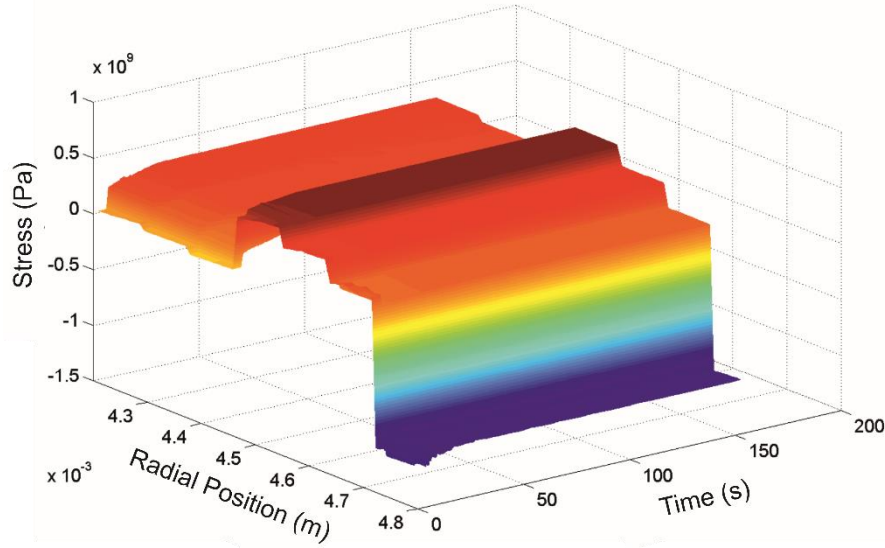
Figure 5.9: Hoop stress during blowdown in a LOCA accident.

Table 5.7: Stress at the start and end of each layer during LOCA accident blowdown.

Transient		Min (MPa)	Max (MPa)
Monolith	Hoop	-37	340
	Radial	-25	-7
	Axial	-123	116
Composite	Hoop	132	560
	Radial	-7	13
	Axial	67	482
EBC	Hoop	-1240	-950
	Radial	-14	3
	Axial	-1371	-1000

The axial stresses in the monolith and in the composite are tensile, presenting values as high as 116 MPa and 482 MPa respectively. To summarize, during the blowdown phase in a LB-LOCA, the hoop stress is the limiting stress, and reaches 340 MPa in the inner monolith considering the worst static case analyzed.

It should be noted that in these calculations it is assumed that no annealing occurs during the high temperature of the cladding, and thus the swelling level remains as it was under the steady state conditions, prior to LOCA. This is conservative, since some annealing will occur, but its magnitude during the short time of LOCA is likely to be negligible.

After LOCA depressurization, in order to reestablish the cladding temperature, water is injected inside the vessel, cooling the uncovered fuel rods. Quenching of the fuel rod by the re-flooding water-front is characterized as a vertical temperature drop of the cladding outer surface. The power after LOCA is ≈4% of the initial power and remains steady for the next 100 seconds. The quench simulation was set for 20 seconds, thus the water front was simulated using 20 spatial functions which regulate the clad external temperature; this allows drifting the water front from the bottom to the upper part using different birth times. The water temperature was set at 373 K. The temperature was changed from the maximal temperature on the cladding surface reached during blowdown according to the simulation (1170 K) to the water temperature (373 K). The reflood was started from the bottom of the cladding and the waterfront was drifted one discretization each second. To set the value, Eq. (5.15) has been used:

$$\frac{x_k^n b + \sum_{j=1}^{n-1} x_k^j\, b}{f_s} = T_f \qquad (5.15)$$

where x_k is the value of the spatial function in the mesh desired (k), b is the prescribed temperature in ADINA on the cladding surface (373 K), f_s is the number of the spatial function used in the simulation, and n is the time step index. The results of the calculations shown in the next figures are at the center axial node of the FEA model for when the induced stress from the quench can be seen (between the 170 and 175 seconds). Figure 5.10 shows the hoop stresses for the three cases as function of time and radial position. The radial and the axial, along with the hoop stresses at the start and at the end of each layer during the reflood phase are presented in Table 5.8. The hoop stress maximum value in the monolith layer is 145 MPa, lower than the hoop stress during the blowdown phase. The composite experiences tensile stresses up to 500 MPa. The highest stress is developed in the EBC layer, which experiences a compressive stress of 1800 MPa. The radial stress remains within reason, with tensile stresses up to 173 MPa in the monolith. The axial stress is compressive in the EBC while exhibits tensile value as high as 600 MPa in the composite and 375 MPa in the monolith.
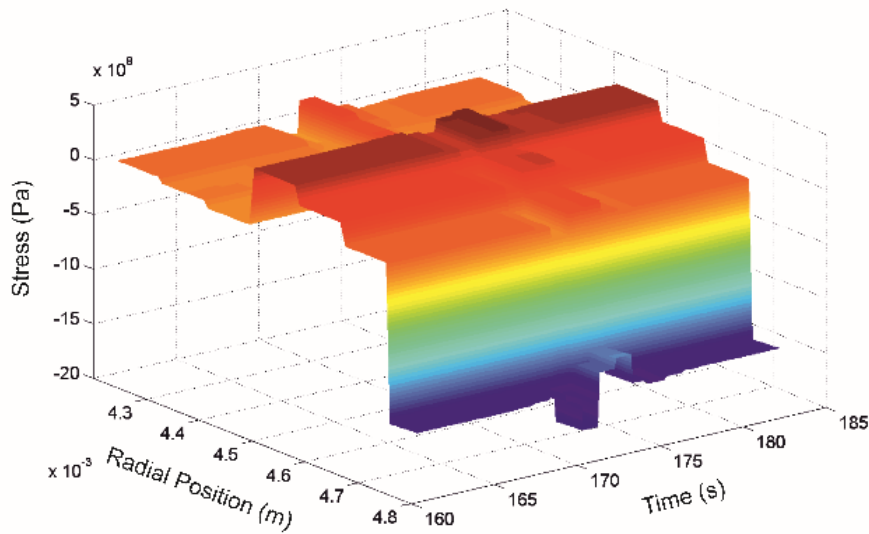
Figure 5.10: Hoop stress during reflood in a LOCA accident.

Table 5.8: Stress at the start and end of each layer during reflood.

Quench		Min (MPa)	Max (MPa)
Monolith	Hoop	-230	145
	Radial	-26	173
	Axial	-182	375
Composite	Hoop	-140	500
	Radial	-14	23
	Axial	15	600
EBC	Hoop	-1800	-1170
	Radial	-64	79
	Axial	-1500	-1150

5.4 Sensitivity study of stresses in the cladding to the swelling

A sensitivity analysis of the CTE influence on the calculated stresses has been performed considering three possible cases:

1. CTE of the CVD material < CTE composite

2. CTE of the CVD material = CTE composite

3. CTE of the CVD material > CTE composite.

150

In case 1, the equation for the swelling in the composite is Eq. (5.16) (T in K) instead of Eq. (5.7).

$$\epsilon^{sw}_{comp} = 0.081 - 1.2 \cdot 10^{-4} \cdot T + 5.4 \cdot 10^{-8} \cdot T^2 \qquad (5.16)$$

Whereas for case 2, Eq. (5.6) is used for both CVD and composite. Case 3 is the same as presented in Sections 5.2 and 5.3. A sensitivity analysis of the CTE influence on the resulting stresses was carried out during steady operation and LOCA. The conservative conditions are taken into account for all the cases. The values of the swelling used for the seven layers in cases I and II are presented in Table 5.9. For these three cases, the conservative static case with high linear heat generation rate (LHGR) and plenum pressure is accounted in order to simulate the operational and the accident conditions. The calculated hoop stresses are shown in Figure 5.11. Restarting from the three steady state cases shown in Figure 5.11, the blowdown and reflood simulations were performed. The results are shown in Table 5.10.

The values in Table 5.10 identify the first case (CVD in the monolith lower than in the CVD) as the most concerning one among the three cases. Judging by the analyzed cases, the thermal and irradiation expansion coefficient plays a strong role in the stress development. In particular having a larger swelling value in one layer with respect to the other, reverses the resultant stresses along the cladding thickness. This sensitivity is best represented by the inner monolith layer, which undergoes compressive stress during operational conditions in the third case (CVD CTE > Composite CVD), while in the other two cases it is under tensile stresses. This is reflected in the lower tensile stresses experienced by the monolith layer in the third case during blowdown and reflood.

Table 5.9: Swelling values for cases I (CTE CVD less than composite) and II.

Layer	Temperature (°C)	CASE I		CASE II	
		CVD	composite	CVD	composite
Inner monolith	827	0.0101		0.0101	
Interm. Monolith	818	0.0104		0.0104	
External monolith	807	0.0107		0.0107	
Inner composite	775		0.0225		0.0117
Interm. Composite	721		0.0244		0.0137
External composite	666		0.0268		0.0160
EBC	636	0.0174		0.0174	
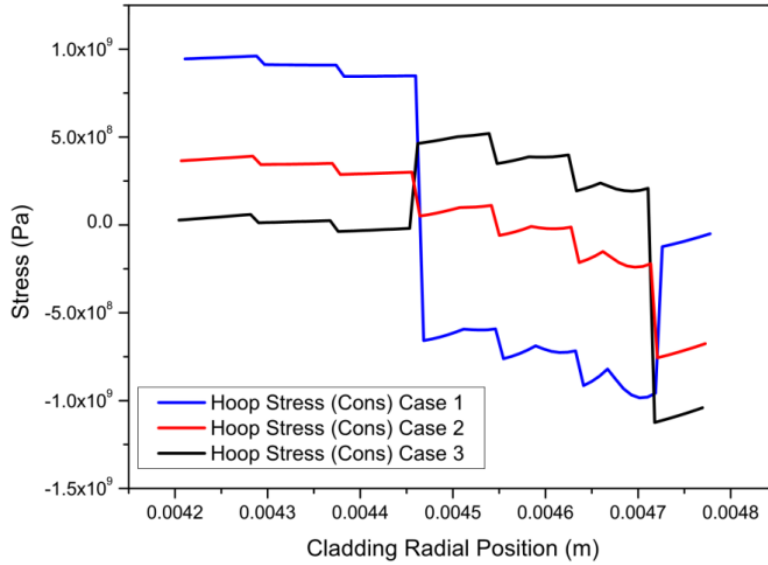
Figure 5.11: Hoop stress calculated for the three cases: CTE of the CVD<composite (CASE I), CTE the same for all the layers (CASE II), CTE of the CVD>composite (CASE III).

Table 5.10: Stress at the start and end of each layer during LOCA accident blowdown and reflood.

		CASE I		CASE II		CASE III	
Blowdown		Min (MPa)	Max (MPa)	Min (MPa)	Max (MPa)	Min (MPa)	Max (MPa)
Monolith	Hoop	840	1236	300	662	-37	340
Composite	Hoop	-1000	-510	-270	156	132	560
EBC	Hoop	-251	38	-820	-600	-1371	-1000
Reflood		Min (MPa)	Max (MPa)	Min (MPa)	Max (MPa)	Min (MPa)	Max (MPa)
Monolith	Hoop	625	1062	84	480	-230	145
Composite	Hoop	-1200	-600	-530	78	-140	500
EBC	Hoop	-800	-175	-1426	-800	-1800	-1170

5.5 Evaluation of the failure rate of SiC cladding

As a brittle material, the probability of failure of SiC composite is associated with the stresses developed in the layers. The monolithic layer raises the highest concern, since cracks can lead to the release of fission products, contaminating the primary system. The Weibull model already discussed in Section 5.1.3 can be applied using the stress calculated under operating conditions and in the case of LOCA accident. The failure probability of the clad fuels in light water reactors has experienced a con-

stant reduction during the last fifty years, and for 2006 a value between $6 \cdot 10^{-5}$ and 10^{-6} has been calculated for the power plants currently in operation (IAEA Nuclear Energy Series NF-T-2.1 2010). Therefore, $2 \cdot 10^{-6}$ is an acceptable value, which has been used for the following analysis to determine the acceptability of the failure probability of SiC. It is noted that this probability of failure is conservative since not all the pins in the core experience the limiting conditions assumed in this analysis. The failure value considered in this analysis is also non-conservative, since only one mode of failure is taken into account, while the failure rates for Zircaloy are due to many different failure modes such as debris and grid to rod fretting. The failure probability of SiC cladding was calculated based on the methodology outlined in Section 5.1.3, using the stresses calculated with the ADINA code. Table 5.11 shows the failure probability of each layer, considering operational loads and accident conditions. The maximum stress in the hoop direction was employed to calculate the probability of failure, according to Eq. (5.17). No failure was assigned in the case the stress was compressive. According to Table 5.11, the composite has 100 % probability to fail.

In order to account for the stresses in the different directions, the criterion based on the von Mises stress is not sufficiently accurate to quantify composite materials failure due to anisotropy (Aiello 2003). On the other hand, the behavior of the monolithic layer can be effectively analyzed using the Von Mises equivalent stress. The monolithic layer is probably the most crucial in the design, since it is needed to protect the hermeticity of the cladding. In order to calculate the equivalent tensile stress for the monolith layer, the analyzed problem can be accounted to be axisymmetric, thus only the principal stresses are considered, as shown in Eq. (5.18).

$$\sigma_{\text{eff}} = \frac{1}{\sqrt{2}}[(\sigma_1 - \sigma_2)^2 + (\sigma_2 - \sigma_3)^2 + (\sigma_3 - \sigma_1)^2]^{\frac{1}{2}} \tag{5.18}$$

The results of the σ_{eff} for the monolith layer under static, blowdown and reflood conditions, along with the probability of failure, are presented in Table 5.12.

Table 5.11: Probability of failure considering the maximum stress in each layer.

	Operation	Blowdown	Reflood
Monolith	$3.1 \ 10^{-4}$	$5.0 \ 10^{-1}$	$1.6 \ 10^{-2}$
Composite	1	1	1
EBC	0	0	0

Table 5.12: Effective stress calculated for the monolith layer with von Mises and failure probability in the conservative case for operating conditions, blowdown and reflood.

Operation		Blowdown		Reflood	
σ_{eff} (MPa)	Failure probability	σ_{eff} (MPa)	Failure probability	σ_{eff} (MPa)	Failure probability
153	0.0203	305	0.3500	217	0.0928

During the transient, the maximum stresses were used to calculate the equivalent stresses. This assumption can be considered too conservative. However, since the maximum stress in the hoop and in the axial direction occurs approximately at the same time, and the radial stress, due to its lower value, does not play a role in the calculations, this is a reasonable premise. The prestresses applied through the manufacturing process can be used to mitigate the effects of possible stresses developed along the SiC thickness during operating and accident conditions.

The prestresses applied to one layer, as more likely the composite, develop an opposite stress in the monolith, which can be calculated from thin annulus stress estimation. The superposition principle can be used to account for the mitigation effect of the prestress on the developed stresses during operation. In Table 5.13, the prestresses required on the monolithic layer to achieve the failure probability required ($2 \cdot 10^{-6}$), which corresponds to a hoop stress of 17 MPa considering a Weibull characteristic strength 369 MPa and a Weibull modulus of 4.4, are presented in the operation, blowdown and reflood cases.

The required prestresses on the composite calculated with the superposition principle are shown in Table 5.13 under the columns composite. The prestress values required on the composite to have the acceptable failure probability have a significant magnitude. The worst case is presented for the blowdown, which requires a prestress on the composite of 306 MPa to meet the required failure probability of $2 \cdot 10^{-6}$, whilst the monolith needs a prestress of 40 MPa on the composite. However it is important to note that these calculations are valid for the conservative case, whereas for the BOL and EOL the stresses developed under static conditions remain compressive. Additionally, by ignoring the pseudo-ductility of the composite layer, the reported stresses are on the conservative side.

Table 5.13: Prestresses required to meet $2 \cdot 10^{-6}$ failure probability under operating, blowdown and re-flood conditions.

Operation (MPa)		Blowdown (MPa)		Reflood (MPa)	
Monolith	Composite	Monolith	Composite	Monolith	Composite
-42	40	-321	306	-126	120

5.6 Conclusions of the FEA calculations

In this work, the calculated stress distributions of SiC cladding for steady operation and for LB-LOCA accident have been presented for different plant conditions and with temperature and time dependent conditions, using temperature-dependent material properties. The expressions for thermal expansion and swelling have been combined in one expansion coefficient term to be plugged in the ADINA code. From the data in the literature, the expansion coefficient higher for the CVD layer has been evaluated as the most likely one to occur; hence this eventuality has been studied accounting for the effect of different reference temperatures on the calculation. The time-dependent calculations were performed for $T_{ref} = 560$ K with the aim of predicting the stresses experienced by the three layers in the SiC cladding during accident conditions. An analysis of the sensitivity of static conditions and LOCA to different swelling was carried out. Moreover, the influence of prestressing was taken into account to mitigate the tensile stress in the SiC cladding layers. In order to perform this analysis, the commercial finite element software ADINA was used.

As a result, considering the calculations performed with the properties in Section 5.1, the most critical scenario in the case of steady-state conditions, is a hoop stress in the monolith as high as 59 MPa, which corresponds to a failure rate of $1.2 \cdot 10^{-3}$. During the LOCA accident, high stresses are mainly experienced during the blowdown, where the monolith reaches 340 MPa and the composite 560 MPa, while during the reflood, the σ_θ stresses are up to 145 MPa for the monolith and 500 for the composite.

According to the sensitivity analysis (Section 5.4) for the three CTE conditions, the failure probability for the monolith layer under static, blowdown and reflood is presented in Figure 5.12.
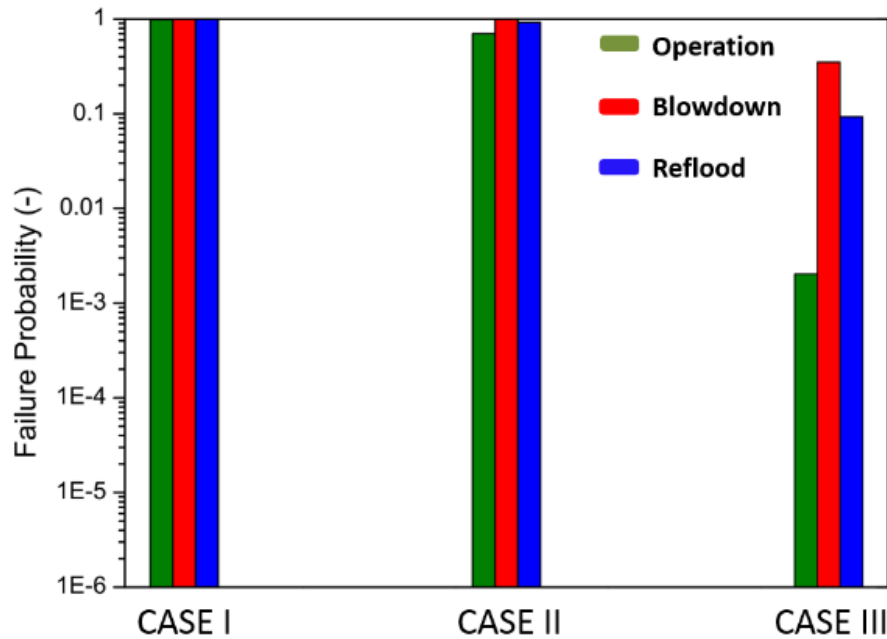
Figure 5.12: Failure probability of monolithic layer for the three cases analyzed (CTE CVD < CTE Composite, CTE CVD = CTE Composite, CTE CVD > CTE Composite).

The equivalent stresses were used to calculate the failure probability. The results show that in cases I and II, the cladding does not withstand the occurring stresses. In case III, during operation conditions the probability of failure is several orders of magnitude lower than in case of accident. Therefore, it is evident that the stresses are strongly reduced in the case the CTE in the monolith is always higher than the CTE in the composite layer. It is also noted that conservative LHGR and plenum pressures were used in this study. However, according to the results presented in Table 5.11, the composite layer fails under these conditions, releasing the stresses to the inner monolith layer. This would considerably increase the failure probability of the monolith layer. The employment of a thicker cladding could be a solution to reduce the intensity of the occurring stresses. Other possible ways of alleviating the high stresses could be realized through a lower heat flux, or through pre-compression of one layer. While the first option could be achieved in a smaller reactor, the second solution can be obtained by synthetizing specimens at high temperature or by mechanically pre-compressing the inner monolith during the deposition of the SiC fibers. The pre-compression obtained in the layer of interest (e.g., the mono-

lith) would be balanced out by pulling under tension the complementary layer: the level of pre-compression needed would systematically result in too high tensile stresses in the complementary layer. For this reason, this option was not discussed in this work.

6. SiC composites quench experiments up to 2000 °C

In this chapter quench experiments on silicon carbide cladding specimens are presented. Such tests are of great importance for the employment of SiC as LWR cladding reactor, since the blowdown and reflood procedure is foreseen in case of LOCA in order to re-establish the temperature and avoiding core melting, as already explained in Chapter 5. The current allowable peak cladding temperature set by the US-NRC for Zry is 1204 °C. This criterion, along with the maximum oxidation criterion (17% ECR), ensure the survival of Zry cladding under the thermal shock during reflood phase of LOCA. The research conducted earlier on Zry suggests designing SiC tests from the current practice based on Zry. On the other hand, the use of a ceramic material such as SiC, diverges from the current expertise. For this reason, it is convenient at this early stage of SiC assessment as cladding for LWR, to test the behavior of the material under conditions that diverge from the usual tests. In this work the performance of SiC cladding, monolith as well as composite samples, was tested in an induction furnace up to 2000 °C and then quenched by water at the highest workable temperature available.

6.1 Experimental details

In this chapter, experimental details of the oxidation and quench of SiC cladding specimens in steam are reported: samples, devices, test conditions and the post-test analysis used to characterize the sample after the tests are described in detail.

6.1.1 Samples

SiC cladding samples, 4 monolithic and 4 composites, 2.5 cm length, were provided by Ceramic Tubular Products Llc. The architecture of the composite is the so-called TRIPLEX, consisting of three SiC layers. The inner is a high-density monolith layer of stoichiometric β-SiC operating as fission product release barrier and providing strength to the cladding. The intermediate is a composite layer made

of SiC fibers[7] in a SiC matrix produced by CVI process, which gives pseudo-ductility. The outer dense layer consists of a CVI deposited SiC and serves as environmental barrier coating (Feinroth 2012). A SEM micrograph of the section of one sample is shown in Figure 6.1.

This CVI coating has been applied during production one time for the first two TRIPLEX samples and two times for the remaining two SiC TRIPLEX samples. The samples are the following:

- 4 monoliths samples, 25 mm long, I/D 8.4 mm, 0.75 mm wall thickness
- 2 triplex single layers, 25 mm long, I/D 8.3 mm, 1.15 mm wall thickness, (T2C, T2D)
- 2 triplex double layers, 25 mm long, I/D 8.2 mm, 1.1 mm wall thickness, (T10C, T11C).

An overview of the samples and the tests performed is given in the Table 6.1. The first monolithic sample (M1) was used to test a different setup with respect to the one already described: it was filled with tungsten as susceptor, isolated from the SiC by alumina rods, to avoid W interactions between both the SiC and the oxidation environment.
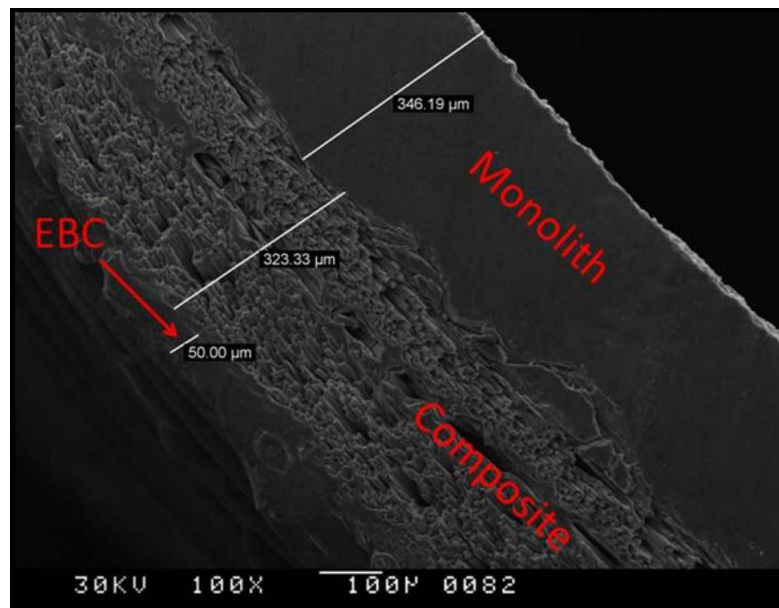
Figure 6.1: Laminated layers of SiC monolith/SiC composite cladding (Stempien 2011).

---

[7] This layer is made from stoichiometric β-SiC fibers, i.e., HiNicalon-S fibers.

Table 6.1: Samples, atmosphere and temperature during quench tests.

Name	Type of sample	Atmosphere	Temperature (°C)	Comments
M1	Monolithic	Argon	2000	Broken
M2	Monolithic	argon+steam	2000	Broken
M3	Monolithic	Argon	2000	Intact
M4	Monolithic	Argon	2000	Intact
T11C	Triplex –double	Argon	2000	Intact
T2C	Triplex	argon+steam	2000	broken
M4_bis	Monolithic	argon+steam	2000	broken
T10C	Triplex –double	argon+steam	2000	Intact
T4D	Triplex	argon+steam	1600	Intact
T4D_bis	Triplex	argon+steam	2000	Intact

The first test was not successful: the temperature did not exceed 1500 °C. Thermal calculations showed that it was due to the thermal conductivity of the alumina. Moreover the sample broke, due to the expansion of the inner material, as shown in Figure 6.2.

The second monolithic sample (M2) was filled with graphite, and this completely new design was kept during the following experiments. After heating up, the sample was quenched during a second test. It must be mentioned that during this work numerous trials with different metals as suceptors were run, in particular, iridium, hafnium, and tantalum. Among these materials, graphite was the best trade-off, and it was used for all the experiments presented in this work. This configuration is firstly introduced in this thesis and allowed reaching 2000 °C.

Figure 6.2: Monolithic sample: first test (M1).

6.1.2 Facility

The samples were heated in an induction furnace, already described in Figure 2.7. Unlike the tests described in Chapter 2, in the experiments reported in this chapter, the specimens are quenched by water after the heating up phase at 2000 °C. In order to quench the sample, a glass cylinder filled with water at 90 °C was moved by a step motor from the bottom part covering the sample in water at 1 cm/s. This procedure requires the sample's holder hanging from the ceiling of the furnace. Therefore, the sample holder was designed as in Figure 6.3. The furnace is connected with a mass spectrometer (MS), which allows monitoring the concentration of exhaust gases. The temperature is measured directly on the sample surface by means of a two-color pyrometer.

6.1.3 Test conditions

For each test, the temperature was raised at a rate of 10 K/min until the required test temperature was reached. Two different protocols were used to test the SiC samples:

a) The annealing was conducted in inert atmosphere with 40 l/h flowing argon up to 2000 °C. This is not a relevant condition for nuclear power plant's accident, nevertheless ppm of oxygen were present according to the MS signal, due to some leakage in the system. After reaching 2000 °C, the samples were quenched by water at 90 °C from the bottom with a velocity of 10 mm/s.
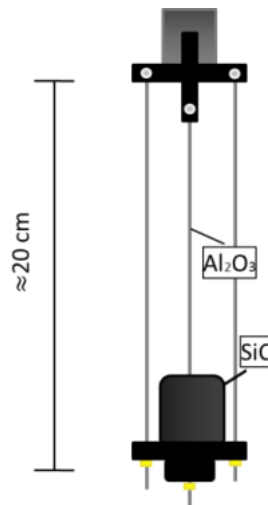
Figure 6.3: Sample holder used in the quench tests.
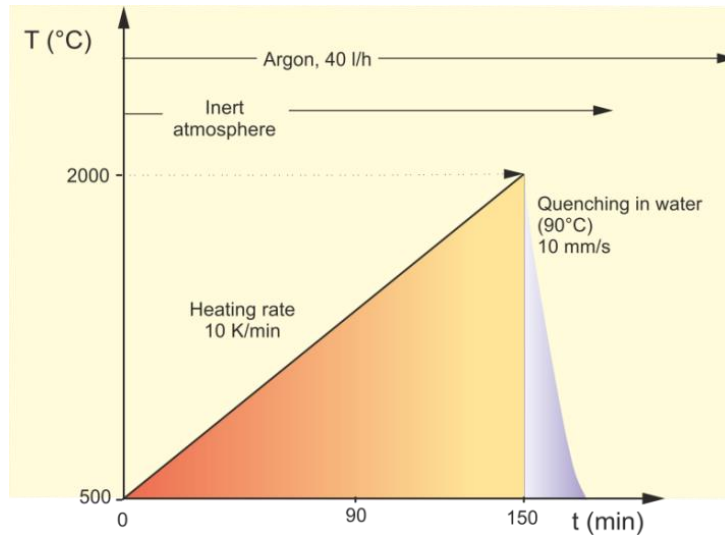
Figure 6.4: Experiments in inert atmosphere.

a) The sample was heated in inert atmosphere (argon 40 l/h) up to 1400 °C. A steam flow of 63 g/h was introduced at this temperature in order to avoid condensation at the bottom of the sample holder, which can occur if the temperature of the specimen is not high enough to warm up the rest of the facility by irradiation. After reaching 2000 °C, the samples were quenched by water at 90 °C from the bottom with a velocity of 10 mm/s (Figure 6.5).
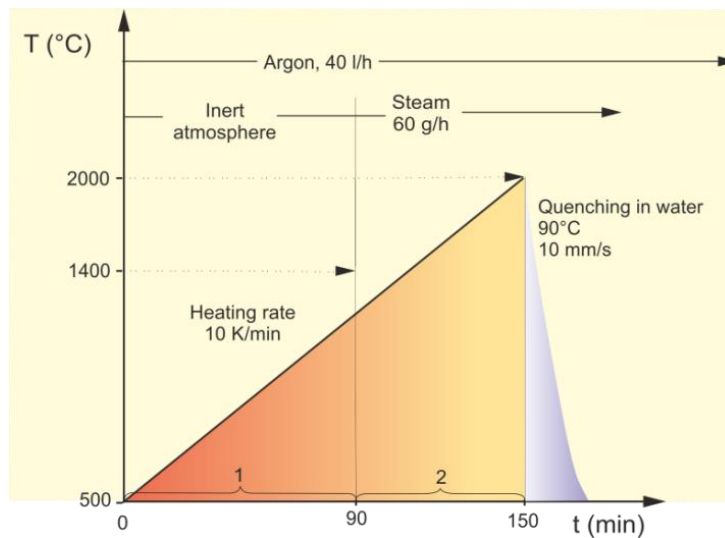
Figure 6.5: Quench test in oxidizing environment.

6.1.4 Post-test analysis

The samples were analyzed before and after the test with optical microscopy, SEM, X-ray and neutron tomography in order to investigate the presence of cracks, which could compromise the fission gas retention. Details have been already explained in Section 2.2.4. These techniques allow internal inspection of the sample depending on the total mass attenuation of the elements atomic number. The evaluation and analysis were done using imaging software (imageJ, VGstudio).

6.2 Results of SiC/SiC quench experiments and comparison with calculations

In this chapter the results of the quench experiments are presented. The monolithic and the composite samples are treated in two different sub-chapters.

6.2.1 Monolithic samples

Two monolithic samples (M3 and M4) were quenched in inert atmosphere and both samples withstand the quench test. The off gas concentration of the gases produced during the tests of the samples M3 and M4 were measured by the mass spectrometer, and it is shown in Figure 6.6.

During the heat-up phase, the argon is almost the 100% of the gas, despite the traces of CO, H_2, O_2 and CO_2, which can be noticed in the graphs. Once the quench occured, the argon sharply decreased due to the H_2O gas formation, which is caused by the water introduction in the quartz chamber. Results of the SEM analysis on the surface of sample M3 are presented in Figure 6.7.

Some powder was found at the bottom of the furnace: after EDX and XRD analysis, it was recognized as amorphous silica. A silica layer was detected on the sample and it is visible in Figure 6.7b and Figure 6.7c. In the latter figure, rounded shaped features are noted on the surface.
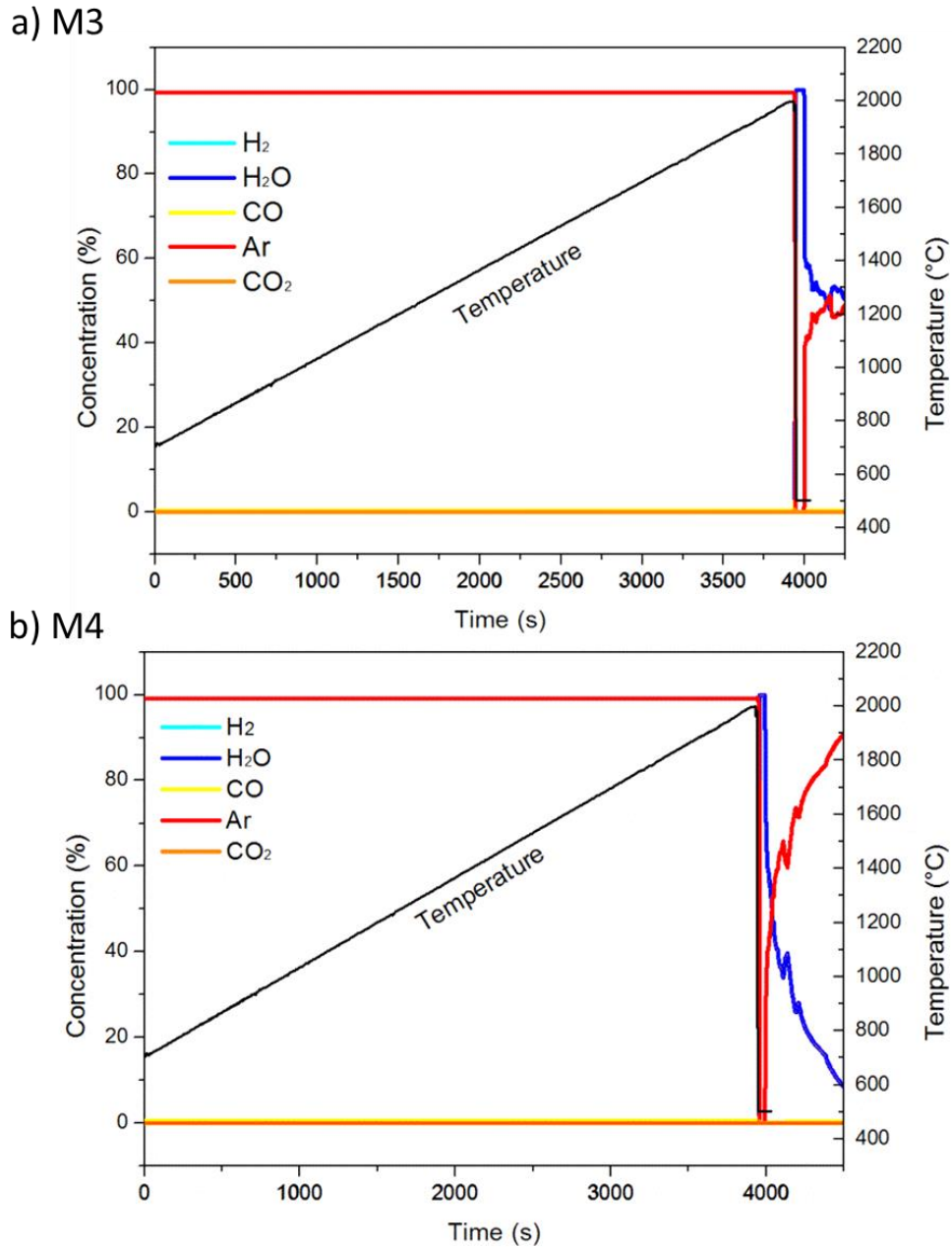
Figure 6.6: Temperature profile and mass spectrometer output of the samples M3 and M4 during oxidation and quench.

The elongation of the circled features is due to a microscope artifact, since the sample's surface was curved. In Figure 6.7c the silica looks dense and without cracks. The light grey part (Magnification in Figure 6.7d) was analyzed by EDX tests and was detected as SiC. This surface shows the typical sintered SiC structure, probably due to the detachment of the silica layer.
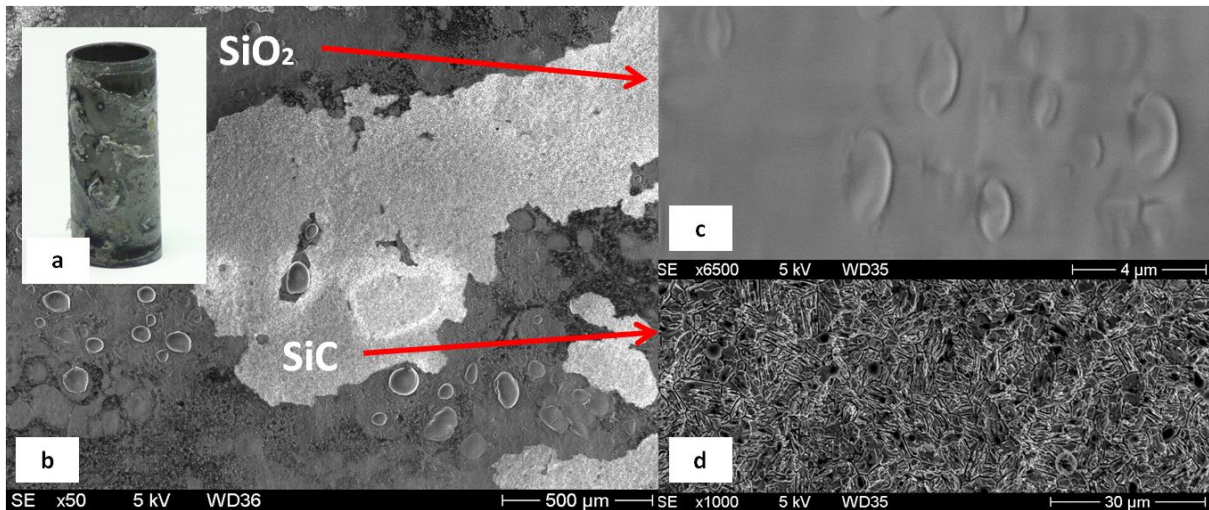
Figure 6.7: Monolithic sample (M3) quenched in inert atmosphere: (a) macroscopic post-test, (b) x50 SEM picture where two regions are visible (dark and lighter), (c) 6500X SEM micrograph of the dark area, (d) 1000X SEM micrograph of the light area.

The monolithic sample (M2) was tested a second time in the steam environment. The gas production measured by the MS is presented in Figure 6.8. As shown in Figure 6.8, the hydrogen production was as high as 2.5 l/h, with some peaks at the higher temperatures.
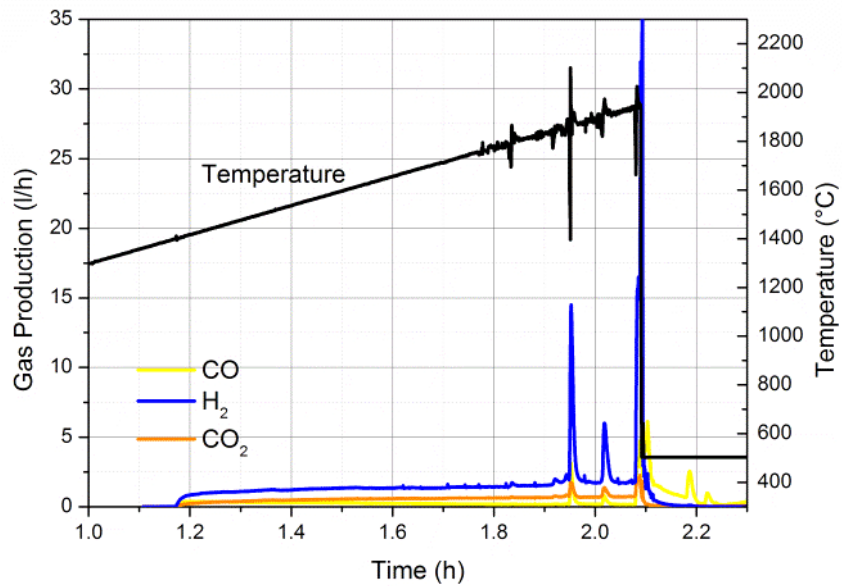
Figure 6.8: Temperature profile and mass spectrometer output during second test with sample M2 during oxidation in steam and quench.

165

The mass loss of the graphite was 0.403 g, meaning that some hydrogen could hail from the susceptor. After the test, the sample resulted broken. However, there are uncertainties on the stresses that have caused the rupture, since it was broken before being quenched by water. The microstructure analysis of the broken sample M2 was performed on the surface and on the section by SEM (Figure 6.9). On the surface, the bubbles are visible; according to the micrograph of the sample's section, the bubbles develop in the silica layer and grow on the surface.

6.2.2 Triplex samples

The two triplex single layers were quenched, one after heating phase in inert atmosphere and the other with pre-oxidation in steam (11C, 2C). Sample 11C remained intact as shown in Figure 6.10, while the sample 2C was broken (Figure 6.11). The video record is showing that already before the quench the second sample was broken. In Figure 6.12 the MS signals of the sample 11C and 2C are presented.
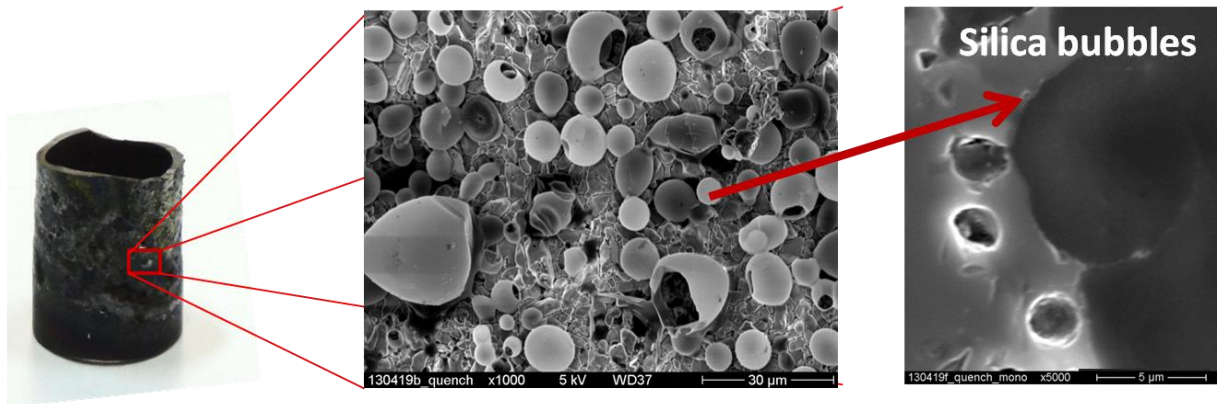
Figure 6.9: SEM micrograph of the monolithic sample (M2) after test in corrosive atmosphere: post-test analysis.
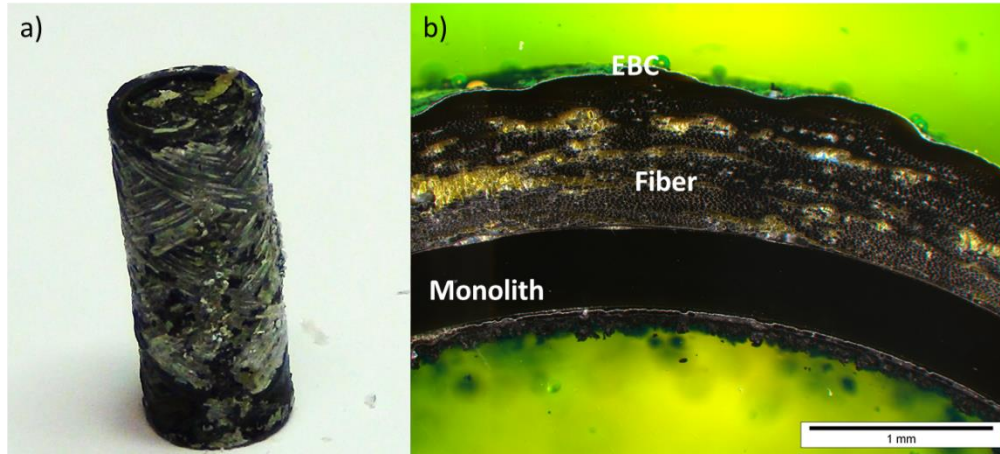
Figure 6.10: (a) Macrograph of sample 11c, (b) micrograph with optical microscope of the section of sample 11C.
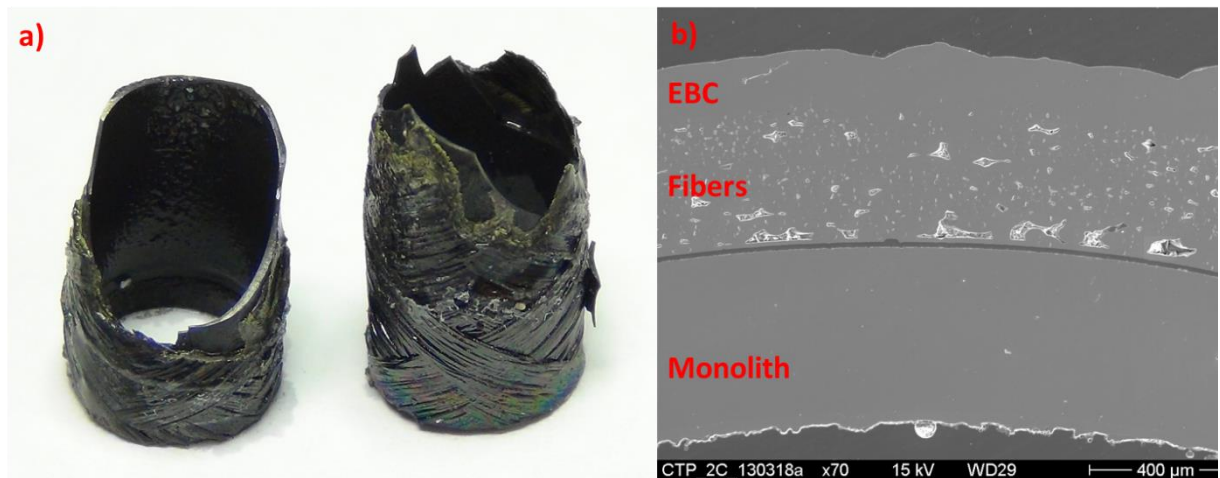
Figure 6.11: Sample 2C: (a) Macrographs of the sample 2C (b) micrographs with SEM.

Focusing on the sample 2C oxidized in steam, the output gas signal showed oscillations during the test, which were due to the condensation of the steam in the MS capillary. This was corrected with a parabolic interpolation (Figure 6.12b). The hydrogen and CO/CO_2 peaks observed in the Figure 6.12b start at about 1920 °C. This could be related to the oxidation of the inner susceptor made of graphite, which would also explain the oscillation of the thermocouple signal. SEM micrographs were done on the broken sample before embedding along the fracture point (Figure 6.13). Figure 6.13b presents the fracture of the sample covered by silica.
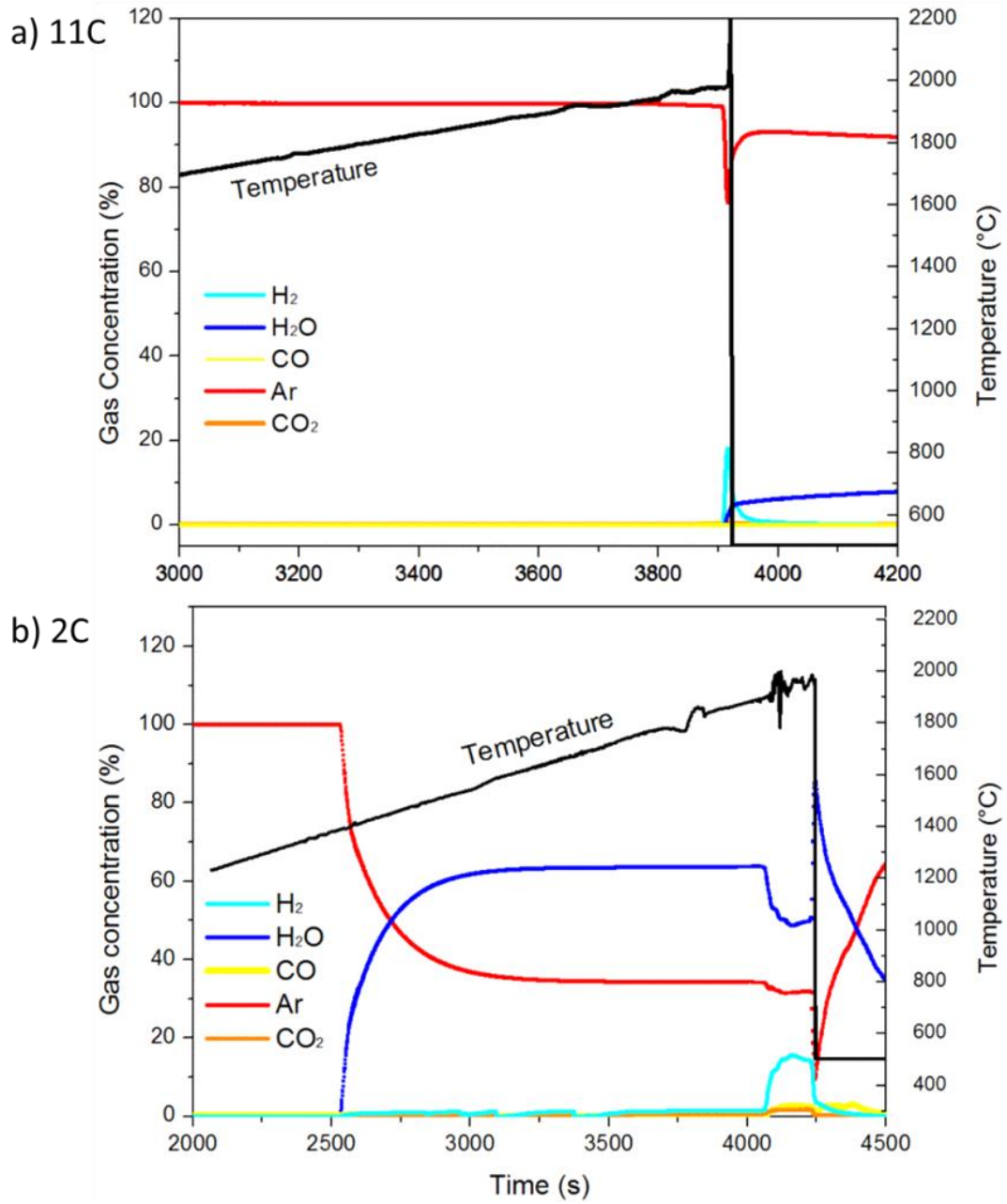
Figure 6.12: Temperature profile and mass spectrometer output of the samples 11C (a) and 2C (b) during oxidation and quench.
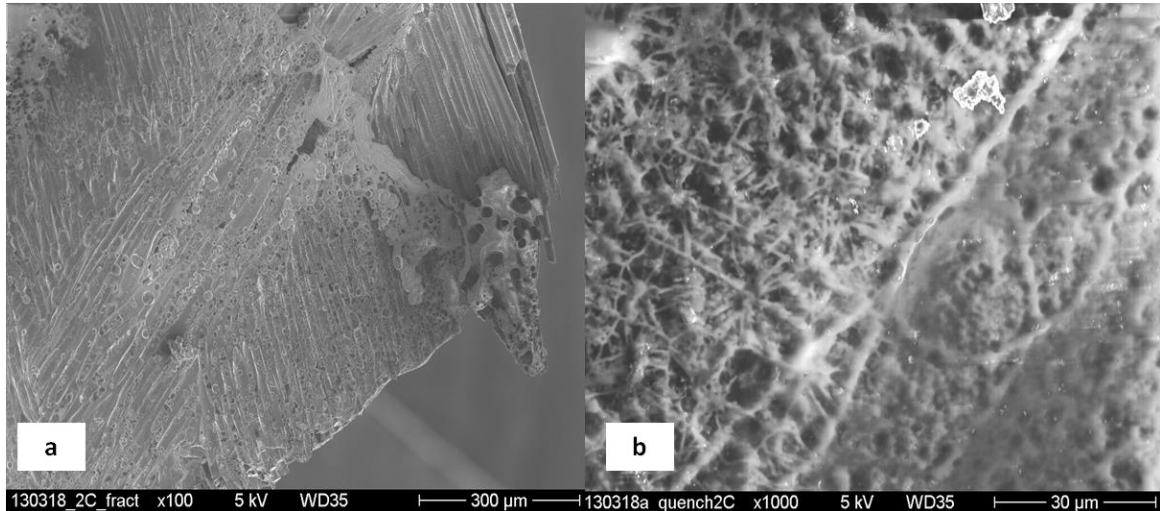
Figure 6.13: Triplex single layer sample 2C (a) fracture surface point, (b) external surface.

The samples T4D and T10C were both oxidized in steam before undergoing the quench procedure. One of the two samples with the two CVI external layers (T10C) was tested in steam atmosphere resulting intact, as shown in Figure 6.14. For this experiment, the two SiC caps, necessary to keep the graphite inside the silicon carbide, were fixed with refractory zirconia glue (Polytec-PT Resbond 904), which can withstand temperatures up to 2200 °C (data sheet of the glue is in Appendix d). This procedure was adopted in order to avoid graphite oxidation. A sequence of images extracted from the video recorded during the annealing in steam and quench in water of sample T10C is in Figure 6.15.

Figure 6.14: Triplex double layer sample T10C after quench.
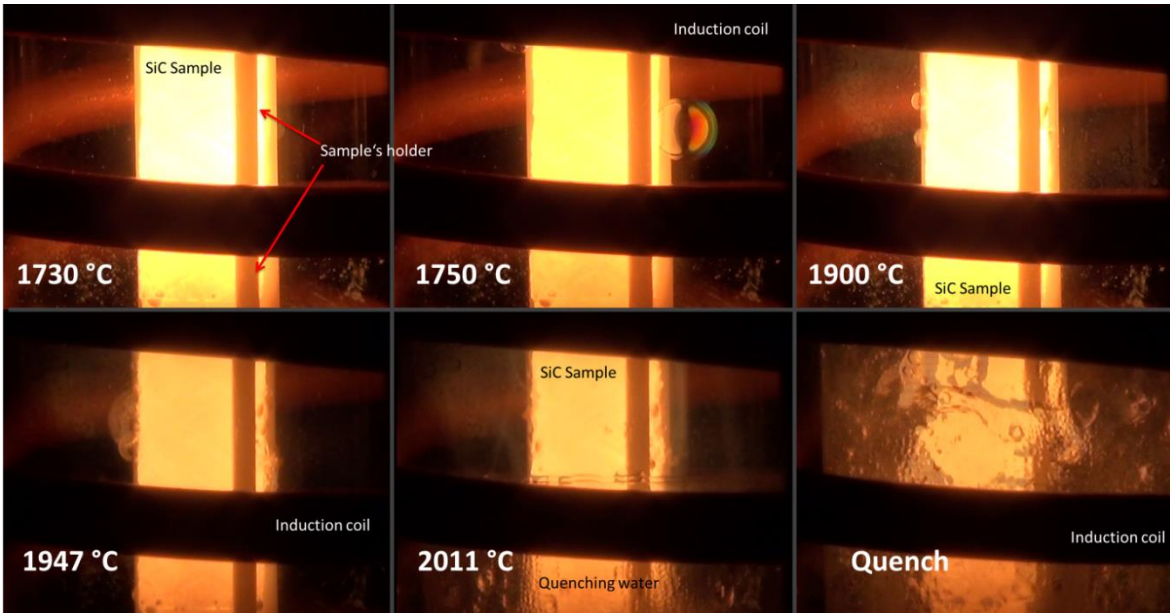
Figure 6.15: Images from the video recorded during typical annealing in steam and quench in water (sample T10C).

The sequence of figures can be correlated to the online gas measurement performed by the mass spectrometer (Figure 6.16). From the gas output of sample T10C, the hydrogen started to be produced at 1400 °C with a sensitive increase after initiation of steam injection. After this, the hydrogen production decreased, probably due to the growing of the silica, which is slowing the kinetics. From 1760 °C many peaks in the hydrogen production are visible, probably due to the silica phase change which occurs at 1710 °C. The temperature profile acquired by the pyrometer is also showing a change, which is probably due to the silica melting occurring at 1710 °C, changing the emissivity of the sample surface. At almost the same temperature (1750 °C) the bubbles are for the first time detected in the video.
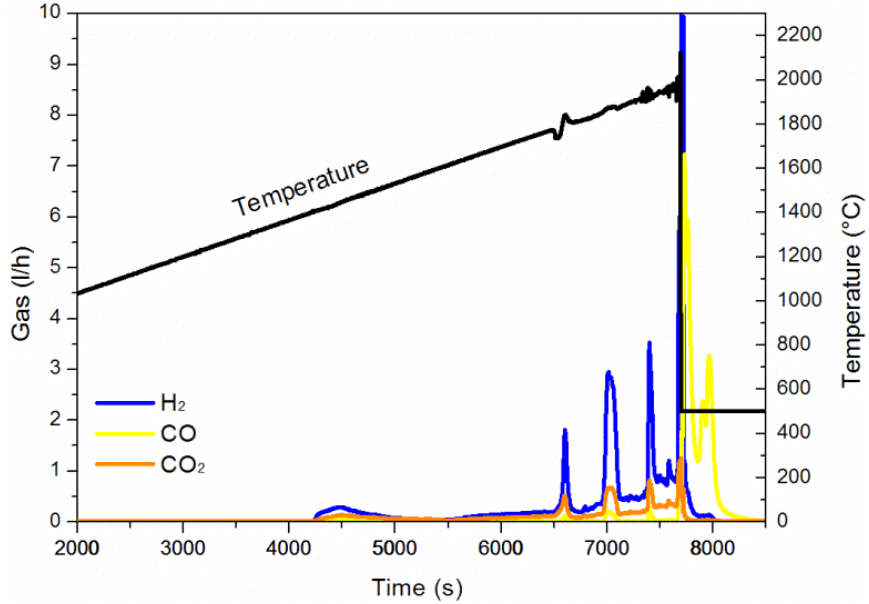
Figure 6.16: Mass spectrometer output of the sample T10C during oxidation and quench.

Under optical inspection, the samples are intact, with the exception of one, which was broken. On the other hand, post-test analyses with X-ray radiography showed cracks in the inner monolith layer on sample T10C (Figure 6.17). The sample was then embedded and cut. Optical and SEM analysis showed cracks in the inner monolithic layer, as presented in Figure 6.18. It can be assumed that thermal stresses faced during the quench generated cracks along the inner monolith layer. The 2D model already described in chapter 5.1 was adapted to calculate the stress occurring along the thickness of the samples oxidized and quenched in the single rod facility.
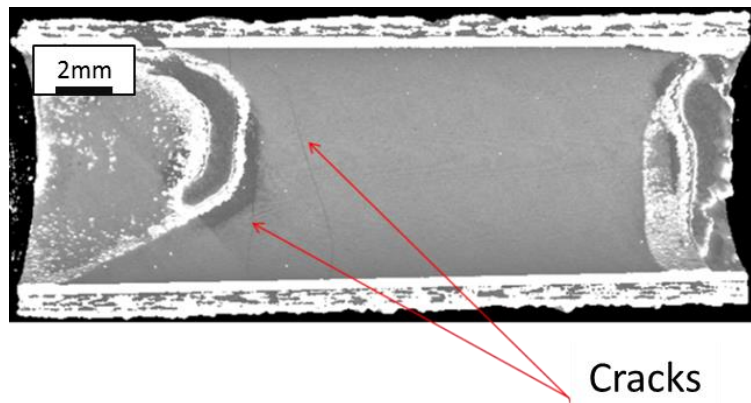
Figure 6.17: X-ray radiography of sample T10C.
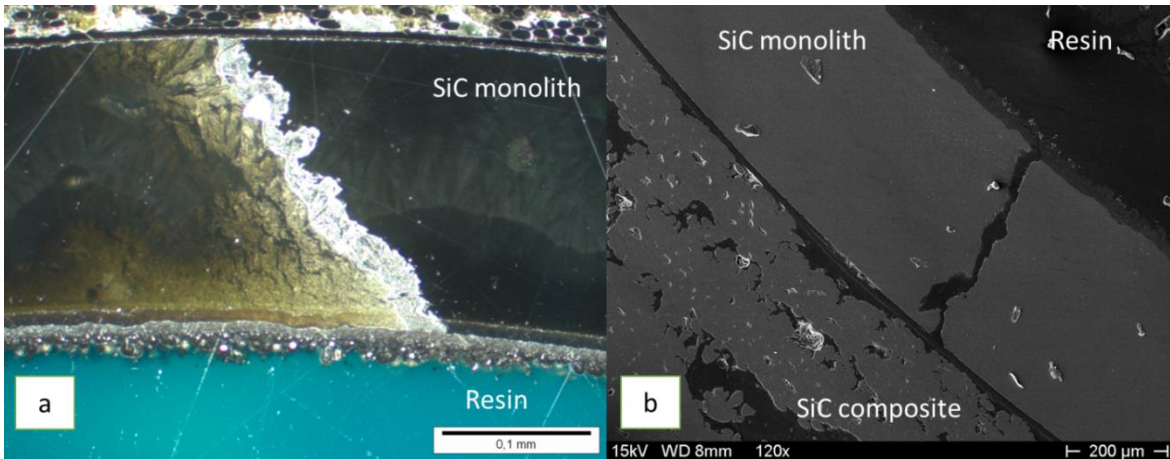
Figure 6.18: T10C triplex sample section analysis (a) optical microscope (b) SEM.

In order to tailor the model to the real case, the swelling part was not included in the thermal expansion coefficient, which was considered for the CVD monolith $4.6 \cdot 10^{-6}$ and for the composite $4 \cdot 10^{-6}$. According to these results, the monolith layer undergoes tensile stresses up to 500 MPa during the quench procedure. Considering the thermal stress due to the temperature gradient in the cladding thickness, lowering the temperature from 2000 °C to 1600 °C would reduce the stress by 20%. For this reason, the last test was run at 1600 °C. After the test at 1600 °C, the sample was investigated by means of X-ray tomography and no cracks were detected. The sample was oxidized and quenched a second time from 2000 °C. Figure 6.19 shows the output of the mass spectrometer of the second oxidation test of sample T4D. The sample underwent strong reaction with the alumina rods of the sample holder, which probably caused the oscillation of the signals starting above 1800 °C in Figure 6.19.
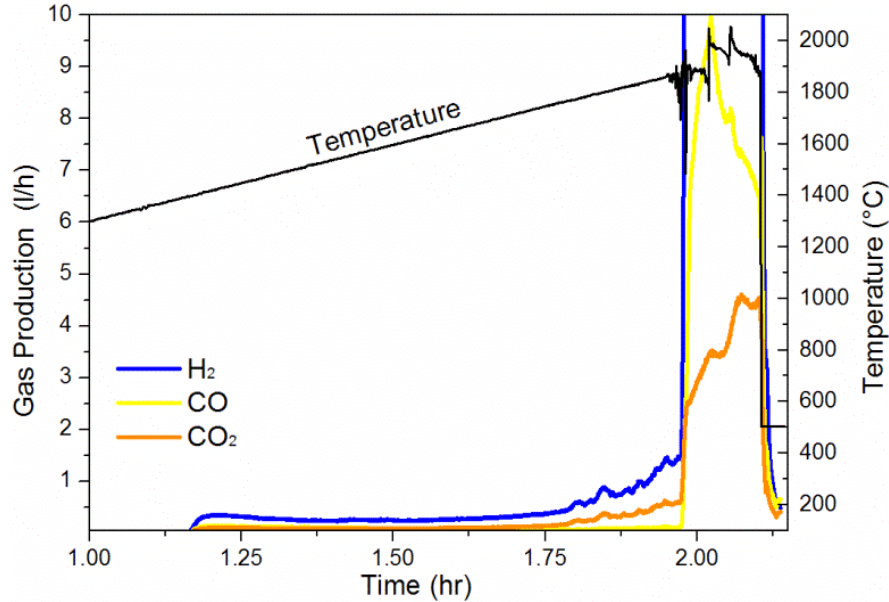
Figure 6.19: Mass spectrometer output of the sample T4D during oxidation and quench.

6.3 Discussion

The quench results showed the survival of the material after heating phase in inert atmosphere, but 2 over 4 samples did not withstand the quench after oxidation in steam. The oxidation took place during the 2 h heating phase and was affecting only the external layer. Nevertheless, this result can be explained considering the cracks and stresses for the monolithic and the single layer triplex. The double layer triplex samples seemed to be more resistant than the monolith, although not enough data have been collected.

Sample T10C was taken into account as the most reliable measurement. The output of the MS in Figure 6.16 shows that after a first peak around 4200 s, the H_2, CO, and CO_2 flows decrease. This can be explained considering the formation of the silica layer from the reaction between SiC and H_2O. The integral hydrogen release of sample T10C is presented in Figure 6.20. Between the points A and B, parabolic shape production is noted (Figure 2.21), due to the developing of SiO_2. However, it cannot be considered pure parabolic behavior, since the measurement was not isothermal. After the B point, the value increases, probably due to the loss of the protective oxide scale. In point C the silica reaches its melting point and the hydrogen starts to increase quite sharply. At point D, quench with water occurred.
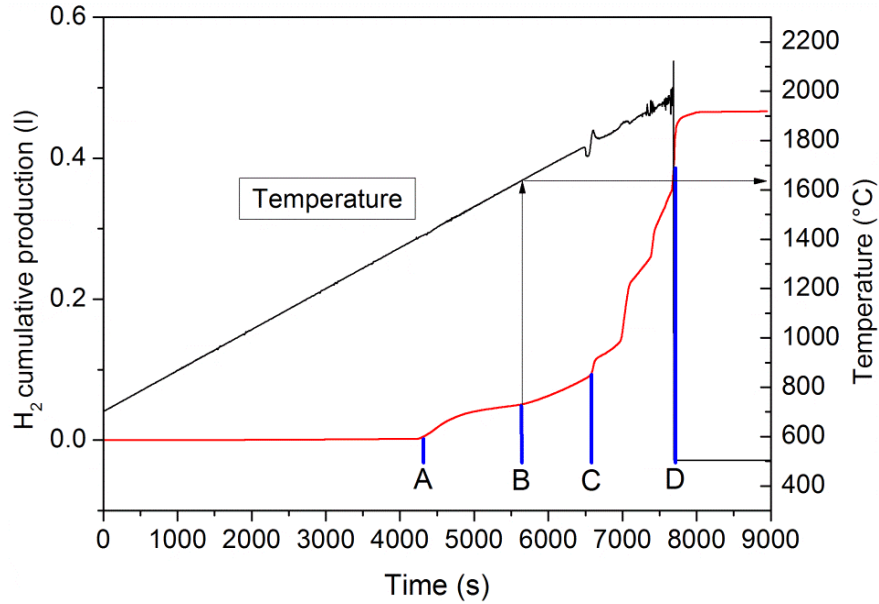
Figure 6.20: Integral of the hydrogen production of the sample T10C.

Comparison with hydrogen produced by Zircaloy with the same temperature profile was performed, considering the area from A to B (which includes the temperature range between 1400 °C and 1600 °C). The results are presented in Figure 6.22.
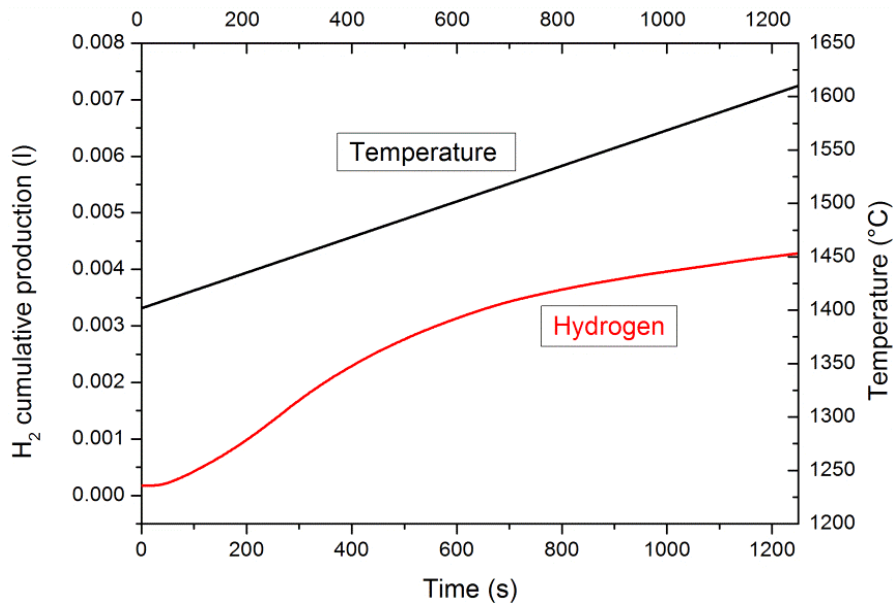
Figure 6.21: Hydrogen production during oxidation of sample T10C between 1400 °C and 1600 °C.
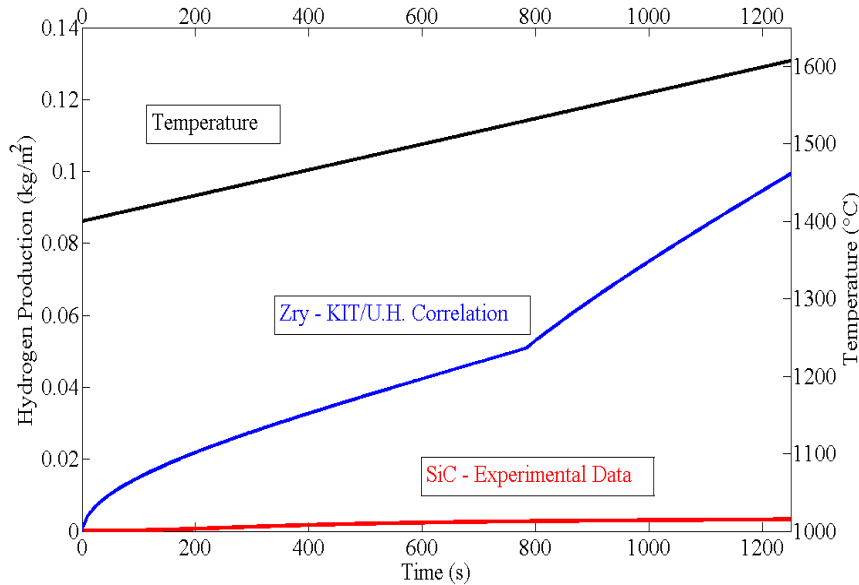
Figure 6.22: Hydrogen produced by oxidation of Zircaloy and SiC (sample T10C between point A and B) under non-isothermal conditions.

Among the different available correlations, a correlation developed at KIT was chosen to calculate the hydrogen release from Zircaloy (Grosse 2010). A numerical code allowed to calculate the hydrogen production following the experimental conditions already described. The resulting hydrogen production is 0.003 kg/m² produced from SiC and 0.12 kg/m² from Zircaloy. According to these data, the hydrogen produced by oxidation of SiC is 40 times lower than the amount produced by the Zircaloy under the same conditions. This is consistent with the results presented by Ishibashi (2014), who calculated the hydrogen generation from SiC during simulated severe accident as one twentieth of the hydrogen produced by Zry.

6.4 Conclusions of the quench tests of SiC multi-layer cladding

In this chapter oxidation and quench experiments of SiC prototypical samples were performed. Samples provided by CTP were heated in an induction furnace up to 1400 °C in argon, and were oxidized during the annealing up to 2000 °C in steam. Once the temperature was reached, the samples underwent quench in water. The samples performed very well, despite the high stresses. The hydrogen produced was measured and compared with the hydrogen produced under the same conditions by Zircaloy. It resulted that SiC produced 40 times lower hydrogen than Zircaloy. It must be noted that

at these temperatures it is difficult to avoid side effects, such as interaction with the sample holder and reaction of the graphite with the oxidant. As a conclusion, it can be affirmed that the silicon carbide has the potential to be applied at very high temperature, and that it can withstand temperature as high as 2000 ℃.

7. Conclusions and recommendations

This work was started in order to investigate the behavior of specific refractory materials under extreme conditions. The focus was on materials that appear as candidate for safety improvements in current reactors in a short/long term, as well as in IV generation reactors. In this frame, silicon carbide is a cutting-edge material, which could serve as cladding for nuclear fuel or as structural material. The aim of this work is to provide insights into two of the open issues that still need assessment to deploy silicon carbide's designs in a nuclear power plants. The first one concerns the behavior of silicon carbide in the case of high-temperature oxidation in steam atmosphere, which is a prototypical condition in light water reactor accident during LOCA. The second concerns the mechanical stresses that develop under operational conditions as well as during accident conditions in the silicon carbide cladding thickness. Interesting results have been obtained in this framework.

In order to study the oxidation, experiments were performed on different silicon carbide designs provided by CEA and CTP at temperature up to 2000 °C. One of the potential SiC/SiC$_f$ designs proposed by the Commissariat à l'Énergie Atomique et aux Énergies Alternatives (CEA) consists in the so-called sandwich cladding, which has a thin tantalum layer between two layers (inner and outer) made of silicon carbide. In order to assess this design, oxidation tests were performed separately on silicon carbide and on tantalum.

The influence of the steam partial pressure was studied on silicon carbide composite samples at 1600 °C. The results have shown different oxidation behavior depending on the steam partial pressure: while at low steam partial pressure (10 kPa) the material oxidized uniformly, at higher steam partial pressure the presence of bubbles on the surface was detected, corrupting the protective silica scale, and leading to mass loss. At higher temperatures (1700 – 1800 °C), the silicon carbide design has shown to withstand at least 1 hour under steam oxidation.

In order to predict the mass loss due to the volatilization of the silica, the equilibrium partial pressures of the gas species produced by the volatilization of the silica were calculated using the CALPHAD

method, by means of the Thermo-Calc software. In order to do this, a new database (Si-C-H-O-Ar) was developed, including the description of the silicon hydroxides $Si(OH)_4$ and $SiO(OH)_2$. Two models already existing in the literature were used to calculate the silica mass loss from the silicon-hydroxide partial pressure, namely the model developed by Opila and that described by Nickel. The calculations of the SiC mass loss performed with the thermodynamic database were benchmarked with experimental data present in the literature. This allows affirming that in the experiments performed in this work, the volatilization of the silica scale is negligible with respect to the mass gain. The major event that is degrading the protective silica scale was the bubbles production, which occurred on the samples' surfaces. Additional studies are required in order to characterize the SiC/SiC$_f$ behavior at temperatures higher than 1600 °C. In this work, despite isothermal experiments at 1700 °C and 1800 °C were performed, the interaction with the sample holders did not permit to test for time longer than 1 h without undergoing severe interaction.

In order to study the second component of the sandwich design, the oxidation of tantalum in steam was performed between 600 °C and 1100 °C using a thermal gravimetric device. Besides the shape used in the sandwich design, tantalum plates were also tested. The tantalum strongly oxidized at each temperature tested with the formation of the highly volumetric Ta_2O_5. Temperatures between 500 °C and 700 °C are of high concern, since the oxide crumbled without being protective. A linear oxidation behavior was detected for each temperature. At 600 and 700 °C, an initial parabolic behavior was detected during the first minutes of the experiments. The hydrogen uptake was also investigated by means of hot extraction. After these tests, the hydrogen uptake by the tantalum resulted higher than the value predicted by the Sieverts' law. Overall, the tantalum did not show optimal performance. Further oxidation studies, including the whole sandwich design, would give a comprehensive behavior of the design and would finally prove whether the SiC/SiC$_f$ combined with a tantalum liner is a good solution for light water reactors.

Oxidation of SiC composite under non-isothermal conditions was performed in steam at temperature up to 2000 °C. After reaching this temperature, quenching in water restored the samples temperature from 2000 °C to 90 °C. This procedure allowed testing both oxidation, as well as mechanical strength. The presence of steam and the temperature higher than the SiO_2 melting point, caused bub-

bles production on the surface of the samples. During oxidation, the hydrogen production was measured with a high sensitivity mass spectrometer. The amount of hydrogen was compared with the hydrogen produced under the same conditions by the oxidation of Zircaloy. The results have shown that the silicon carbide produces at least 40 times less hydrogen than Zircaloy.

Not all the samples tested withstood the quench, and some presented cracks in the inner monolith, detected with X-ray tomography inspection. This procedure somewhat reproduced the conditions that occur during a LOCA accident, in particular regarding the thermal stresses in the cladding. On the other hand, this facility was not under pressure, which is the case in the real situation. Moreover, the change of material's properties due to the irradiation is not taken into account. To have a more precise comprehension of the stresses occurring along the silicon carbide thickness in operational and under accident conditions, finite element analysis was employed. By means of the commercial FEA software ADINA, a 2D model of the 3-layered SiC/SiC$_f$ sample (monolith-composite-EBC) was used to simulate operational and accident conditions. In this simulation the material properties and the influence of irradiation, as well as the pressure depending on the life in core, were carefully accounted. Among the material's properties, the swelling induced by irradiation plays a strong role on the performance of the SiC. In order to include the swelling in the simulation, this phenomenon was combined with the thermal expansion in one coefficient (CTE). Composite and monolith SiC react differently in case of irradiation. Moreover, different fiber types can present slightly different expansion due to the swelling. Since only few experimental data are available in the literature, a sensitivity study was run in this work in order to quantify the influence of the swelling on the developed stresses. The three cases studied were identified according to the magnitude of the expansion coefficient (thermal expansion plus swelling) in the CVD and in the composite layer: the first case considered the CTE higher in the CVD, then the CTE was considered constant in all the layers, and lastly the CTE was considered higher for the composite. The results of this analysis show that it would be preferable to employ a cladding in such a way that the thermal expansion of the inner and the outer layer is higher than the thermal expansion of the composite. According to the failure probability calculated using the Weibull model, this specific cladding has the lowest failure with respect to the others cases studied, and this is equals to 2 10^{-3} under operational conditions, 0.5 during blowdown and 0.1 during reflood. A possible way to mitigate the effect of the accident on the SiC cladding is to apply prestresses on the monolith or on the composite

layers. This would reduce the failure probability of the cladding in case of accident. During operation conditions, a prestress of 42 MPa on the composite would allow meeting the prestress required ($2 \cdot 10^{-6}$). However, a prestress of 321 MPa would be required to prevent failure in case of blowdown. This prestress would be too high for the composite layer, therefore an improvement of the mechanical properties of the cladding would be recommended.

The experiments performed in this work at the higher range of temperatures provide positive results. Finally, silicon carbide and silicon carbide composites have the possibility to be employed in the future nuclear industry. However, even though the behavior of SiC is clear at temperatures up to 1600 °C, oxidation at higher temperatures still requires assessment.

The mechanical properties of the SiC architecture should be further improved in order to allow the cladding withstanding the stresses occurring in accident conditions. The use of the sandwich design with the tantalum liner should be restricted to the GFR project, due to the strong interaction of tantalum with water vapor.

A. Appendix

A.1 ESK SiC chemical analysis

Table A.1: Results of the chemical analysis of the ESK SiC.

Description	%w	SiC SEK	
	Limit of determination	Mean Value	Standard Deviation
Li	0.0001	< 0.0001	
B	0.006	0.328	0.005
N	0.01	0.092	0.005
O	0.01	0.124	0.002
Na	0.0005	< 0.0005	
Mg	0.0002	0.0045	0.0003
Al	0.005	0.0413	0.003
P	0.05	< 0.05	
S	0.005	< 0.005	
K	0.0007	< 0.0007	
Ca	0.0002	0.0187	0.0010
Ti	0.002	0.0087	0.0004
V	0.05	< 0.05	
Cr	0.001	0.0019	0.0001
Mn	0.0003	0.0005	0.00001
Fe	0.006	0.0405	0.0008
Co	0.0002	< 0.0002	
Ni	0.002	< 0.002	
Cu	0.0005	< 0.0005	
Zn	0.0002	0.0035	0.0001
As	0.007	< 0,007	
Se	0.005	< 0.005	
Rb	0.005	< 0.005	
Sr	0.0001	< 0.0001	
Y	0.0001	< 0.0001	
Zr	0.0001	0.0024	0.00002
Nb	0.001	< 0.001	
Mo	0.05	< 0.05	
Ru	0.005	< 0.005	
Rh	0.002	< 0.002	

Pd	0.002	< 0.002
Ag	0.001	< 0.001
Cd	0.0001	< 0.0001
Sn	0.01	< 0.01
Sb	0.002	< 0.002
Te	0.002	< 0.002
Ba	0.0001	< 0.0001
La	0.005	< 0.005
Ce	0.002	< 0.002
Nd	0.001	< 0.001
Sm	0.001	< 0.001
Eu	0.0001	< 0.0001
Gd	0.0002	< 0.0002
Ho	0.0002	< 0.0002
Yb	0.0001	< 0.0001
Lu	0.0001	< 0.0001
Hf	0.0002	< 0.0002
Ta	0.0005	< 0.0005
W	0.002	< 0.002
Re	0.0005	< 0.0005
Os	0.01	< 0.01
Ir	0.001	< 0.001
Pt	0.005	< 0.005
Au	0.002	< 0.002
Pb	0.001	< 0.001
Bi	0.002	< 0.002
Summe		0.6665

A.2 SiC composite elemental analysis

Table A.2: Elemental analysis of the SiC cladding samples provided by the CEA laboratories.

SiC Fibers				CVD SIC			
Element	IGA (ppm)	Element	GDMS (ppm)	Element	IGA Concentration (%at)	Element	GDMS (ppm)
C	50.0%	B	2.0	C	51.7	B	2.54
N	170	C	Matrix	N	0.0089	C	matrix
O	8500	Na	0.31	O	0.35	Na	< 0.04
S	-	Mg	0.17	S		Mg	< 0.04
		Al	2.8	H	0.032	Al	< 0.007
		Si	Matrix			Si	matrix
		P	1.7			P	0.058
		S	57			S	4.4
		Cl	44			Cl	0.12
		K	0.12			K	<0.03
		Ca	1.9			Ca	0.15
		Ti	0.05			Ti	< 0.04
		Cr	7.7			Cr	< 0.1
		Fe	50			Fe	< 0.02
		Co	0.04			Co	< 0.01
		Ni	0.41			Ni	0.03
		Cu	0.08			Cu	< 0.01
		As	0.53			As	< 0.01
		Zr	0.05			Zr	<0.002
		Nb	< 0.01			Nb	< 0.01
		Mo	< 0.01			Mo	< 0.01
		Sn	< 0.008			Sn	< 0.008
		Hf	< 0.006			Hf	< 0.005

Ta	< 1		Ta	< 1
W	0.23		W	< 0.001
Pt	< 0.005		Pt	< 0.005

A.3 Alumina glue

Figure A.1: Data sheet of the glue used for the oxidation experiments.

Polytec PT
Polymere Technologien

Datenblatt
Resbond 989

Version 4, 06/2013

Hochreiner Keramikklebstoff

Zum Feuchte-Schutz empfindlicher elektronischer Baugruppen. Einkomponentig, einfach anwendbar auf Glas, Metall, Keramik, Graphit und Silizium-Carbid. Härtung bei Raum-Temperatur erzeugt höchste Festigkeiten und exzellenten Schutz gegen Feuchte, Chemikalien und Lösungsmittel. Eventuell ist eine Nachhärtung empfohlen.

Typische Eigenschaften

Anzahl der Komponenten	1
Lagerfähigkeit bei 23°C	6 Monate
Topfzeit an Luft	2h
Härtung	RT – durch Verdunsten des Binders

Thermische Eigenschaften

Temperaturbeständigkeit	1648°C
Wärmeleitfähigkeit	2,16 $W \cdot m^{-1} K^{-1}$
Thermische Ausdehnung	8,1 (10^{-6}K)

Elektrische Eigenschaften

Spez. Elektr. Widerstand	$10^8 \Omega$ cm
Dielektr. Spannungsfestigkeit	7,9 kV/mm

Mechanische Eigenschaften

Biegungsfestigkeit	770 N/cm²
Druckfestigkeit	2100 N/cm²

Fließ- und Verarbeitungseigenschaften

Lieferform	cremige, weiße Paste
Basis	Aluminiumoxid
Partikelgröße (durchschn./max)	20/44 µm

Weitere Informationen finden Sie:

- im Sicherheitsdatenblatt von Resbond 989

Zur Beachtung:

Vorstehende Angaben können nur allgemeine Hinweise sein. Bei den aufgeführten Eigenschaften und Leistungsmerkmalen handelt es sich um circa-Werte, diese sind nicht Teil der Produktspezifikation. Wegen der außerhalb unseres Einflusses liegenden Verarbeitungs- und Anwendungsbedingungen und der Vielzahl unterschiedlicher Materialien empfehlen wir, in jedem Fall zunächst ausreichende Eigenversuche durchzuführen. Eine Haftung für konkrete Anwendungsergebnisse kann daher aus den Angaben und Hinweisen in diesem Merkblatt nicht abgeleitet werden.
Mit Erscheinen dieser Ausgabe verlieren alle vorhergehenden technischen Merkblätter ihre Gültigkeit.
Sicherheitsrelevante Daten können dem Sicherheitsdatenblatt entnommen werden.

POLYTEC PT GMBH   Polymere Technologien
Polytec-Platz 1-7 ● 76337 Waldbronn ● Germany
Tel. ++49(0) 7243 604-4000 ● FAX ++49 (0) 7243 604-4200 ● Email: info@polytec-pt.de ● http://www.polytec-pt.de

:

A.4 Zirconia glue

Figure A.2: Data sheet of the glue used for the quench experiments.

Polytec PT
Polymere Technologien

Datenblatt
Resbond 904

Version 3, 06/2008

Keramikklebstoff für sehr hohe Temperaturen

Typische Eigenschaften

Anzahl der Komponenten	1
Lagerfähigkeit bei 23 °C	12 Monate
Topfzeit an Luft	24h
Härtung	Raumtemperatur – durch Verdunsten des Binders

Thermische Eigenschaften

Temperaturbeständigkeit	2200 °C
Wärmeleitfähigkeit	1,4 $W \cdot m^{-1} K^{-1}$
Thermische Ausdehnung	7,3 $(10^{-6} K)$

Elektrische Eigenschaften

Spez. Elektr. Widerstand	$10^8 \Omega$ cm
Dielektr. Spannungsfestigkeit	9,8 kV/mm

Mechanische Eigenschaften

Biegungsfestigkeit	2100 N/cm²
Druckfestigkeit	4200 N/cm²

Fließ- und Verarbeitungseigenschaften

Lieferform	Paste
Basis	ZrO_2
Partikelgröße (durchschn./max)	20/44 µm

Weitere Informationen finden Sie:

- im Sicherheitsdatenblatt von Resbond 904

Zur Beachtung:

Vorstehende Angaben können nur allgemeine Hinweise sein. Bei den aufgeführten Eigenschaften und Leistungsmerkmalen handelt es sich um circa-Werte, diese sind nicht Teil der Produktspezifikation. Wegen der außerhalb unseres Einflusses liegenden Verarbeitungs- und Anwendungsbedingungen und der Vielzahl unterschiedlicher Materialien empfehlen wir, in jedem Fall zunächst ausreichende Eigenversuche durchzuführen. Eine Haftung für konkrete Anwendungsergebnisse kann daher aus den Angaben und Hinweisen in diesem Merkblatt nicht abgeleitet werden.
Mit Erscheinen dieser Ausgabe verlieren alle vorhergehenden technischen Merkblätter ihre Gültigkeit.
Sicherheitsrelevante Daten können dem Sicherheitsdatenblatt entnommen werden.

B. Curriculum vitae and publications

Curriculum Vitae

Education

2001 - 2006	L.S.S. Talete, Rome, Italy
09/2006 - 11/2009	Bachelor´s degree in Energy Engineering La Sapienza University of Rome, Italy
11/2009 - 01/2012	Master´s degree in Energy Engineering La Sapienza University of Rome, Italy
03/2011 – 03/2012	Research internship at the JRC Institute for Transuranium Elements (ITU) Germany

PhD Studies

15/04/2012	Beginning of the PhD at the Institute of Applied Materials – Applied Materials Physics (IAM-AWP) Karlsruhe Institute of Technology (KIT)
06/2013 – 11/2013	Visiting PhD student in the Prof. Kazimi's group at the Massachusetts institute of Technology (MIT)
02/2016	PhD oral exam at KIT Referent: Prof. Dr. hans Jürgen Seifert (IAM-AWP, KIT) Co-referent: Prof. Dr.-Ing Thomas Schulenberg (IKET, KIT)

Publications (peer-reviewed)

V. Angelici Avincola, D.M. Cupid, H.J. Seifert, *Thermodynamic Modeling of the Silica Volatilization in Steam Related to Silicon Carbide, Oxidation Journal of the European Ceramic Society, 35(14), 2015*

V. Angelici Avincola, M. Grosse, M. Steinbrück, *Oxidation at high temperatures in steam atmosphere and quench of silicon carbide composites for nuclear application,* Nuclear Engineering and Design, accepted

V. Angelici Avincola, U. Stegmaier, M. Steinbrück, H.J. Seifert, *Oxidation of Tantalum at High Temperatures in Steam Atmosphere,* Oxidation of Metals, accepted

V. Angelici Avincola, P. Guenoun, K. Shirvan, *Mechanical Performance of SiC multi-layer cladding in PWRs,* submitted to Nuclear Engineering and Design

O. Seeger, V. Avincola, M. Laurie, P.D. Bottomley, V.V. Rondinella, H.J. Allelein, *Experimental Assessment of Accident Scenarios for the High Temperature Reactor Fuel System,* ATW-International Journal for Nuclear Power, 58(2013) p. 618-625

Presentations and Posters

V. Angelici Avincola, *Silicon Carbide Composites Tests for LWRs and GFRs in the Frame of the MatISSE Project,* 21th Intern. Quench Workshop, Karlsruhe, Germany, October 27-29, 2015

V. Avincola, *High Temperature Steam Oxidation Performance of Coatings for Zircaloy,* 20th Intern. Quench Workshop, Karlsruhe, Germany, November 11-14, 2014

V.Avincola, *Oxidation and Quench of Silicon Carbide Composites in High Temperature Corrosive Environments*, 20th Intern. Quench Workshop, Karlsruhe, Germany, November 11-14, 2014

V. Avincola, K. Shirvan, M.S. Kazimi, *Stress Analysis study of Silicon Carbide Cladding Under Accident Conditions*, ANS Annual Conference, Topical Meeting on Nuclear Fuels & Structural Materials for Next Generation Nuclear Reactors, Reno (NV), USA, June 15-19, 2014

V. Avincola, M. Steinbrück, H.J. Seifert, *Oxidation of Silicon Carbide Composites at Very High Temperature with Final Quenching*, Junior Euromat 2014, Lausanne, Switzerland, July 21-25, 2014

M. Pantano, V. Avincola, P. A. de Seze, T. McKrell, M.S. Kazimi*, High Temperature Steam Oxidation Performance of Max-Phase (Ti$_2$AlC) Coated Zirlo*, International Congress on Advances in Nuclear Power Plants, Charlotte (NC), USA, April 6-9, 2014

V. Avincola, M. Große, U. Stegmaier, M. Steinbrück, *Silicon Carbide as Accident Tolerant Cladding: Oxidation and Quench at Very High Temperature,* American Nuclear Society Student Conference, State College (PA), USA, April 3-5, 2014

V. Avincola, M. Große, M. Steinbrück, *Oxidation at High Temperature of Silicon Carbide in Dry Oxygen and Steam Atmosphere,* Materials for Energy Conference, Karlsruhe, Germany, May 20-22, 2013

V. Avincola, M. Große, U. Stegmaier, M. Steinbrück, *Oxidation in Steam and Quenching of Silicon Carbide as Cladding for Nuclear Power Plants,* American Nuclear Society Student Conference, Boston (MA), USA, April 4-6, 2013

V. Avincola, P.D. Bottomley, V.V. Rondinella, *Oxidation Studies of Nuclear Graphite NBG-17 and NBG-18 with KORA device*, 13th International Nuclear Graphite Specialists Meeting, Meitingen, Germany, September 23-26, 2012

V. Avincola, M. Steinbrück, *Oxidation of Silicon Carbide in Oxygen and Water Steam at High Temperature,* 18th Intern. Quench Workshop, Karlsruhe, Germany, November 20-22, 2012

References

Adamsky, R.F., 1959. Oxidation of Silicon Carbide in the Temperature Range 1200 to 1500 °C. *The Journal of Physical Chemistry*, 63(2), pp.305–307.

Adelsberg, L.M., St. Pierre, G.R. & Speiser, R., 1968. Kinetics of the Oxidation of Tantalum by Water Vapor. *Transactions of the Metallurgical Society of AIME*.

Aiello, G. et al., 2003. Modeling of Mechanical Behavior and Design Criteria for SiCf/SiC Composite Structures in Fusion Reactors. *Fusion Engineering and Design*, 65(1), pp.77–88.

Allendorf, M.D. et al., 1995. Theoretical Study of the Thermochemistry of Molecules in the Si-O-H System. *Journal of Physical Chemistry*, 99, pp.15285–15293.

Andersson, J.-O. et al., 2002. Thermo-Calc & DICTRA, Computational Tools for Materials Science. *Calphad*, 26(2), pp.273–312.

Arias, M., Sarrazin, P. & Danger, G., 1981. Tantalum Corrosion at High-Temperature by Steam. *Acta Cientifica Venezolana*, 32(4), pp.286–289.

Ashby, M.F. & Jones, D.R.H., 2005. *Engineering Materials 1: an Introduction to Properties, Applications and Design* 3rd ed. Elsevier.

Baboian, R., 2005. *Corrosion Tests and Standards: Application and Interpretation: (MNL 20)* 2nd edition AST.

Balat-Pichelin, M., Charpentier, L. & Audubert, F., 2010. High Temperature Oxidation of SiC under Helium with Low Oxygen Partial Pressure. *ECS Transactions*, 25(25), pp.123–131.

Bansal, N.P. & Lamon, J., 2015. *Ceramic Matrix Composites: Materials, Modeling and Technology*, Wiley.

Barron, R.F. & Barron, B.R., 2012. *Design for Thermal Stresses*, New Jersey: John Wiley & Sons.

Bathe, K.J., 2000. *ADINA Theory and Modeling Guide. Report ARD 00-7*, Watertown (MA).

Ben-Belgacem, M. et al., 2014. Thermo-mechanical Analysis of LWR SiC/SiC Composite Cladding. *Journal of Nuclear Materials*, 447(1–3), pp.125–142.

Bind, J.-M., 1978. Phase transformation during hot-pressing of cubic SiC. *Materials Research Bulletin*, 13(2), pp.91–96.

Bouzouita, K. & Desmaison, J., 2002. Oxidation Mechanism of Tantalum in Carbon Dioxide. *Journal of Alloys and Compounds*, 336(1-2), pp.270–279.

Brachet, J.C. et al., 2014. CEA Studies on Advanced Nuclear Fuel Claddings for Enhanced Accident Tolerant LWRs Fuel (LOCA and beyond LOCA conditions). In *Contribution of Materials Investigations and Operating Experience to LWRs' Safety, Performance and Reliability France, Avignon.*

Bragg-Sitton, S., 2014. Development of Advanced Accident- Tolerant Fuels for Commercial LWRs. *Nuclear News*, (March), pp.83–91.

Buet, E. et al., 2012. Influence of Chemical and Physical Properties of the last Generation of Silicon Carbide Fibres on the Mechanical Behaviour of SiC/SiC Composite. *Journal of the European Ceramic Society*, 32(3), pp.547–557.

Bunsell, A.R. & Piant, A., 2006. A Review of the Development of Three Generations of Small Diameter Silicon Carbide Fibres. *Journal of Materials Science*, 41(3), pp.823–839.

Bürgel, R., Jürgen Maier, H. & Niendorf, T., 2011. *Handbuch Hochtemperatur- Werkstofftechnik*, Wiesbaden: Vieweg+Teubner.

Carpenter, D.M., 2010. *An Assessment of Silicon Carbide as a Cladding Material for Light Water Reactors*. MIT PhD Thesis.

Carpenter, D.M., 2006. *Assessment of Innovative Fuel Designs for High Performance Light Water Reactors*. MIT MS Thesis.

Chandrasekharan, R. et al., 2005. Thermal Oxidation of Tantalum Films at Various Oxidation States from 300 to 700°C. *Journal of Applied Physics*, 98, pp.1–10.

Chase, M., 1998. NIST-JANAF Thermochemical Tables, 4th Edition. *Journal of Physical and Chemical Reference Data*, Monograph, p.1952.

Costello, J.A. & Tressler, R.E., 1986. Oxidation Kinetics of Silicon Carbide Crystals and Ceramics: I, In Dry Oxygen. *Journal of the American Ceramic Society*, 69(9), pp.674–681.

Cowgill, M.G. & Stringer, J., 1960. The Effect of Oxygen Pressure on the High Temperature Oxidation Of tantalum. *Journal of the Less Common Metals*, 2, pp.233–240.

CTP, 2014. Private Communication.

Darnell, A.J., 1968. The Characterization of High-Temperature Vapors. John L. Margrave. *Science*, 161(3841), pp.562–563.

Davis, J.R., 1997. *ASM Specialty Handbook: Heat-Resistant Materials*, ASM International.

Deal, B.E. & Grove, A.S., 1965. General Relationship for the Thermal Oxidation of Silicon. *Journal of Applied Physics*, 36(12), p.3770.

DeHoff, R., 2006. *Thermodynamics in Materials Science* Second Edition, CRC Editors.

Dinsdale, A.T., 1991. SGTE Data for Pure Elements. *Calphad*, 15, pp.317–425.

Doremus, R.H., 2001. *Diffusion of Reactive Molecules in Solids and Melts*, John Wiley & Sons.

Doremus, R.H., 2002. Viscosity of Silica. *Journal of Applied Physics*, 92(12), p.7619.

Drowart, J. et al., 2005. High-temperature Mass Spectrometry: Instrumental Techniques, Ionization Cross-Sections, Pressure Measurements, and Thermodynamic Data (IUPAC Technical Report). *Pure and Applied Chemistry*, 77(4), pp.683–737.

Edgar, C.U., States, U. & Corporation, S., 1964. Enhancement of Diffusion-Limited Rates of Vaporization of Metals. *Vacuum*, 14, p.137.

Farmer, M.T. et al., 2014. Scoping Assessments of ATF Impact on Late-stage Accident Progression Including Molten Core–concrete Interaction. *Journal of Nuclear Materials*, 448(1-3), pp.534–540.

Feinroth, H., 2012. Silicon Carbide TRIPLEX™ Fuel Clad for Accident Resistance and Durability. In *1st ICMST Conference*.

Forquin, P. et al., 2003. Experiments and modelling of the compressive behaviour of two SiC ceramics. *Mechanics of Materials*, 35, pp.987–1002.

Franzen, H.F., Khan, A.S. & Peterson, D.T., 1977. The Solubility of Hydrogen in Tantalum at High Temperatures. *Journal of the Less Common Metals*, 55(1), pp.143–147.

Gao, W., 2008. *Developments in High Temperature Corrosion and Protection of Materials*, Elsevier.

Garg, S. & Krishnamurthy, N., 1996. The O-Ta (oxygen-tantalum) System. *Journal of Phase Equilibria*, 17(1), pp.63–77. Figure reprinted with permission of Springer.

Gaskell, D.R., 2003. *Introduction to the Thermodynamics of Materials, Fifth Edition*, Figure reprinted with permission of CRC Press.

George, N.M. et al., 2015. Neutronic Analysis of Candidate Accident-tolerant Cladding Concepts in Pressurized Water Reactors. *Annals of Nuclear Energy*, 75, pp.703–712.

Goto, T., 2006. High Temperature Passive Oxidation Mechanism of CVD SiC. *Materials Science Forum*, 522-523, pp.27–36.

Goto, T. & Homma, H., 2002. High-temperature Active/passive Oxidation and Bubble Formation of CVD SiC in O_2 and CO_2 Atmospheres. *Journal of the European Ceramic Society*, 22(14-15), pp.2749–2756.

Goto, T., Homma, H. & Hirai, T., 2002. Effect of Oxygen Partial Pressure on the High-Temperature Oxidation of CVD SiC. *Corrosion Science*, 44, pp.359–370.

Gröbner, J., Lukas, H.L. & Aldinger, F., 1996. Thermodynamic Calculation of the Ternary System Al-Si-C. *Calphad*, 20(2), pp.247–254.

Grosse, M., 2010. Comparison of the High Temperature Steam Oxidation Kinetics of Advanced Cladding Materials. *Nuclear Technology*, 170, pp.272–279.

Grosse, M. et al., 2009. Influence of Oxide Layer Morphology on Hydrogen Concentration in Tin and Niobium Containing Zirconium Alloys after High Temperature Steam Oxidation. *Journal of Nuclear Materials*, 385(2), pp.339–345.

Gulbransen, E.A., Andrew, K.F. & Brassart, F.A., 1966. The Oxidation of Silicon Carbide at 1150° to 1400°C and at 9×10^{-3} to 5×10^{-1} Torr Oxygen Pressure. *Journal of The Electrochemical Society*, 113(12).

Gulbransen, E.A. & Jansson, S.A., 1972. The High-temperature Oxidation, Reduction, and volatilization Reactions of Silicon and Silicon Carbide. *Oxidation of Metals*, 4(3), pp.181–201.

Gupta, S.V., 2012. *Mass Metrology*, Springer.

Guy, A.G., 1976. *Essentials of Materials Science*, McGraw-Hill. Permission requested to McGraw-Hill.

Hack, K., 2008. *The SGTE Casebook, CRC Press* 2nd Edition. K. Hack, CRC press.

Hannam, A.L. & Shaffer, P.T.B., 1969. Revised X-ray diffraction line intensities for silicon carbide polytypes. *Journal of Applied Crystallography*, 2(45).

Hashimoto, A., 1992. The effect of H_2O Gas on Volatilities of Planet-forming Major Elements. I - Experimental Determination of Thermodynamic Properties of Ca-, Al-, and Si-hydroxide Gas Molecules and its Application to the Solar Nebula. *Geochimica et Cosmochimica Acta*, 56(1), pp.511–532.

Heuer, A.H. & Lou, V.L.K., 1990. Volatility Diagrams for Silica, Silicon Nitride, and Silicon Carbide and Their Application to High-Temperature Decomposition and Oxidation. *Journal American Ceramic Society*, 73(10), pp.2785–3128.

Hildenbrand, D.L. & Lau, K.H., 1998. Comment on "Thermochemistry of Gaseous SiO(OH), SiO(OH)$_2$, and SiO$_2$,"[J. Chem. Phys. 101, 6076 (1994)]. *The Journal of Chemical Physics*, 108(15), p.6535.

Hildenbrand, D.L. & Lau, K.H., 1994. Thermochemistry of gaseous SiO(OH), SiO(OH)$_2$, and SiO$_2$. *The Journal of Chemical Physics*, 101(7), p.6076.

Hinze, J.W. & Graham, H.C., 1976. The Active Oxidation of Si and SiC in the Viscous Gas-Flow Regime. *Journal of The Electrochemical Society*, 123(7), p.1066.

Hinze, J.W., Tripp, W.C. & Graham, H.C., 1975. *Mass Transport Phenomena in Ceramics* A. R. Cooper & A. H. Heuer, Boston, MA: Springer US.

Ho, P. & Melius, C.F., 1990. Theoretical Study of the Thermochemistry of Fluorosilanes (SiFn and SiHnFm) Compounds and Hexafluorodisilane. *The Journal of Physical Chemistry*, 94(12), pp.5120–5127.

Hodkiewicz, J., 2010. *Characterizing Carbon Materials with Raman Spectroscopy* Scientific., Thermo Fisher Scientific.

Hoshino, T. et al., 2003. Diffusion of molecular and atomic oxygen in silicon oxide. *Japanese Journal of Applied Physics, Part 1: Regular Papers and Short Notes and Review Papers*, 42, pp.3560–3565.

IAEA Nuclear Energy Series NF-T-2.1, 2010. *Review of Fuel Failures in Water Cooled Reactors*, Vienna.

INL, 2005. *RELAP5-3D© Code Manual Volume I: Code Structure, System Models, and Solution Methods: INEEL-EXT-98-00834, Revision 2.4*,

Irene, E.A., 1977. Silicon Oxidation Studies: The Role of H$_2$O. *Journal of The Electrochemical Society*, 124(11), p.1757.

Ishibashi, R. et al., 2014. Development of Inherently Safe Technologies for Large Scale BWRs: (4) Hydrogen Explosion Prevention System Using SiC Fuel Claddings. In *Volume 3: Next Generation Reactors and Advanced Reactors; Nuclear Safety and Security*. ASME, p. V003T06A052.

Jacobson, N., Myers, D., et al., 2005. Interactions of Water Vapor with Oxides at Elevated Temperatures. *Journal of Physics and Chemistry of Solids*, 66(2-4), pp.471–478.

Jacobson, N., Opila, E.J., et al., 2005. Thermodynamics of Gas Phase Species in the Si–O–H System. *The Journal of Chemical Thermodynamics*, 37(10), pp.1130–1137.

Jacobson, N.S., 1993. Corrosion of Silicon-Based Ceramics in Combustion Environments.

Jagodzinski, H., 1949. Eindimensionale Fehlordnung in Kristallen und ihr Einfluss auf die Rontgeninterferenzen. I. Berechnung des Fehlordnungsgrades aus den Rontgenintensitaten. *Acta Crystallographica*, 2(1).

Jellinek, H.H.G., 1986. The Thermal Dissociation of Water: the Forgotten Literature. *Journal of Chemical Education*, 63(12), p.1029.

Jorgensen, P.J. et al., 1960. Effects of Oxygen Partial Pressure on the Oxidation of Silicon Carbide. *Journal of the American Ceramic Society*, 43(4), pp.209–212.

Jorgensen, P.J., Wadsworth, M.E. & Cutler, I.B., 1961. Effects of Water Vapor on Oxidation of Silicon Carbide. *Journal of the American Ceramic Society*, 44(6), pp.258–261.

Kalen, J.D., Boyce, R.S. & Cawley, J.D., 1991. Oxygen Tracer Diffusion in Vitreous Silica. *Journal of the American Ceramic Society*, 74(1), pp.203–209.

Katoh, Y. et al., 2014. Continuous SiC Fiber, (CVI) SiC Matrix Composites for Nuclear Applications: Properties and Irradiation Effects. *Journal of Nuclear Materials*, 448(1–3), pp.448–476.

Katoh, Y. et al., 2007. Current Status and Critical Issues for Development of SiC Composites for Fusion Applications. *Journal of Nuclear Materials*, 367-370 A(2007), pp.659–671.

Katoh, Y. et al., 2011. Stability of SiC and Its Composites at High Neutron Fluence. *Journal of Nuclear Materials*, 417(1-3), pp.400–405.

Katoh, Y. et al., 2010. Thermophysical and Mechanical Properties of Near-stoichiometric Fiber CVI SiC/SiC Composites after Neutron Irradiation at Elevated Temperatures. *Journal of Nuclear Materials*, 403(1-3), pp.48–61.

Katoh, Y., Kishimoto, H. & Kohyama, A., 2002. Low Temperature Swelling in Beta-SiC Associated with Point Defect Accumulation. *Materials Transaction*, 43(4), pp.612–616.

Katsui, H., Oguma, M. & Goto, T., 2014. Carbon Interlayer Between CVD SiC and SiO_2 in High-Temperature Passive Oxidation N. Jacobson, *Journal of the American Ceramic Society*, 97(5), pp.1633–1637.

Kilpatrick, M. & Lott, S.K., 1965. Reaction of Flowing Steam with Refractory Metals Niobium and Tantalum. *Journal of the Less Common Metals*, 8(5), p.299.

Kim, D. et al., 2015. Fabrication and Measurement of Hoop Strength of SiC Triplex Tube for Nuclear Fuel Cladding Applications. *Journal of Nuclear Materials*, 458, pp.29–36.

Kim, H.-E. & Moorhead, A.J., 1990. Effects of Active Oxidation on the Flexural Strength of a-Silicon Carbide. *Journal American Ceramic Society*, 73(7), pp.1868–1872.

Kleykamp, H., 1998. Gibbs Energy of Formation of SiC: a Contribution to the Thermodynamic Stability of the Modifications. *Berichte der Bunsengesellschaft für physikalische Chemie*, 102(9), pp.1231–1234.

Kofstad, P., 1962a. On The Defect Structure of Ta2O5. *Journal of The Electrochemical Society*, 109(9), p.776.

Kofstad, P., 1962b. Oxidation of Tantalum in Temperature range 500-700 degrees °C. *Journal of the Institute of Metals*, 90(7).

Kofstad, P., 1963a. Studies of the Oxidation of Tantalum at 1000°–1300°C. *Journal of the Less Common Metals*, 5, pp.158–170.

Kofstad, P., 1963b. The Oxidation Behavior of Tantalum at 700°–1000°C. *Journal of The Electrochemical Society*, 110(6), p.491.

Kofstad, P. & Krudtaa, O.J., 1963. High Temperature Metallographic Microscope Studies of the Initial Oxidation of Tantalum. *Journal of the Less Common Metals*, 5(6), pp.477–492.

Koyanagi, T., Kondo, S. & Hinoki, T., 2011. The Influence of Sintering Additives on the Irradiation Resistance of NITE SiC. *Journal of Nuclear Materials*, 417(1-3), pp.435–439.

Krikorian, O.H., 1970. Thermodynamics of the Silica-Steam System. In *Presented at the Symposium on Engineering with Nuclear Explosives (unpublished).* Las Vegas, NV.

Kumashiro, Y., 2000. *Electric Refractory Materials*, CRC Press.

Lamkin, M.A., Riley, F.L. & Fordham, R.J., 1992. Oxygen Mobility in Silicon Dioxide and Silicate Glasses: a Review. *Journal of the European Ceramic Society*, 10(5), pp.347–367.

Lee, Y. et al., 2013. Safety Assessment of SiC Cladding Oxidation Under Loss of Coolant Accident. *Nuclear Technology*.

Lee, Y., 2013. *Safety of Light Water Reactor Fuel with Silicon Carbide Cladding*. MIT PhD thesis.

Lee, Y. & Kazimi, M.S., 2015. A Structural Model for Multi-layered Ceramic Cylinders and its Application to Silicon Carbide Cladding of Light Water Reactor Fuel. *Journal of Nuclear Materials*, 458, pp.87–105.

Li, S. et al., 2010. Microstructural Evolution of Coating-modified 3D C/SiC Composites after Annealing in Wet Oxygen at Different Temperatures. *Corrosion Science*, 52(9), pp.2837–2845.

Liao, F. et al., 2003. High-rate chemical vapor deposition of nanocrystalline silicon carbide films by radio frequency thermal plasma. *Materials Letters*, 57, pp.1982–1986.

Lou, V.L.K., Mitchell, T.E. & Heuer, A.H., 1985. REVIEW - Graphical Displays of the Thermodynamics of High-Temperature Gas-Solid Reactions and Their Application to Oxidation of Metals and Evaporation of Oxides. *Journal of the American Ceramic Society*, 68(2), pp.49–58.

Lukas, H.L., Fries, S.G. & Sundman, B., 2007. *Computational Thermodynamics: The CALPHAD Method* Cambridge.

Madou, M.J., 2002. *Fundamentals of Microfabrication: The Science of Miniaturization* 2nd edition, CRC Press.

McCafferty, E., 2010. *Introduction to Corrosion Science*, Springer.

Mieskowski, D.M., Mitchell, T.E. & Heuer, A.H., 1984. Bubble Formation in Oxide Scales on SiC. *Journal American Ceramic Society*, 67(1), pp.17–18.

Mills, R.L. et al., 2010. Total bond energies of exact classical solutions of molecules generated by MILLSIAN 1.0 compared to those computed using modern 3–21 G and 6–31 G* basis sets. *Physics Essays*, 23(1), pp.153–199.

More, K.L. et al., 2000. Observations of Accelerated Silicon Carbide Recession by Oxidation at High Water-Vapor Pressures. *Journal of the American Ceramic Society*, 83(1), pp.211–13.

Narushima, T. et al., 1994. Active-to-Passive Transition and Bubble Formation for High-Temperature Oxidation of Chemically Vapor-Deposited Silicon Carbide in CO-CO$_2$ Atmosphere. *Journal of the American Ceramic Society*, 77(4), pp.1079–1082.

Narushima, T. et al., 1990. High-Temperature Oxidation of Chemically Vapor-Deposited Silicon Carbide in Wet Oxygen at 1823 to 1923 K. *Journal of the American Ceramic Society*, 73(12), pp.3580–3584.

Narushima, T. et al., 1997. High-temperature Oxidation of Silicon Carbide and Silicon Nitride. *Materials Transactions - JIM*, 38(10), pp.821–835.

National Research Council, 1970. *High-temperature Oxidation-Resistant Coatings: Coatings for Protection from Oxidation of Superalloys, Refractory Metals, and Graphite*, Washington: National Academy of Sciences.

Nickel, K.G., 1992. The role of condensed silicon monoxide in the active-to-passive oxidation transition of silicon carbide. *Journal of the European Ceramic Society*, 9(1), pp.3–8.

De Nicola, M. et al., 1995. Étude Cinétique de l'Oxydation Thermique du Tantale dans Atmosphères Mixtes Oxygène - Vapeur d'Eau. *Journal de Chimie-Physique et de Physico-Chimie Biologique*, 92(5), pp.1142–1153.

Niffenegger, M. & Reichlin, K., 2012. The Proper Use of Thermal Expansion Coefficients in Finite Element Calculations. *Nuclear Engineering and Design*, 243, pp.356–359.

Norman, N., Kofstad, P. & Krudtaa, O.J., 1962. Metallic Oxide Phases of Niobium and Tantalum II. Metallographic Studies. *Journal of the Less Common Metals*, 4(2), pp.124–137.

Nozawa, T. et al., 2012. Determination and Prediction of Axial/off-axial Mechanical Properties of SiC/SiC Composites. *Fusion Engineering and Design*, 87(5-6), pp.803–807.

OECD, 2009. *Nuclear Fuel Behaviour in Loss-of-coolant Accident (LOCA) Conditions*,

Ogura, Y. & Morimoto, T., 2002. Mass Spectrometric Study of Oxidation of SiC in Low-Pressure Oxygen. *Journal of The Electrochemical Society*, 149(4), pp.J47 – J52.

Opila, E.J., 1995. Influence of Alumina Reaction Tube Impurities on the Oxidation of Chemically-Vapor-Deposited Silicon Carbide. *Journal of the American Ceramic Society*, 78(4), pp.1107–1110.

Opila, E.J., 2003. Oxidation and Volatilization of Silica Formers in Water Vapor. *Journal of the American Ceramic Society*, 86(8), pp.1238–1248.

Opila, E.J., 1999. Variation of the Oxidation Rate of Silicon Carbide with Water-Vapor Pressure. *Journal of the American Ceramic Society*, 36(3), pp.625–636.

Opila, E.J., 2004. Volatility of Common Protective Oxides in High-Temperature Water Vapor: Current Understanding and Unanswered Questions. In *Materials Science Forum*. pp. 765–774.

Opila, E.J., Fox, D.S. & Jacobson, N.S., 1997. Mass Spectrometric Identification of Si – O – H (g) Species from the Reaction of Silica with Water Vapor at Atmospheric Pressure. *Journal American Ceramic Society*, 80(4), pp.1009–1012.

Opila, E.J. & Hann, R.E., 1997. Paralinear Oxidation of CVD SiC in Water Vapor. *Journal of the American Ceramic Society*, 80(1), pp.197–205.

Opila, E.J. & Smialek, J.L., 1999. SiC Recession Caused by SiO_2 Scale Volatility under Combustion Conditions: II, Thermodynamics and Gaseous-Diffusion Model. *Journal of the American Ceramic Society*, 82, pp.1826–1834.

Opila & Jacobson, N.S., 1995. SiO(g) Formation from SiC in Mixed Oxidizing-reducing Gases. *Oxidation of Metals*, 44, pp.527–544.

Pantano, M. et al., 2014. High Temperature Steam Oxidation Performance of MAX PHASE Ti_2AlC Coated Zirlo. In *Proceedings of ICAPP 2014*. Charlotte, USA.

Park, D.J. et al., 2015. A study of the oxidation of FeCrAl alloy in pressurized water and high-temperature steam environment. *Corrosion Science*, 94, pp.459–465.

Park, D.J. et al., 2014. Oxidation Behavior of Silicon Carbide at 1200°C in Both Air and Water–vapor-rich Environments. *Corrosion Science*, 88, pp.416–422.

Pint, B.A. et al., 2013. High temperature oxidation of fuel cladding candidate materials in steam–hydrogen environments. *Journal of Nuclear Materials*, 440(1-3), pp.420–427.

Plyasunov, A. V., 2011. Thermodynamic Properties of H4SiO4 in the Ideal Gas State as Evaluated from Experimental Data. *Geochimica et Cosmochimica Acta*, 75(13), pp.3853–3865.

Pongrácz, A., 2009. *SiC Nanocrystals on Si*. Budapest University of Technology: PhD thesis.

Prater, J.T. & Courtright, E.L., 1987. Oxidation of Zircaloy-4 in Steam at 1300 °C to 2400 °C. In *Zirconium in the Nuclear Industry, 7th International Symposium, ASTM STP 939,* Philadelphia: R.B. Adamson and L.F.P Van Swan, American Society for Testing and Materials, pp. 489–503.

Predel, B., 1996. *H-Ta (Hydrogen-Tantalum)* O. Madelung, Volume 5f of the series Landolt-Börnstein - Group IV Physical Chemistry.

Presser, V. & Nickel, K.G., 2008. Silica on Silicon Carbide. *Critical Reviews in Solid State and Materials Sciences*, 33(1), pp.1–99. Figure reprinted with permission of Taylor and Francis Group LLC Books

Ramsdell, L.S., 1947. Studies on Silicon Carbide. *American Mineralogist*, 32, pp.64–82.

Reich, S. & Thomsen, C., 2004. Raman Spectroscopy of Graphite. *Philosophical transactions. Series A, Mathematical, physical, and engineering sciences*, 362, pp.2271–2288.

Richards, K.J. & Wadsworth, M.E., 1954. Oxidation Kinetics of Tantalum in Carbon Dioxide. *Transactions of the Metallurgical Society of AIME*, 230(32).

Riedel, R. & Chen, I.-W., 2013. *Ceramics Science and Technology, Applications*, John Wiley & Sons.

Riedel, R. & Chen, I.-W., 2011. *Ceramics Science and Technology, Materials and Properties*, John Wiley & Sons.

Robinson, R.C. & Smialek, J.L., 1999. SiC Recession Caused by SiO_2 Scale Volatility under Combustion Conditions: I, Experimental Results and Empirical Model. *Journal of the American Ceramic Society*, 82(7), pp.1817–1825.

Rodríguez-Viejo, J. et al., 1993. 18O Diffusion through Amorphous SiO_2 and Cristobalite. *Applied Physics Letters*, 63(14), p.1906.

Rosinski, S. et al., 2001. *Effects of Radiation on Materials: 20th International Symposium*, ASTM STP1405.

Rutz, L. & Bockhorn, H., 2007. Theoretical Study of the Structure, Properties and Formation of SiO_2 Clusters. In Chania, Crete: Third European Combustion Meeting 2007.

Sangster, R.C., 2005. *Formation of Silicon Nitride: From the 19th to the 21st Century* Uetikon-Zu. M. S. Foundations.

San-Martin, A. & Manchester, F.D., 1991. The H-Ta (hydrogen-tantalum) System. *Journal of Phase Equilibria*, 12(3), pp.332–343. Figure reprinted with permission of Springer.

Sarva, S. & Nemat-Nasser, S., 2001. Dynamic compressive strength of silicon carbide under uniaxial compression. *Materials Science and Engineering A*, 317, pp.140–144.

Schneider, B. et al., 1998. A Theoretical and Experimental Approach to the Active-to-passive Transition in the Oxidation of Silicon Carbide: Experiments at High Temperatures and Low Total Pressures. *Journal of Materials Science*, 33(2), pp.535–547.

Scientific Group Thermodata, 2014. www.sgte.org.

Shirvan, K. & Kazimi, M.S., 2014. Technical and Economic Viability of Ceramic Multi-Layer Composite SiC Cladding for LWRs. In *IAEA, Oakridge National Lab, 2014.*

Singh, D. et al., 2012. *Mechanical Properties and Performance of Engineering Ceramics and Composites VII - Wiley Online Library*,

Singhal, S.C., 1976. Oxidation Kinetics of Hot-Pressed Silicon Carbide. *Journal of Materials Science*, 11, pp.1246–1253.

Snead, L.L. et al., 2007. Handbook of SiC Properties for Fuel Performance Modeling. *Journal of Nuclear Materials*, 371(1-3), pp.329–377.

Stempien, J.D., 2011. *Behavior of Triplex Silicon Carbide Fuel Cladding Designs Tested Under Simulated PWR Conditions*. MIT MS Thesis.

Stephens, J.R. & Garlick, R.G., 1966. *Compatibility of Tantalum, Columbium, abd their Alloys with Hydrogen in Presence of Temperature Gradient.*

Stephenson, N.C. & Roth, R.S., 1971. Structural Systematics in the Binary System Ta_2O_5-WO_3. V. The Structure of the Low-temperature Form of Tantalum Oxide L-Ta_2O_5. *Acta Crystallographica B*, 27, pp.1037–1044.

Stewart, R.B. & Jacobsen, R., 1989. Thermodynamic Properties of Argon from the Triple Point to 1200 K with Pressure to 1000 MPa. *Journal of Physical and Chemical Reference Data*, 18(2).

Stringer, J., 1967. Rate-Controlling Processes in the High-Temperature Oxidation of Tantalum. *Journal of The Electrochemical Society*, 114(5), p.428.

Stringer, J., 1968. The Oxidation of Tantalum at High Temperatures: Geometrical Effects. *Journal of the Less Common Metals*, 16(1), pp.55–64.

Sukjai, Y. et al., 2013. Fuel Performance Evaluation of Thick SiC Clad PWR Fuel. *CANES Report MIT-ANP-TR-149*.

Taxak, M., Kumar, S. & Krishnamurthy, N., 2013. Thermodynamic Parameters for the Ta – Cr – H Solid Solution from Equilibrium (P – C – T) data. *The Journal of Chemical Thermodynamics*, 67, pp.48–54.

Tedmon, C.S., 1966. The Effect of Oxide Volatilization on the Oxidation Kinetics of Cr and Fe-Cr Alloys. *Journal of the Electrochemical Society*, 113(8), pp.766–768.

Terrani, K.A. et al., 2014. Silicon Carbide Oxidation in Steam up to 2 MPa. *Journal of the American Ceramic Society*, 97(8), pp.2331–2352.

Tortorelli, P.F. & More, K.L., 2003. Effects of High Water-Vapor Pressure on Oxidation of Silicon Carbide at 1200°C. *Journal of the American Ceramic Society*, 86(8), pp.1249–1255.

Vaughan, D.A., Stewart, O.M. & Schwartz, C.M., 1960. *Determination of Interstitial Solid-Solubility Limit in Tantalum and Identification of the Precipitate Phases*,

Voitovich, V.B. et al., 1995. High-temperature Oxidation of Tantalum of Different Purity. *Oxidation of Metals*, 43(5-6), pp.509–526.

Wagner, C., 1958. Passivity During the Oxidation of Silicon at Elevated Temperatures. *Journal of Applied Physics*, 29, pp.1295–1297.

Wagstaff, F., 1969. Crystallization and Melting Kinetics of Cristobalite. *Journal of the American Ceramic Society*, 49(3), pp.118–121.

Whitmarsh, C.L., 1962. *Review of Zircaloy-2 and Zircaloy 4 Properties Relevant to N.S. Savannah Reactor Design*,

Yueh, K., Carpenter, D. & Feinroth, H., 2010. Clad in Clay. *Nuclear Engineering International*, 55(666), pp.14–16.

Zabinski, J.S. & McDevitt, N.T., 1995. *Raman Spectra of Inorganic Compounds Related to Solid State Tribochemical Studies*,

Zhang, F. et al., 2014. A Combined Thermodynamic/Kinetic Modeling Approach to Predict SiC Recession Due to SiO_2 Scale Volatility Under Combustion Environments. *Journal of Phase Equilibria and Diffusion*, 35(6), pp.724–734. Figure reprinted with permission of Springer.

Ziegler, G., Heinrich, J. & Wötting, G., 1987. Relationships between Processing, Microstructure and Properties of Dense and Reaction-bonded Silicon Nitride. *Journal of Materials Science*, 22(9), pp.3041–3086.

Zinkle, S.J. et al., 2014. Accident Tolerant Fuels for LWRs: a Perspective. *Journal of Nuclear Materials*, 448(1-3).

Acknowledgements

I am extremely grateful to my Professor Dr, Hans Juergen Seifert, for the advice he has provided throughout all the years I spent working on the thesis. He continually allowed this manuscript to be my own work, but steered me in the right direction whenever it was needed. His deep insights helped me at various stages of my research.

Besides my advisor, I would like to thank Prof. Thomas Schulenberg for his willingness to read the thesis and help with his comments the improvement of the work.

This thesis would not have been possible unless the support of my supervisor, Dr. Martin Steinbrueck, whose encouragement, guidance and support from the initial to the final level enabled me to develop an understanding of the subject. I owe my deepest gratitude to Mirco Große for his advices and to Ulrike Stegmaier and Petra Severloh, who were always willing to help me during the hard time in the lab. I acknowledge the help provided by Dr. Harald Leiste, Dr. Thomas Bergfeldt and Dr. Monika Rinke during the XRD, chemical analyses and Raman spectroscopy. I thank Ms. Cathrin Schuler and Ms. Jutta Howell for the help they provided during these years.

I am thankful to Dr. Damian Cupid, who was willing to help me with CALPHAD. The joy and enthusiasm he has for research was contagious and motivational for me.

I thank all the people in the department that were part of the everyday life at IAM. My office mates Melanie, Dajian, Christoph, Maren made every day of my PhD time a good day. A special thank to Alex, who always provided encouragement and support whenever I was in need of it. Thanks to Petronela, with whom discussions late evenings were really fruitful.

It has been a great honor for me to work with Prof. Kazimi during my visiting period at MIT. I will never forget his humanity and his advices. I am very thankful he gave me the possibility to work in his group in 2013. May his soul rest in peace. I fondly thank Dr. Shirvan, who was a friend and a guide in the impervious world of FEA, always with patience and enthusiasm. Remarkable was the contribution